



UNIVERSITÀ  
DEGLI STUDI  
FIRENZE

SCUOLA DI SCIENZE MATEMATICHE,  
FISICHE E NATURALI

CORSO DI LAUREA MAGISTRALE  
IN SCIENZE FISICHE E ASTROFISICHE

# Ultracold chromium - lithium fermionic mixtures with resonant interactions

Miscele fermioniche ultrafredde di  
cromo - litio con interazioni risonanti

## Candidate

Stefano Finelli (ID number 6029347)

## Thesis Advisors

Dr. Matteo Zaccanti

Prof. Marco Fattori

Academic Year 2020/2021

Thesis not yet defended.

---

**Ultracold chromium - lithium fermionic mixtures with resonant interactions**  
Master Thesis, University of Florence

2021 Stefano Finelli.

This thesis has been typeset by  $\text{\LaTeX}$  and the UniFiTh class.

Version: October 11, 2021

Author's email: [stefano.finelli1@stud.unifi.it](mailto:stefano.finelli1@stud.unifi.it)

## Abstract

In this thesis I report on the first experimental realization of ultracold mixtures of fermionic chromium ( $^{53}\text{Cr}$ ) and lithium ( $^6\text{Li}$ ) atoms, and on an extensive investigation of their interspecies collisional properties.

Our strategy to attain ultralow temperatures with such a novel system relies on an all-optical approach. Atoms are first collected in a double-species magneto-optical trap (MOT), where different laser cooling stages are employed to reach temperatures of a few hundreds of microkelvins, close to the Doppler limit. Within an overall MOT loading time of seven seconds, we produce cold clouds containing more than  $5 \times 10^8$  Li atoms and  $8 \times 10^7$  Cr atoms, demonstrating more than a 100-fold increase in the cold chromium sample, relative to previous studies. The two atomic species are then directly loaded from the MOT into a bichromatic optical dipole trap (BODT), realized by a combination of high-power infrared laser beams (confining more tightly Li than Cr) and green light (tightly confining Cr and anti-confining Li). By carefully adjusting the intensity of the green trapping beam, which strongly blue-shifts the chromium laser cooling transition – thus creating an effective dark spot for the chromium MOT – we are able to collect within the BODT more than  $10^6$  Cr and  $10^7$  Li atoms, at temperatures of about 300  $\mu\text{K}$ . We then reach the ultracold regime by relying on efficient evaporative cooling of the two lowest Zeeman states of lithium, achieved near the homonuclear Feshbach resonance at 832 Gauss, and on sympathetic cooling of the chromium component, polarized in its lowest Zeeman sublevel. After a 5 s-long evaporation stage, only slightly longer than the optimum one for evaporation of single-species Li samples, we obtain chromium-lithium mixtures comprising up to  $3 \times 10^5$  Cr and  $1 \times 10^6$  Li atoms, in thermal equilibrium at ultralow temperatures of about 5  $\mu\text{K}$ .

With such a novel ultracold heteronuclear system, so far uniquely available in our lab worldwide, we have performed extensive Feshbach loss spectroscopy involving up to six different scattering channels. This experimental effort, which constitutes one among the main achievements of my thesis work, has led to the discovery of about 50 heteronuclear Feshbach resonances, located at magnetic fields spanning from 0 to 1500 G. Such a large amount of scattering resonances, which include both *s*-wave and higher-order partial wave features, constitutes the foundation for a quantum-collisional model for  $^{53}\text{Cr}$ - $^6\text{Li}$  mixtures, with potentially predictive power also for all other chromium-lithium isotopic pairs. The model is being developed by our theory collaborator, Prof. A. Simoni (University of Rennes), a world-renown expert of multichannel calculations.

Notably, our experimental activity has already enabled us to identify a few, sufficiently broad Cr-Li *s*-wave Feshbach resonances. Our work thus constitutes a first, crucial step towards a wealth of next-future experimental studies in the quantum-degenerate regime: From the investigation of exotic few- and many-body phenomena in resonantly interacting Fermi mixtures, to the realization of dipolar quantum gases of CrLi ground-state molecules, characterized by both a large electric and magnetic dipole moment.

In the final part of this work, I also describe the design of a high-resolution imaging setup for lithium and chromium atoms, which I developed during my initial period in

the lab. The bi-chromatic microscope objective, which I devised and simulated with the ray-tracing software OSLO, exploits solely six off-the-shelf optical components, thus making its practical realization easy and inexpensive. The present setup is optimized to be both diffraction-limited over a sizeable numerical aperture  $NA = 0.4$ , and free from longitudinal chromatic aberrations for the imaging wavelengths of the two species ( $\lambda_{Li} = 671$  nm and  $\lambda_{Cr} = 425.5$  nm, respectively). The theoretically achievable resolution, on the order of  $1 \mu\text{m}$ , combined with a diffraction-limited field of view of about  $200 \mu\text{m}$ , makes the design discussed in this work appealing for both high-resolution microscopy and optical manipulation of lithium-chromium quantum mixtures.

# Contents

<b>Introduction</b>	<b>vii</b>
<b>1 Atom-atom interactions</b>	<b>1</b>
1.1 Elements of scattering theory . . . . .	2
1.2 Low-energy scattering . . . . .	6
1.3 Scattering by a square potential barrier . . . . .	7
1.4 Scattering by a square potential well . . . . .	9
1.4.1 Bound states of the square potential well . . . . .	10
1.5 Levinson’s theorem applied to the square well . . . . .	11
1.6 The Ramsauer-Townsend effect . . . . .	14
1.7 Shape resonances . . . . .	16
1.8 Unitary limit and effective range . . . . .	17
1.8.1 The zero-range and effective range approximations . . . . .	19
1.9 Scattering of identical particles . . . . .	20
1.10 More realistic atomic interactions . . . . .	21
1.10.1 Selection rules . . . . .	23
1.11 Feshbach resonances . . . . .	24
1.12 Multi-channel scattering: a toy model . . . . .	26
1.13 Magnetic tuning of Feshbach resonances . . . . .	29
1.14 Inelastic collisions and loss mechanisms . . . . .	30
1.14.1 Feshbach loss spectroscopy: an introduction . . . . .	31
<b>2 Experimental setup</b>	<b>33</b>
2.1 Lithium . . . . .	34
2.2 Chromium . . . . .	35
2.3 Lithium laser setup . . . . .	36
2.3.1 High-field imaging . . . . .	38
2.4 Chromium laser setup . . . . .	41
2.4.1 Cr red repumpers . . . . .	43
2.5 The MOT optical setup . . . . .	44
2.6 Bichromatic optical dipole trap . . . . .	46
<b>3 Production of ultracold Li-Cr mixtures</b>	<b>49</b>
3.1 Loading of the Li-Cr MOT . . . . .	49
3.1.1 Loading of the Li MOT . . . . .	49
3.1.2 Loading of the Cr MOT . . . . .	51
3.2 Loading of the BODT . . . . .	52
3.2.1 Optimization of gray-molasses and ODT loading power . . . . .	54
3.2.2 Compensation of Cr light shift: the “dark” spot . . . . .	55
3.2.3 Polarization of Cr via spin-exchange collisions . . . . .	56
3.3 Evaporation trajectories . . . . .	58
3.3.1 Production of a Li crossover superfluid . . . . .	58

3.3.2	Production of a Li degenerate Fermi gas . . . . .	60
3.3.3	Production of ultracold Li-Cr mixtures . . . . .	61
<b>4</b>	<b>Feshbach loss spectroscopy</b>	<b>63</b>
4.1	Sample preparation and typical experimental conditions . . . . .	63
4.2	Relevant loss mechanisms . . . . .	64
4.3	Feshbach scans . . . . .	66
4.4	Analysing loss data . . . . .	72
4.4.1	Two-body losses in ultracold Li-Cr mixtures . . . . .	73
4.4.2	Three-body losses in ultracold Li-Cr mixtures . . . . .	76
4.5	Final remarks . . . . .	80
<b>5</b>	<b>Design of a bichromatic high-resolution objective</b>	<b>81</b>
5.1	Introduction . . . . .	84
5.2	Chromatic aberrations and color correction . . . . .	91
5.3	Simulations with OSLO . . . . .	97
5.4	Simulations results . . . . .	99
5.4.1	Design #1 . . . . .	101
5.4.2	Design #2a . . . . .	105
5.4.3	Design #2b . . . . .	107
5.4.4	Design #3 . . . . .	113
5.5	Final remarks . . . . .	118
	<b>Conclusions</b>	<b>119</b>

# Introduction

In the field of atomic physics, the last few decades have been marked by the tremendous progress in the production and manipulation of ultracold and quantum gases. The implications of such developments, ranging from high-precision spectroscopy and accurate measurements of time and fundamental constants [1], to quantum computing and quantum simulations of model hamiltonians [2], have spread and extended well beyond the field itself. An ever-growing number of experimental and theoretical publications has appeared since the early days of laser cooling, and an increasing number of groups are currently working on the many branches emerged in this research area.

From a historical point of view, the realization of the first Bose-Einstein condensate (BEC) in 1995 [3, 4], with dilute gaseous samples of alkali metals, not only constituted a milestone achievement (awarded with the 2001 Nobel prize) *per se*, but also represented a key starting point for a variety of fascinating investigations on the properties of quantum matter. Just to name a few, soon after atomic BECs were available, their long-range phase coherence, as well as their superfluid behaviour, were experimentally demonstrated [5, 6, 7]. Nowadays, the field is considered rather mature, and numerous reviews on Bose-Einstein condensates and their applications exist in the literature, see e.g. Refs. [8, 9] and references therein.

It was soon realized that the various techniques developed to cool, trap, manipulate and probe bosonic atoms could also have been applied to fermionic species. Fermions do not exhibit an “evident” phase transition as they are cooled down to ultracold temperatures [10], i.e. their quantum statistics does not allow for a macroscopic occupation of a single quantum state. Nevertheless, the realization of the first degenerate Fermi gas in 1999 [11] has paved the way for a wealth of intriguing studies on this kind of systems. After some first characterizations of the ideal Fermi gas and of its statistical and collisional properties [12, 13], the interest quickly moved to fermions in optical lattices and two-component Fermi mixtures near Feshbach resonances. The former are the essential ingredient for quantum simulation of various solid state systems, see e.g. Ref. [14] and references therein. The latter have attracted much interest due to their remarkable stability in the regime of strong interactions [15, 16], a somewhat unexpected feature that is not encountered in bosonic systems. Indeed, in a two-component Fermi gas, three-body recombination processes (the main source of heating and losses in strongly-interacting bosonic samples) are substantially inhibited by Pauli’s exclusion principle. This notable fact allows for the simulation of strongly correlated electronic materials with ultracold fermionic species. A further milestone achievement of the field, closely related to the physics of Feshbach resonances, was the realization of long-lived ultracold molecules formed by two fermionic atoms [16, 17], which – being long-lived composite bosons – can Bose condense [18, 19, 20], paving the way to the exploration of fermionic superfluidity throughout the BEC-BCS interaction crossover [21]. Such *Feshbach molecules* are weakly bound (or quasi-bound) dimers in a highly excited roto-vibrational state. Different techniques can be used to bring these shallow compounds down to their absolute ground state, where they exhibit large electric dipole moments [22].

Furthermore, the introduction of a “heavy-light” mass asymmetry within a fermionic mixture is expected to promote a rich variety of exotic quantum states that are difficult to realize, or even unattainable, with currently available equal-mass systems. For few-particle physics, heteronuclear fermion mixtures are predicted to exhibit various  $N > 2$ -body cluster states and scattering resonances: Among others, a proper mass imbalance may lead to the existence of the Efimov effect [23, 24], as well as to the emergence of non-Efimovian clusters [24, 25, 26] with universal properties. At the many-body level, the natural mismatch of the Fermi surfaces of a mass-imbalanced Fermi mixture is expected to greatly enhance the observation of paradigmatic regimes of unconventional superfluidity [27]. A sufficiently large mass asymmetry may indeed promote pair condensation into non-zero momentum states, thereby leading to the celebrated FFLO-type ordering [28, 29], and it can favour the creation of “breached-paired” or Sarma superfluid states with exotic gapless excitations [30, 31], at experimentally achievable temperatures.

The specific choice for the chromium-lithium mixture is primarily motivated by the exceptional few-body properties of this system, which cannot be obtained with any other atom-atom combination, and that lay the ground for a wealth of possibilities, going well beyond the scope of presently available systems. The peculiar mass ratio of  $^{53}\text{Cr}$  and  $^6\text{Li}$  ( $M/m = 8.8$ ) is predicted to support, in the region of repulsive Cr-Li interactions, three- and four-body cluster states [24, 25, 32] with universal character and  $p$ -wave (i.e.  $\ell = 1$ ) symmetry, never observed in any physical system so far. In turn, the availability of these exotic few-particle states near a Cr-Li Feshbach resonance may potentially allow, for the first time, the resonant tuning of few-body ( $p$ -wave) elastic interactions, on top of the standard two-body ( $s$ -wave) ones. This will uniquely enable to controllably investigate novel many-body regimes of ultracold fermionic matter in the presence of strong, non-perturbative few-body correlations. Besides these two main points, it is worth noticing that the Cr-Li system represents also an extremely appealing candidate for realizing ground state polar molecules with both electric and magnetic dipole moments.

The realization of chromium-lithium mixtures in the ultracold regime, and the discovery of about 50 interspecies Cr-Li Feshbach resonances, both achieved during my work period in the lab, constitute a very promising starting point for future investigations with the novel CrLi quantum simulator.

My thesis work has been carried out in the Cr-Li lab at the Department of Physics of the University of Florence, under the supervision of Dr. Matteo Zaccanti.

At the beginning of my lab activity, the whole experimental apparatus that allows us to produce Cr-Li mixtures was already prepared. I participated in the construction of new parts of the so-called *PoLiChroM machine* (namely, the high-field imaging setups for Li and Cr), and in the optimization of some among the experimental routines (in particular those regarding evaporation ramps, RF population transfers, and Feshbach loss spectroscopy). Once the machine was optimized, I contributed to the acquisition of extensive Feshbach scans, targeted to the detection of interspecies scattering resonances. As anticipated, we experimentally unveiled around 50 heteronuclear Cr-Li Feshbach resonances, which constitute an exceptional experimental input for a refined Cr-Li quantum collisional model, currently under development by our theory collaborator, Prof. A. Simoni (University of Rennes).

---

Finally, as a side and totally independent project, I also designed a bichromatic high-resolution imaging system for our mixture. The objective, devised and simulated with the ray-tracing software OSLO, relies only on six catalogue lenses, and it is optimized to be both diffraction-limited over a sizeable numerical aperture  $NA = 0.4$ , and free from longitudinal chromatic aberrations for the imaging wavelengths of the two species ( $\lambda_{\text{Li}} = 671 \text{ nm}$  and  $\lambda_{\text{Cr}} = 425.5 \text{ nm}$ , respectively). The theoretically achievable resolution, on the order of  $1 \text{ }\mu\text{m}$ , combined with a diffraction-limited field of view of about  $200 \text{ }\mu\text{m}$ , makes the design discussed in this work appealing for both high-resolution microscopy and optical manipulation of lithium-chromium quantum mixtures.

This thesis is organized as it follows:

- Chapter 1 summarizes the theoretical background to describe ultracold atomic collisions. In particular, after recalling fundamental elements of scattering theory and reviewing pairwise atomic interactions, a basic overview of Feshbach resonances is provided.
- Chapter 2 illustrates the complex optical setup of our experimental machine, with which we produce the laser lights to cool, trap, and image lithium and chromium samples.
- Chapter 3 outlines the experimental procedures that we employ to produce ultracold Cr-Li mixtures, from the loading of the double-species magneto-optical trap (MOT), to the final evaporation ramps in a bichromatic optical dipole trap (BODT).
- Chapter 4 reports on the outcome of the extensive heteronuclear Feshbach loss spectroscopy that we performed on our ultracold mixtures. Phenomenological models to interpret and analyse the experimental data are presented, with results compared with theoretical predictions.
- Chapter 5 describes the design and optimization of a bichromatic high-resolution objective, with preliminary results concerning the most relevant figures of merit, obtained with ray-tracing simulations.



# Chapter 1

## Atom-atom interactions

In this chapter I summarize the most relevant features of the interaction between two neutral atoms in a cold, dilute atomic gas.

First, I briefly introduce different kinds of potentials that can be used for a “first order” description of the two-body interactions. Secondly, I invest some pages on (a simplified version of) the quantum theory of scattering, reviewing a couple of elementary examples that help illustrating the role of the *scattering length*, a key parameter of the problem. In general, I give particular emphasis to situations that involve *resonant scattering*. Anyway, this first part is by no means an exhaustive review of the subject; rather, it has to be regarded as a practical way to gain insight into the problem, and to introduce the relevant quantities and the standard notation. An extensive treatment of the topic can be found in many textbooks, e.g. Refs. [33, 34, 36, 37, 38, 47].

Finally, after taking into account more realistic atomic interactions, I present the phenomenon of the so-called *Feshbach resonances*, and discuss their importance in the context of ultracold atom experiments.

As a first step in the study of atomic collisions, let us consider some among the physical mechanisms that can give rise to an interaction between different atoms. In the case of neutral atoms (e.g. alkali metals, or two-electron atoms), the interaction at large distances is due to induced dipole-dipole contributions, and has an attractive character. On the contrary, at very short distances, electrostatic effects come into play, and the potential features a repulsive “hard wall”. The simplest function that one can use to describe this kind of interaction is the *Lennard-Jones potential*

$$V_{\text{LJ}}(r) = -\frac{C_6}{r^6} + \frac{C_{12}}{r^{12}} \quad (1.1)$$

which is isotropic, and has a *short-range* character (the meaning of this last statement will be clarified in the following). Besides, we also note that  $V_{\text{LJ}}(r)$  has a minimum, which falls typically on the Å scale.

In the case of dipolar atoms (e.g. transition metals, rare earths), a dipole-dipole contribution to the interaction potential may be not negligible. If the sample is polarized, one can conveniently write

$$V_{\text{dd}}(\vec{r}) = \frac{\mu_0 \mu^2}{4\pi} \frac{(1 - 3 \cos^2 \theta)}{r^3} \quad (1.2)$$

where  $\mu_0$  is the vacuum magnetic permeability, and  $\mu$  is the atomic magnetic dipole moment.<sup>1</sup> This potential is not isotropic (both its sign and modulus depend on the angle  $\theta$  between the dipoles), and can be considered as a borderline case of *long-range* interaction.

---

<sup>1</sup>Neutral atoms have no permanent electric dipole moment.

Before going through the machinery of scattering theory, an important point to be emphasized is the concept of *diluteness* of the atomic gas. Indeed, even if atomic samples can be brought to the quantum-degenerate regime, their spatial density remains pretty low compared to classical gases. For instance, in the case of Bose-Einstein condensates (BECs), atomic densities are typically on the scale of  $10^{14} \text{ cm}^{-3}$ , yielding average interparticle distances  $d \sim 0.2 \text{ }\mu\text{m}$ . At the same time, the typical range for the interaction is on the order of  $100 a_0 \simeq 50 \text{ \AA}$ , where  $a_0$  is the Bohr radius. Hence, being such an interaction range much shorter than  $d$ , we can consider the atomic sample as *dilute*, and  $V_{\text{LJ}}(r)$  as a *contact-like* potential. This, in turn, leads to two important simplifications: on the one hand (when performing many-body calculations) we can replace  $V_{\text{LJ}}(r)$  with a  $\delta$ -like potential, adjusting the coupling strength in order to get the same final results for the (two-body) scattering problem. On the other hand, since ( $N > 2$ )-body collisions in a dilute gas are much rarer than two-body processes, we can mainly focus on the latter, neglecting (for the moment) other few- and many-body contributions.

In any case, atoms in ultracold gases collide at very low energies, so a quantum-mechanical treatment of the scattering problem is required.

## 1.1 Elements of scattering theory

To begin our study on atomic collision, let us consider the simplest scattering problem; namely, the non-relativistic elastic scattering of two distinguishable spinless particles (with masses  $m_1$  and  $m_2$ ), interacting via a (real) central potential.<sup>2</sup> We can write the Schrödinger equation in the center of mass frame<sup>3</sup>

$$\left[ \frac{p^2}{2m} + V(r) \right] \psi(\vec{r}) = E \psi(\vec{r}) \quad (1.3)$$

where  $m = m_1 m_2 / (m_1 + m_2)$  is the reduced mass,  $\vec{p} = \hbar \vec{k} = \vec{p}_2 - \vec{p}_1$  is the relative momentum, and  $E = (\hbar k)^2 / 2m > 0$  is the scattering energy. Without loss of generality [34], we can model the incoming effective single-particle wavefunction  $\psi_i$  with a plane wave propagating along the  $z$ -axis, and (at large distances) the scattered fraction  $\psi_s - \psi_i$  with a modulated spherical wave:

$$\psi_i(\vec{r}) \simeq e^{i k z} \quad (1.4a)$$

$$\psi_s(\vec{r}) \simeq e^{i k z} + f(k, \theta) \frac{e^{i k r}}{r} \quad (\text{for large } r) \quad (1.4b)$$

where the *scattering amplitude*  $f(k, \theta)$  (which generally may also depend on the azimuthal angle  $\varphi$  and on the final wavevector  $k'$ ) carries all the information about the interaction.

From the standard definition of probability current ( $\vec{j}_n = \frac{\hbar}{m} \Im \mathbf{m}[\psi^* \vec{\nabla} \psi]$ ), we can readily compute the radial<sup>4</sup> scattered current for a given angle  $\theta \neq 0$ . This results

<sup>2</sup>More realistic situations with respect to ultracold atomic collisions are considered towards the middle of this chapter.

<sup>3</sup>It can be shown that integrated quantities, such as the total scattering cross section (defined in the following), do not depend on the chosen reference frame, see App. 2 in Ref. [36].

<sup>4</sup>In spherical coordinates the gradient operator reads  $\vec{\nabla} = \hat{r} \partial_r + \hat{\theta} r^{-1} \partial_\theta + \hat{\varphi} (r \sin(\theta))^{-1} \partial_\varphi$ , so the leading contribution for  $r \rightarrow \infty$  is given by the radial term. Moreover, as soon as  $f(k, \theta)$  is obtained (see Eq. (1.18b)), it can be shown that the scattered current is purely radial [48].

in  $j_s(k, \theta) = \frac{v}{r^2} |f(k, \theta)|^2$ , where  $v$  (the relative velocity of the particles) directly gives the incident flux for the chosen normalization. The outgoing scattered flux in the solid angle  $d\Omega$  is given by  $d\Phi_s = j_s \cdot r^2 d\Omega$ . Hence the *differential cross section*, defined as the ratio between  $d\Phi_s$  and the incident flux (per unit solid angle), reads

$$\frac{d\sigma}{d\Omega} = |f(k, \theta)|^2 \quad (1.5a)$$

The total elastic cross section is therefore given by

$$\sigma_{\text{el}}(k) = \int d\Omega \left( \frac{d\sigma}{d\Omega} \right) = 2\pi \int_0^\pi d\theta \sin(\theta) |f(k, \theta)|^2 \quad (1.5b)$$

In order to proceed with analytical calculations, it is convenient to perform the *partial wave expansion*

$$\psi(\vec{r}) = \sum_{\ell=0}^{\infty} \sum_{m=-\ell}^{+\ell} R_{\ell,m}(r) Y_{\ell,m}(\theta, \varphi) = \sum_{\ell=0}^{\infty} R_{\ell,0}(r) Y_{\ell,0}(\theta) \quad (1.6)$$

where  $R_{\ell,m}(r)$  denote the radial wavefunctions, and  $Y_{\ell,m}(\theta, \varphi)$  are the spherical harmonics. In the case of a central potential, due to the cylindrical symmetry of the problem (one direction is fixed by the incoming wavevector), terms with  $m \neq 0$  do not contribute to the sum.<sup>5</sup> Moreover, since spherical harmonics form a complete orthogonal set of angular momentum eigenstates, partial waves associated with different values of  $\ell$  do not interfere with one another. By inserting Eq. (1.6) into Eq. (1.3), one finds that the radial wavefunctions must satisfy

$$-\frac{\hbar^2}{2m} \left[ \frac{1}{r^2} \frac{\partial}{\partial r} \left( r^2 \frac{\partial}{\partial r} \right) - \frac{\ell(\ell+1)}{r^2} \right] R_\ell(r) + V(r) R_\ell(r) = E R_\ell(r) \quad (1.7a)$$

Hence, by defining the “reduced” radial wavefunctions  $U_\ell(r) = r \cdot R_\ell(r)$ , and the dimensionless parameter  $\rho = kr$ , Eq. (1.7a) becomes

$$\left[ \frac{\partial^2}{\partial \rho^2} - \frac{\ell(\ell+1)}{\rho^2} + 1 \right] U_\ell(\rho) = \tilde{V}(\rho) U_\ell(\rho) \quad (1.7b)$$

where  $\tilde{V}(\rho) = V(\rho)/E$  is the dimensionless potential. In the trivial case in which  $\tilde{V}(\rho)$  identically vanishes, Eq. (1.7b) reduces to the well-known *Riccati-Bessel equation*, that supports two different families of solutions

$$\hat{j}_\ell(\rho) = \rho \cdot j_\ell(\rho); \quad \hat{n}_\ell(\rho) = -\rho \cdot n_\ell(\rho) \quad (1.8)$$

where  $j_\ell(\rho)$  and  $n_\ell(\rho)$  are the spherical Bessel and von Neumann functions, respectively. The following expansions<sup>6</sup> and recurrence relation will be quite helpful [35]

$$j_\ell(\rho \rightarrow 0) \simeq \frac{\rho^\ell}{(2\ell+1)!!} \quad (1.9a) \quad j_\ell(\rho \rightarrow \infty) \simeq \frac{\sin(\rho - \frac{\ell\pi}{2})}{\rho} \quad (1.10a)$$

$$n_\ell(\rho \rightarrow 0) \simeq -\frac{(2\ell-1)!!}{\rho^{\ell+1}} \quad (1.9b) \quad n_\ell(\rho \rightarrow \infty) \simeq -\frac{\cos(\rho - \frac{\ell\pi}{2})}{\rho} \quad (1.10b)$$

$$f'_\ell(\rho) = \frac{\ell}{\rho} f_\ell(\rho) - f_{\ell+1}(\rho) \quad (1.11)$$

<sup>5</sup>From now on, we will drop the  $m$  subscript when denoting the radial wavefunctions.

<sup>6</sup>The double factorial in Eq. (1.9b) is defined such that  $(-1)!! = 1$ , see also Refs. [36, 37].

where  $f_\ell$  stands either for  $j_\ell$  or  $n_\ell$ , and the prime denotes the derivative with respect to the argument. It is worth noticing that spherical Bessel functions are regular at the origin, while spherical von Neumann functions are not.

In the asymptotic region, where the potential is negligible, we can look for solutions of Eq. (1.7b) in the form<sup>7</sup>

$$U_\ell^{(2)}(k, r \rightarrow \infty) = \alpha_\ell(k) \left[ \hat{j}_\ell(\rho) + \beta_\ell(k) \hat{n}_\ell(\rho) \right] \quad (1.12)$$

Here,  $\alpha_\ell(k)$  are just normalization factors, whereas  $\beta_\ell(k)$  are mixing coefficients that fully characterize the scattering process. If we assume that  $V(r) \simeq 0$  beyond a certain (arbitrarily large) distance  $R_0$ , these coefficients can be obtained by requiring the logarithmic derivative of the radial wavefunction to be continuous at  $r = R_0$ . This leads to

$$\beta_\ell(k) = \frac{\rho_0 j_\ell'(\rho_0) - \mathfrak{L}_\ell^{(1)} j_\ell(\rho_0)}{\rho_0 n_\ell'(\rho_0) - \mathfrak{L}_\ell^{(1)} n_\ell(\rho_0)} \quad (1.13a)$$

where  $\rho_0 = kR_0$ , and  $\mathfrak{L}_\ell^{(1)}$  is the dimensionless logarithmic derivative of the (possibly numerically-computed [37]) wavefunction at short distances, evaluated for  $r = R_0$ :

$$\mathfrak{L}_\ell^{(1)} = R_0 \cdot \left. \left( \frac{\partial R_\ell^{(1)}}{\partial r} \right) \right|_{R_0} = \rho_0 \cdot \left. \left( \frac{\partial U_\ell^{(1)}}{\partial \rho} \right) \right|_{\rho_0} - 1 \quad (1.13b)$$

By defining<sup>8</sup>

$$\beta_\ell(k) = \tan(\delta_\ell(k)) \quad (1.14a)$$

$$\alpha_\ell'(k) = \frac{\alpha_\ell(k)}{\cos(\delta_\ell(k))} \quad (1.14b)$$

our solution in Eq. (1.12) takes the simple form

$$U_\ell^{(2)}(k, r \rightarrow \infty) = \alpha_\ell'(k) \sin\left(kr - \frac{\ell\pi}{2} + \delta_\ell(k)\right) \quad (1.15)$$

where the *phase shifts*  $\delta_\ell(k)$  are the key parameters that entirely encode the scattering process: in other words, knowledge of these quantities completely solves our two-body problem. For large  $r$ , the total wavefunction thus reads

$$\psi^{(2)}(\vec{r}) = \sum_{\ell=0}^{\infty} \frac{\alpha_\ell'(k)}{kr} \sin\left(kr - \frac{\ell\pi}{2} + \delta_\ell(k)\right) Y_{\ell,0}(\theta) \quad (1.16)$$

This expression has to be compared with Eq. (1.4b). To this end, another useful formula is the *Bauer expansion* of a plane wave in terms of spherical harmonics [38]

$$e^{ikz} = e^{ikr \cos(\theta)} = \sum_{\ell=0}^{\infty} \sqrt{4\pi(2\ell+1)} (i)^\ell j_\ell(kr) Y_{\ell,0}(\theta) \quad (1.17a)$$

<sup>7</sup>Actually, we point out here that this entire procedure (and line of reasoning) is valid only if the scattering potential  $V(r)$  decays faster than  $1/r$  as  $r \rightarrow \infty$ . For instance, in the case of *Coulomb scattering*, one finds that the incoming and outgoing wavefunctions are (logarithmically) distorted even at asymptotic distances [37], thus not being properly described by Eqs. (1.4).

<sup>8</sup>Note that, from Eq. (1.14a),  $\delta_\ell(k)$  is only defined modulo  $\pi$ . For the moment, we can safely ignore this fact, as such an ambiguity does not compromise our analysis. Anyway, it will be specifically addressed in Sec. 1.5.

which, in the asymptotic limit, approaches (see Eq. (1.10a))

$$e^{ikz} \simeq \sum_{\ell=0}^{\infty} \sqrt{4\pi(2\ell+1)} \frac{(i)^\ell}{kr} \sin\left(kr - \frac{\ell\pi}{2}\right) Y_{\ell,0}(\theta) \quad (1.17b)$$

From a first comparison of Eqs. (1.17b) and (1.16), one realizes that the main difference between the free and the scattered state lies in the presence of the phase shifts  $\delta_\ell(k)$ .<sup>9</sup> More precisely, by inserting Eq. (1.17b) into Eq. (1.4b) and equating the result to Eq. (1.16), after some algebraic manipulations one finds

$$\alpha_{\ell'}(k) = \sqrt{4\pi(2\ell+1)} (i)^\ell e^{i\delta_\ell(k)} \quad (1.18a)$$

$$f(k, \theta) = \frac{\sqrt{4\pi}}{k} \sum_{\ell=0}^{\infty} \sqrt{2\ell+1} e^{i\delta_\ell(k)} \sin(\delta_\ell(k)) Y_{\ell,0}(\theta) \quad (1.18b)$$

where it should be emphasized that the scattering amplitude  $f(k, \theta)$  is fully determined by the phase shifts. Therefore, due to the orthogonality of spherical harmonics, the total (elastic) cross section reads

$$\sigma_{\text{el}}(k) = \sum_{\ell=0}^{\infty} \sigma_\ell(k) = \frac{4\pi}{k^2} \sum_{\ell=0}^{\infty} (2\ell+1) \sin^2(\delta_\ell(k)) \quad (1.19)$$

In the case of a central potential, this constitutes an absolutely general result: the total elastic cross section is given by the sum over the independent contributions of every single partial wave, each of these contributions being in turn entirely determined by the corresponding phase shift.

We conclude this section by pointing out that Eq. (1.19) can be recast into another quite meaningful form. Indeed, from the properties of spherical harmonics it follows that  $Y_{\ell,0}(\theta=0) = \sqrt{(2\ell+1)/4\pi}$ . Therefore we have

$$\sigma_{\text{tot}}(k) = \frac{4\pi}{k} \Im \left[ f(k, \theta=0) \right] \quad (1.20)$$

This last relation, known as the *optical theorem*, essentially expresses the conservation of the probability current [36]: in other words, the scattering cross section quantifies the removal of particles from the incident flux. Further, when compared to Eq. (1.19), it shows that in general the scattering amplitude is complex, with  $\Im[f(k, \theta=0)]$  being always positive. As we will discuss in the following section, quantum gases in the so-called *s-wave regime* represent an exception to this rule, as the imaginary part of  $f(k, \theta=0)$  vanishes for  $k \rightarrow 0$  [48].

Lastly, yet importantly, the optical theorem is not restricted to elastic scattering, being also valid for inelastic processes [37].

<sup>9</sup>Note that, in the absence of a scattering potential, i.e. if  $V(r) = 0 \quad \forall r$ , the internal solution reduces to  $U_\ell^{(1)}(\rho) = \hat{j}_\ell(\rho)$ , aside from normalization factors. Therefore, the numerator on the r.h.s. of Eq. (1.13a) vanishes, together with  $\beta_\ell(k)$  and  $\delta_\ell(k)$ , and one recovers the free particle solution. Hence, the scattering phase shifts are seen to arise from the action of  $V(r)$ . On the other hand, the term  $-\frac{\ell\pi}{2}$  in the argument of the asymptotic wavefunction vanishes only for  $\ell = 0$ . It is ultimately related to the centrifugal potential (see Sec. 1.2), thus being commonly referred to as the *centrifugal phase shift*.

## 1.2 Low-energy scattering

In the context of ultracold atoms, the partial wave expansion (Eq. (1.6)) is particularly important: the reason, as we shall see in this section, is that at low energies only a few partial waves yield non-negligible contributions to the scattering cross section. Indeed, by inspection of Eq. (1.7a), one realizes that the centrifugal potential essentially acts as a repulsive term, which dominates over the interaction at large distances. Thus, one actually deals with an effective potential

$$V_{\text{eff}}(r) = V(r) + \frac{\hbar^2}{2m} \frac{\ell(\ell+1)}{r^2} \quad (1.21)$$

which, when  $V(r)$  is given by Eq. (1.1), features a local maximum somewhere near the van der Waals range  $R_0$ . Typically, the height of this maximum, ranging around a few mK, is much smaller than the (short-distance) potential depth, which can be instead on the order of hundreds of kelvins. Nevertheless, ultracold atoms have kinetic energies that lie well below these values: thus, a colliding pair approaching with orbital angular momentum  $\ell > 0$  must actually *tunnel* through the centrifugal barrier in order to experience the interaction potential  $V(r)$ . It can be shown (e.g. with the WKB method [39]) that the tunneling probability rapidly drops as the collisional energy decreases: therefore, in the limit of  $T \rightarrow 0$ , only a few partial waves will actively contribute to the scattering process. A more formal and quantitative approach to get the same result is based on the so-called *Wigner's threshold law* [40], that can be summarized as [46]:

*For a scattering potential that behaves like  $V(r) \sim r^{-\alpha}$  for large  $r$ , in the low-energy limit the phase shifts  $\delta_\ell(k)$  scale as*

$$\delta_\ell(k \rightarrow 0) \propto k^{(2\ell+1)} \quad \text{if } 2\ell \leq \alpha - 3 \quad (1.22a)$$

$$\delta_\ell(k \rightarrow 0) \propto k^{(\alpha-2)} \quad \text{if } 2\ell \geq \alpha - 3 \quad (1.22b)$$

This rather general result can be understood on the basis of our calculations (at least when  $2\ell \leq \alpha - 3$ ) by making use of Eqs. (1.9) and (1.11) into Eq. (1.13a). Thereby, defining  $L_\ell^{(1)} = \lim_{k \rightarrow 0} \mathfrak{L}_\ell^{(1)}$ , and provided that  $L_\ell^{(1)} \neq -(\ell + 1)$ , one finds<sup>10</sup>

$$\beta_\ell(k \rightarrow 0) = \tan(\delta_\ell(k \rightarrow 0)) \simeq \frac{\rho_0^{2\ell+1}}{(2\ell+1) [(2\ell-1)!!]^2} \frac{(\ell - L_\ell^{(1)})}{(\ell + 1 + L_\ell^{(1)})} \quad (1.23)$$

<sup>10</sup>If, “by accident”,  $L_\ell^{(1)} = -(\ell + 1)$  for a particular  $\ell$ , the tangent of the corresponding phase shift  $\delta_\ell$  diverges. With a not completely satisfactory yet simple argument, one could conclude that in such a situation  $\delta_\ell = (2n + 1) \frac{\pi}{2}$ , with  $n$  being an integer number. Therefore, from Eq. (1.18b):

$$f(k, \theta) = \frac{\sqrt{4\pi}}{k} \sum_{\ell=0}^{\infty} \sqrt{2\ell+1} (i)^{4n+1} Y_{\ell,0}(\theta)$$

Hence, the  $\ell$ -th contribution to the total cross section diverges as  $1/k^2$ , namely  $\sigma_\ell(k) \simeq 4\pi(2\ell + 1) \cdot k^{-2}$ . This is a first example of *resonant scattering* (more precisely, this is a *zero-energy resonance*). A more formal approach is presented in Sec. 1.8.

On the other hand, one also realizes that for  $L_0^{(1)} = 0 \implies \beta_0(k \rightarrow 0) = 0$ . Hence, under this condition, in the low-temperature limit the scattering would be suppressed even for *s*-wave collisions. This is instead a manifestation of the *Ramsauer-Townsend effect*, better discussed in Sec. 1.6.

Hence, following from Eqs. (1.19) and (1.22), for each term  $\sigma_\ell(k)$  in the sum we have

$$\sigma_\ell(k \rightarrow 0) \propto k^{4\ell} \quad \text{if } 2\ell \leq \alpha - 3 \quad (1.24a)$$

$$\sigma_\ell(k \rightarrow 0) \propto k^{2(\alpha-3)} \quad \text{if } 2\ell \geq \alpha - 3 \quad (1.24b)$$

Therefore, for a *short-range potential* (i.e. any potential falling off with  $\alpha > 3$ ), at very low temperatures the  $\ell = 0$  (i.e. *s-wave*) scattering cross section approaches a constant value, whereas contributions from higher partial waves are strongly suppressed. In this case, one can conveniently define the *s-wave scattering length* as

$$a_s = - \lim_{k \rightarrow 0} \frac{\tan(\delta_0(k))}{k} \quad (1.25a)$$

Note that, with the help of Eq. (1.23), we have

$$a_s = R_0 \frac{L_0^{(1)}}{L_0^{(1)} + 1} \quad (1.25b)$$

By inserting Eq. (1.25a) into Eq. (1.19), we can express the total elastic cross section in the zero-energy limit as

$$\sigma_{\text{el}}(k \rightarrow 0) = 4\pi a_s^2 \quad (1.26)$$

The latter is a celebrated result of scattering theory: for a central *short-range* potential, the low-energy scattering is to first order isotropic, and the total cross section approaches a constant value, which is solely determined by the *s-wave* scattering length (i.e. not by  $k$ ). Actually, this very last statement is strictly valid only in the context of off-resonant scattering, which anyway encompasses the majority of cases. The concept of *resonant scattering* will be introduced later, and an expression for the resonant cross-section is derived in Sec. 1.8.

In the following, we will briefly review some basic examples of scattering problems, in order to gain a better understanding of the physical meaning of  $a_s$ .

Before that, we remark that in the case of dipolar interactions (where  $\alpha = 3$ , see Eq. (1.2)), from Wigner's law one finds that – even for  $k \rightarrow 0$ , all partial waves actively contribute to the total cross section, each contribution being (to first order)  $k$ -independent in the low-temperature limit.

### 1.3 Scattering by a square potential barrier

The real interaction potential experienced by two atoms is a quite complicated function, as we shall discuss later. Let us here examine a couple of toy models in order to gain more insights into the problem, especially to better understand the physical meaning of the scattering length. In particular, we start by considering a (3D) spherical barrier of the kind

$$V(r) = \begin{cases} V_0 & \text{for } r < b \\ 0 & \text{for } r > b \end{cases} \quad (1.27)$$

where  $V_0 = (\hbar k_0)^2/2m$ . The situation is depicted in Fig. 1.1a. The Schrödinger equation for the reduced radial wavefunction reads (see Eqs. (1.7))

$$\left[ -\frac{\hbar^2}{2m} \partial_r^2 + \frac{\hbar^2 \ell(\ell+1)}{2mr^2} + V(r) - E \right] U_\ell(r) = 0 \quad (1.28)$$

In the limit of low-energy scattering, invoking Wigner's law we neglect all contributions from partial waves with  $\ell > 0$ . Within this approximation, the centrifugal barrier vanishes, yielding

$$\partial_r^2 U_0(r) - (k_0^2 - k^2) U_0(r) = 0 \quad (r < b) \quad (1.29a)$$

$$\partial_r^2 U_0(r) + k^2 U_0(r) = 0 \quad (r > b) \quad (1.29b)$$

We look for solutions of Eqs. (1.29) with positive energy, in the limit of  $k \rightarrow 0$  (i.e.  $E < V_0$ ). In the inner region ( $r < b$ ) we can write

$$U_0^{(1)}(r) = A_1 \sinh\left(\sqrt{k_0^2 - k^2} r\right) \quad (1.30a)$$

since the total radial wavefunction, namely  $R_0(r) = U_0(r)/r$ , must be regular at the origin. On the other hand, in the outer region ( $r > b$ ) we have

$$U_0^{(2)}(r) = A_2 \sin(kr) + B_2 \cos(kr) = C_2 \sin(kr + \delta_0(k)) \quad (1.30b)$$

where  $\delta_0(k \rightarrow 0) = -ka_s$ , see Eq. (1.25a). The wavefunction and its first derivative need to be continuous everywhere, so our solutions must satisfy the boundary condition

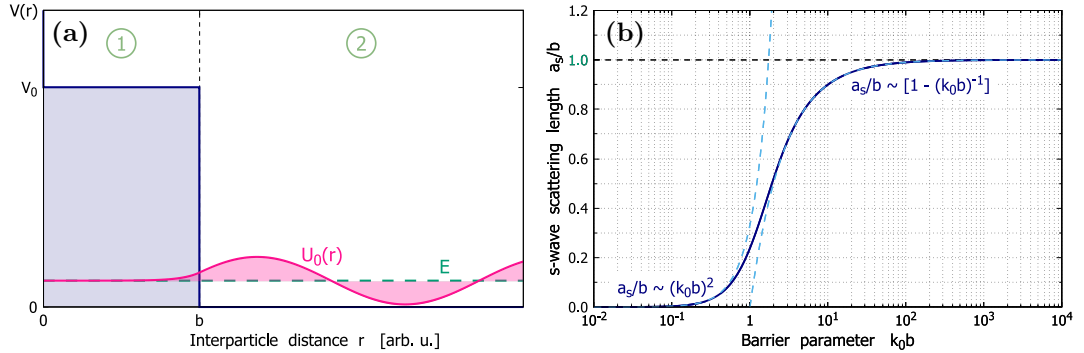
$$\frac{1}{\sqrt{k_0^2 - k^2}} \tanh\left(\sqrt{k_0^2 - k^2} b\right) = \frac{1}{k} \tan(k(b - a_s)) \quad (1.31a)$$

We can consider Eq. (1.31a) as an equation for  $a_s$ . By taking the limit of  $k \rightarrow 0$ , the scattering length is given by

$$a_s = b \left(1 - \frac{\tanh(k_0 b)}{k_0 b}\right) \quad (1.31b)$$

and its trend, with respect to the barrier parameter  $k_0 b$ , is shown in Fig. 1.1b. The most relevant feature is that, for such a repulsive potential barrier, the scattering length is always a positive quantity. Indeed, when  $k_0 b \rightarrow 0$ ,  $a_s$  tends to zero as  $(k_0 b)^2$ ; then, as  $k_0 b \rightarrow \infty$ , it approaches its maximum value  $a_s^{\max} = b$ , yielding a total cross section  $\sigma_0^{\max} = 4\pi b^2$  (which is four times larger than the corresponding classical result). When compared to Eq. (1.26), this last relation offers a simple physical picture of the scattering length: indeed, the latter can be understood as the radius of an effective ‘‘hard sphere’’ that reproduces the same low-energy phase shift.

**Figure 1.1** – Scattering by a repulsive square potential barrier: (a) sketch. (b) Low-energy (s-wave) scattering length.



## 1.4 Scattering by a square potential well

Let us now study the scattering by a (3D) spherical well, that we take as

$$V(r) = \begin{cases} -|V_0| & \text{for } r < b \\ 0 & \text{for } r > b \end{cases} \quad (1.32)$$

This potential, sketched in Fig. 1.2a, may be regarded as an extremely rough approximation of the real interatomic interaction (see, e.g., Eq. (1.1)). Anyway, despite its simplicity, this model provides many useful insights into real-world scattering phenomena, so it deserves a careful examination.

Following the steps of the previous section, by taking the limit of  $s$ -wave scattering we can cast the Schrödinger equation as

$$\partial_r^2 U_0(r) + (k_0^2 + k^2) U_0(r) = 0 \quad (r < b) \quad (1.33a)$$

$$\partial_r^2 U_0(r) + k^2 U_0(r) = 0 \quad (r > b) \quad (1.33b)$$

Note that in this case, for positive energies, there are no classically forbidden regions. We look for solutions of Eqs. (1.33) in the form

$$U_0^{(1)}(r) = A_1 \sin\left(\sqrt{k_0^2 + k^2} r\right) \quad (r < b) \quad (1.34a)$$

$$U_0^{(2)}(r) = C_2 \sin(k(r - a_s)) \quad (r > b) \quad (1.34b)$$

Then, from the application of boundary conditions at  $r = b$ , we obtain

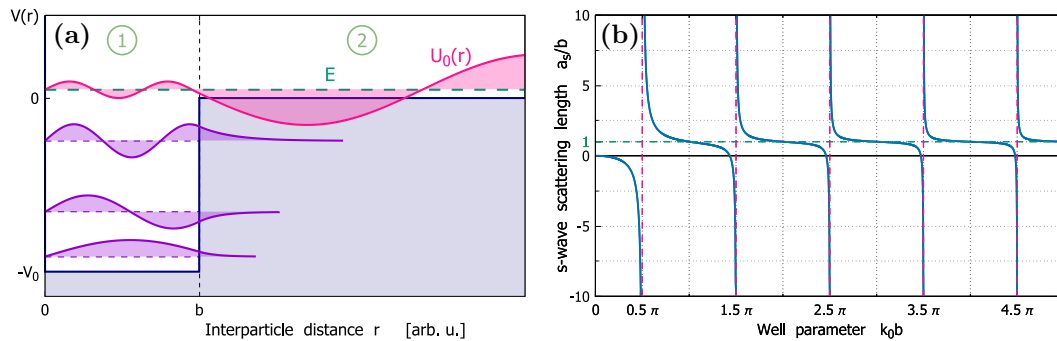
$$\frac{1}{\sqrt{k_0^2 + k^2}} \tan\left(\sqrt{k_0^2 + k^2} b\right) = \frac{1}{k} \tan(k(b - a_s)) \quad (1.35a)$$

Lastly, by solving Eq. (1.35a) for  $a_s$  when  $k \rightarrow 0$ , one finds

$$a_s = b \left(1 - \frac{\tan(k_0 b)}{k_0 b}\right) \quad (1.35b)$$

As shown in Fig. 1.2b, this result is quite different from the one obtained for the repulsive barrier (see Eq. (1.31b)). In this case, while for  $k_0 b \rightarrow 0$  the scattering length goes to zero (from negative values) as  $-(k_0 b)^2$ , a quite peculiar behaviour is

**Figure 1.2** – Scattering by a square potential well: (a) sketch, showing also the lowest  $\ell = 0$  bound states. (b) Low-energy ( $s$ -wave) scattering length.



encountered whenever  $k_0 b$  approaches an odd multiple of  $\frac{\pi}{2}$ . Indeed,  $a_s$  exhibits a set of singularities, near which it both diverges and changes sign, passing abruptly from  $-\infty$  to  $+\infty$ . As we shall see in the following section, this striking difference with respect to the repulsive barrier ultimately arises from the fact that a potential well can support *bound states*, and it turns out to be a general property of (sufficiently strong) attractive potentials. Lastly, we highlight how these resonance-like features become narrower as  $k_0 b$  is progressively increased, yielding a value of  $a_s$  that is “almost everywhere” close to  $b$  (hence positive). The latter is a quantum-mechanical effect known as *quantum reflection*.

### 1.4.1 Bound states of the square potential well

The square-well potential (see Eq. (1.32)) can also support solutions with negative energy, i.e. bound states. Following a procedure analogous to the one that yielded Eqs. (1.33), but now assuming  $E = -\hbar^2 k^2/2m < 0$ , we obtain

$$\partial_r^2 U_0(r) + (k_0^2 - k^2) U_0(r) = 0 \quad (r < b) \quad (1.36a)$$

$$\partial_r^2 U_0(r) - k^2 U_0(r) = 0 \quad (r > b) \quad (1.36b)$$

The inner and outer region solutions of Eqs. (1.36) are, respectively

$$U_0^{(1)}(r) = A_1 \sin\left(\sqrt{k_0^2 - k^2} r\right) \quad (r < b) \quad (1.37a)$$

$$U_0^{(2)}(r) = C_2 e^{-kr} \quad (r > b) \quad (1.37b)$$

and they must satisfy the boundary condition

$$\frac{1}{\sqrt{k_0^2 - k^2}} \tan\left(\sqrt{k_0^2 - k^2} b\right) = -\frac{1}{k} \quad (1.38a)$$

Given  $k_0$  and  $b$ , this equation can be numerically solved to find the discrete set of bound states energies. However, we are now interested to look at Eq. (1.38a) from a different perspective: while keeping the potential range  $b$  fixed, we search for those particular values of  $k_0$  that yield a bound state with  $E \rightarrow 0^-$ . Thus, in the limit of  $k \rightarrow 0$ , Eq. (1.38a) becomes

$$\frac{\tan(k_0 b)}{k_0} = -\frac{1}{k} \xrightarrow[k \rightarrow 0]{} -\infty \quad (1.38b)$$

that is satisfied if

$$k_0 b = (2n + 1 + \varepsilon) \frac{\pi}{2} \quad (1.38c)$$

with  $n$  being an integer number, and  $\varepsilon \rightarrow 0^+$ . One immediately realizes that Eq. (1.38c) is actually the same condition which, from Eq. (1.35b), gives singularities in  $a_s$ . Namely, the scattering length diverges whenever the potential well parameter  $k_0 b$  is such that a (weakly) bound state with  $E \rightarrow 0$  is supported by  $V(r)$ . In particular, when  $a_s \gg 0$ , the potential supports a (weakly) bound state, whereas for  $a_s \ll 0$  there exists a virtual state close to  $E = 0$  (relatively to the scattering threshold). This is a general result of scattering theory, known as *Levinson's theorem* [41], that holds for a wide class of two-body interaction potentials. Moreover, it is

worth noticing that, for such a weakly-bound state, from Eqs. (1.38b) and (1.35b) we can express the binding energy as

$$E_b = -\frac{\hbar^2 k^2}{2m} \simeq -\frac{\hbar^2}{2m(b-a_s)^2} \simeq -\frac{\hbar^2}{2m a_s^2} \quad (1.39)$$

where the last (approximate) equality follows from  $a_s$  being very large when Eq. (1.38c) holds. Thus we understand that, ultimately, the (low-energy) scattering length is closely related to the position of the least bound (or virtual) state of the scattering potential. In particular, when a *scattering resonance* is closely approached, it can be shown that Eq. (1.39) holds regardless of the details of the interaction, giving rise to what is commonly referred to as the *universal behaviour*.

## 1.5 Levinson's theorem applied to the square well

Before proceeding further, let us step back to our definition of the phase shifts, namely Eq. (1.14a). One realizes that defining  $\delta_\ell(k)$  by means of the mixing coefficients  $\beta_\ell(k)$  actually fixes the former quantities only modulo  $\pi$ . This ambiguity can be overcome. The starting point is to write (see Eq. (1.13a))

$$\delta_\ell(k) = \tan^{-1} \left[ \frac{\rho_0 j_\ell'(\rho_0) - \mathfrak{L}_\ell^{(1)} j_\ell(\rho_0)}{\rho_0 n_\ell'(\rho_0) - \mathfrak{L}_\ell^{(1)} n_\ell(\rho_0)} \right] \quad (1.40)$$

with the phase shifts being now uniquely defined in the range  $[-\frac{\pi}{2}; \frac{\pi}{2}]$ . However, following this path, they turn out to be not continuous functions of  $k$  (i.e. of the scattering energy  $E$ ), which is physically unpleasant. Indeed, as  $E$  varies,  $\delta_\ell$  would have a jump of  $\pi$  whenever it reaches  $\pm\frac{\pi}{2}$  [37].

To better frame the situation, aiming for an absolute definition of  $\delta_\ell(k)$ , let us remind that:

- for  $V \rightarrow 0$ ,  $\delta_\ell(k) \rightarrow 0 \quad \forall \ell, k$ : in other words, if the potential vanishes, there is no scattering;
- for  $E \rightarrow \infty$ ,  $\delta_\ell(k \rightarrow \infty) \rightarrow 0$ : if the kinetic energy is very large, the effects of the potential are negligible, and the relative motion is unperturbed;
- for  $E \rightarrow 0$ ,  $\delta_\ell(k \rightarrow 0) \rightarrow 0$ : as long as Wigner's law holds.<sup>11</sup>

For sake of simplicity, let us consider the square-well potential. The first point can be exploited as an absolute reference for the phase shifts: namely, we *define*  $\delta_\ell(k)$  to be zero (for any  $\ell, k$ ) when  $V_0 = 0$ , which is a reasonable assumption. Then, we build a continuous solution by manually adding or subtracting a contribution of  $\pi$  whenever necessary. This is performed in two steps: first, we work in the low-energy limit and, starting from  $V_0 = 0$ , we progressively increase the potential depth, removing any encountered jump during the process. Secondly, for any fixed  $V_0$ , starting from  $E \rightarrow \infty$  (where we assume again  $\delta_\ell(k \rightarrow \infty) = 0$ ), we gradually

<sup>11</sup>To be more precise, Wigner's law refers to the *tangent* of the phase shifts, meaning that Eqs. (1.22) actually hold for  $\beta_\ell$ . Alternatively, as we shall derive shortly, one could argue that  $\delta_\ell(k \rightarrow 0) \rightarrow 0$ , *but modulo*  $\pi$ , and provided off-resonant scattering is concerned.

reduce the energy, correcting for discontinuities in a similar fashion. These two procedures should converge. In the end, what we are going to find essentially is:

$$\Delta_\ell = \delta_\ell(k \rightarrow 0) - \delta_\ell(k \rightarrow \infty) \neq 0 \quad (1.41a)$$

$$\Delta_\ell^{\text{eff}} = \tan(\delta_\ell(k \rightarrow 0)) - \tan(\delta_\ell(k \rightarrow \infty)) = 0 \quad (1.41b)$$

which means that  $\Delta_\ell$  is an integer multiple of  $\pi$ .

Let us start by considering a  $s$ -wave (i.e.  $\ell = 0$ ) scattering state, such as the one of Eqs. (1.34). In this simple case, we can explicitly compute the internal logarithmic derivative (see Eq. (1.13b))

$$\mathfrak{L}_0^{(1)}(k) = \tilde{k}_0 b \cot(\tilde{k}_0 b) - 1 \quad (1.42)$$

where  $\tilde{k}_0^2 = k_0^2 + k^2$ , and we have set  $R_0 = b$ . By inserting Eq. (1.42) into Eq. (1.40), and by making use of the explicit form of  $j_0$  and  $n_0$  [35], one finds

$$\tan(\delta_0(k)) = \frac{\frac{k}{\tilde{k}_0} \tan(\tilde{k}_0 b) - \tan(kb)}{1 + \frac{k}{\tilde{k}_0} \tan(\tilde{k}_0 b) \cdot \tan(kb)} \quad (1.43)$$

Defining  $\mathfrak{A} = \tan^{-1} \left[ \frac{k}{\tilde{k}_0} \tan(\tilde{k}_0 b) \right]$  and  $\mathfrak{B} = kb$ , and applying simple trigonometric identities, we obtain

$$\delta_0(k) = \tan^{-1} \left[ \frac{k}{\tilde{k}_0} \tan(\tilde{k}_0 b) \right] - kb \quad (1.44a)$$

where we leave open the possibility of adding or subtracting integer multiples of  $\pi$ . Let us first examine the behaviour of Eq. (1.44a) as a function of  $k_0$  (that is essentially the potential depth), taking the limit  $k \rightarrow 0$  (so  $\tilde{k}_0 \simeq k_0$ ) and keeping  $b$  fixed, see Fig. 1.3a (blue line). At low energies and for shallow potential depths,  $\delta_0$  is a positive quantity (so the scattering length will be negative, as we have seen in Fig. 1.2b). If we increase  $k_0$  up to  $k_0 b = \frac{\pi}{2}$  we find that, while  $\tan(k_0 b)$  diverges,  $\delta_0$  “only” shows a finite discontinuity, passing abruptly from  $\frac{\pi}{2}$  to  $-\frac{\pi}{2}$ . It is interesting to notice that evaluating  $L_0^{(1)} = \lim_{k \rightarrow 0} \mathfrak{L}_0^{(1)}$  under the assumption  $k_0 b = \frac{\pi}{2}$  yields  $L_0^{(1)} = -1$ . This is the “accidental” condition  $L_\ell^{(1)} = -(\ell + 1)$  which could have made Eq. (1.23) ill-defined. As we learned in Sec. 1.4.1,  $k_0 b = \frac{\pi}{2}$  corresponds to the appearance of the first bound ( $s$ -)state in the square well, at zero binding energy. When this happens, the scattering length diverges, whereas the total cross section scales as  $k^{-2}$  (see Sec. 1.8): this situation is referred to as a *zero-energy resonance*. If we keep increasing  $k_0$  until  $\frac{\pi}{2} < k_0 b < \frac{3}{2}\pi$ , far from boundaries we have

$$\delta_0(k \rightarrow 0) \simeq kb \left( \frac{\tan(k_0 b)}{k_0 b} - 1 \right) \xrightarrow[k \rightarrow 0]{} 0^- \quad (1.44b)$$

Thus, to make  $\delta_0$  a continuous and monotonic function of  $k_0$ , we must add a contribution of  $\pi$  whenever a new  $s$ -wave bound state “enters” the well. Thereby we obtain

$$\lim_{k \rightarrow 0} \delta_0(k) = N_0 \pi \quad (1.45a)$$

where

$$N_0 = \text{Floor} \left[ \sqrt{\frac{2mb^2 V_0}{\pi^2 \hbar^2}} + \frac{1}{2} \right] \quad (1.45b)$$

is the number of  $s$ -wave bound states supported by the potential, assuming that none of them is at threshold. Conversely, when  $V_0$  is such that the  $(N_0 + 1)$ -th  $s$ -wave bound state is about to be supported, we have

$$\lim_{k \rightarrow 0} \delta_0(k) \simeq \left( N_0 + \frac{1}{2} \right) \pi \quad (1.45c)$$

Note that Eq. (1.45c) describes an *anomalous* low-energy phase shift, in the sense that it does not approach 0 modulo  $\pi$ , thus violating Wigner's law. As already pointed out, this originates from the zero-energy logarithmic derivative being  $L_0^{(1)} = -1$  when  $k_0 b$  is an odd multiple of  $\frac{\pi}{2}$ . The resulting (corrected) behaviour of  $\delta_0(k)$  is plotted in Fig. 1.3a (green line). A similar study can also be carried out for higher angular momenta ( $\ell > 0$ ). In particular, one finds [36]

$$\lim_{k \rightarrow 0} \delta_\ell(k) = N_\ell \pi \quad (1.45d)$$

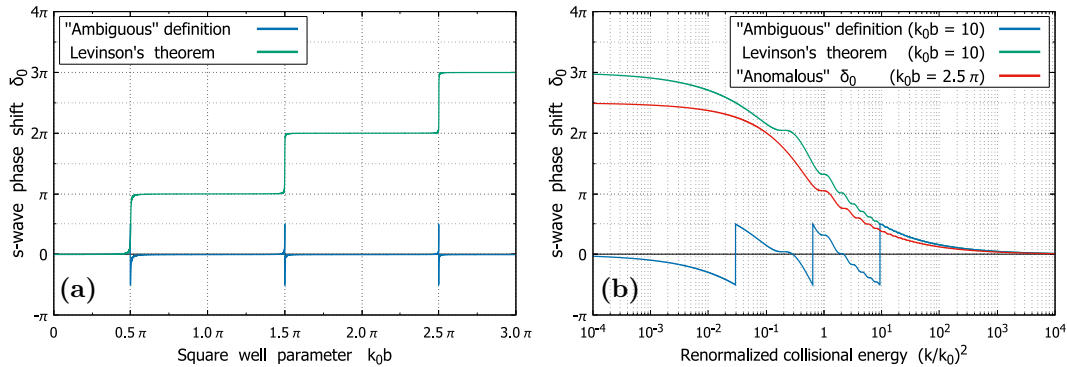
where  $N_\ell$  is the number of supported bound states with angular momentum  $\ell > 0$ , including those at zero binding energy. The generalization of this result to a broad class of short-ranged two-body interaction potentials constitutes the Levinson's theorem [33, 37].

We now turn to the investigation of the  $s$ -wave phase shift as a function of the collisional energy. We choose (and fix) an arbitrary value for  $k_0 b$ , and we consider the high-energy behaviour of  $\delta_0$ . We immediately realize that Eq. (1.44a) is not a good starting point in this case, as it provides  $\delta_0(k \rightarrow \infty) \neq 0$  (unless, of course, one takes the modulo operation). In this regard, Eq. (1.40) better suits our purpose, as the numerator inside the square brackets vanishes for  $k \rightarrow \infty$ . As we decrease the energy,  $\delta_0$  increases smoothly. The only exceptions occur when the denominator vanishes, i.e. whenever

$$\mathfrak{L}_0^{(1)} = \rho_0 \frac{n_0'(\rho_0)}{n_0(\rho_0)} \longrightarrow \tilde{\rho}_0 \cot(\tilde{\rho}_0) = -\rho_0 \tan(\rho_0) \quad (1.46)$$

with  $\tilde{\rho}_0 = \tilde{k}_0 b$ , see Fig. 1.3b (blue line). As we shall better examine in the next section, when Eq. (1.46) holds, the  $s$ -wave scattering cross section is *unitary-limited* (Ramsauer-Townsend "maximum"). In the present discussion, our goal is simply to solve Eq. (1.46) numerically, in order to be able to correct for jumps in Eq. (1.40). The outcome of such a procedure is plotted in Fig. 1.3b for  $k_0 b = 10$  (green line)

**Figure 1.3** – Phase shift  $\delta_0$  for a square-well potential: (a) as a function of the trap depth, in the low-energy limit; (b) as a function of the collisional energy, for fixed trap depths. The blue and the green lines are obtained from Eqs. (1.40) and (1.47), respectively. The red line shows an example of anomalous behaviour when a bound state is at threshold.



and  $k_0 b = \frac{5}{2} \pi$  (red line). As one can appreciate, once jumps are removed, the phase shift varies smoothly and monotonically with the energy. Most importantly,  $\delta_0(k \rightarrow \infty) \rightarrow 0$ , as expected for a (nearly) free particle, while reaching at zero energy the value predicted by Levinson's theorem.

We conclude this section pointing out that, in the simple case of the square-well potential, it is possible to write an analytic formula for  $\delta_0$  that correctly reproduces the results of the above methods, both as a function of  $k$  and  $k_0$ :

$$\delta_0(k, k_0) = \tan^{-1} \left[ \frac{k}{\tilde{k}_0} \tan(\tilde{k}_0 b) \right] - kb + \text{Floor} \left[ \frac{\tilde{k}_0 b}{\pi} + \frac{1}{2} \right] \quad (1.47)$$

recalling that  $\tilde{k}_0 = \sqrt{k_0^2 + k^2}$ . Eq. (1.47) was found semi-empirically during the study of this problem.

## 1.6 The Ramsauer-Townsend effect

The square well toy model can be further exploited to explore the regime of cold but finite temperatures. Let us start by considering the scattering solutions ( $E > 0$ ) of Eq. (1.28), with  $V(r)$  given by Eq. (1.32). For each  $\ell \geq 0$ , in the inner region we have

$$U_\ell^{(1)}(r) = A_\ell \hat{j}_\ell(\tilde{k}_0 r) \quad (1.48)$$

where  $A_\ell$  is a normalization constant. Therefore, from Eq. (1.13b), we obtain<sup>12</sup>

$$\mathfrak{L}_\ell^{(1)}(k) = \tilde{k}_0 b \frac{j_\ell'(\tilde{k}_0 b)}{j_\ell(\tilde{k}_0 b)} \quad (1.49)$$

which, once inserted into Eq. (1.13a), yields

$$\tan(\delta_\ell(k)) = \frac{\rho_0 j_\ell(\tilde{\rho}_0) j_\ell'(\rho_0) - \tilde{\rho}_0 j_\ell'(\tilde{\rho}_0) j_\ell(\rho_0)}{\rho_0 j_\ell(\tilde{\rho}_0) n_\ell'(\rho_0) - \tilde{\rho}_0 j_\ell'(\tilde{\rho}_0) n_\ell(\rho_0)} \quad (1.50)$$

with  $\tilde{\rho}_0 = \tilde{k}_0 R_0 = \tilde{k}_0 b$ . Our interest is to study Eq. (1.50) as a function of  $k$ , keeping the potential parameters fixed. In particular, for each  $\ell$ , we search for those values of  $k$  that make either the numerator or the denominator vanish. In practice, they can be obtained by numerically solving

$$\rho_0 \frac{j_\ell'(\rho_0)}{j_\ell(\rho_0)} = \tilde{\rho}_0 \frac{j_\ell'(\tilde{\rho}_0)}{j_\ell(\tilde{\rho}_0)} \quad (\text{num.} = 0) \quad (1.51a)$$

$$\rho_0 \frac{n_\ell'(\rho_0)}{n_\ell(\rho_0)} = \tilde{\rho}_0 \frac{j_\ell'(\tilde{\rho}_0)}{j_\ell(\tilde{\rho}_0)} \quad (\text{den.} = 0) \quad (1.51b)$$

When Eq. (1.51a) is satisfied,  $\tan(\delta_\ell) = 0$ . Hence  $\delta_\ell$  is an integer multiple of  $\pi$ , and we conclude from Eq. (1.19) that the corresponding partial cross section  $\sigma_\ell$  vanishes. This is commonly referred to as a *Ramsauer-Townsend (RT) minimum*.

Conversely, when Eq. (1.51b) holds,  $\tan(\delta_\ell)$  diverges. In this case,  $\delta_\ell$  is an odd multiple of  $\frac{\pi}{2}$ , and the corresponding partial cross section reads  $\sigma_\ell = 4\pi(2\ell+1)k^{-2}$ . This is the so-called *unitary limit*, which will be discussed in Sec. 1.8. Anyway, for the moment, let us label this condition as a “RT maximum”.

In Fig. 1.4 we plot the first few partial cross sections as a function of  $k(T)$ , computed

<sup>12</sup>One could easily check that Eq. (1.49) reduces to Eq. (1.42) when  $\ell = 0$ .

starting from Eqs. (1.19) and (1.50), for  $V_0/k_B = 600$  K ( $k_B$  is the Boltzmann's constant),  $b \simeq 67 a_0$ , and  $m$  being the reduced mass of the Li-Cr system (these are just some arbitrary values). The most pronounced feature is the oscillatory behaviour of the partial cross sections, each of them fluctuating between zero and the corresponding unitary limit: this is the well-known *Ramsauer-Townsend effect* [43, 44], first observed in electron scattering experiments. Anyway, it is worth pointing out that RT maxima do not coincide with local maxima of  $\sigma_\ell$ : the latter are always found at a slightly lower temperature, owing to the additional  $k^{-2}$  factor. We conclude this section by noting that, for a generic potential, Eqs. (1.51) read

$$\mathfrak{L}_\ell^{(1)}(k) = \rho_0 \frac{j_\ell'(\rho_0)}{j_\ell(\rho_0)} = \ell - \rho_0 \frac{j_{\ell+1}(\rho_0)}{j_\ell(\rho_0)} \quad (\text{RT min.}) \quad (1.52a)$$

$$\mathfrak{L}_\ell^{(1)}(k) = \rho_0 \frac{n_\ell'(\rho_0)}{n_\ell(\rho_0)} = \ell - \rho_0 \frac{n_{\ell+1}(\rho_0)}{n_\ell(\rho_0)} \quad (\text{RT max.}) \quad (1.52b)$$

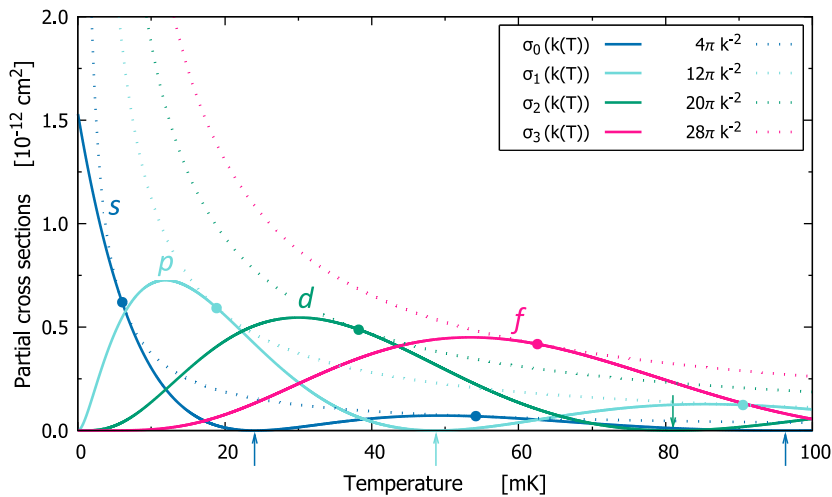
where we used Eq. (1.11). In the limit of  $k \rightarrow 0$ , to first order we have (see Eqs. (1.9))

$$L_\ell^{(1)} \simeq \ell \quad (\text{“zero-energy RT min.”}) \quad (1.53a)$$

$$L_\ell^{(1)} \simeq -(\ell + 1) \quad (\text{“zero-energy RT max.”}) \quad (1.53b)$$

These last results could also have been inferred starting from Eq. (1.23). One could check that, for a short-range potential, Eq. (1.53b) describes the appearance of a bound  $\ell$  state at zero binding energy. Under this condition, scattering in the  $\ell$ -th partial wave would in principle be resonant for  $k \rightarrow 0$  (zero-energy resonance). Anyway, the centrifugal barrier strongly suppresses any  $\ell > 0$  contribution in the zero-temperature limit, thus effectively preventing the observation of such resonances in any  $\ell \neq 0$  channel.<sup>13</sup>

**Figure 1.4** – Partial cross-sections as a function of the collisional energy, expressed in temperature units. Dotted lines show the respective unitary limits (see Sec. 1.8). Arrows and dots indicate RT minima and maxima, respectively.



<sup>13</sup>In other words, for  $\ell > 0$  the width of such resonances becomes vanishingly small as  $k \rightarrow 0$ . Nonetheless, they can be observed at finite temperatures, see Sec. 1.7.

## 1.7 Shape resonances

Generally speaking, the partial cross sections  $\sigma_\ell(k)$  are slowly-varying (oscillating) functions of the scattering energy, see again Fig. 1.4. Anyway, a quite peculiar behaviour is encountered if Eq. (1.52b) happens to have a solution for a small but finite value of  $k$ , namely  $0 < k < K_c$ , where  $K_c$  is the maximum height of the centrifugal barrier<sup>14</sup> (expressed as a wavevector). For the square-well potential of Eq. (1.32), one has  $K_c b = \sqrt{\ell(\ell+1)}$  for any given  $\ell$ . In this case, it is clear that  $0 < k < K_c$  may only be satisfied if  $\ell > 0$ .<sup>15</sup> Let us define

$$\mathfrak{J}_\ell^{(2)}(k) = \rho_0 \frac{j_\ell'(\rho_0)}{j_\ell(\rho_0)}; \quad \mathfrak{N}_\ell^{(2)}(k) = \rho_0 \frac{n_\ell'(\rho_0)}{n_\ell(\rho_0)} \quad (1.54)$$

In Fig. 1.5a we plot these two quantities together with  $\mathfrak{L}_\ell^{(1)}(k)$  (see Eq. (1.49)), after having finely adjusted our square-well parameters in order to obtain the desired solution (for the  $\ell = 2$  partial wave). Following the discussion on the RT effect, intersections of  $\mathfrak{L}_\ell^{(1)}(k)$  and  $\mathfrak{J}_\ell^{(2)}(k)$  correspond to zeroes of the partial scattering cross section  $\sigma_\ell$ , whereas when  $\mathfrak{L}_\ell^{(1)}$  crosses  $\mathfrak{N}_\ell^{(2)}(k)$  one has a *unitary-limited*  $\sigma_\ell(k)$  (see Sec. 1.8). Note that  $\mathfrak{J}_\ell^{(2)}(k \rightarrow 0) = \ell$  and  $\mathfrak{N}_\ell^{(2)}(k \rightarrow 0) = -(\ell+1)$ , in agreement with Eqs. (1.53).

In most cases,  $\mathfrak{L}_\ell^{(1)}(k)$  crosses alternatively  $\mathfrak{J}_\ell^{(2)}(k)$  and  $\mathfrak{N}_\ell^{(2)}(k)$ . The peculiar solution we are looking for is encountered when, at low energies, two consecutive intersections with  $\mathfrak{N}_\ell^{(2)}(k)$  occur. In particular, if one of these falls at  $k < K_c$ , the whole situation has a simple physical interpretation [36]: our attractive potential is such that it supports a *metastable*  $\ell$ -state, that is trapped behind the centrifugal barrier. Of course, this is not a real bound state, as it acquires a finite lifetime owing to the finite probability to tunnel out of the centrifugal barrier. Anyway, its existence produces a sharp resonance feature in the corresponding partial cross section  $\sigma_\ell$ , see Fig. 1.5b. Typically, these resonance phenomena depend critically on the potential parameters, so they are commonly referred to as *shape resonances* [36].

The characteristic lineshape of the (partial) scattering cross section near a shape resonance can be derived from a simple argument [36, 49]. If the denominator of Eq. (1.13a) undergoes a “sharp” zero-crossing, the corresponding phase shift rapidly changes by  $\pi$ . Thus, in a small energy region  $[E_r - \Gamma/2; E_r + \Gamma/2]$ , and neglecting the (slowly-varying) background contribution, we can approximate  $\delta_\ell$  as

$$\delta_\ell(k) \simeq \tan^{-1} \left[ \frac{\Gamma/2}{E_r - E} \right] \quad (1.55)$$

reminding that  $E = \hbar^2 k^2 / 2m$  is the collision energy. Hence, from Eq. (1.19) we have

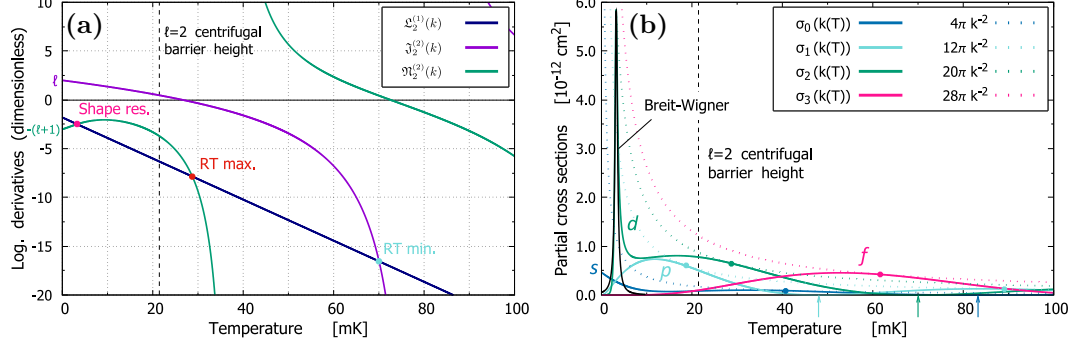
$$\sigma_\ell(k) \simeq \frac{4\pi}{k^2} (2\ell + 1) \frac{\Gamma^2/4}{(E - E_r)^2 + \Gamma^2/4} \quad (1.56)$$

which is known as the (one-level) *Breit-Wigner formula* [45]. The lorentzian term in Eq. (1.56) introduces a strong dependence of the scattering cross section on the

<sup>14</sup>Here with “centrifugal barrier” we mean the repulsive tail of the effective potential  $V_{\text{eff}}(r)$ , sum of the interaction and centrifugal potentials, that arises for  $r \gtrsim R_0$ , see again Eq. (1.21) and the initial discussion in Sec. 1.2.

<sup>15</sup>A toy model for a square-well potential with a built-in additional barrier is presented in Ref. [42].

**Figure 1.5** – (a) The quantities  $\mathfrak{L}_2^{(1)}(k)$  (blue),  $\mathfrak{J}_2^{(2)}(k)$  (violet), and  $\mathfrak{N}_2^{(2)}(k)$  (green) for a square-well potential tailored to support a quasi-bound  $d$ -state ( $k_0 b \simeq 130.4983\pi$ ). (b) Resulting partial cross-sections as a function of the collisional energy. Note the sharp resonance in the  $d$ -wave channel, well described by Eq. (1.56).



collisional energy. In particular, for  $E = E_r$  (i.e. on top of the resonance), the partial cross section  $\sigma_\ell$  reaches its unitary-limited value (see Sec. 1.8).

Within the approximation of Eq. (1.55), the resonance width is given by

$$\Gamma = -2 \left[ \left( \frac{\partial \cot(\delta_\ell(k))}{\partial E} \right) \Big|_{E_r} \right]^{-1} \quad (1.57a)$$

Further, if the resonance occurs at very low energies, we have (see Eq. (1.23))

$$\Gamma(E_r \rightarrow 0) \simeq \frac{2\hbar^2}{mb^2} \left[ \frac{\ell - L_\ell^{(1)}}{[(2\ell + 1)!!]^2 (\ell + 1 + L_\ell^{(1)})} \right] \cdot \rho_r^{2\ell+3} \quad (1.57b)$$

where  $\rho_r^2 = 2mb^2 E_r / \hbar^2$ . Consequently,  $\Gamma(E_r)$  becomes narrower the more  $E_r$  is reduced ( $\rho_r^{2\ell+3}$  goes to zero faster than  $(\ell + 1 + \mathfrak{L}_\ell^{(1)}(k \rightarrow 0))$ ), as already pointed out at the end of the last section.

## 1.8 Unitary limit and effective range

It is important to realize that, while  $a_s$  may effectively diverge near a scattering resonance, the total cross section actually does not, for any finite  $k$  value. This could have already been inferred from Eq. (1.19), as it is clear that the contribution of each partial wave has an upper bound of

$$\sigma_\ell^{\max}(k) = \frac{4\pi}{k^2} (2\ell + 1) \quad (1.58)$$

which depends only on  $k = k(T)$ . In a more formal approach, one can always define the  $s$ -wave scattering length as in Eq. (1.25a). However, when  $a_s \rightarrow \pm\infty$ , the approximation  $\tan(\delta_0(k)) \approx \sin(\delta_0(k)) \approx \delta_0(k)$  does not hold. Instead, going back to the general expression for  $f(k, \theta)$ , i.e. Eq. (1.18b), and writing  $e^{i\delta_\ell(k)} \sin(\delta_\ell(k)) = [\cot(\delta_\ell(k)) - i]^{-1}$ , in the limit of  $k \rightarrow 0$  one can expand

$$\cot(\delta_0(k)) \simeq -\frac{1}{k a_s} + \frac{1}{2} k r_e + \dots \quad (1.59)$$

where we have considered only the  $s$ -wave contribution. The parameter  $r_e$ , often conveniently recast as  $r_e = -2R^*$ , is called the *effective range*.<sup>16</sup> Following from Eq. (1.59), the low-energy  $s$ -wave scattering amplitude can be expressed as

$$f_0(k \rightarrow 0, \theta) = \frac{1}{k \cot(\delta_0(k)) - ik} \simeq -\frac{1}{a_s^{-1} + R^*k^2 + ik} \quad (1.60)$$

It should be emphasized that Eq. (1.59) is a legitimate expansion in the regime of  $s$ -wave scattering: since typically  $r_e \sim b$  ( $b$  is the potential range), the effective range correction to the scattering amplitude is of relative order  $kb$ , whereas  $p$ -wave contributions scale as  $(kb)^3$  [47].

Besides, note that the last expression in Eq. (1.60) has the characteristic form of a Breit-Wigner resonance. This becomes apparent if we recast it in energy units:

$$f_0(E \rightarrow 0, \theta) \simeq -\frac{\frac{\hbar}{\sqrt{2m}} \tilde{\gamma}}{E - E_r + i\gamma\sqrt{E}} \quad (1.61)$$

with  $E_r = -\hbar^2/(2mR^*a_s)$  and  $\tilde{\gamma} = \hbar/(\sqrt{2m}R^*)$ . Indeed, by using Eq. (1.61) in Eq. (1.5b), one retrieves the Breit-Wigner formula (see Eq. (1.56)), with  $\Gamma^2 = 4\tilde{\gamma}^2E$ . The parameter  $2\tilde{\gamma}\sqrt{E}/\hbar$  represents the decay rate of the quasi-bound state that yields the scattering resonance [42]. Note that  $E_r$  and  $\tilde{\gamma}$  are entirely determined by  $a_s$  and  $R^*$  (and vice versa).

From Eqs. (1.5b) and (1.60), the total low-energy (i.e.  $s$ -wave) scattering cross section can be written as

$$\sigma_0(k) \simeq \frac{4\pi a_s^2}{(1 + R^*k^2a_s)^2 + k^2a_s^2} \stackrel{(R^*=0)}{=} \frac{4\pi a_s^2}{1 + k^2a_s^2} \quad (1.62)$$

where the last expression is obtained setting  $R^* = 0$ . Alternatively, and equivalently, one can define a  $k$ -dependent scattering length that includes effective range corrections [49]

$$a(k) = -\frac{\tan(\delta_0(k))}{k} \simeq \frac{a_s}{1 + R^*k^2a_s} \quad (1.63)$$

where we used Eq. (1.59). With this definition, Eq. (1.62) reads

$$\sigma_0(k) \simeq \frac{4\pi a^2(k)}{1 + k^2a^2(k)} \quad (1.64)$$

From Eqs. (1.62) and (1.64), one realizes that  $\sigma_0(k)$  has an upper bound of  $4\pi k^{-2}$ , in accordance with Eq. (1.58). In the low-temperature regime, when the scattering cross section takes this limiting value, the effects of the interaction are independent from the details of the potential, and the system is said to be in the *unitary limit* [46]. In particular, if  $R^* = 0$  the unitary limit occurs whenever  $a_s$  diverges, i.e. on top of a scattering resonance. Conversely, when  $R^* \neq 0$ ,  $\sigma_0(k)$  is unitary-limited for  $R^*k^2a_s = -1$ .

In general, a scattering resonance is said to be *narrow* if  $R^*$  is large and positive ( $R^* \gg b$ ) [42]. Under this condition, the unitary limit is always found on the so-called “BCS” side of the resonance [46], namely for  $a_s = -1/(R^*k^2) < 0$ .

<sup>16</sup>A detailed discussion on the role of  $R^*$  can be found in Ref. [42].

### 1.8.1 The zero-range and effective range approximations

In some sense, the two-body scattering problem essentially consists in determining how the asymptotic wavefunction  $U_\ell^{(2)}(r)$  is affected by its short-distance counterpart, see again Eqs. (1.12) and (1.13). Anyway, if one is not directly interested in the inner region solution of the Schrödinger equation, the so-called *zero-range approximation* can be applied. Basically, one extrapolates the asymptotic wavefunction towards the origin, and imposes a boundary condition at  $r = 0$  that properly accounts for the real scattering phase shift, thus effectively replacing Eq. (1.13a).<sup>17</sup> Namely, given Eq. (1.15), for each partial wave we have

$$\mathfrak{U}_\ell^{(0)}(k) = \frac{\left(\frac{\partial U_\ell^{(2)}}{\partial r}\right)\Big|_{r=0}}{U_\ell^{(2)}(r=0)} = k \cot\left(\delta_\ell(k) - \frac{\ell\pi}{2}\right) \quad (1.65a)$$

These are known as the *Bethe-Peierls (BP) boundary conditions*. Conceptually, the scattering problem may appear simplified, as one has merely to deal with a “free” solution of the Schrödinger equation. Actually, knowledge of  $\delta_\ell(k)$  is still required, so in principle Eq. (1.65a) is by no means easier to solve than Eqs. (1.7). However, in the *s*-wave regime we can perform the *effective range expansion* given by Eq. (1.59), so that the BP boundary condition (for *s*-wave scattering) reads

$$\mathfrak{U}_0^{(0)}(k \rightarrow 0) = \frac{\left(\frac{\partial U_0^{(2)}}{\partial r}\right)\Big|_{r=0}}{U_0^{(2)}(r=0)} \simeq -\frac{1}{a_s} + \frac{1}{2}k^2 r_e \quad (1.65b)$$

Eq. (1.65b) definitely constitutes a great simplification: With no need for the entire functional form of  $\delta_\ell(k)$ , nor for the details of the scattering potential  $V(r)$  (as long as it is short-ranged), the low-energy collisional properties of ultracold atoms can be completely characterized by just two parameters, namely the *s*-wave scattering length and the *effective range*.<sup>18</sup> As a corollary, any arbitrary (pseudo-)potential able to correctly reproduce the values of  $a_s$  and  $r_e$  can be used to solve the scattering problem. Anyway, in most real-world situations, experimental input is unavoidably required to determine these two key parameters.

<sup>17</sup>In the case of a square-well potential (see Eq. (1.32)), one can imagine to decrease the potential range  $b$  down to 0, while constantly adjusting  $k_0$  in order to keep  $a_s$  unchanged: hence, the name of *zero-range* approximation.

<sup>18</sup>The *zero-range* approximation that results from neglecting  $r_e$  in Eq. (1.65b) directly translates into a radial dependence of the wavefunction of the kind  $k(r - a_s)$ . This is precisely the form in which we sought our solutions, see again Eqs. (1.30b) and (1.34b).

## 1.9 Scattering of identical particles

Before taking into account more accurate potentials to model atomic interactions, let us extend our framework to deal with indistinguishable<sup>19</sup> particles. Generally speaking, when one tackles a system of identical quantum objects, symmetry considerations are fundamental. In our case, the two-particle wavefunction must be properly symmetrized by taking into account the quantum statistics of the investigated atoms:

$$\psi(\vec{r}_1, \vec{r}_2) = \varepsilon \psi(\vec{r}_2, \vec{r}_1) \quad \text{where } \varepsilon = \begin{cases} 1 & \text{for bosons} \\ -1 & \text{for fermions} \end{cases}$$

In the two-body problem, exchanging the two particles corresponds to a parity transformation: in other words, when identical particles are considered, it is not possible to distinguish between the scattering angles  $\theta$  and  $\pi - \theta$ . Accordingly, a properly symmetrized asymptotic scattering state takes the form

$$\psi_s(\vec{r}) \simeq \frac{1}{\sqrt{2}} (e^{ikz} + \varepsilon e^{-ikz}) + \frac{1}{\sqrt{2}} [f(k, \theta) + \varepsilon f(k, \pi - \theta)] \frac{e^{ikr}}{r} \quad (1.66)$$

By repeating the analysis of Sec. 1.1 with this wavefunction, we can straightforwardly obtain the symmetrized differential cross section<sup>20</sup>

$$\frac{d\sigma}{d\Omega} = \frac{1}{2} |f(k, \theta) + \varepsilon f(k, \pi - \theta)|^2 \quad (1.67)$$

It is worth stressing that the sum of the scattering amplitudes is carried out before the squared modulus: this leads to interference effects in the scattering cross section. From Eq. (1.18b) and from the parity of spherical harmonics, it follows that

$$[f(k, \theta) + \varepsilon f(k, \pi - \theta)] = \sum_{\ell=0}^{\infty} f_{\ell}(k, \theta) [1 + \varepsilon (-1)^{\ell}] = \sum_{\ell=0}^{\infty} f_{\ell}(k, \theta) \cdot \tilde{\varepsilon}_{\ell} \quad (1.68)$$

having defined  $f_{\ell}(k, \theta)$  as the  $\ell$ -th term in the sum of Eq. (1.18b). Therefore, the total elastic cross section for identical particles is given by

$$\sigma_{\text{el}}(k) = \frac{4\pi}{k^2} \sum_{\ell=0}^{\infty} \tilde{\varepsilon}_{\ell} (2\ell + 1) \sin^2(\delta_{\ell}(k)) \quad (1.69)$$

where we used  $\tilde{\varepsilon}_{\ell}^2 = 2\tilde{\varepsilon}_{\ell}$ . Overall, the interference term in  $\sigma_{\text{el}}(k)$  arises from the combination of quantum statistics and symmetry properties of spherical harmonics. In the case of bosons (fermions), the factor  $\tilde{\varepsilon}_{\ell}$  is equal to 2 for even (odd) partial waves, whereas it cancels out for terms of the opposite parity. More explicitly:

$$\sigma_{\text{bos}}(k) = \frac{8\pi}{k^2} \sum_{\substack{\ell \\ (\text{even})}}^{\infty} (2\ell + 1) \sin^2(\delta_{\ell}(k)) \quad (1.70a)$$

$$\sigma_{\text{fer}}(k) = \frac{8\pi}{k^2} \sum_{\substack{\ell \\ (\text{odd})}}^{\infty} (2\ell + 1) \sin^2(\delta_{\ell}(k)) \quad (1.70b)$$

<sup>19</sup>For “indistinguishable” we mean two *identical* atoms in the *same* internal state. In this case, the spin part of the wavefunction is necessarily symmetric under the exchange of the two particles. A detailed treatment of collisions involving same species atoms in *different* internal states can be found in Refs. [36, 48].

<sup>20</sup>Note that in this case, for the definition of the differential cross-section, one should refer to the *total* incoming flux (towards the origin), which is still given by  $v = \hbar k/m$ . This accounts for the factor  $1/2$  in Eq. (1.67).

Ultimately, when two indistinguishable atoms undergo a collision event, only half of the partial waves effectively contribute to the total cross section: the remaining constitute symmetry-forbidden channels. In the case of identical fermions, this implies that collisions will be fully suppressed in the zero-temperature limit, as long as the interaction potential is short-ranged and Wigner's threshold law holds. Thus, an ultracold sample of identical fermionic atoms represents an exquisite realization of an *ideal Fermi gas*.

## 1.10 More realistic atomic interactions

We now move to consider additional contributions to the atom-atom interaction, and discuss their role in the context of (ultra)cold collisions. To introduce the notation, let us remind that a single free atom has electronic spin  $\vec{s}$  and orbital angular momentum  $\vec{l}$ , that are coupled (by the spin-orbit interaction) to the total electronic angular momentum  $\vec{j} = \vec{s} + \vec{l}$ . The latter will in turn combine with the nuclear spin  $\vec{i}$  to yield the total angular momentum of the atom  $\vec{f} = \vec{i} + \vec{j}$ . Atomic states labeled by the quantum number  $j$  ( $f$ ) are called *fine states* (*hyperfine states*). If an external magnetic field is applied, these states split into  $2j + 1$  ( $2f + 1$ ) Zeeman sublevels, each of which is labelled by the quantum number  $m_j$  ( $m_f$ ). Generally speaking, under a magnetic field  $f$  (or  $j$ , in the absence of the hyperfine interaction) ceases to be a good quantum number, but it can be still retained as a label to specify the adiabatically connected zero-field energy level. The true eigenstates for  $B \neq 0$  will be referred to as the *Breit-Rabi states*.

Let us examine how good atomic quantum numbers are modified by interatomic interactions. We assume to deal with atoms having a non-zero nuclear spin (i.e. an hyperfine structure), but clearly our results will hold for  $\vec{i}_1 = 0$  and/or  $\vec{i}_2 = 0$  as well. When tackling a two-body collision event, one can distinguish between two different regimes: two far-apart atoms are essentially free, and their internal state is entirely described by  $|\psi\rangle = |f_1, m_{f_1}\rangle + |f_2, m_{f_2}\rangle$ . Conversely, when the particles get close to each other, exchange and dipolar interactions break the hyperfine couplings, leading to a direct coupling of the two electronic spins. In the case of alkali atoms  $s_1 = s_2 = 1/2$ , so the total electronic spin  $\vec{S} = \vec{s}_1 + \vec{s}_2$  is associated with the quantum number  $S = 0, 1$ . States having  $S = 0$  ( $S = 1$ ) are called *singlet* (*triplet*) states. If we consider instead heteronuclear collisions in the Li-Cr mixture, the two electronic spins  $s_{\text{Li}} = 1/2$  and  $s_{\text{Cr}} = 3$  can either couple to  $S = 5/2$  (*sextet*) or to  $S = 7/2$  (*octuplet*).

Let us analyse more carefully the interaction between two neutral atoms that are close together. At short interatomic distances, a more accurate hamiltonian to describe the two-atom problem can be chosen as [50]

$$\hat{H} = \hat{H}_0 + \hat{H}_{\text{int}} \quad (1.71a)$$

where

$$\hat{H}_0 = \hat{T}_{\text{kin}} + \hat{H}_{\text{hf}} + \hat{H}_{\text{zee}} \quad (1.71b)$$

$$\hat{H}_{\text{int}} = \hat{H}_{\text{vdW}} + \hat{H}_{\text{ex}} + \hat{H}_{\text{dd}} \quad (1.71c)$$

are the unperturbed and the interaction hamiltonians, respectively. The former is the sum of three contributions, namely the relative kinetic energy, the hyperfine

interaction and the Zeeman energy:

$$\hat{T}_{\text{kin}} = \frac{\hbar^2 k^2}{2m} \quad (1.72a)$$

$$\hat{H}_{\text{hf}} = \frac{A_1^{\text{hf}}}{\hbar^2} (\vec{s}_1 \cdot \vec{i}_1) + \frac{A_2^{\text{hf}}}{\hbar^2} (\vec{s}_2 \cdot \vec{i}_2) \quad (1.72b)$$

$$\hat{H}_{\text{zee}} = -\frac{1}{\hbar} [\mu_{\text{B}} g_s (\vec{s}_1 + \vec{s}_2) - \mu_{\text{N}} (g_{i,1} \vec{i}_1 + g_{i,2} \vec{i}_2)] \cdot \vec{B} \quad (1.72c)$$

with  $A_q^{\text{hf}}$  ( $q = 1, 2$ ) being the atomic hyperfine constants,  $\mu_{\text{B}}$  ( $\mu_{\text{N}}$ ) the Bohr (nuclear) magneton, and  $g_s$  ( $g_{i,q}$ ) the electronic (nuclear)  $g$ -factor. Eq. (1.71b) is basically the sum of two independent single-particle hamiltonians, written in the center of mass frame. Therefore, it is diagonal in the Breit-Rabi basis.

In the interaction hamiltonian, the first term essentially accounts for the attractive (van der Waals) part of the Lennard-Jones potential (see Eq. (1.1)):

$$\hat{H}_{\text{vdW}}(r) = -\frac{C_6}{r^6} - \frac{C_8}{r^8} - \frac{C_{10}}{r^{10}} + \dots \quad (1.73)$$

where we are now considering a more accurate multipole expansion. We stress that  $\hat{H}_{\text{vdW}}$  is spin-independent, so it cannot couple different internal states. In the asymptotic limit, and in the absence of long-range dipolar interactions,  $C_6/r^6$  is the leading term of the interatomic potential. Anyway, as we are aiming for a better short-range description of the interaction, the ‘‘repulsive hard wall’’ term in Eq. (1.1) needs to be replaced. To this end, the second term of Eq. (1.71c) represents the exchange interaction, which arises from the anti-symmetrization of the total electronic wavefunction. This term is strongly dependent on the overlap between the single-atom electronic wavefunctions, so it becomes relevant at short interatomic distances. It can be expressed as<sup>21</sup>

$$\hat{H}_{\text{ex}}(r) = V_{\text{ex}}(r) \frac{(1 + 4 \vec{s}_1 \cdot \vec{s}_2)}{2(s_1 + s_2)} \quad (1.74a)$$

$$\text{with } V_{\text{ex}}(r) = C_{\text{ex}} r^{-\beta_{\text{ex}}} e^{-r/r_{\text{ex}}} \quad (1.74b)$$

where  $C_{\text{ex}}$ ,  $\beta_{\text{ex}}$  and  $r_{\text{ex}}$  are constants that characterize the strength and the range of the interaction, respectively. Being spin-dependent, the exchange hamiltonian can couple different internal (hyperfine) states, although always conserving the total electronic spin and the projection of the total internal angular momentum, namely  $S$  and  $M_f = m_{f_1} + m_{f_2}$ , respectively.<sup>22</sup> Hence, this interaction may induce transitions between different internal states, that are commonly referred to as *spin-exchange collisions*. They often result in atom losses, as it will be discussed in Sec. 1.14. Anyway, we remark that owing to the conservation of  $M_f$ , the so-called *stretched states*  $|f, m_f = \pm f\rangle$  are immune against transitions induced by  $\hat{H}_{\text{ex}}$ .

Lastly, the third term in Eq. (1.71c) accounts for dipolar interactions. It can be further decomposed into spin-spin interaction and second-order spin-orbit coupling

$$\hat{H}_{\text{dd}}(r) = \hat{H}_{\text{ss}}(r) + \hat{H}_{\text{so}}(r) \quad (1.75a)$$

<sup>21</sup>The normalization of the spin-dependent term in Eq. (1.74a) has been chosen such that, when at least one of the two spins has a value of  $1/2$ ,  $\hat{H}_{\text{ex}}(r) = \pm V_{\text{ex}}(r)$ .

<sup>22</sup>Owing to its central radial dependence,  $\hat{H}_{\text{ex}}$  conserves the relative orbital angular momentum  $\ell$  and its projection  $m_\ell$ .

with

$$\hat{H}_{\text{ss}}(r) = V_1(r) V_s(\vec{s}_1, \vec{s}_2) \quad (1.75\text{b})$$

$$\hat{H}_{\text{so}}(r) = V_2(r) V_s(\vec{s}_1, \vec{s}_2) \quad (1.75\text{c})$$

Note that the spin dependence is the same for the two contributions. The spatial one, by contrast, is starkly different. Namely, the spin-spin interaction scales as  $r^{-3}$  (which is the characteristic long-range behaviour of dipole-dipole interactions), whereas  $V_2(r)$  drops exponentially with increasing interatomic distance [50]. Generalizing Eq. (1.2) to the case of arbitrarily oriented spins, we can take

$$V_s(\vec{s}_1, \vec{s}_2) = - \left[ [\vec{r} \otimes \vec{r}]^{(2)} \otimes [\vec{s}_1 \otimes \vec{s}_2]^{(2)} \right]^{(0)} = \vec{s}_1 \cdot \vec{s}_2 - \frac{3(\vec{s}_1 \cdot \vec{r})(\vec{s}_2 \cdot \vec{r})}{r^2} \quad (1.76)$$

Note that this term arises from the combination of rank-2 spin and spatial tensors. Therefore, to first order,  $\hat{H}_{\text{dd}}$  can couple internal states that differ by either 0 or 2 units of spin  $S$ , and/or of orbital angular momentum  $\ell$ . By gathering together the previous results, for large  $r$  we can write

$$\hat{H}_{\text{dd}}(r) = \left( \frac{C_{\text{ss}}}{r^3} - C_{\text{so}} e^{-r/r_{\text{so}}} \right) \left[ \vec{s}_1 \cdot \vec{s}_2 - \frac{3(\vec{s}_1 \cdot \vec{r})(\vec{s}_2 \cdot \vec{r})}{r^2} \right] \quad (1.77)$$

where  $C_{\text{ss}}$ ,  $C_{\text{so}}$  and  $r_{\text{so}}$  are constants that characterize the strength of the spin-spin and of the spin-orbit interaction, and the range of the latter, respectively.

### 1.10.1 Selection rules

As we have discussed the possibility for  $\hat{H}_{\text{int}}$  to induce transitions between different internal atomic states, we need to account for the appropriate selection rules, some of which have already been introduced. We stress that, besides the quantum numbers that characterize individual atoms,  $\ell$  and  $m_\ell$  – namely, the orbital angular momentum associated with the incoming partial wave and its projection along the magnetic field axis – have to be considered as well. As we have reviewed in Sec. 1.9, for non-identical particles all possible values of  $\ell$  are allowed. Conversely, for identical bosons (fermions), only even (odd) partial waves yield non-zero contributions to the scattering cross section, as a consequence of the (anti-)symmetrization of the total wavefunction. In some sense, this constitutes a first selection rule.

Furthermore, summarizing the results of Sec. 1.10, we observe that:

- $\hat{H}_{\text{vdW}}$  does not couple different states;
- $\hat{H}_{\text{ex}}$  can induce transitions with  $\Delta S = 0$ ;  $\Delta M_f = 0$ ;  $\Delta \ell = 0$ ;  $\Delta m_\ell = 0$ ;
- $\hat{H}_{\text{dd}}$  can induce transitions with  $\Delta S = 0, \pm 2$ ;  $\Delta M_f = 0, \pm 1, \pm 2$ ;  $\Delta \ell = 0, \pm 2$ ;  $\Delta m_\ell = 0, \pm 1, \pm 2$ .

Anyway, we emphasize that these findings are only valid in the context of first-order perturbation theory. To generalize, when the whole interaction hamiltonian is taken into account, the only *strict* selection rule that has to be followed is the conservation of the total angular momentum projection along the  $\vec{B}$  field axis

$$M_{\text{tot}} = M_f + m_\ell = m_{f_1} + m_{f_2} + m_\ell \quad (1.78)$$

Thus we have:  $M_{\text{tot}} = M'_{\text{tot}}$ , where the prime denotes quantities evaluated after the collision.

In the following we will investigate how  $\hat{H}_{\text{int}}$  affects the scattering properties of ultracold atoms. We will introduce the notion of *scattering channel*, and the so-called *molecular basis*. In order to gather the whole discussion on selection rules together, let us anticipate here some results to point out that, when a collision between two identical bosons (fermions) is concerned, only molecular channels with even (odd) values of orbital angular momentum are relevant for the problem. Besides, in a scattering process involving distinguishable particles – although all possible values of  $\ell$  are allowed – due to symmetry arguments, incoming even (odd) partial waves will only couple to even (odd) molecular states and/or partial waves in the exit channel.

### 1.11 Feshbach resonances

We now present a brief introduction to the topic of *Feshbach resonances*, a rather general quantum-mechanical phenomenon that in the context of ultracold atoms provides a tool for tuning the scattering amplitude (and, correspondingly, the interaction between the atoms) by means of an external homogeneous magnetic field. Before that, we briefly introduce the notion of *scattering channel*.

Let us consider two atoms that are interacting via the interatomic pair potential (see Sec. 1.10), and let us focus on their internal states. As we have already mentioned, two far-apart atoms are entirely described by their respective hyperfine quantum numbers ( $f$  and  $m_f$ ), together with the two quantum numbers associated with the relative motion ( $\ell$  and  $m_\ell$ ). Accordingly, we can label this quantum state by means of the *scattering channel*

$$\alpha = \{ f_1, m_{f_1}, f_2, m_{f_2}, \ell, m_\ell \}$$

This is the so-called *separated atom basis*, that is essentially an extension of the Breit-Rabi basis that includes orbital motion. Curly braces indicate that a proper symmetrization must be chosen when dealing with identical particles [51].

On the other hand, when the two atoms approach each other, they experience an interaction potential that is much stronger than the hyperfine interaction. As we have discussed in Sec. 1.10, this leads to a direct coupling of the two electronic spins. The standard way to treat the problem is to first couple the individual electronic and nuclear spins to form  $\vec{S} = \vec{s}_1 + \vec{s}_2$  and  $\vec{I} = \vec{i}_1 + \vec{i}_2$ , respectively. Then, the total electronic and nuclear spins are combined to get the total internal spin  $\vec{F} = \vec{S} + \vec{I}$ . Lastly,  $\vec{F}$  and  $\vec{\ell}$  couple to give the total angular momentum of the dimer,  $\vec{F}_{\text{tot}} = \vec{F} + \vec{\ell}$ .

The main point is that the quantum numbers that characterize the atoms at large distances are different from those that properly describe them when they are close together: in other words, the “molecular” interaction potential is not diagonal on the basis of the hyperfine (or the Breit-Rabi) states. Thus, at short distances, a convenient way to label a scattering channel is

$$A = \{ S, I, F, \ell, F_{\text{tot}}, M_{\text{tot}} \}$$

which is often referred to as the *molecular basis*.

The scattering problem becomes particularly interesting when multiple molecular

channels exist. The latter can be adiabatically connected to different sets of hyperfine (free) states  $|f_1', m_1'\rangle$  and  $|f_2', m_2'\rangle$ , or in other words to different scattering channels

$$\alpha' = \{f_1', m_{f_1}', f_2', m_{f_2}', \ell', m_{\ell'}\}$$

If the asymptotic energy of a given channel  $\alpha'$  is higher (lower) than (or equal to) the scattering energy  $E$ , that channel is said to be *closed* (*open*), see Fig. 1.6.

Generally speaking, different scattering channels may be coupled by the hyperfine interaction, or by some among the interaction terms discussed in Sec. 1.10. In particular, the former case can be understood by conveniently recasting the hyperfine and Zeeman hamiltonians (see Eqs. (1.72b) and (1.72c)) as

$$\hat{H}_{\text{BR}} = \hat{H}_{\text{hf}} + \hat{H}_{\text{zee}} = \hat{H}^{(+)} + \hat{H}^{(-)} \quad (1.79)$$

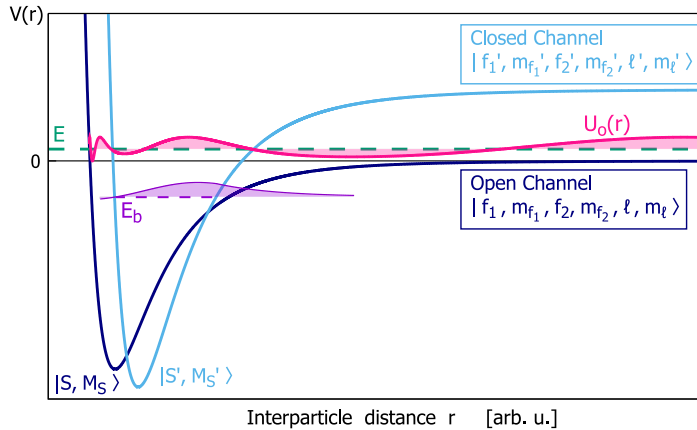
where

$$\hat{H}^{(+)} = \frac{1}{2\hbar^2} (A_1^{\text{hf}} \vec{i}_1 + A_2^{\text{hf}} \vec{i}_2) \cdot \vec{S} - \frac{1}{\hbar} (\mu_{\text{B}} g_s \vec{S} - \mu_{\text{N}} g_{i,1} \vec{i}_1 - \mu_{\text{N}} g_{i,2} \vec{i}_2) \cdot \vec{B} \quad (1.80a)$$

$$\hat{H}^{(-)} = \frac{1}{2\hbar^2} (A_1^{\text{hf}} \vec{i}_1 - A_2^{\text{hf}} \vec{i}_2) \cdot (\vec{s}_1 - \vec{s}_2) \quad (1.80b)$$

As one immediately realizes,  $\hat{H}^{(+)}$  is diagonal on the molecular basis, whereas  $\hat{H}^{(-)}$  can couple states having different  $S$ .<sup>23</sup> This, in turn, implies that two colliding atoms will somehow experience the effects of different molecular potentials.<sup>24</sup> Anyway, since the involved couplings are typically weak, in most cases they just lead to some small (perturbative) corrections. Nevertheless, the situation dramatically changes when the scattering energy approaches that of a bound state supported by a closed channel. In this case, scattering effects will be strongly enhanced, in a somewhat similar fashion to the scattering resonances encountered before. This is actually a quite general phenomenon in quantum mechanics, that takes the name of *Fano-Feshbach resonance* (FR).<sup>25</sup> FRs play a central role in atomic physics experiments, as they

**Figure 1.6** – Sketch of open and closed scattering channels.



<sup>23</sup>In any case,  $\hat{H}_{\text{BR}}$  does not act on the spatial wavefunction.

<sup>24</sup>For instance, with regard to the Li-Cr mixture, this means that the exaplet and octuplet scattering channels will be coupled.

<sup>25</sup>It should be noted, however, that FRs in ultracold gases slightly differ from those studied in nuclear physics, in the sense that the former occur in the zero-energy limit when external fields are applied, whereas the latter are typically investigated by varying the collisional energy.

allow to enhance (or in some cases to suppress) the scattering cross section by means of an external homogeneous magnetic field. This indeed becomes feasible since, in general, different scattering channels have different magnetic dipole moments. Hence, application of an external field effectively changes the relative energy detuning between the (entrance) scattering channel and the bound states supported by the closed channels. Ultimately, this can be exploited to experimentally adjust the scattering length  $a_s$  (or, more generally, the scattering amplitude  $f_\ell(k, \theta)$ ).

In the following, we will tackle an elementary toy model able to capture the main features of Feshbach resonances.

### 1.12 Multi-channel scattering: a toy model

Let us consider a simple scattering problem in which only two different channels exist. The open (entrance) channel is described by a potential well  $V_o(r)$  analogous to the one introduced in Sec. 1.4, while the closed channel is modelled with an infinite spherical well  $V_c(r)$ . These two wells are assumed to have the same radial width  $b$ , but different potential offsets (measured with respect to the asymptotic potential energy of the open channel  $V_o(r = \infty)$ ):

$$V_o(r) = \begin{cases} -V_o & \text{for } r < b \\ 0 & \text{for } r > b \end{cases} \quad \text{with } V_o = \frac{\hbar^2 k_o^2}{2m} \quad (1.81a)$$

$$V_c(r) = \begin{cases} -V_c & \text{for } r < b \\ +\infty & \text{for } r > b \end{cases} \quad \text{with } V_c = \frac{\hbar^2 k_c^2}{2m} \quad (1.81b)$$

The situation is depicted in Fig. 1.7a. In the trivial case in which the two channels are decoupled, the problem reduces to solving two independent Schrödinger equations

$$\left[ -\frac{\hbar^2}{2m} \partial_r^2 + V_o(r) - E \right] U_o(r) |O\rangle = 0 \quad (1.82a)$$

$$\left[ -\frac{\hbar^2}{2m} \partial_r^2 + V_c(r) - E \right] U_c(r) |C\rangle = 0 \quad (1.82b)$$

This is essentially the same problem that we treated in Sec. 1.4. By contrast, if a coupling between the two channels exists, the radial wavefunction can be sought as

$$\vec{U}(r) = \alpha_o U_o(r) |O\rangle + \alpha_c U_c(r) |C\rangle = \begin{pmatrix} \alpha_o U_o(r) \\ \alpha_c U_c(r) \end{pmatrix} \quad (1.83)$$

where  $|\alpha_o|^2 + |\alpha_c|^2 = 1$ . The Schrödinger equation then reads

$$\partial_r^2 \vec{U}(r) + \widehat{W}(r) \vec{U}(r) = 0 \quad (1.84a)$$

with

$$\widehat{W}(r) = \begin{cases} \widehat{W}_1 = \begin{pmatrix} k^2 + k_o^2 & Q \\ Q & k^2 + k_c^2 \end{pmatrix} & \text{for } r < b \\ \widehat{W}_2 = \begin{pmatrix} k^2 & 0 \\ 0 & -\infty \end{pmatrix} & \text{for } r > b \end{cases} \quad (1.84b)$$

where we have assumed that the coupling is effective only for  $r < b$  (inner region).

Thus, in the outer region, we straightforwardly have

$$\partial_r^2 U_o^{(2)}(r) + k^2 U_o^{(2)}(r) = 0 \quad (1.85a)$$

$$\partial_r^2 U_c^{(2)}(r) - \infty U_c^{(2)}(r) = 0 \quad (1.85b)$$

Namely,  $r > b$  is strictly forbidden for the closed-channel component. The solutions of Eqs. (1.85) are readily found (see also Eq. (1.34b))

$$U_o^{(2)}(r) = B_o \sin(k(r - a_s)) \quad (1.86a)$$

$$U_c^{(2)}(r) = 0 \quad (1.86b)$$

On the other hand, the situation in the inner region is more complicated, as one has to deal with a system of two coupled equations:

$$\partial_r^2 U_o^{(1)}(r) + (k^2 + k_o^2) U_o^{(1)}(r) + Q U_c^{(1)}(r) = 0 \quad (1.87a)$$

$$\partial_r^2 U_c^{(1)}(r) + (k^2 + k_c^2) U_c^{(1)}(r) + Q U_o^{(1)}(r) = 0 \quad (1.87b)$$

Eqs. (1.87) are easier to handle in the rotated basis that diagonalizes  $\widehat{W}_1(r)$ . In the limit of small coupling ( $Q \ll k_o^2, k_c^2, (k_o^2 - k_c^2)$ ), one finds

$$\begin{pmatrix} \tilde{U}_o \\ \tilde{U}_c \end{pmatrix} = \begin{pmatrix} 1 & \gamma \\ -\gamma & 1 \end{pmatrix} \begin{pmatrix} U_o \\ U_c \end{pmatrix} \quad (1.88a)$$

$$\widetilde{W}_1 = \begin{pmatrix} k^2 + k_o^2 + \gamma Q & 0 \\ 0 & k^2 + k_c^2 - \gamma Q \end{pmatrix} \quad (1.88b)$$

where  $\gamma = Q/(k_o^2 - k_c^2)$  is the mixing parameter. The two resulting uncoupled equations

$$\partial_r^2 \tilde{U}_o^{(1)}(r) + (k^2 + k_o^2 + \gamma Q) \tilde{U}_o^{(1)}(r) = 0 \quad (1.89a)$$

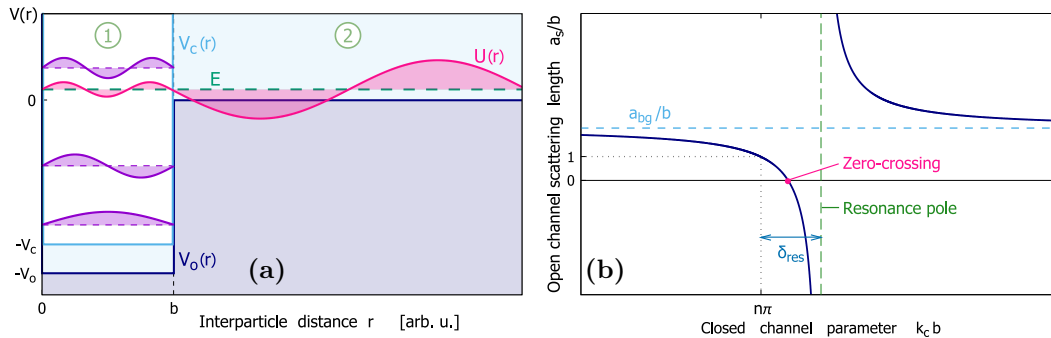
$$\partial_r^2 \tilde{U}_c^{(1)}(r) + (k^2 + k_c^2 - \gamma Q) \tilde{U}_c^{(1)}(r) = 0 \quad (1.89b)$$

can now be readily solved

$$\tilde{U}_o^{(1)}(r) = \tilde{A}_o \sin\left(\sqrt{k^2 + k_o^2 + \gamma Q} r\right) \simeq \tilde{A}_o \sin(k_o r) \quad (1.90a)$$

$$\tilde{U}_c^{(1)}(r) = \tilde{A}_c \sin\left(\sqrt{k^2 + k_c^2 - \gamma Q} r\right) \simeq \tilde{A}_c \sin(k_c r) \quad (1.90b)$$

**Figure 1.7** – Scattering by two coupled channels (toy model): (a) sketch, showing also the lowest  $\ell = 0$  bound states of the closed channel. (b) Low-energy ( $s$ -wave) scattering length near a Feshbach resonance.



where the final result is obtained by considering the limit of weak coupling and low-energy scattering ( $k, Q \ll k_o, k_c$ ). Our interest lies mainly in the mixing parameter  $\gamma$ . If we transform back to the original basis

$$\begin{pmatrix} U_o \\ U_c \end{pmatrix} = \begin{pmatrix} 1 & -\gamma \\ \gamma & 1 \end{pmatrix} \begin{pmatrix} \tilde{U}_o \\ \tilde{U}_c \end{pmatrix} \quad (1.91)$$

we can write

$$U_o^{(1)}(r) \simeq \tilde{A}_o \sin(k_o r) - \gamma \tilde{A}_c \sin(k_c r) \quad (1.92a)$$

$$U_c^{(1)}(r) \simeq \tilde{A}_c \sin(k_c r) + \gamma \tilde{A}_o \sin(k_o r) \quad (1.92b)$$

At this stage, we have to impose the boundary conditions at  $r = b$ . This is rather straightforward for the closed channel, as the outer region is strictly forbidden

$$\tilde{A}_c \sin(k_c b) + \gamma \tilde{A}_o \sin(k_o b) = 0 \quad \longrightarrow \quad \tilde{A}_c = -\gamma \frac{\sin(k_o b)}{\sin(k_c b)} \tilde{A}_o \quad (1.93a)$$

For the open channel, after some algebra one can find

$$\frac{(1 + \gamma^2)}{[k_o \cot(k_o b) + \gamma^2 k_c \cot(k_c b)]} = \frac{\tan(k(b - a_s))}{k} \quad (1.93b)$$

and, by taking once again the limit of  $k \rightarrow 0$  and  $\gamma \ll 1$

$$\frac{1}{(b - a_s)} = \frac{k_o}{\tan(k_o b)} + \gamma^2 \frac{k_c}{\tan(k_c b)} \quad (1.93c)$$

This last relation links  $a_s$  to the characteristic parameters of the potential: as one can appreciate, both channels yield a contribution. We can define the *background scattering length* as the solution (for  $a_s$ ) of Eq. (1.93c) when  $\gamma = 0$ :

$$a_{\text{bg}} = b \left( 1 - \frac{\tan(k_o b)}{k_o b} \right) \quad (1.94)$$

where we immediately recognize our previous result for the finite square well, see again Eq. (1.35b). Then we can recast Eq. (1.93c) as

$$\frac{1}{\left(\frac{a_s}{b} - 1\right)} = \frac{1}{\left(\frac{a_{\text{bg}}}{b} - 1\right)} - \gamma^2 \frac{k_c b}{\tan(k_c b)} \quad (1.95a)$$

or, alternatively

$$a_s = b + (a_{\text{bg}} - b) \frac{\tan(k_c b)}{\tan(k_c b) - \gamma^2 k_c (a_{\text{bg}} - b)} \quad (1.95b)$$

In most cases, the closed channel contribution to the (open channel) scattering length will be small, as the coupling is weak. Nonetheless, when  $k_c b \simeq n\pi$  the second term on the right hand side of Eq. (1.95a) may actually diverge. As one can easily check, the condition  $k_c b = n\pi$  corresponds to the  $n$ -th bound state of the (uncoupled) infinite well having exactly zero energy (relatively to the asymptotic value of  $V_o(r)$ ). Consequently, in the low-temperature limit such a bound state is *resonant* with the scattering energy, thus greatly affecting the collision process.

This toy model qualitatively describes the FR phenomenon. The characteristic behaviour of  $a_s$ , given by Eqs. (1.95), is shown in Fig. 1.7b. It is interesting to note that for  $k_c b = n\pi$  the scattering length is actually finite, having a value equal to  $b$ . The *resonance pole* is instead found at  $k_c b = n\pi + \delta_{\text{res}}$ , where

$$\delta_{\text{res}} = (n\pi) \gamma^2 \frac{(a_{\text{bg}} - b)}{b} \quad (1.96)$$

is sometimes called the *resonance shift*, and represents the difference between the unperturbed position of the bound state (i.e.  $k_c b = n\pi$ ) and its actual location when a coupling  $\gamma \neq 0$  between the two channels exists. Some units of  $\delta_{\text{res}}$  away from the resonance pole, the scattering length approaches its background value: on one side of the singularity, this leads to a *zero-crossing* of  $a_s$ , as shown in Fig. 1.7b. Note that, since  $b$  can be interpreted as the closed channel scattering length (see the final remark in Sec. 1.4), the result of Eq. (1.96) is consistent with the analysis of Ref. [53].

### 1.13 Magnetic tuning of Feshbach resonances

In general, the scattering energy will not be resonant with any bound state of the closed channels: namely, the condition  $k_c b \simeq n\pi$  will not be automatically satisfied. Indeed, the rare exceptions found in nature ( $^{133}\text{Cs}$  being one of the most notable examples [50]) should be considered as accidental coincidences. Anyway, since different channels typically have different magnetic moments, the application of an external magnetic field actually introduces a relative Zeeman shift between them, thus effectively *tuning* the bound states energies with respect to the scattering energy  $E$  of the open channel. To describe this effect, let us consider again our toy model and, for sake of simplicity, let us assume that the magnetic moments of the two channels are  $\mu_o = 0$ , and  $\mu_c \neq 0$ , respectively. Hence, application of a static magnetic field  $B$  changes the energy of the closed channel as

$$V_c'(r) = V_c(r) - \mu_c B \quad (1.97a)$$

$$(k_c')^2 = \frac{2m}{\hbar^2} (V_c - \mu_c B) \quad (1.97b)$$

Let us suppose that  $k_c' b = n\pi$  for a certain magnetic field  $B_{\text{res}}$ . Then, in a small field region around  $B_{\text{res}}$ , we can write

$$k_c' b \simeq n\pi + \alpha (B - B_{\text{res}}) \quad \text{with} \quad \alpha = -\frac{mb^2}{n\pi\hbar^2} \mu_c \quad (1.98)$$

By defining the *resonance magnetic pole* and the *resonance magnetic width* as

$$B_0 = B_{\text{res}} + \Delta_B \quad (1.99a)$$

$$\Delta_B = -\gamma^2 k_c \frac{(a_{\text{bg}} - b)^2}{\alpha a_{\text{bg}}} \quad (1.99b)$$

we can recast Eq. (1.95a) as a function of  $B$ , retrieving the familiar form

$$a_s(B) = a_{\text{bg}} \left( 1 - \frac{\Delta_B}{B - B_0} \right) \quad (1.100)$$

Hence, near a FR the scattering length exhibits a dispersive lineshape, with  $a_{\text{bg}}$  representing its off-resonant value (note that  $a_{\text{bg}}$  is also the value of  $a_s$  when  $\gamma = 0$  in Eq. (1.100)). Both  $a_{\text{bg}}$  and  $\Delta_{\text{B}}$  can be either positive or negative quantities [46]. Note that, in analogy with Eq. (1.55), the resonant contribution to the phase shift near a FR can be expressed as [49]

$$\delta_{\ell}(\text{B}) \simeq \tan^{-1} \left[ \frac{\Gamma_{\text{B}}/2}{\text{B}_0 - \text{B}} \right] \quad (1.101)$$

where  $\Gamma_{\text{B}} = \Gamma/\delta\mu$ , and  $\delta\mu$  is, in general, the differential magnetic moment between the closed and the open channel, i.e.  $\delta\mu = \mu_c - \mu_o$ . Using Eq. (1.101) in Eq. (1.25a), and comparing the result to Eq. (1.100), we obtain  $\Gamma_{\text{B}} = -2k a_{\text{bg}} \Delta_{\text{B}}$ . Finally, taking into account the relations between  $\Gamma$ ,  $\tilde{\gamma}$  and  $R^*$  (see Sec. 1.8), we find

$$R^* = \frac{\hbar^2}{2m a_{\text{bg}} \delta\mu \Delta_{\text{B}}} \quad (1.102)$$

which is the same result reported by Petrov in Ref. [42]. Accordingly, given the reduced mass, whether a magnetic FR is *large* (i.e.  $R^* \sim b$ ) or *narrow* (i.e.  $R^* \gg b$ ) is determined by the background scattering length, the differential magnetic moment, and the resonance magnetic width. Note that the product  $a_{\text{bg}} \delta\mu \Delta_{\text{B}}$  is always a positive quantity.

## 1.14 Inelastic collisions and loss mechanisms

The study of elastic collisions is of great importance in the field of ultracold atoms, as it lays the ground for the optimization of evaporative cooling stages, and for few- and many-body studies based on quantum gases. Anyway, in real-world situations, atoms will also experience *inelastic* collision events, i.e. scattering processes in which the relative kinetic energy is not conserved. Such processes are connected with an internal state change of at least one of the two atoms (or, in other words, the entrance and the exit channels do not coincide). In most cases, the kinetic energy gain is by far larger than the trap depth, so inelastic collisions often lead to atom losses.

Generally, loss mechanisms are grouped according to the number of ultracold particles involved in the process: the main contributions arise from one-, two-, and three-body losses. The former are due to background-gas collisions, i.e. collisions between one atom of the sample and one atom/molecule of the residual gas in the vacuum chamber. These may actually be even elastic collisions, but occurring at a very large kinetic energy, as the background gas is in thermal equilibrium with the chamber walls. Being one-body processes (only the number of cold particles is counted), they are independent from the presence of a Feshbach resonance, and in general from the value of the scattering length.

As already mentioned, two-body losses arise from inelastic two-body collisions: the kinetic energy gain resulting from the change of the internal state (or, in other words, from the decay into a lower energy scattering channel) is typically larger than the trap depth. It is worth stressing again that atoms prepared in the lowest internal state are immune to two-body losses.

Lastly, yet importantly, a collision involving three atoms can produce a dimer and a free atom, the latter carrying away (part of) the released binding energy as kinetic energy. Note that, due to energy and momentum conservation, molecule/dimer formation is forbidden for two-body collisions. Once again, in most cases the released kinetic energy is greater than the trap depth, thus resulting in the loss of each of the three involved particles.

By combining these three loss mechanisms, we can write a differential rate equation for the number of trapped atoms. For instance, for a sample containing only one atomic species, we have

$$\dot{N}(t) = -K_1 N(t) - K_2 \int d\vec{r} n^2(\vec{r}, t) - K_3 \int d\vec{r} n^3(\vec{r}, t) \quad (1.103)$$

where  $n(\vec{r}, t)$  is the spatial density of the atomic cloud, and  $K_j$  is the (thermally-averaged)  $j$ -body loss coefficient. The latter can vary by many orders of magnitude depending on atomic species (and isotopes), even if no FRs are present. Moreover, these quantities are strongly affected by the external magnetic field, as they depend on the scattering length: for instance, the three-body coefficient  $K_3$  scales as  $a_s^4$  for bosonic gases [46].

### 1.14.1 Feshbach loss spectroscopy: an introduction

Generally speaking, the resonant enhancement of the scattering cross section leads to an increase of atom losses. Indeed, inelastic loss spectroscopy has proven to be one of the most effective techniques to detect Feshbach resonances in ultracold gases. Near a FR, inelastic collisions are greatly enhanced as a consequence of the strong coupling between Feshbach bound states and “inelastic” exit channels [46]. For instance, in the case of alkali atoms, the spin-exchange rate  $K_2^{\text{ex}}$  from channel  $\alpha$  to  $\alpha'$  is given by [52]

$$K_2^{\text{ex}} = 4\pi (a_t - a_s)^2 v_f |\langle f_1', m_{f_1}', f_2', m_{f_2}' | \vec{s}_1 \cdot \vec{s}_2 | f_1, m_{f_1}, f_2, m_{f_2} \rangle|^2 \quad (1.104)$$

with  $a_s$  ( $a_t$ ) being the singlet (triplet)  $s$ -wave scattering length, and  $v_f$  the relative final velocity

$$v_f = \sqrt{\frac{2}{m} \left( \frac{\hbar^2 k^2}{2m} + E_{\text{hf},1} + E_{\text{hf},2} - E'_{\text{hf},1} - E'_{\text{hf},2} \right)} \quad (1.105)$$

where  $E_{\text{hf},j}$  is the hyperfine energy of the  $j$ -th atom, and the prime denotes quantities evaluated after the collision.

On top of that, three-body losses are also strongly enhanced near a FR. Nonetheless, while this is a well-established fact for bosonic species, the situation concerning fermionic atoms is more complicated, owing to Pauli suppression effects [46, 54]. Generally speaking, in most cases a FR is accompanied by a loss feature. However, some fermionic systems characterized by broad resonances exhibit a remarkable stability in the regime of strong interactions [46], a delightful, unexpected discovery that has laid the ground for many fascinating and intriguing studies on strongly interacting fermions.



## Chapter 2

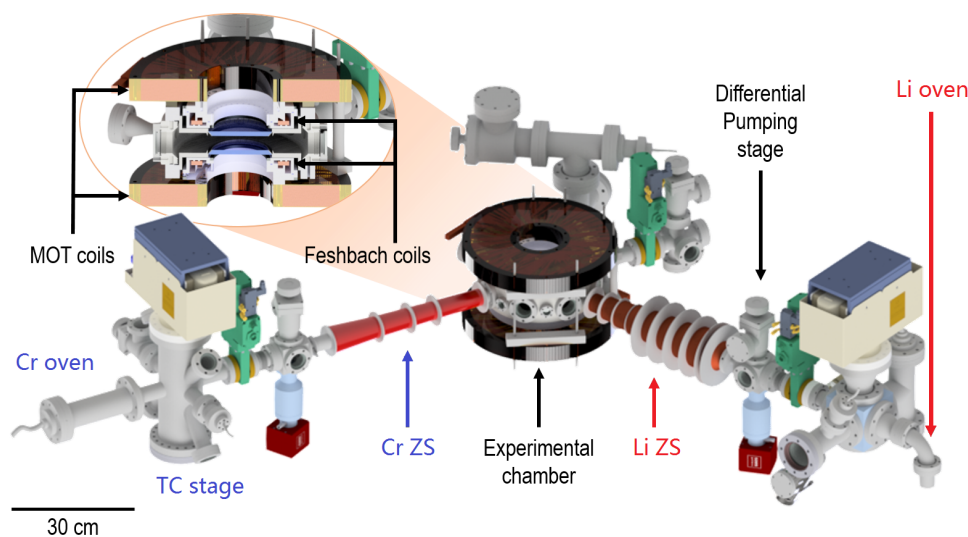
# Experimental setup

In this chapter I concisely illustrate the experimental setup that allows us to produce ultracold Cr-Li mixtures, mainly focusing on the optical part. A more detailed description of the *PoLiChroM* apparatus, which was already set up at the beginning of my lab activity, can be found in Refs. [55, 56]. For instance, Fig. 2.1 depicts the vacuum chambers and magnetic coils setups. About those, here I just highlight the choice of employing two different ovens and Zeeman slower (ZS) tubes, owing to the rather different sublimation temperatures of the two elements (roughly 400 °C for Li and 1500 °C for Cr, respectively). Furthermore, interspecies collisional properties of Li and Cr atoms were not known at the time the machine was being designed. Besides, the magnetic setup also features two different sets of coils, namely the “MOT” and the “FB” coils, the role of which will be better clarified in Chapter 3.

In the following, I provide a basic overview of the optical setup, focusing on the progress and improvements developed during the period of my thesis. Specifically, the first part of the chapter is devoted to the description of the challenging optical scheme needed to produce cooling lights for lithium and chromium samples. As an introduction to this topic, the relevant optical properties of Li and Cr atoms are briefly summarized (useful additional information can be found in Refs. [59, 60]).

Secondly, I illustrate the optical setup that surrounds the experimental cell, where most of the cooling lights converge. In particular, the last section describes the bichromatic optical dipole trap (BODT) setup, a part of which has already been subject of a publication [58].

**Figure 2.1** – Overview of the vacuum and magnetic coils setups of the *PoLiChroM* machine. Figure taken from Ref. [56].

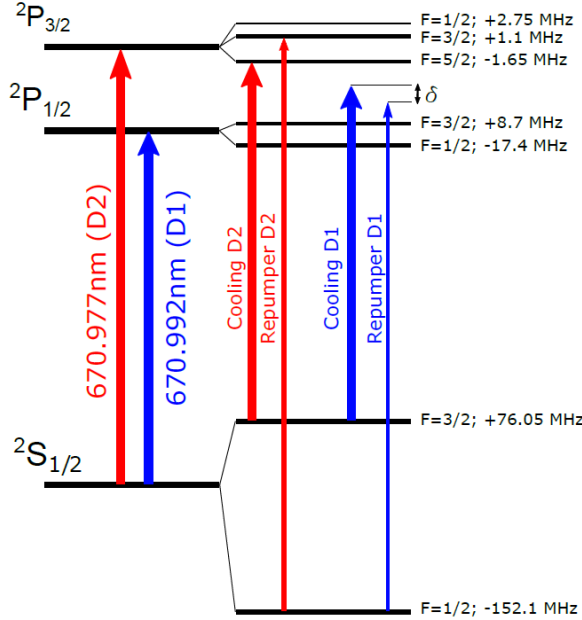


## 2.1 Lithium

Lithium, having atomic number  $Z = 3$ , is the lightest alkali metal. It is found in nature as a mixture of the two stable isotopes,  ${}^6\text{Li}$  and  ${}^7\text{Li}$  (with relative abundances around 8% and 92%, respectively); the former (latter) – being formed by three protons, three (four) neutrons, and three electrons – is a composite fermion (boson). With regard to optical properties, the ground state electronic configuration reads  $1s^2 2s^1$ : in spectroscopic notation, this corresponds to a  ${}^2S_{1/2}$  state. The first excited level is actually a fine structure doublet, whose states can be classified as  ${}^2P_{1/2}$  and  ${}^2P_{3/2}$ , respectively. Optical transitions that connect the ground state to these two fine states are historically referred to as D1 ( $\lambda_{D1} = 670.992 \text{ nm}$ ) and D2 ( $\lambda_{D2} = 670.977 \text{ nm}$ ), respectively.<sup>1</sup> The interaction between the nuclear spin and the total electronic angular momentum further splits the fine levels into hyperfine manifolds. In the case of  ${}^6\text{Li}$ , the nuclear spin being  $i_{\text{Li}} = 1$ , the ground state splits into a doublet, whose levels (separated by 228.2 MHz) are labeled by the total angular momentum quantum number  $f = 1/2, 3/2$ , respectively. On the other hand, the energy splittings of the excited  ${}^2P$  levels are definitely smaller: for instance, those relative to the  ${}^2P_{3/2}$  state entirely lie within the natural linewidth of the D2 line ( $\gamma_{D2} = 5.87 \text{ MHz}$ ).

The optical transitions exploited to perform laser cooling on our samples of  ${}^6\text{Li}$  atoms are sketched in Fig. 2.2. The first cooling stages rely on the D2 line, namely on the  ${}^2S_{1/2} |f = 3/2\rangle \rightarrow {}^2P_{3/2} |f' = 5/2\rangle$  transition. However, due to the aforementioned small hyperfine splittings of the excited state, a not perfectly polarized light may

**Figure 2.2** – Fine and hyperfine levels of  ${}^6\text{Li}$  (not to scale). Red arrows show the transitions employed for standard laser cooling procedures, while blue arrows refer to the grey molasses stage. Figure taken from Ref. [56].



<sup>1</sup>The specified wavelengths are referred to  ${}^6\text{Li}$  [59]. We also report here that the saturation intensities of these two lines are  $I_{\text{sat}}^{\text{Li},D1} = 7.59 \text{ mW/cm}^2$  and  $I_{\text{sat}}^{\text{Li},D2} = 2.54 \text{ mW/cm}^2$ , respectively [59].

also drive undesired  $|f = 3/2\rangle \rightarrow |f' = 3/2\rangle$  population transfers, which in turn could bring atoms out from the cooling cycle. For this reason, a repumper beam addressing the  $|f = 1/2\rangle \rightarrow |f' = 3/2\rangle$  transition is required.

Moreover, while being loaded into the optical dipole trap,  ${}^6\text{Li}$  atoms are further cooled by means of a gray molasses stage, exploiting the D1 line [64]. A description of this additional sub-Doppler cooling mechanism, together with a first characterization of the related experimental parameters (in free-space), can be found in Ref. [57].

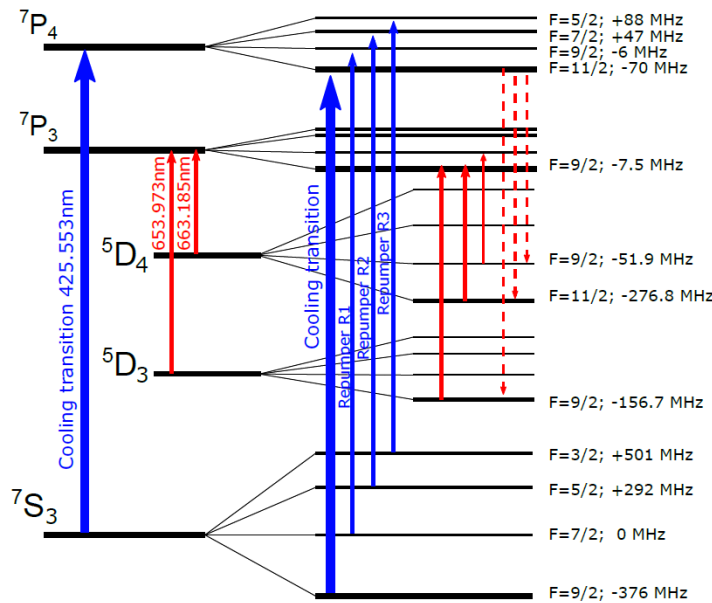
## 2.2 Chromium

Chromium (atomic number  $Z = 24$ ) is a transition metal with four stable isotopes:  ${}^{50}\text{Cr}$ ,  ${}^{52}\text{Cr}$ ,  ${}^{53}\text{Cr}$  and  ${}^{54}\text{Cr}$ . The present discussion is mainly focused on  ${}^{53}\text{Cr}$  (relative abundance 9.5%), which is the only fermionic one among those.

The ground state electronic configuration of Cr reads  $[\text{Ar}] 3d^5 4s^1$ : following Hund's rules, this leads to a spectroscopic  ${}^7S_3$  ground state. An interesting property of this state is the relatively large (compared to alkali metals) magnetic dipole moment of  $6\mu_B$ . Such a sizeable moment enables strong magnetic confinement, and could possibly allow for the study of dipolar effects in the ultracold/degenerate regime [60, 65].

The fine and hyperfine structures of  ${}^{53}\text{Cr}$  (nuclear spin  $i_{\text{Cr}} = 3/2$ ), shown in Fig. 2.3, are both quite rich: accordingly, a more involved laser cooling scheme (compared to the Li one) is required. In particular, besides the cooling light that relies on the strong  ${}^7S_3 |f = 9/2\rangle \rightarrow {}^7P_4 |f' = 11/2\rangle$  transition ( $\lambda = 425.55 \text{ nm}$  in vacuum, natural linewidth  $\gamma_{\text{Cr}} = 5.02 \text{ MHz}$ , and saturation intensity  $I_{\text{sat}}^{\text{Cr}} = 8.52 \text{ mW/cm}^2$  [60]), up to three blue repumpers (denoted by R1, R2, and R3) are needed for an optimum working of the magneto-optical trap (MOT) stage. Furthermore, owing to a

**Figure 2.3** – Fine and hyperfine levels of  ${}^{53}\text{Cr}$  (not to scale). Solid blue arrows indicate the transitions employed for laser cooling. Red dashed arrows show possible leaks to metastable  ${}^5D$  states. Red solid arrows indicate the transitions exploited to pump  ${}^5D$ -state atoms back into the cooling cycle. Figure adapted from Ref. [56].



finite spontaneous decay probability towards metastable  $^5D$  states,<sup>2</sup> three additional red repumpers (denoted by RR1, RR2 and RR3, and working at  $\lambda_1 = 663.2$  nm,  $\lambda_2 = 654.0$  nm and  $\lambda_3 \simeq \lambda_1$ , respectively) are employed to bring atoms back into the cooling cycle, exploiting the  $^7P_3$  level [56, 65].

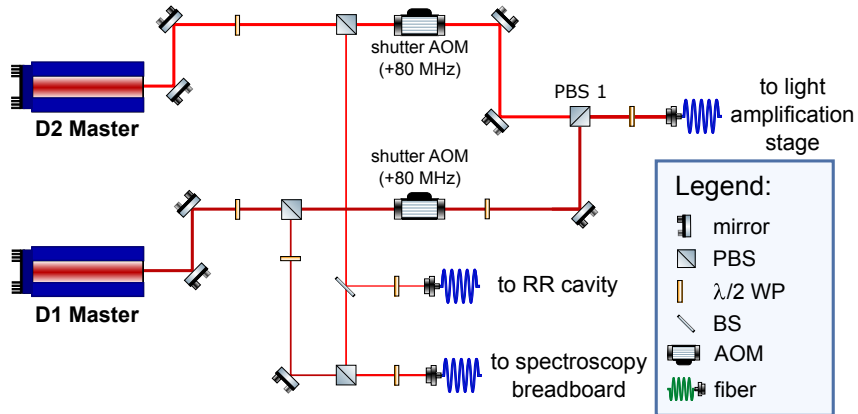
### 2.3 Lithium laser setup

The optical setup that provides the light beams employed to cool and manipulate Li atoms is sketched in Figs. 2.4 and 2.5. The main sources of laser light are two independent commercial diode lasers (Toptica TA-Pro,  $\lambda = 671$  nm,  $P_{\text{out}} \sim 200$  mW), that generate the optical frequencies for the D1 and D2 atomic transitions, respectively. First, a small fraction (about 10 mW) of each beam is sent to the locking scheme, assembled on a dedicated spectroscopy breadboard. A detailed description of this scheme can be found in Ref. [55]. Here I just report the two locking transitions, namely  $^2S_{1/2} |f = 3/2\rangle \rightarrow ^2P_{1/2} |f' = 1/2\rangle$  (D1) and  $^2S_{1/2} |f = 3/2\rangle \rightarrow ^2P_{3/2}$  (D2), respectively, and the fact that, before entering the spectroscopy cell, the D1 (D2) light is sent through a double-pass acousto-optic modulator (AOM), which sets the frequency detuning to  $-2 \times 87$  MHz ( $-2 \times 140$  MHz) with respect to the related atomic transition. Besides, I also mention that a pickup of the D2 light is sent to a Fabry-Perot cavity, which is in turn employed for the locking scheme of chromium's red repumpers (see Sec. 2.4.1).

The largest parts of the two master beams, prepared with orthogonal polarizations, are overlapped on a polarizing beam-splitter cube (PBS 1), and then coupled to a fiber that delivers them to the amplification stage. In order to select and control the desired light during the experiment, two single-pass AOMs (both working at  $+80$  MHz, and essentially acting as fast switches) are placed before the PBS.

At the fiber output, the optical path is split into two branches: one for the cooling and one for the repumper light. Both beams are sent through double-pass AOMs (whose working frequencies are centred around  $+2 \times 80$  MHz and  $+2 \times 200$  MHz, respectively), and then injected into two different commercial tapered amplifiers (Toptica BoosTA), each of which delivers about 300 mW of optical power. By

Figure 2.4 – Sketch of the Li optical setup: laser sources for D1 and D2 lights.



<sup>2</sup>The natural linewidths of the involved intercombination transitions are  $\Gamma_{(^7P_4 \rightarrow ^5D_4)} \simeq 127$  Hz and  $\Gamma_{(^7P_4 \rightarrow ^5D_3)} \simeq 42$  Hz, respectively.



direct light either into the ZS or the imaging fiber, when its frequency is set to  $-85$  MHz or to  $-110$  MHz, respectively. The imaging AOMs are instead exploited to produce the optical frequencies needed to probe Li atoms at high magnetic fields (see Sec. 2.3.1).

A schematic illustration of the various steps followed in the preparation of Li cooling lights is shown in Figs. 2.6a and 2.6b.

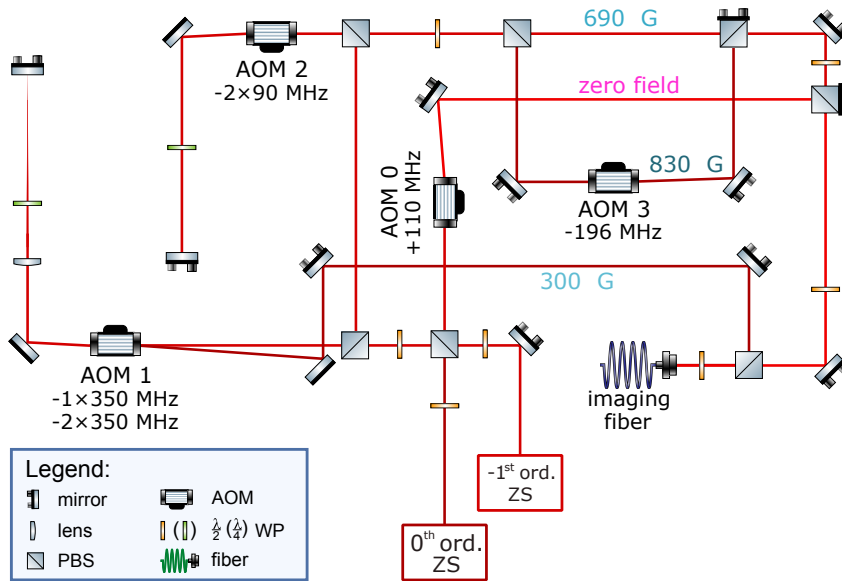
### 2.3.1 High-field imaging

In the course of our standard experimental routines (see Chapter 3), we regularly employ high magnetic fields (up to 1500 G) to confine and manipulate Li (and Cr) samples. In particular, our interest is mainly directed towards three specific fields, namely 300 G, 690 G, and 830 G. The last two are characterized by remarkably broad FRs involving the three lowest spin-mixtures of  ${}^6\text{Li}$ , whereas the first one corresponds to local maxima (in absolute value) of their respective off-resonant scattering lengths.

During my first days in the lab, I took part in the realization of a high-field absorption imaging setup for Li atoms. The optical scheme, sketched in Fig. 2.7 and physically assembled on a dedicated breadboard, consists of a combination of four AOMs, the interplay of which yields the imaging frequencies for different spin-mixtures of Li, at the three aforementioned magnetic fields, as well as at 0 G. The imaging light is delivered by the ZS beam, as soon as the corresponding AOM frequency is set to 110 MHz (see again Fig. 2.5). Both the 0<sup>th</sup> and the  $-1^{\text{st}}$  diffraction orders, as well as both cooler and repumper lights, are exploited.

First, the two ZS AOM diffraction orders are overlapped on a PBS, which in turn immediately splits the optical path into zero- and high-field branches. The former essentially consists of a sole additional AOM (0), which is employed to compensate the red detuning of the ZS light. On the other hand, the high-field branch includes three different paths, each of which is designed to provide the imaging light for a particular magnetic field. In practice, light is first sent to a 350 MHz AOM (1), which

Figure 2.7 – Optical scheme for the high-field imaging of Li.



simultaneously works both in single- and in double-pass mode. This AOM's frequency needs to be adjusted according to the spin mixture that has to be imaged (see below). To prevent possible misalignments arising from such an operation, the modulator is aligned in a so-called *cat-eye* configuration, where – after the first pass – light is focused on the surface of a retro-reflecting mirror. After the second pass, both the 0<sup>th</sup> and the –1<sup>st</sup> diffraction orders are collected. The former provides the 300 G light, so it is immediately coupled to the imaging fiber. Conversely, the latter is first sent through a double-pass AOM (2) working at  $-2 \times 90$  MHz, and subsequently split into the 690 G and 830 G paths. The first of these two is then directly coupled to the fiber, whereas the second one is first sent to the last AOM (3), which operates in single-pass at  $-196$  MHz.

Several  $\lambda/2$  waveplates are employed to guide the laser beam into the proper optical path. Once the latter is chosen, the remaining are blocked, in order to avoid any undesired light during the imaging pulses.

Before reporting the comprehensive list of working parameters, let us show how the appropriate imaging frequencies can be practically computed. As we discussed in Sec. 1.10, under an external magnetic field, atomic (hyperfine) states split into Zeeman components. In the case of alkali metals, the energy splittings of the ground state hyperfine manifold are given by the celebrated *Breit-Rabi formula* [61, 62]

$$\Delta E_{\text{BR}}(\text{B}) = Y(\text{B}) - \frac{hA_{\text{hf}}}{4} \left[ 1 \mp (2I + 1) \sqrt{1 + \frac{2m_f}{I + \frac{1}{2}} X(\text{B}) + X^2(\text{B})} \right] \quad (2.1a)$$

where

$$X(\text{B}) = \frac{(g_j - g_i)}{hA_{\text{hf}} (I + \frac{1}{2})} \mu_{\text{B}} \text{B}; \quad Y(\text{B}) = g_i m_f \mu_{\text{B}} \text{B} \quad (2.1b)$$

with  $h = 2\pi\hbar$ ,  $A_{\text{hf}}$  being the atomic hyperfine constant, and  $g_i$  the nuclear  $g$ -factor relatively to  $\mu_{\text{B}}$ .<sup>3</sup> In the square brackets of Eq. (2.1a), the + (–) sign refers to states with  $f = 1/2$  ( $f = 3/2$ ). Anyway, it should be noted that there exists a “sign problem” for the  $|f = 3/2, m_f = -3/2\rangle$  stretched state. Namely, for  $\text{B} > \text{B}^*$ , where

$$\text{B}^* = \frac{hA_{\text{hf}} |m_f|}{\mu_{\text{B}} (g_j - g_i)} \left[ 1 + \sqrt{1 - \left( \frac{2I + 1}{2m_f} \right)^2} \right] \quad (2.2)$$

the – sign should be replaced by +. We stress that Eq. (2.1a) only applies to the electronic ground state of a  $j = 1/2$  atom: in any other case, the energy shifts have to be computed numerically. However, as far as the  ${}^2P_{3/2}$  state of  ${}^6\text{Li}$  is concerned, due to its small hyperfine splittings, we can approximate the exact result with<sup>4</sup>

$$\Delta E_{\text{Zee}}(\text{B}) = g_j m_j \mu_{\text{B}} \text{B} \quad (2.3)$$

which is the usual expression for the Zeeman shift, neglecting the hyperfine structure. A plot of Eqs. (2.1a) and (2.3) is shown in Fig. 2.8. Additionally, we also exploit

<sup>3</sup>The nuclear  $g$ -factor is typically small (for  ${}^6\text{Li}$ :  $g_i \simeq 4.5 \cdot 10^{-4}$ ). As such, one could even safely neglect it in calculations.

<sup>4</sup>The introduced error is on the order of the natural linewidth  $\gamma_{\text{D}2}$ , so it can be easily corrected experimentally.

**Figure 2.8** – Breit-Rabi diagrams for  ${}^6\text{Li}$ : (a) ground state energy shift (exact formula, see Eq. (2.1a)), (b)  ${}^2P$  states energy shift (approximate formula, see Eq. (2.3)).

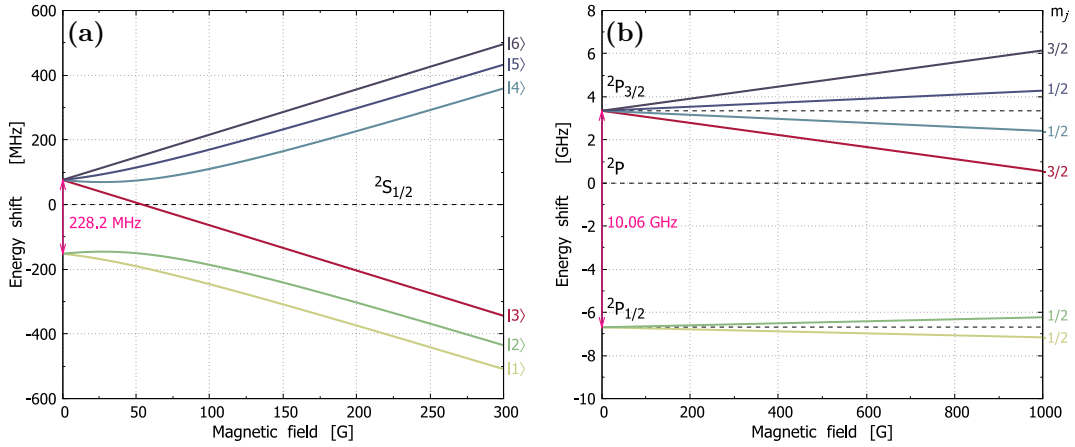


Fig. 2.8a to introduce our notation to refer to Li spin states: they are labeled by Li  $|n\rangle$  ( $n = 1, 2, 3, \dots$ ) in order of increasing energy in an external magnetic field.<sup>5</sup> By taking the difference between Eqs. (2.3) and (2.1a), one can compute the light frequencies needed to probe Li atoms at different fields. In particular, our interest lies in the three lowest spin states (namely Li $|1\rangle$ , Li $|2\rangle$ , and Li $|3\rangle$ ), and in their possible binary combinations. Hence, as already mentioned, the imaging setup is devised to provide – upon minimal changes – the appropriate lights for each of these spin mixtures, relatively to the four magnetic fields of interest (including 0 G).

We now report the full list of working parameters. The following settings are kept fixed among each configuration:

- Spectroscopy AOM: 140 MHz ;
- Shutter AOM: 80 MHz ;
- Zeeman slower AOM: 110 MHz ;
- Imaging AOM 0: 110 MHz
- Imaging AOM 2: 90 MHz
- Imaging AOM 3: 196 MHz

On the other hand, Tabs. 2.1, 2.2, and 2.3 report the specific settings for each spin-mixture.

**Table 2.1** – Imaging settings for the Li $|1\rangle$ -Li $|2\rangle$  mixture.

B [G]	Rep. AOM (Li $ 1\rangle$ )	Cool. AOM (Li $ 2\rangle$ )
828.5	199.0 MHz	106.0 MHz
689	199.0 MHz	106.0 MHz
$\sim 310$	199.0 MHz	106.0 MHz
0	214.0 MHz	(same as Li $ 1\rangle$ )

<sup>5</sup>A completely analogous convention is adopted for the internal states of Cr.

**Table 2.2** – Imaging settings for the Li|1⟩-Li|3⟩ mixture.

Imaging AOM 1: 343 MHz  
 – Li|1⟩: Repumper,  $-1^{\text{st}}$  ord. ZS AOM  
 – Li|3⟩: Cooler,  $-1^{\text{st}}$  ord. ZS AOM

B [G]	Rep. AOM (Li 1⟩)	Cool. AOM (Li 3⟩)
828.5	185.0 MHz	106.0 MHz
689	185.0 MHz	106.0 MHz
~ 320	185.0 MHz	106.0 MHz
0	214.0 MHz	99.0 MHz

**Table 2.3** – Imaging settings for the Li|2⟩-Li|3⟩ mixture.

Imaging AOM 1: 357 MHz  
 High fields:  
 – Li|2⟩: Cooler,  $0^{\text{th}}$  ord. ZS AOM  
 – Li|3⟩: Cooler,  $0^{\text{th}}$  ord. ZS AOM  
 Zero-field:  
 – Li|2⟩: Repumper,  $-1^{\text{st}}$  ord. ZS AOM  
 – Li|3⟩: Cooler,  $-1^{\text{st}}$  ord. ZS AOM

B [G]	Cool. AOM (Li 2⟩)	Cool. AOM (Li 3⟩)
828.5	106.0 MHz	65.0 MHz
689	106.0 MHz	64.5 MHz
~ 310	106.0 MHz	64.5 MHz

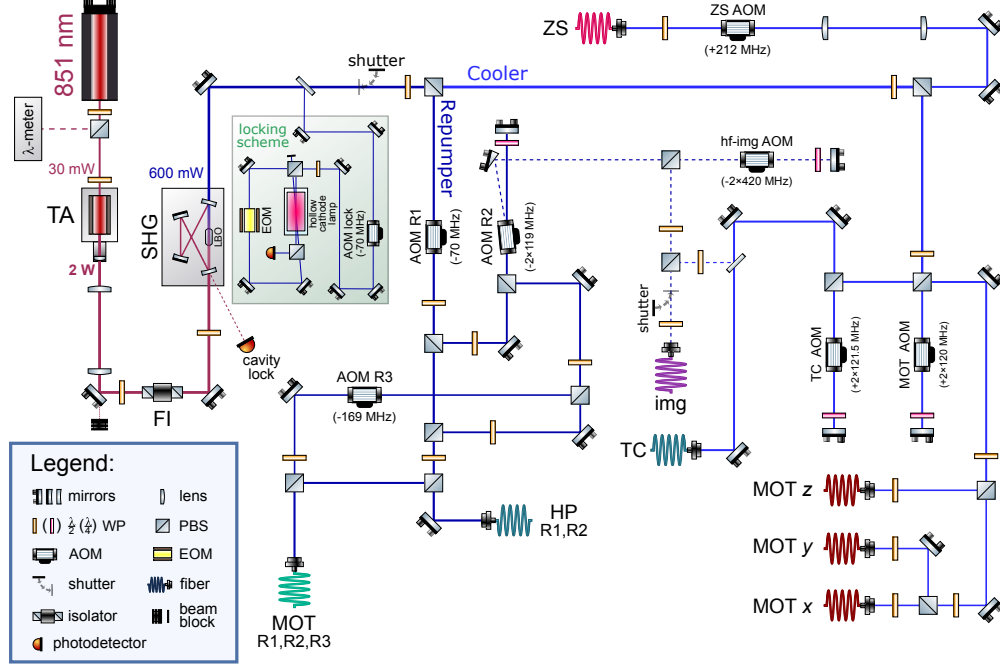
B [G]	Rep. AOM (Li 2⟩)	Cool. AOM (Li 3⟩)
0	214.0 MHz	99.0 MHz

## 2.4 Chromium laser setup

The optical setup devoted to the production of Cr cooling and trapping (blue) lights is sketched in Fig. 2.9. Laser light is provided by a commercial diode laser (Toptica DL) working at  $\lambda = 851$  nm, with a typical (maximum) output power of 30 mW (150 mW). The beam is readily injected into a home-made tapered amplifier (TA), which increases the optical power up to 3 W. The outgoing beam shape is adjusted by means of a cylindrical telescope and, subsequently, light is first sent through a Faraday isolator (FI), and then injected into a home-made frequency doubling cavity. The latter is realized in a bow-tie configuration, and relies on a LBO crystal for the second harmonic generation (SHG) stage: with an overall conversion efficiency of about 30%, the cavity delivers roughly 600 mW (when seeded with 2 W) at  $\lambda = 425.5$  nm.

First, a pickup of the blue light is sent to the locking scheme, which implements a modulation transfer spectroscopy (MTS) configuration on a commercial hollow cathode lamp. The reader is again referred to Ref. [55] for the description of this scheme, together with the one employed for the SHG cavity lock. Here I just mention that the locking transition is actually the  ${}^7S_3 \rightarrow {}^7P_4$  line of the (most abundant) bosonic isotope  ${}^{52}\text{Cr}$ .

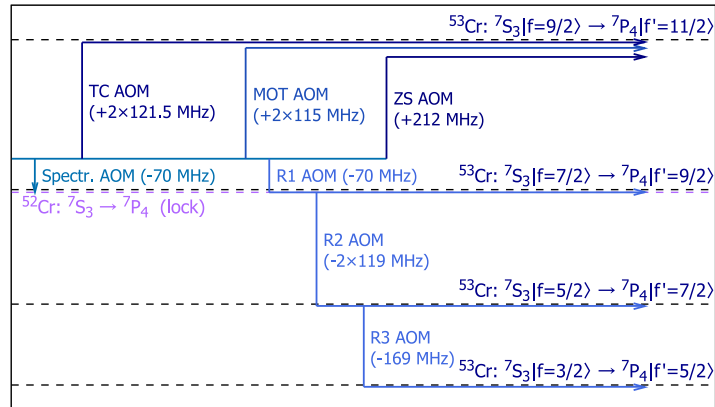
**Figure 2.9** – Sketch of the Cr optical setup to produce cooling, repumping, and imaging lights.



Secondly, after passing through a mechanical shutter (that allows to entirely block any blue light on the atoms during the evaporative cooling stage, see Chapter 3), the main optical path is divided into cooler and repumper branches. Cooling light is further split into ZS, MOT and transverse cooling (TC) beams, respectively: Each of them passes through a different AOM, in order to allow for independent choices of the detunings. In particular, ZS light is injected into a single-pass AOM working at +212 MHz, whereas MOT and TC lights are sent through double-pass AOMs working at approximately  $+2 \times 120$  MHz. Once prepared, each beam is coupled to a dedicated optical fiber, and delivered either to the science chamber (ZS, MOT) or to the chromium oven (TC). Before this, MOT light is actually split into “x”, “y” and “z” beams (as in the case of Li), while a small fraction of TC light is extracted to realize the zero-field imaging.

In the repumper branch, a series of three AOMs in cascade configuration provides the three blue repumper beams (namely: R1, R2, and R3). In particular, the first AOM (−70 MHz) produces the optical frequency for R1. Part of this light is directed

**Figure 2.10** – Preparation of Cr cooling lights (Cr MOT loading stage).



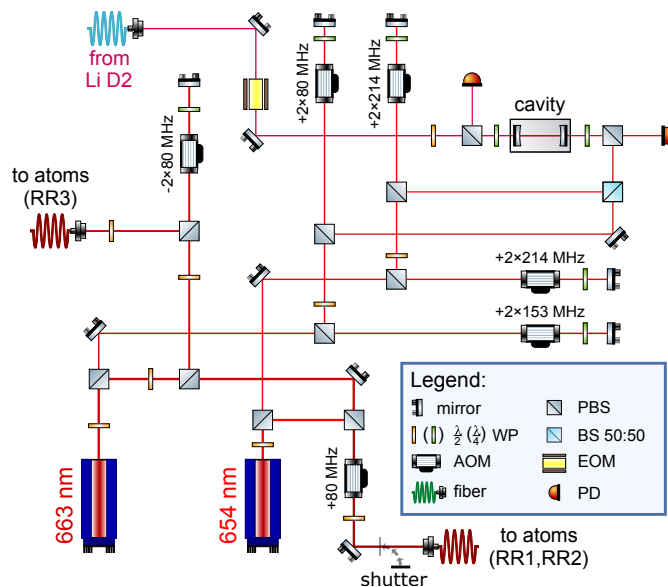
towards the second AOM ( $-2 \times 119$  MHz), which in turn yields R2. Eventually, a fraction of R2 light is sent to the third AOM ( $-169$  MHz), thereby generating R3. Once prepared, R1 and R2 are recombined on a PBS, and subsequently split into hyperfine pumping (HP) and MOT repumper beams. The former is directly coupled to a fiber and delivered to the chromium oven, while the latter is first recombined with R3, and then brought to the science chamber by another optical fiber. Lastly, the 0<sup>th</sup> diffraction order of the R2 AOM is employed for the high-field (830 G) imaging of Cr absolute ground state (i.e.  $Cr|1\rangle$ , or  $|f = 9/2, m_f = -9/2\rangle$ ). This is accomplished by means of a double-pass AOM ( $-2 \times 420$  MHz), after which the high-field imaging path is recombined with the TC pickup (zero-field imaging), before being coupled to the imaging fiber. Fig. 2.10 schematically depicts the preparation of Cr cooling lights for the MOT stage.

### 2.4.1 Cr red repumpers

As anticipated in Sec. 2.2, even with the combined action of the three blue repumpers (R1, R2, and R3), the  $^{53}\text{Cr}$  cooling transition remains slightly leaky. This owes to the presence of metastable  $^5D$  states, that can be populated via spontaneous decay from the excited  $^7P_4$  level. A set of three “red” repumpers (RR1, RR2, and RR3) is used to bring atoms back into the cooling cycle, exploiting the  $^7P_3$  level (see again the  $^{53}\text{Cr}$  level scheme in Fig. 2.3).

The optical setup that provides these three repumper lights is sketched in Fig. 2.11. The light sources are two independent diode lasers (Toptica DL-Pro), operating at  $\lambda_{1,3} = 663$  nm ( $^5D_4 \rightarrow ^7P_3$ ) and  $\lambda_2 = 654$  nm ( $^5D_3 \rightarrow ^7P_3$ ), respectively. The former is employed to generate both RR1 and RR3, while the latter is used to produce RR2. First, at the two laser outputs, a fraction of each light is sent to the locking setup. This relies on a Fabry-Perot (FP) transfer cavity ( $L = 5$  cm, FSR = 1.5 GHz,  $Finesse > 200$ ), which is actively stabilized exploiting the (already locked) lithium D2 line as a reference. In short, D2 light is modulated with an electro-optic modulator (EOM), and then injected into the cavity. The reflection from the FP is monitored with a photodetector (PD), and the cavity is locked to a resonance peak. Red repumpers lights are injected from the opposite side, and their reflection is recorded on a different PD. Two distinct current modulations on the master sources allow to

**Figure 2.11** – Sketch of the optical setup that provides Cr red repumpers.



separate the two signals by electronic means. The two optical frequencies are then locked to the nearest cavity mode. Note that, before entering the FP, each light passes through two double-pass AOMs in cascade configuration (see Fig. 2.11 for the working frequencies), which compensate for the frequency offset with respect to the locking point. A more technical description of this locking scheme, involving also the electronics, can be found in Ref. [55].

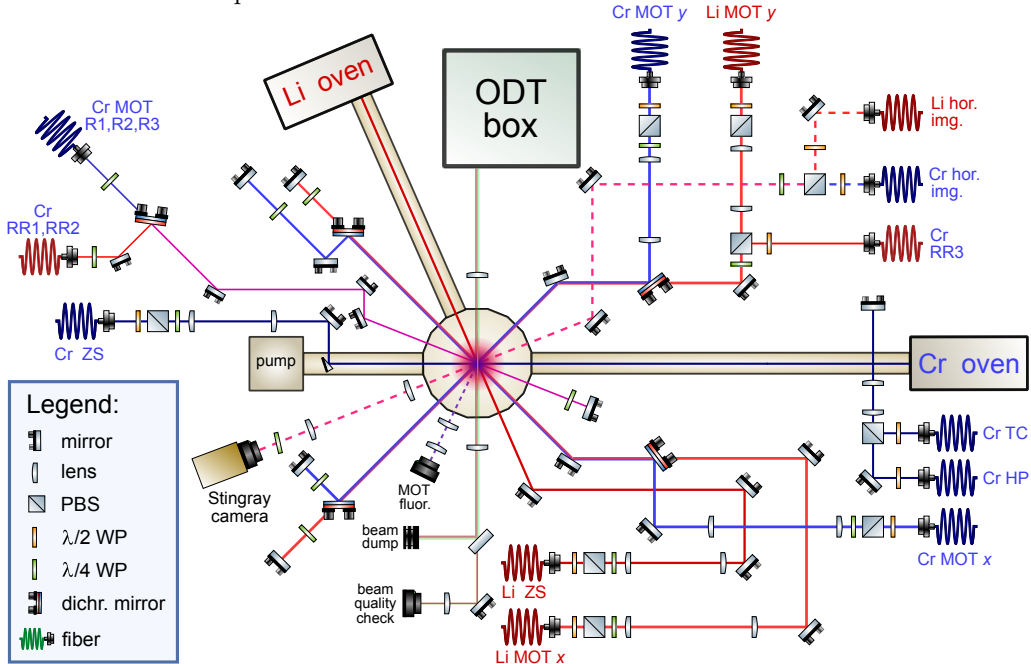
The largest part of the two master beams is sent to the atoms. In particular, RR1 and RR2 are recombined on a PBS, and then coupled to a fiber that delivers them to the experimental cell. A single-pass AOM (+80 MHz) is placed before the fiber, to be possibly employed as a fast switch. Actually, as the timescale to repump  $^5D$  states is rather slow (tens of ms), we eventually found no need for such a fast switch. Anyway, this AOM has been kept in the setup, as its frequency shift helps in the realization of the locking scheme. Importantly, before recombining RR1 and RR2, a fraction of the former is extracted to produce RR3. The appropriate optical frequency is reached by means of a double-pass AOM working at  $-2 \times 80$  MHz. For convenience, this light is brought to the science cell via a different, dedicated fiber.

## 2.5 The MOT optical setup

The various fibers injected with Li and Cr lights converge towards the main optical table, which hosts the two ovens, the whole vacuum and magnetic coils setups, as well as the ODT box (see Sec. 2.6). Here, each beam is properly shaped and aligned on the experimental cell, as described in the following. A schematic in-plane visualization of the optical setup that surrounds the science chamber is shown in Fig. 2.12.

First, I illustrate the Li part of the setup. The ZS beam, prepared with  $\sigma^+$  polarization, is first magnified with a 1:3 telescope to reach a beam waist of approximately 5 mm, and then directed towards the Li oven. The telescope is slightly uncollimated, in order to focus light onto the oven nozzle. This beam carries 70 mW (25 mW) of

**Figure 2.12** – Sketch of the Li-Cr cooling/trapping optical setup. The vertical direction, which includes the MOT-z beams and the vertical imaging, is not shown in this picture.



cooling (repumping) light, which yields  $I/I_{\text{sat}}^{\text{Li,D2}} \simeq 70$  ( $I/I_{\text{sat}}^{\text{Li,D2}} \simeq 25$ ).<sup>6</sup>

As previously anticipated, our MOT is realized by three mutually-orthogonal retro-reflected beams (labelled “ $x$ ”, “ $y$ ” and “ $z$ ”, respectively). The three Li MOT beams exit their respective fiber collimator with a beam waist of roughly 1 mm. Each one is prepared with  $\sigma^-$  polarization, and magnified with a 1:6 telescope. They are then directed towards the science chamber, where they cross at approximately  $90^\circ$  angles. Power in the horizontal plane is evenly distributed among  $x$ - and  $y$ - beams, with 25 mW ( $I/I_{\text{sat}}^{\text{Li,D2}} \simeq 17$ ) of cooling and 12 mW ( $I/I_{\text{sat}}^{\text{Li,D2}} \simeq 8$ ) of repumping light. Along the vertical ( $z$ ) direction, instead, we employ 20 mW ( $I/I_{\text{sat}}^{\text{Li,D2}} \simeq 14$ ) and 10 mW ( $I/I_{\text{sat}}^{\text{Li,D2}} \simeq 7$ ) of cooling and repumping light, respectively.

The Cr part of the optical setup is more involved than the Li one. The ZS beam, which in this case contains solely 26 mW of cooling light ( $I/I_{\text{sat}}^{\text{Cr}} \simeq 5.4$ ), is prepared with  $\sigma^+$  polarization and magnified by means of a 1:2 telescope, providing a final beam waist of 5 mm. It is then directed towards the Cr oven with the help of an in-vacuum mirror.

To increase the  $^{53}\text{Cr}$  flux, a stage of transverse cooling (TC) and hyperfine pumping (HP) is implemented at the oven output. This is essentially a 2D optical molasses (only one dimension is shown in Fig. 2.12), realized by a pair of retro-reflected beams. The two TC (HP) beams employ 14 mW (10 mW) of total optical power, and their shape is adjusted with a cylindrical telescope in order to maximize the interaction with the atomic flux.

The three Cr MOT beams leave the fiber collimators with a waist of roughly 2.6 mm, which is magnified by a 1:3 telescope on each axis. The in-plane beams have a total power of 4.5 mW, while the vertical beam has a power of 3 mW. They are all prepared with  $\sigma^-$  polarization, and overlapped with the corresponding Li beams on dichroic mirrors. When the bichromatic MOT beams leave the experimental cell, red and blue lights are again split by dichroic mirrors, before being retro-reflected. In this way, Li and Cr beams can be aligned and adjusted independently, and monochromatic waveplates can be used, thus improving polarization control.

As introduced in Sec. 2.2, up to six repumper lights are needed to completely close the  $^{53}\text{Cr}$  cooling transition. The three blue repumpers (R1, R2, and R3) are delivered to the main optical table via a single fiber (aside from the fraction of R1 and R2 that realizes the HP stage at the oven), whereas two different fibers are employed for red repumpers (one carries RR1 and RR2, the other RR3). The beam containing R1, R2, and R3 is sent to the experimental cell, after which it is retro-reflected. Such a 1D configuration avoids the formation of a bosonic  $^{52}\text{Cr}$  MOT on top of the fermionic one,<sup>7</sup> while still providing a good repumping efficiency. RR1 and RR2 are superimposed to the blue repumpers by means of a dichroic mirror, after which they all follow the same optical path. RR3 is instead overlapped on a PBS with the Li MOT- $y$  beam.

Fig. 2.12 also shows the horizontal absorption imaging path. This is typically employed to image Li atoms, but (upon minimal changes) it can also be used for Cr. The imaging is performed with a Stingray camera, with an overall 2:1 demagnification.

<sup>6</sup>As a reminder: the average intensity of a collimated gaussian beam can be expressed as  $I_0 = 2P/(\pi w_0^2)$ , where  $P$  is the total power, and  $w_0$  the beam waist [89].

<sup>7</sup>As shown in Fig. 2.10, R1 is (nearly) resonant with the  $^{52}\text{Cr}$  cooling transition.

The probe beam has a waist of roughly 5 mm, with a typical power of  $1 \div 2$  mW (providing  $I/I_{\text{sat}}^{\text{Li,D}^2} \simeq 1$  for Li). The vertical imaging path, instead, is not shown in Fig. 2.12. It is assembled on the breadboard that hosts the optics for the two MOT- $z$  beams, which is installed above the science chamber. In this case, light is collected onto a low-noise Andor camera, with the chip cooled down to  $-50^\circ\text{C}$ . As such, we usually employ this imaging path to probe Cr samples, as their signal is typically weaker than the Li one. Again, upon minimal changes (i.e. merely exchanging two fibers) Li atoms can be imaged in the vertical direction as well. Besides the two absorption imaging paths, a simple fluorescence imaging performed with a CCD camera (controlled by a RaspberryPi, which also acquires the data) provides a real-time, *in-situ* monitoring of the double MOT.

Lastly, Fig. 2.12 also shows the BODT path. The optical setup that realizes our bichromatic dipole trap is described in Sec. 2.6. Here I just mention that, after passing through the experimental cell, a pickup of the two high-power beams is sent to a Thorlabs camera, and serves as a monitor for the beams quality. The largest part of the two lights is instead safely directed to a beam dump.

## 2.6 Bichromatic optical dipole trap

In our Li-Cr mixture, we reach ultracold temperatures by sympathetically cooling  $^{53}\text{Cr}$  atoms via forced evaporation of  $^6\text{Li}$ , where the latter is prepared in a spin-mixture of the two lowest Breit-Rabi states (i.e.  $|\text{Li}|1\rangle$  and  $|\text{Li}|2\rangle$ ), and the magnetic field is conveniently chosen near the corresponding 832 G Feshbach resonance. Evaporation is performed in a bichromatic optical dipole trap, the description of which is the subject of this section.

First, as already mentioned, the choice of an optical dipole trap (and, accordingly, of an all-optical approach towards the ultracold/degenerate regime) allows us to select a convenient magnetic field (i.e. characterized by good Li-Li and Cr-Li collisional properties) where to carry out the evaporation stage. Secondly, we opted for a *bichromatic* trap, realized by overlapping an infrared ( $\lambda_{\text{IR}} = 1070$  nm) and a green ( $\lambda_{\text{GR}} = 532$  nm) laser beam, in order to enable a selective control of the trap depth for each species. In fact, the infrared (IR) light, being red-detuned with respect to both Li and Cr lowest optical transitions, acts as a trapping potential for both species.<sup>8</sup> By contrast, the green (GR) light strongly confines Cr atoms, while anti-confining Li. By adjusting the ratio between IR and GR powers, one can optimize the evaporation trajectory in order to efficiently cool Cr atoms, with as few losses as possible.<sup>9</sup>

To ensure a good spatial overlap between lithium and chromium density profiles, the trap is designed such that the two ODT beams feature the same waist ( $w_0 \simeq 45$   $\mu\text{m}$ ) on the atomic clouds (i.e. at the focus position). The choice of the beam waist results from a compromise between a good trapping volume (which scales as  $w_0^2 z_{\text{R}} \sim w_0^4/\lambda$ , where  $z_{\text{R}} = \pi w_0^2/\lambda$  is the Rayleigh length) and a not-too-shallow trap depth (which,

<sup>8</sup>The IR light alone provides a trap depth roughly 2.5 times deeper for Li than for Cr atoms [55], which by itself is not convenient for the sympathetic cooling stage.

<sup>9</sup>Indeed, initial Cr samples are typically much smaller than Li ones. Thus, given the remarkable efficiency with which lithium atoms can be evaporatively cooled, they are exploited as a cooling agent for the chromium component.

for a fixed power, scales as  $\sim 1/w_0^2$ ).<sup>10</sup> Besides, a trap with a small beam waist ( $w_0 \lesssim 20 \mu\text{m}$ ) may suffer from astigmatism, which can reduce the overall confinement and introduce artifacts in the trapping potential.

The ODT optical setup is also devised to minimize the so-called *thermal lensing* effect. The latter arises as a consequence of the inhomogeneous heating to which optics are subjected when hit by a non-uniform (high-)intensity profile. The resulting local deformations cause each element to act as an effective lens, thereby producing a time- and intensity-dependent *thermal focal shift*. Such an undesired effect is particularly detrimental in a BODT (especially if one of the beams is anti-trapping), as thermal lensing – being strongly wavelength-dependent – can significantly alter the effective trapping potential experienced by different atomic species, resulting in a sizeable reduction of the density overlap, and hence in a serious decrease of the sympathetic cooling efficiency. A detailed characterization of the thermal lensing effects in our setup, together with the approach followed to minimize them, can be found in Ref. [58].

Another issue concerning the simultaneous trapping of two different atomic species lies in the different *gravitational sags*, that in turn can considerably reduce the density overlap in the ultracold/degenerate regime (i.e. when the trap depth is shallow). This problem can be addressed with a small magnetic field gradient, exploiting the different ratios between magnetic moment and mass of the two species. An accurate study of this effect, combined with a simulation of an optimum magnetic field gradient, can be found in Ref. [57].

In the following, the optical scheme that realizes our trap (shown in Fig. 2.13), is described. Generally speaking, as any optical material unavoidably introduces some degree of thermal aberrations, the number of optics is kept as low as possible. Besides, all lenses mounted on the setup are realized in UV fused silica, with an anti-reflection “V-coating” at 1064/532 nm.

The IR source is a high-power multimode fiber laser (IPG Photonics YLR-300), which can deliver up to 300 W of optical power, with an output beam waist of 2.2 mm (and negligible ellipticity). The GR source is instead a high-power single-mode CW fiber laser (IPG Photonics GLR-50), providing a maximum power of 50 W, with an output beam waist of 1.1 mm (again with negligible ellipticity). In order to finely control the optical power during the experimental cycle, each beam passes through a dedicated AOM. The two 1<sup>st</sup> diffraction orders are employed for the ODT, whereas the 0<sup>th</sup> orders are directed to a beam dump.<sup>11</sup> Adjusting the RF modulation amplitude allows one to control the diffraction efficiency, thus providing a tool to rapidly and precisely tune the trap depth.<sup>12</sup> However, during the initial stages of

<sup>10</sup>With a 45  $\mu\text{m}$  beam waist, given the maximum output powers of our laser sources (see below), one can achieve trap depths on the order of 1.5 mK, well suitable to capture atoms directly from the MOT cloud, where  $T \sim 200 \div 300 \mu\text{K}$ .

<sup>11</sup>This actually refers to the “old” 1D setup, see the final remark of this section.

<sup>12</sup>The IR laser power can also be controlled by changing the current via the computer program. However, there is a minimum power of roughly 13 W below which lasing is not sustained. Thus, tuning the AOM efficiency provides a way to reach shallower trap depths.

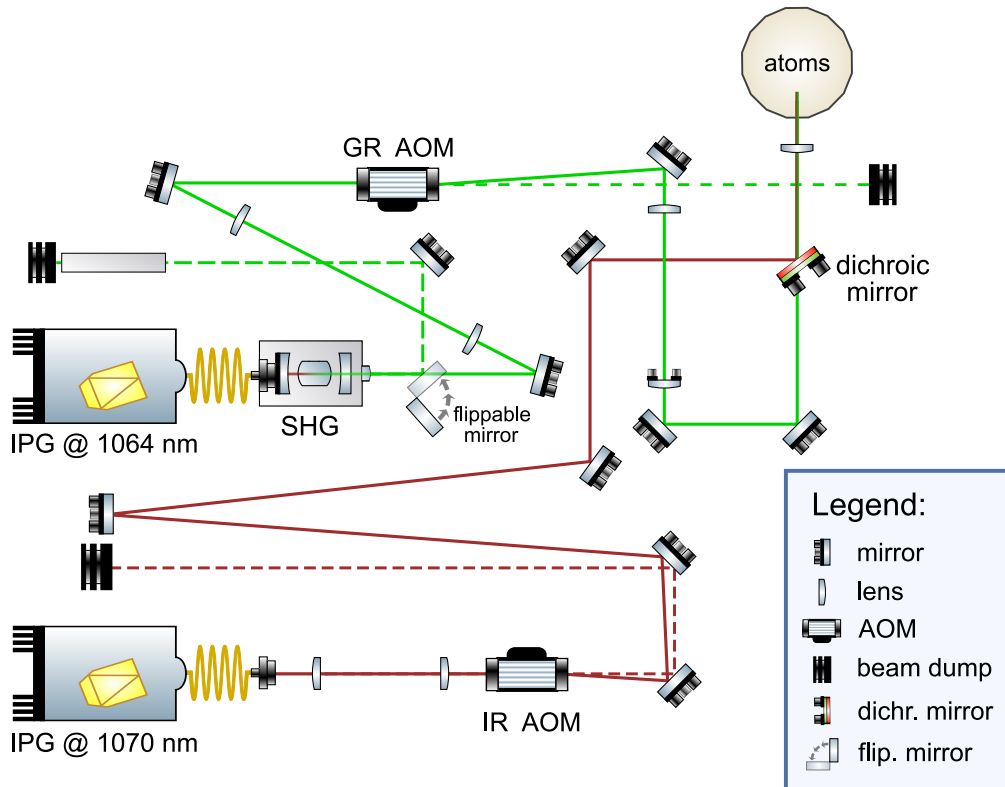
I also mention here that a similar strategy is not directly applicable to the 532 nm source, as its switch-on time and its response to changes in the current are extremely slow, on the order of several seconds. Therefore, we decided to keep this laser always switched on at 40 W, employing a flippable mirror to send light to a water-cooled beam dump when not needed on the atoms.

loading, a relatively high optical power is demanded. As such, in order to maximize the diffraction efficiency (with respect to input power), before entering the AOM each beam passes through a demagnifying telescope that reduces the two waists by a factor of 4. After the AOM, the GR beam passes through a second 1:1 telescope, with which the final beam waist can be properly adjusted.

Lastly, the IR and GR beams are recombined on a dichroic mirror, and directed towards the last (common) lens ( $f = 250$  mm), which focuses them on the atoms. The overlap between the two beams is found to be a rather critical parameter. Accordingly, the last lens of the GR path (before the dichroic mirror) is installed on a kinematic mount, acting also as a tilter to finely align the 532 nm beam, in order to precisely match the IR path.

As a final note, while this thesis was being written, the ODT setup has been modified to implement a (bichromatic) crossed ODT. The two supplementary beams are delivered by the 0<sup>th</sup> diffraction order of each AOM. In complete analogy to the scheme described above, they pass through two additional AOMs (where first diffraction order is collected), before being sent to the atoms. Such a trap configuration provides a much stronger confinement in the (former) “axial” direction, greatly increasing the density of trapped atoms, and thus ensuring a better spatial overlap between the two clouds.

Figure 2.13 – Sketch of the bichromatic ODT setup.



## Chapter 3

# Production of ultracold Li-Cr mixtures

This chapter outlines the experimental procedures, devised during this thesis work, that we follow to produce ultracold samples of fermionic  ${}^6\text{Li}$  and  ${}^{53}\text{Cr}$  atoms.

In the first section, I describe the sequential loading of our double-species MOT, and the subsequent laser cooling stages that we employ to further decrease its temperature. The discussion here is kept separate between lithium and chromium, although many of these stages occur simultaneously.

Secondly, I present our method to efficiently transfer atoms into the BODT, directly from the steady-state MOT. In particular, I focus on three critical steps needed to obtain large and polarized samples.

Lastly, in Sec. 3.3, I illustrate the evaporation trajectories that bring our samples down to ultracold temperatures. This represents the starting point for any experiment in the ultracold regime with the Cr-Li mixture. I also report here the experimental routines to produce degenerate samples of  ${}^6\text{Li}$ , which we initially took as a reference to optimize the evaporation stage.

### 3.1 Loading of the Li-Cr MOT

Our strategy to load the Li-Cr MOT relies on a 8 seconds-long duty cycle, where we perform a sequential loading of the two species. In the first 6 s, lithium atoms are collected in the trap in the absence of chromium. Then, the Li ZS field and lights are switched off, and the Cr MOT is loaded in roughly 2 s. The two clouds are further cooled and squeezed by means of compressed MOT (CMOT) stages, where the laser intensities and the detunings are decreased.

In the following subsections, the entire loading routine is described in more detail.

#### 3.1.1 Loading of the Li MOT

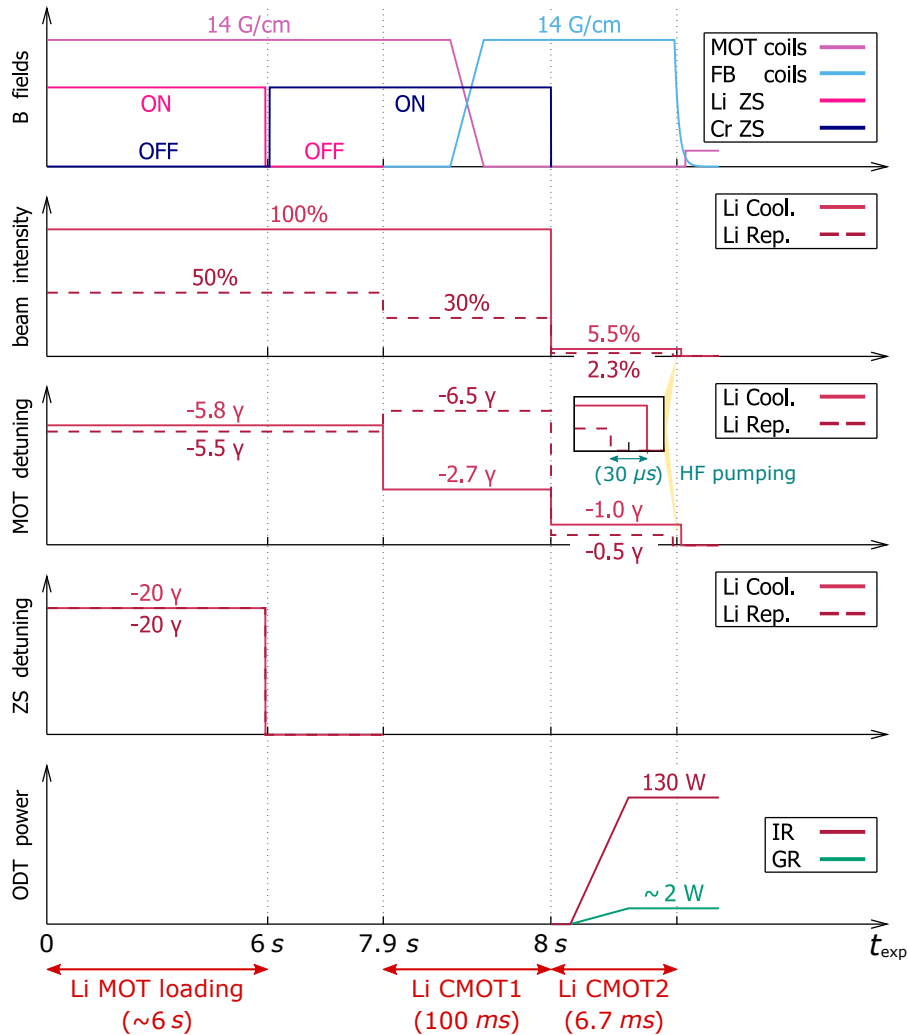
The experimental procedure to load the  ${}^6\text{Li}$  MOT is depicted in Fig. 3.1. As the cycle begins ( $t_{\text{exp}} = 0$ ), the ZS and MOT lights are switched on, initially prepared as shown previously in Fig. 2.6a. The relative intensities of cooling and repumping beams are set to 100% ( $P \simeq 25$  mW,  $I/I_{\text{sat}}^{\text{Li,D}2} \simeq 17$ ) and 50% ( $P \simeq 12$  mW,  $I/I_{\text{sat}}^{\text{Li,D}2} \simeq 8$ ), respectively. At the same time, the Li ZS field is also switched on, and current in the MOT coils, operating in anti-Helmholtz (A-H) configuration, is raised to 25 A, providing an in-plane gradient of  $\sim 14$  G/cm at the quadrupole center.<sup>1</sup>

<sup>1</sup>The MOT coils have a relatively large inner radius of 7.2 cm, designed to match the ZS magnetic field in order to optimize the collection efficiency (see Ref. [55] for more details). However, as a drawback, their complete switch-off time is rather long, on the order of  $\sim 50$  ms.

After a loading time on the order of 6 s, the Li ZS lights and field are switched off: at this point, the Cr MOT loading begins (see next subsection). Lithium atoms are held in the trap for the entire duration of the process ( $\sim 2$  s), without significant losses. Given the loading parameters, the MOT temperature is found to be relatively high, on the order of 3 mK. Accordingly, when the atom number is saturated, we further cool our cloud by reducing the intensities and the detunings of the MOT beams. Speaking of Li, this is realized by means of two consecutive CMOT stages, namely CMOT1 and CMOT2. The former starts approximately at  $t_{\text{exp}} = 7.9$  s, and lasts for 100 ms. The latter immediately follows, with a duration of 6.7 ms. During CMOT1, the detunings of cooling and repumping lights are set to  $\delta_{\text{cool}} = -2.7 \gamma_{\text{D2}}$  and  $\delta_{\text{rep}} = -6.5 \gamma_{\text{D2}}$ , respectively, and the repumper intensity is reduced to  $I_{\text{rep}} = 30\%$ . During CMOT2, instead, we set  $\delta_{\text{cool}} = -1.0 \gamma_{\text{D2}}$  and  $\delta_{\text{rep}} = -0.5 \gamma_{\text{D2}}$ , with  $I_{\text{cool}} = 5.5\%$  and  $I_{\text{rep}} = 2.3\%$ , respectively. This allows us to reach temperatures on the order of  $200 \div 300 \mu\text{K}$ , with peak spatial densities of a few  $10^{11} \text{ cm}^{-3}$ .

Two more aspects of this loading routine should be pointed out. First, towards the middle of the CMOT1 stage, we transfer the atoms in the field generated by the FB coils, which – due to their lower inductance – can be switched off significantly faster. The transfer is accomplished by a 20 ms-long linear ramp, where we lower

**Figure 3.1** – Schematic representation of the experimental sequence to load the Li MOT (axes are not to scale).



the current in the MOT coils, while simultaneously increasing that in the FB coils. Secondly, note that, during the cooling cycle, Li atoms are continuously removed from their hyperfine ground state by the action of the repumper beam, see again Fig. 2.2. To populate the  $|f = 1/2\rangle$  state back, we perform, at the end of CMOT2, a 30  $\mu\text{s}$ -long pulse of hyperfine pumping (HP), simply realized by switching off the repumper light before the cooling one. The net effect is an optical pumping of Li atoms in the lowest hyperfine level, without significant heating.

At  $t_{\text{exp}} \simeq 8$  s (actually, during the CMOT2 stage), we start to load atoms into the ODT. The entire ODT loading procedure is the subject of Sec. 3.2. However, I anticipate here that, after CMOT2, lithium D2 lights are switched off, together with the quadrupole field. Subsequently, a gray-molasses stage operating on the D1 line is employed to further cool the Li cloud, see Sec. 3.2.1.

### 3.1.2 Loading of the Cr MOT

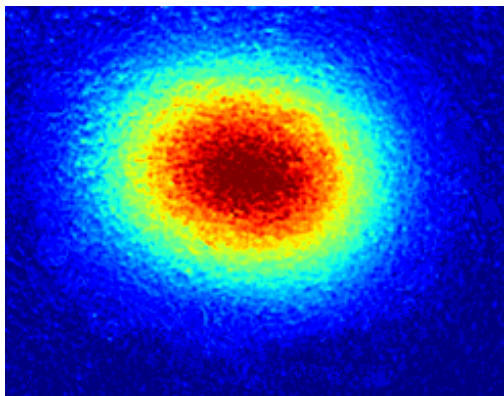
As already mentioned, the Cr MOT loading starts at  $t_{\text{exp}} \simeq 6$  s, following the Li one. The process, schematically represented in Fig. 3.3, lasts for roughly 2 s, as the Cr atom number saturates rather quickly owing to strong light-assisted collisions. During the loading time, Cr cooling and repumping lights are prepared as shown previously in Fig. 2.10, and as reported with more detail in Tab. 3.1.

Similarly to the case of Li, once the atom number is saturated, the Cr cloud is further cooled by means of a (single) CMOT stage: intensities of the MOT and blue repumper beams are decreased to 25 % and 3 % of their initial value, respectively, and the detuning of the former is set to  $-1.3 \gamma_{\text{Cr}}$ . This stage lasts for 4 ms, and its end coincides with that of Li CMOT2. As better discussed in the next section, a 20  $\mu\text{s}$ -long HP pulse at the end of Cr CMOT is employed to transfer atoms in the  $|f = 9/2\rangle$  manifold.

Lastly, during the entire loading sequence, the three red repumper lights (RR1, RR2, and RR3) are kept always on. They are switched off a couple of ms after the end of the Cr CMOT stage.

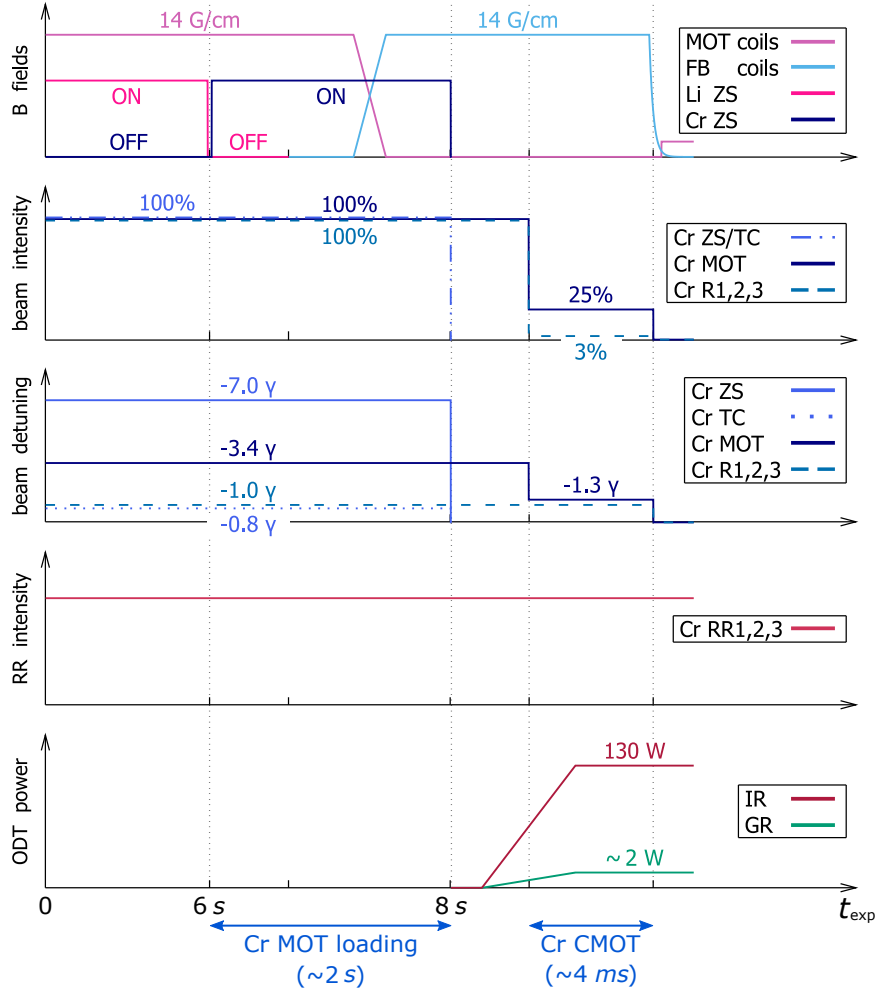
Fig. 3.2 shows a typical absorption image of the chromium MOT cloud, with  $N_{\text{Cr}} = 1.2 \times 10^7$  atoms. To the best of our knowledge, based on what is reported in the literature [65], this is the largest  $^{53}\text{Cr}$  MOT ever produced (by more than a factor of  $\sim 100$ ). This notable improvement owes to the reduction of light-assisted collisions, which is achieved by employing small intensities and relatively large detunings.

**Figure 3.2** – Absorption image of a  $^{53}\text{Cr}$  MOT with  $1.2 \times 10^7$  atoms. **Table 3.1** – Chromium MOT parameters during the loading stage.



Beam	$P$ [mW]	$\delta/\gamma_{\text{Cr}}$
ZS	26	-7.0
MOT- $x, y$	4.5	-3.4
MOT- $z$	3.5	-3.4
R1(MOT)	9.0	-1.0
R2(MOT)	4.0	-0.8
R3(MOT)	4.0	-1.0
TC- $x', y'$	7.0	-0.8
R1(HP)- $x', y'$	5.0	-1.0
R2(HP)- $x', y'$	5.0	-0.8

**Figure 3.3** – Schematic representation of the experimental sequence to load the Cr MOT (axes are not to scale).



### 3.2 Loading of the BODT

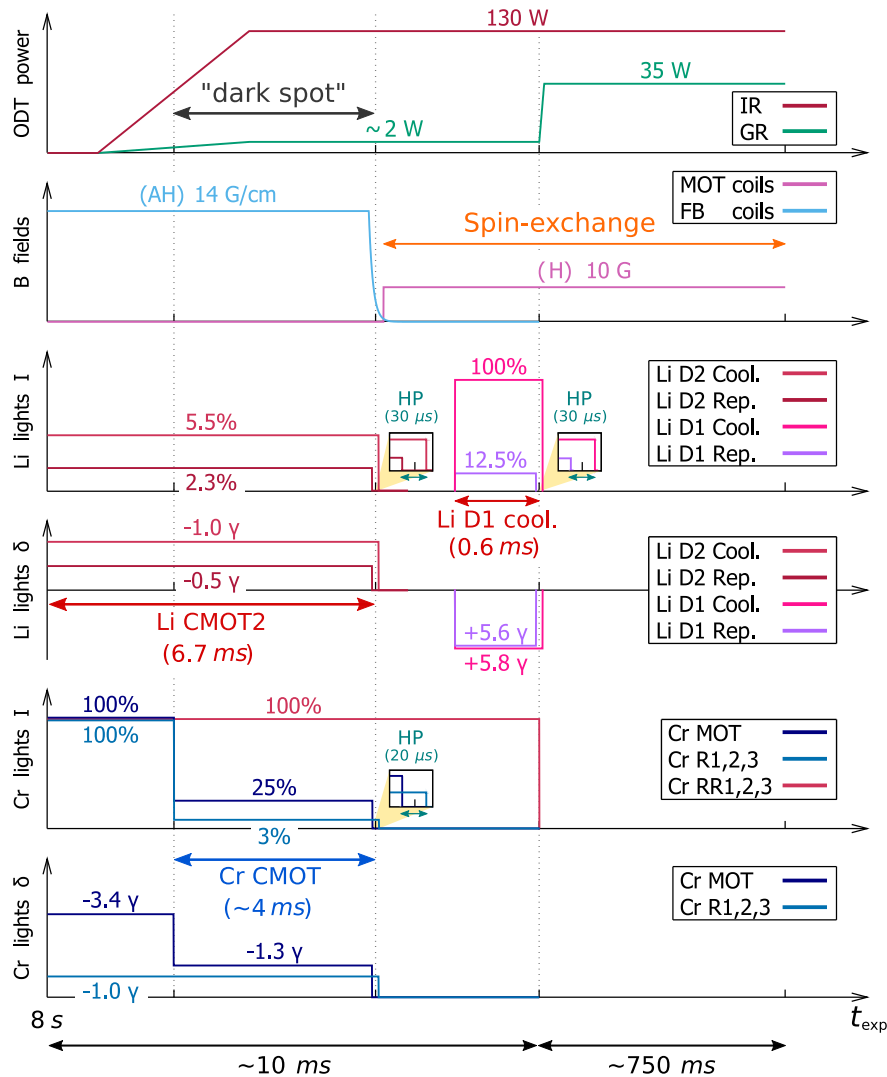
This section describes our approach to load the optical dipole trap, where we perform evaporative cooling, directly from the steady-state MOT. A schematic representation of the whole sequence is shown in Fig. 3.4.

The ODT is switched on during the Li CMOT2 and Cr CMOT stages. With a 3 ms linear ramp, power in the IR and GR beams is raised to 130 W and  $\sim 2$  W, respectively. Once the CMOT stages are accomplished, the quadrupole field is quickly switched off, and a small bias field is applied. Shortly after, a gray-molasses stage is performed on Li atoms, helping to further cool the cloud, thereby improving the loading efficiency. Then, as soon as all cooling lights are switched off, the GR power is raised to 35 W, to provide a better confinement of the Cr component.

Three critical aspects of this loading routine deserve a dedicated discussion. First, the strong IR beam induces a “dangerous” light shift of the Cr cooling transition, causing the CMOT lights to shift towards the blue (i.e. closer to resonance), and thus greatly increasing the light-assisted collisional loss rate. To overcome such a detrimental issue, the initial intensity of the 532 nm beam is carefully adjusted to

compensate for this shift, thus creating an effective “dark spot” (see Sec. 3.2.2). While the light-shift compensation has turned out to be remarkably efficient, the initial trap depth provided by such a combination of infrared and green light is unfavourable for our sympathetic cooling purposes, being deeper for lithium than for chromium. Accordingly, once Cr CMOT lights are switched off, the GR power has to be increased to obtain a more suitable starting point for the evaporation stage. As anticipated, before that, we perform an additional cooling stage on Li, which lasts approximately 600  $\mu\text{s}$  and relies on the D1 line. The optimum parameters for this latter stage, and for the ODT power at loading, are discussed in Sec. 3.2.1. Lastly, yet importantly, for many applications it is desirable to work with a polarized sample, i.e. with atoms in a well-defined  $|f, m_f\rangle$  state (or mixture). In particular, we carry out evaporative cooling with lithium atoms prepared in a spin-mixture of  $\text{Li}|1\rangle$  ( $|1/2, 1/2\rangle$ ) and  $\text{Li}|2\rangle$  ( $|1/2, -1/2\rangle$ ), and chromium atoms mostly polarized in the  $\text{Cr}|1\rangle$  state ( $|9/2, -9/2\rangle$ ). While the Li spin-mixture is readily prepared with a short HP pulse, the task of polarizing the Cr sample has turned out to be more challenging than we expected, but, at the same time, also quite interesting. This topic is the subject of Sec. 3.2.3.

**Figure 3.4** – Schematic representation of the experimental sequence to load the ODT (axes are not to scale).



### 3.2.1 Optimization of gray-molasses and ODT loading power

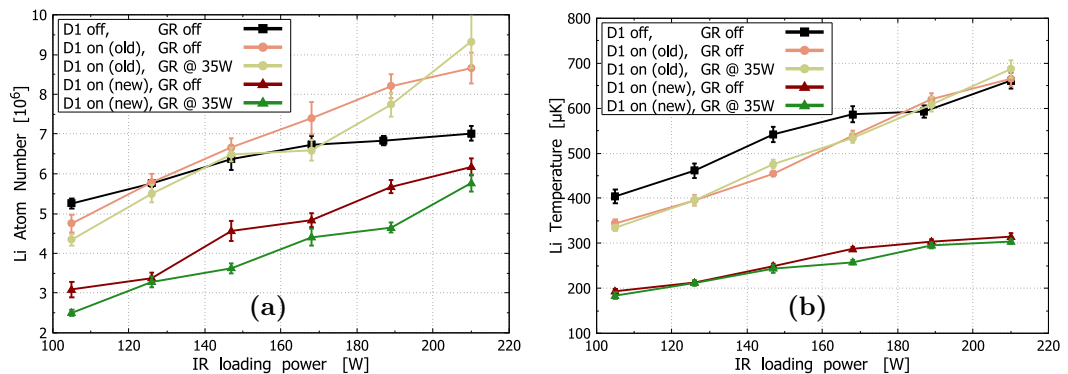
To provide a more favourable starting condition for the evaporation, a gray-molasses cooling stage,<sup>2</sup> exploiting the D1 line, is applied on Li atoms. It starts roughly 3 ms after the end of CMOT2, lasting for 600  $\mu\text{s}$ . D1 cooling lights are prepared as shown in Fig. 2.6b: The cooler and repumper beams are blue-detuned by  $5.8 \gamma_{\text{Li}}$  and  $5.6 \gamma_{\text{Li}}$ , respectively, closely matching the Raman condition  $\Delta_{\text{Raman}} = \delta_{\text{cool}} - \delta_{\text{rep}} = 0$  [63]. Relative intensities are set to  $I_{\text{cool}} = 100 \%$  and  $I_{\text{rep}} = 12.5 \%$ , respectively. Similarly to the CMOT2 stage, when the gray-molasses is accomplished, a 30  $\mu\text{s}$ -long HP pulse is applied to transfer atoms in the lowest hyperfine state (i.e. the  $f = 1/2$  manifold). When all D1 lights are finally switched off, the GR laser power is raised to 35 W, in order to provide a stronger confinement for the Cr component.

As previously mentioned, a first characterization of the optimal parameters for the gray-molasses stage (operated in free-space) was carried out in Ref. [57]. During my work period in the lab, I participated in a subsequent optimization of those parameters, aimed to efficiently apply D1 cooling in the presence of the BODT. The optimization involved laser intensities and detunings, as well as the time duration of the process and its location within the loading cycle. The final optimum parameters are those already reported above.

At the same time, we also monitored the Li atom number and temperature as a function of the IR loading power, see Figs. 3.5a and 3.5b. As a comparison, the figures also report the results obtained with “old” (free-space) D1 parameters, with which the gray-molasses stage in the ODT barely has any effect. Conversely, after optimization, we were able to reduce  $T$  by a factor of  $\sim 2$ , losing less than 50 % of the atoms.<sup>3</sup> Indeed, with  $P_{\text{IR}} = 130 \text{ W}$ , we get  $3.2(2) \times 10^6$  atoms at  $T \simeq 200 \mu\text{K}$ , which represents a reasonable starting point for the evaporation stage.

In any case, we found that the 532 nm light has negligible effects on the D1 cooling efficiency, thus the GR loading power can safely be optimized looking at Cr atoms only (see Sec. 3.2.2).

**Figure 3.5** – Optimization of the initial trap depth: Li atom number (a) and temperature (b) as a function of the IR loading power. Lines are merely a guide to the eye.



<sup>2</sup>Gray-molasses are sub-Doppler cooling stages that combine the Sisyphus effect with a velocity-selective coherent population trapping (VSCPT) technique. A theoretical analysis applied to fermionic Li atoms can be found in Ref. [64].

<sup>3</sup>For a thermal gas in a harmonic potential, at fixed trap depth the phase-space density (PSD) scales as  $\sim N/T^3$ . Hence, reducing both  $T$  and  $N$  by a factor of 2 yields a 4-fold increase in PSD.

### 3.2.2 Compensation of Cr light shift: the “dark” spot

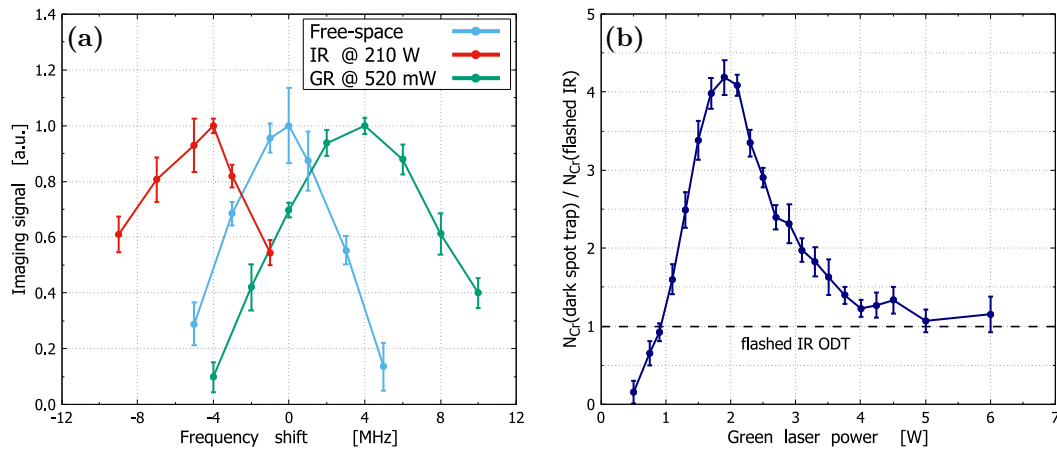
As anticipated above, the high-power IR beam employed for the ODT induces a detrimental light shift of the Cr cooling transition, causing the CMOT light to shift towards the blue, and thus increasing light-assisted collisional losses. Interestingly, owing to the existence of a 533 nm transition involving the excited  ${}^7P_4$  state of the cooling cycle, we found that a relatively small amount of GR light can be used to (over-)compensate for the IR-induced light shift, thereby enabling an efficient loading directly from the steady-state MOT.

As a proof of principle, we measured the light shifts induced by IR and GR lights on the Cr imaging transition. In practice, we imaged the chromium cloud *in-situ* in the presence of either 210 W of IR power (and no GR light), or 520 mW of GR power (and no IR light). In each case, the light shift is measured by scanning the imaging frequency, and comparing the peak signal with the one measured in free-space (i.e. with both IR and GR lights off). The outcome is shown in Fig. 3.6a: with  $P_{\text{IR}} = 210$  W and  $P_{\text{GR}} = 0$ , we measured a (trap-averaged) shift of  $-4.5(5)$  MHz (i.e. the cooling transition shifts towards the red, hence the CMOT lights relatively move towards the blue). On the other hand, with just  $P_{\text{GR}} = 520$  mW and  $P_{\text{IR}} = 0$ , the (trap-averaged) shift reads  $+4.0(5)$  MHz (hence, opposite in sign). Accordingly, a relatively small GR power can be effectively used to (over-)compensate for the IR-induced light shift, thereby allowing the Cr CMOT stage to be operated in the presence of the ODT, and thus greatly enhancing the loading efficiency.

The optimal parameters are ultimately found by measuring the number of Cr atoms loaded in the ODT (with 130 W of IR) as a function of the GR power, see Fig. 3.6b. The optimum is found at  $P_{\text{GR}} \simeq 2$  W, which corresponds to an effective  $-12$  MHz  $= -2.3 \gamma_{\text{Cr}}$  detuning of the CMOT light. Thanks to this light-shift compensation, we are able to obtain samples of up to  $1.5 \times 10^6$  Cr atoms in the BODT, measured 150 ms after loading.

A totally different loading strategy, which relies on abruptly switching on (“flashing”) the IR beam at 210 W, after all blue lights are turned off, yields instead Cr samples smaller by a factor of 4.

**Figure 3.6** – Dark-spot for Cr atoms: light shift of the Cr cooling transition (a), and Cr atom number as a function of the GR power, with 130 W of IR light (b).



### 3.2.3 Polarization of Cr via spin-exchange collisions

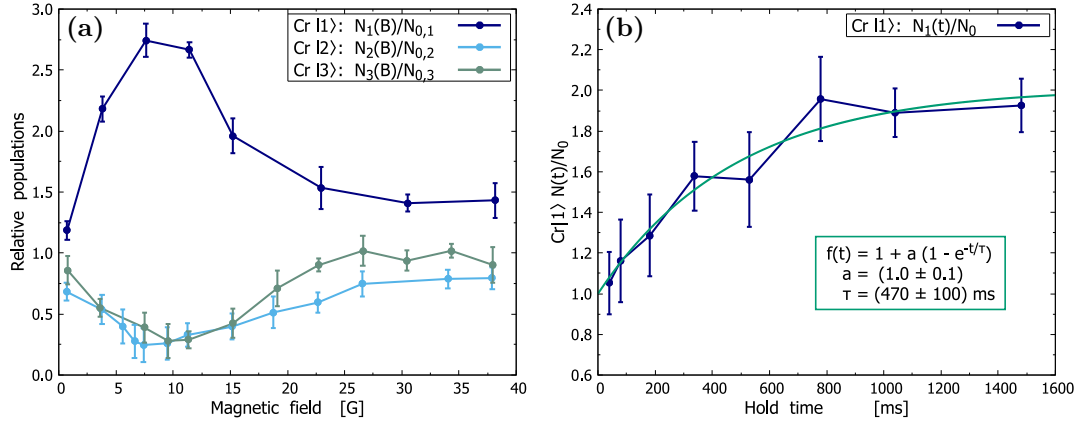
In many cases, it is desirable to work with polarized samples, i.e. with atoms in a well-defined  $|f, m_f\rangle$  state (where the latter, in the presence of a magnetic field, has to be intended merely as a label to identify the adiabatically-connected Breit-Rabi state). For instance, Feshbach loss spectroscopy requires well-defined scattering channels in order to avoid potential misassignments of loss features. On the other hand, evaporative cooling of fermionic atoms needs at least two different (i.e. distinguishable) kinds of particles to ensure thermalization. As anticipated, our route towards the ultracold/degenerate regime relies on evaporative cooling of lithium (in a 50% – 50% spin-mixture of  $\text{Li}|1\rangle$  and  $\text{Li}|2\rangle$ ), with simultaneous sympathetic cooling of chromium. To prepare the Li spin-mixture, we perform a 30  $\mu\text{s}$ -long HP pulse at the end of the gray-molasses stage, completely analogous to the one that follows CMOT2. A similar technique is also applied on Cr, with a 20  $\mu\text{s}$ -long HP pulse at the end of the CMOT stage, realized by switching off the cooling lights before the three blue repumpers (note that the roles of cooler and repumpers are exchanged with respect to the Li case, see again Figs. 2.2 and 2.3). However, as the  $|f = 9/2\rangle$  hyperfine level contains 10 Zeeman components, which in principle could be equally populated, the HP pulse alone is not enough to guarantee a polarized chromium sample. To this end, early attempts to realize an optical  $m_f$ -pumping stage were unfortunately not successful. Nonetheless, we empirically found that, at a particular magnetic field of about 10 G, spin-exchange collisions (i.e. two-body inelastic collision events where angular momentum is exchanged, bringing atoms towards energetically-lower spin-states) are remarkably enhanced, similarly to what observed in K-Li mixtures [66]. For such a small field, the released kinetic energy is lower than the trap depth (given the initial intensities of the ODT beams), thus atoms undergoing spin-changing collisions remain confined in the optical trap. The process has a timescale on the order of  $\sim 1$  s, and features a rather peculiar resonance-like behaviour with respect to the magnetic field. Indeed, we later found (see Chapter 4) that these features are connected to Feshbach resonances in the  $\text{Cr}|3\rangle + \text{Li}|2\rangle$  and  $\text{Cr}|2\rangle + \text{Li}|2\rangle$  scattering channels.

As a first step, we checked whether the initial  $m_f$  populations in the ODT showed some “spontaneous” degree of polarization. Given a total of roughly  $1.5 \times 10^6$  Cr atoms, we measured the atom number in the three lowest spin states (i.e.  $\text{Cr}|1\rangle = |9/2, -9/2\rangle$ ,  $\text{Cr}|2\rangle = |9/2, -7/2\rangle$  and  $\text{Cr}|3\rangle = |9/2, -5/2\rangle$ ), 300 ms after the standard loading routine (i.e. ramping up the ODT beams in 3 ms, with an optimized “dark spot”). In practice,  $N_{\text{tot}}$  is measured at zero field, whereas the  $m_f$  populations,  $N_i$ , are measured with spin-selective imaging at  $B > 0$ . Results are reported in Tab. 3.2: the initial Cr polarization is actually quite favourable, as essentially only the three lowest spin states are populated. While the reasons behind this finding are not entirely clear, we can exclude that such a behaviour is due to some “magic effects” during the dark spot stage, as a similar trend is observed also for a “flashed” IR trap (although

**Table 3.2** – Relative population of Cr  $m_f$  sublevels after loading into the ODT.

State	$N_i/N_{\text{tot}}$ [%]
$\text{Cr} 1\rangle$	60(6)
$\text{Cr} 2\rangle$	40(7)
$\text{Cr} 3\rangle$	< 13

**Figure 3.7** – Spin-exchange stage to polarize the Cr sample: (a) population of the lowest  $m_f$  states as a function of the magnetic field, for a fixed hold time  $\Delta t_{\text{hold}} = 1$  s; (b)  $\text{Cr}|1\rangle$  population growth as a function of the hold time, for a fixed  $B \simeq 10$  G.



with lower atom numbers). Rather, we ascribe such a favourable polarization of the sample to the MOT light, which is expected to drive mostly  $\sigma^-$  transitions. We then investigated the behaviour of the system when held in the trap for a fixed  $\Delta t_{\text{hold}} = 1$  s, at different magnetic fields. Our hope was to find a convenient field at which atoms would undergo spin-exchange collisions (also referred to as “purifying collisions”): hence, large enough to appreciably split the  $m_f$  sublevels, but, at the same time, small enough such that the released kinetic energy would not exceed the trap depth.

In practice, to generate a constant magnetic field, when the MOT quadrupole field (provided by the FB coils) is turned off, we switch the MOT coils from A-H to Helmholtz (H) configuration, and then set an appropriate current. The optical trap for these measurements is provided by 130 W of IR and 35 W of GR light, as it follows from the standard loading routine.

The scan results are shown in Figure 3.7a: surprisingly, we observe a rather clear resonance-like feature, appearing as an enhancement of  $\text{Cr}|1\rangle$  atom number, and as a dip in  $\text{Cr}|2\rangle$  and  $\text{Cr}|3\rangle$  populations. It is worth noticing that, while the  $\text{Cr}|1\rangle$  trend can be explained in simple terms (i.e. the spin-exchange rate initially grows with  $B$ , but, at high fields, atoms acquire enough kinetic energy to leave the trap, hence there is no gain in the ground state population), the behaviour of  $\text{Cr}|2\rangle$  and  $\text{Cr}|3\rangle$  is less obvious: there is no apparent reason, based on the simple argument above, for the sudden increase of their population, back to their  $B = 0$  levels, for  $B > 10$  G. Rather, such a trend points towards a resonant enhancement of two-body losses.

At the same time, we also monitored the atom number in the two spin-states of Li (not shown in the figure). Based on energy and angular momentum conservation, we expect  $\text{Li}|2\rangle$  to be the preferential partner for spin-exchange collisions, via  $\text{Li}|2\rangle + \text{Cr}|n\rangle \rightarrow \text{Li}|1\rangle + \text{Cr}|n-1\rangle$  ( $n = 2, 3$ ). As supposed, we found that the  $\text{Li}|2\rangle$  population decreases, whereas the number of  $\text{Li}|1\rangle$  atoms remains constant within the error bars. This yields an effective population imbalance in the Li mixture, the effects of which are better discussed in Sec. 3.3.3.

Generally speaking,  $m_f$ -polarization of Cr via the spin-exchange stage works nicely, enabling us to more than double the population of the absolute ground state, and yielding almost perfectly pure samples. However, as it could be potentially hazardous

(both in the short, as well as in the long run) to keep more than 150 W of (nearly) focused light on the experimental cell for long times, we investigated the timescale characterizing these spin-changing collisions, aiming to optimize the time duration of this stage. In practice, for a fixed field  $B \simeq 10$  G (corresponding to the peak gain in  $\text{Cr}|1\rangle$  population), we measured the  $\text{Cr}|1\rangle$  atom number as a function of  $\Delta t_{\text{hold}}$ , see Fig. 3.7b. Fitting data with an exponential growth function, we find a time constant  $\tau_{\text{sp.ex}} = 470(100)$  ms, with an asymptotic two-fold relative increase of the population. Accordingly, as the atom number is already close to saturation after roughly 800 ms, we decided to set the duration of the spin-exchange stage to 750 ms.

### 3.3 Evaporation trajectories

In this section I present the evaporation trajectories that we follow to attain ultralow temperatures.

During my first period in the lab, the chromium oven was being repaired by the manufacturer, so a flux of Cr atoms was not available for the experiment. Accordingly, the ODT evaporation ramps were initially tested on Li atoms only, employing solely the IR beam. To this end, the first step has been the production of a Li crossover superfluid, on top of the 832 G  $\text{Li}|1\rangle$ - $\text{Li}|2\rangle$  Feshbach resonance. Secondly, we realized a degenerate Fermi gas (DFG), ramping the field down to 300 G during the final stages of evaporation. Lastly, as soon as the Cr oven came back to the lab and the high vacuum was restored, we re-optimized the evaporation stage in the presence of the GR beam, aiming to an efficient sympathetic cooling of the chromium component.

#### 3.3.1 Production of a Li crossover superfluid

The first step taken in the degenerate regime has been the production of a Li crossover superfluid (CSF), which was attained in the lab shortly before the beginning of my thesis. I provide here an outline of the employed experimental routine.

The Li MOT is loaded as described in Sec. 3.1.1, including the two CMOT stages, but allowing for a slightly longer loading time (roughly 7 s). Starting 8 ms before the end of CMOT1, we switch the IR ODT on, ramping the power up to 150 W in 3 ms. The GR beam is not employed in this case. At the end of CMOT2 we apply the first HP pulse, then we switch the quadrupole field off and set the coils to H configuration. Subsequently, we perform the gray-molasses stage, with the second 30  $\mu\text{s}$ -long HP pulse in the end. Once cooling lights are switched off, we ramp the magnetic field up to 830 G in 50 ms, and then start evaporating. The selected evaporation ramps are exponential functions in the form

$$P(t) = A \cdot (e^{t/\tau} - 1) + B \quad (3.1a)$$

with

$$A = \frac{P_{\text{in}} - P_{\text{fin}}}{1 - e^{\Delta t/\tau}} \quad \text{and} \quad B = P_{\text{in}} \quad (3.1b)$$

where  $P_{\text{in}}$  and  $P_{\text{fin}}$  are the initial and final powers, respectively,  $\tau$  is the characteristic time constant, and  $\Delta t$  is the time duration of the ramp. To produce Li crossover superfluids, we employ two different ramps: The first one is relatively fast, to avoid high intensities impinging on the vacuum windows for long times, and results from lowering the injection current of the IR source. The second one is slower and

smoother, ensuring a good thermalization of the sample, and it is realized by tuning the IR AOM diffraction efficiency. The two ramps are plotted in Fig. 3.8, and their parameters are reported in Tab. 3.3. Fig. 3.9 displays a series of time-of-flight (TOF) absorption images of the final sample, containing up to  $N = 4 \times 10^5$  superfluid pairs, showing the characteristic inversion of the aspect ratio.

**Figure 3.8** – Evaporation ramps employed to produce a  ${}^6\text{Li}$  crossover superfluid.

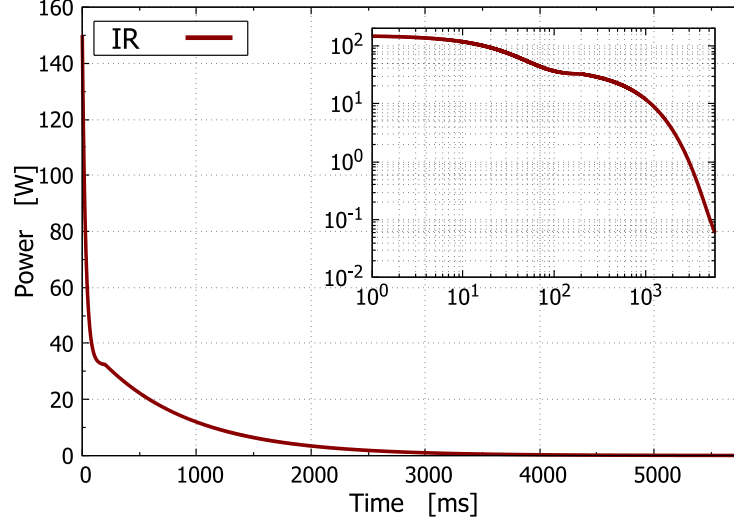
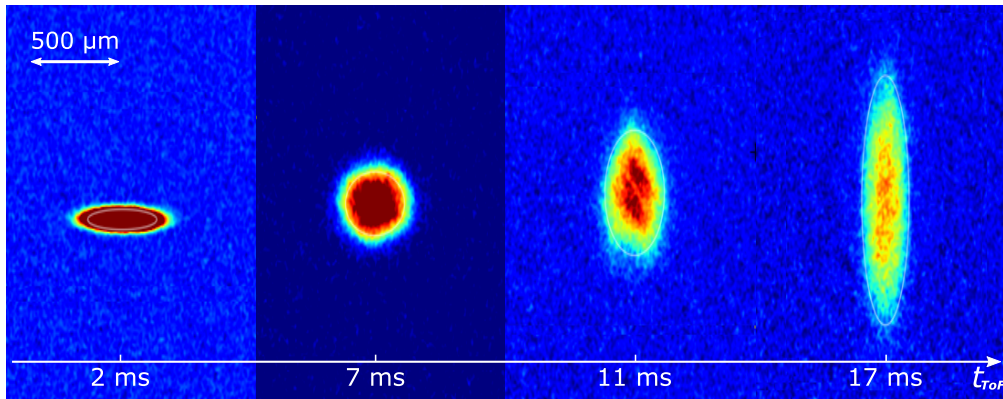


**Table 3.3** – Evaporation ramps employed to produce a  ${}^6\text{Li}$  crossover superfluid.

	$P_{\text{in}}$ [W]	$P_{\text{fin}}$ [W]	$\Delta t$ [ms]	$\tau$ [ms]
Ramp 1 (current)	150	32.5	200	-30
Ramp 2 (AOM)	32.5	0.06	5600	-800

**Figure 3.9** – Time of flight images of a  ${}^6\text{Li}$  crossover superfluid with  $4 \times 10^5$  pairs.



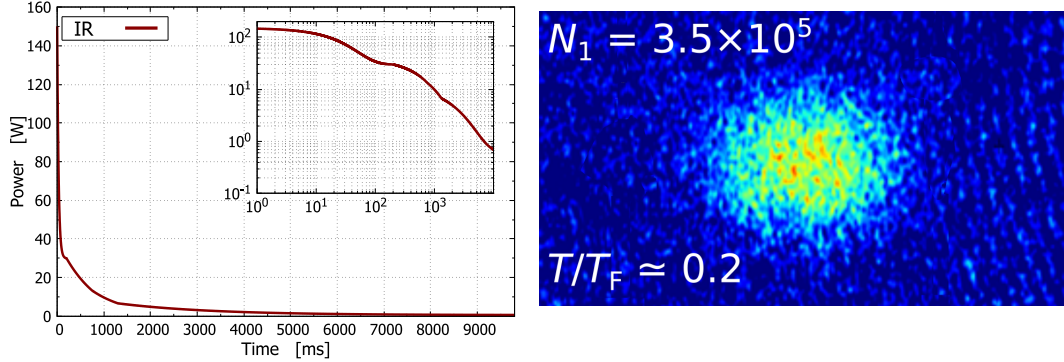
### 3.3.2 Production of a Li degenerate Fermi gas

After the realization of the crossover superfluid, the second step was the production of a Li degenerate Fermi gas (DFG). The first part of the experimental routine, from the MOT loading to the beginning of the evaporation stage, is completely analogous to the one employed for the CSF (see Sec. 3.3.1). The main differences are the evaporation ramps and the final magnetic field. In particular, in this case we apply four different exponential ramps, plotted in Fig. 3.10 (left), the parameters of which are reported in Tab. 3.4. Between the third and the fourth one, we lower the magnetic field down to 300 G, a value that yields a Li|1>-Li|2 scattering length of  $-250 a_0$  [67]. Note that the overall time duration of the evaporation stage is longer compared to the CSF case, as the magnitude of the scattering cross section at  $B = 300$  G is lower than its resonant (i.e. unitary-limited) value. Lastly, we image our sample (at  $B = 300$  G), before switching the magnetic field off. A typical long-TOF absorption image of a Li|1> DFG is shown in Figure 3.10 (right). The spherical shape signals the filling of the Fermi sphere.

**Table 3.4** – Evaporation ramps employed to produce a  ${}^6\text{Li}$  degenerate Fermi gas.

	$P_{\text{in}}$ [W]	$P_{\text{fin}}$ [W]	$\Delta t$ [ms]	$\tau$ [ms]
Ramp 1 (current)	150	30	200	-30
Ramp 2 (current)	30	13.3	550	-800
Ramp 3 (AOM)	13.3	6.7	550	-800
Ramp 4 (AOM)	6.7	0.7	8500	-2000

**Figure 3.10** – Evaporation ramps employed to produce a  ${}^6\text{Li}$  DFG (left), and long-TOF absorption image of the sample (right).



### 3.3.3 Production of ultracold Li-Cr mixtures

I present here the evaporation trajectories that we follow to produce ultracold LiCr mixtures. The double-species MOT and the BODT are loaded as described in Secs. 3.1 and 3.2, respectively. Once the spin-exchange stage is accomplished (i.e. at  $t_{\text{exp}} \simeq 8.75$  s), we ramp the magnetic field up to 830 G, and we start the evaporation stage. As previously discussed, the initial trap depth provided by 130 W of IR and 35 W of GR light is unfavourable for our sympathetic cooling purposes, being deeper for Li than for Cr. Accordingly, we perform a first, relatively fast evaporation ramp where we decrease the IR power only, keeping the GR power fixed. Then, once the optimum ratio  $P_{\text{IR}}/P_{\text{GR}}$  is reached, subsequent ramps are designed to keep such ratio fixed. The evaporation ramps are plotted in Fig. 3.11, and their parameters are reported in Tab. 3.5. After the third ramp, the mixture is thermalized at  $T = 5$   $\mu\text{K}$ . Further decreasing the temperature below this point, while keeping good atom numbers, has turned out to be rather challenging. The reasons might lie in a reduction of the overlap between the two density distributions (for which a crossed ODT has been implemented in the lab, see the final remark in Sec. 2.6), as well as in the Li spin population imbalance caused by the spin-exchange stage. Indeed, we found that the number of Li $|2\rangle$  atoms is essentially zeroed after the third ramp. While such a scenario might be even regarded as convenient for subsequent Feshbach spectroscopy scans, the optimum strategy to further decrease the temperature is currently under investigation in the lab.

It should be emphasized that the total temporal duration of the three ramps in

**Figure 3.11** – Evaporation ramps employed to produce ultracold Cr-Li mixtures.

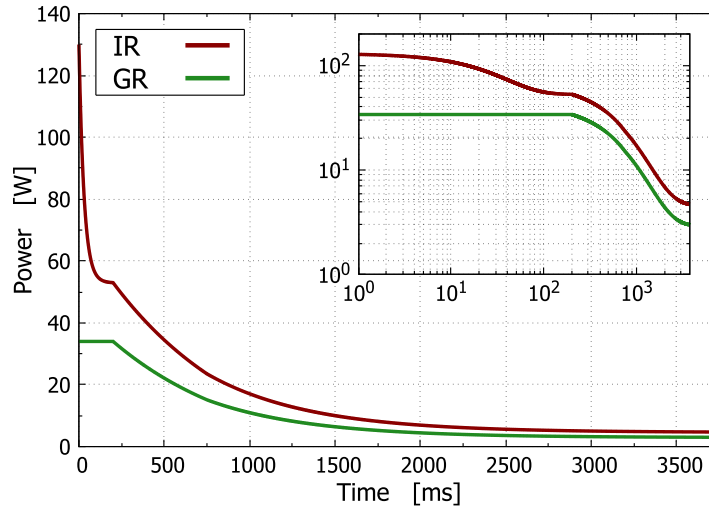


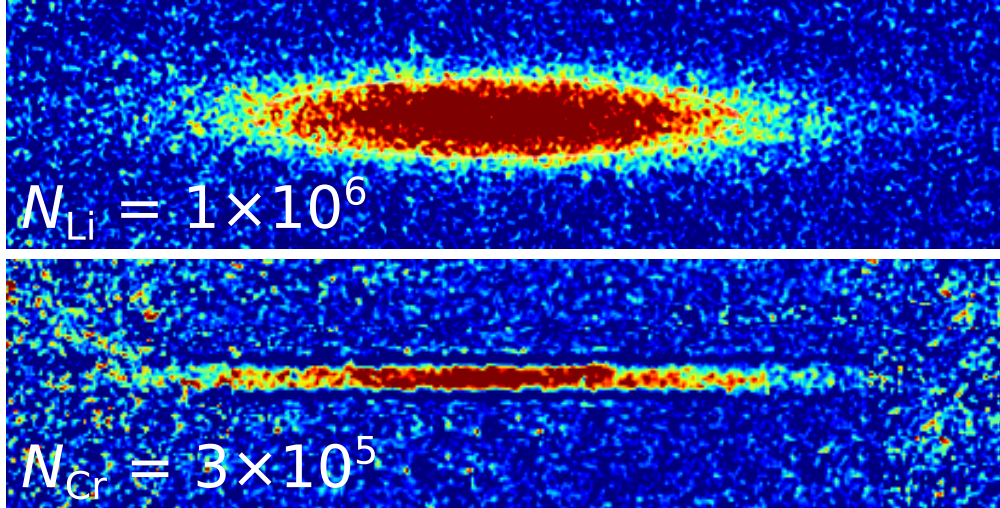
**Table 3.5** – Evaporation ramps employed for the sympathetic cooling stage.

		$P_{\text{in}}$ [W]	$P_{\text{fin}}$ [W]	$\Delta t$ [ms]	$\tau$ [ms]
Ramp 1	IR (current)	130	53	200	-30
	GR	35	35	200	$-\infty$
Ramp 2	IR (current)	53	24	550	-800
	GR (AOM)	35	15	550	-800
Ramp 3	IR (AOM)	24	4.7	3000	-600
	GR (AOM)	15	3.0	3000	-600

Tab. 3.5 is comparable to those performed on Li atoms only (at  $B = 830$  G), for the same final temperature (i.e. trap depth), see again Fig. 3.8. This means that the sympathetic cooling stage is rather efficient (i.e. the mixture thermalizes relatively fast), a fact that points towards good interspecies collisional properties.

Fig. 3.12 shows two typical absorption images of ultracold Li and Cr clouds, containing up to  $N_{\text{Li}} = 1 \times 10^6$  and  $N_{\text{Cr}} = 3 \times 10^5$ , respectively, at  $T = 5$   $\mu\text{K}$ .

**Figure 3.12** – Ultracold lithium-chromium sample with  $N_{\text{Li}} = 1 \times 10^6$  and  $N_{\text{Cr}} = 3 \times 10^5$ , at  $T = 5$   $\mu\text{K}$ .



## Chapter 4

# Feshbach loss spectroscopy

In this Chapter, I report on the experimental results obtained by performing extensive Feshbach loss spectroscopy on our ultracold Li-Cr mixtures. First, I outline the preliminary steps that we take to prepare the sample for Feshbach magnetic scans. Here, the starting point is provided by our standard duty-cycle to produce ultracold Li-Cr mixtures, already described in the previous Chapter. Secondly, I briefly discuss the most relevant loss mechanisms that are involved in our experiments, recalling a few earlier results from Chapter 1. I then present the results of our spectroscopic measurements, which involve up to six different scattering channels, reporting the data in the magnetic field regions of interest, and listing the empirical parameters that we use to label the loss features. Lastly, in Sec. 4.4, I discuss a couple of phenomenological models that can be used to fit the observed lineshapes, reporting the results of the analysis compared with current theoretical predictions.

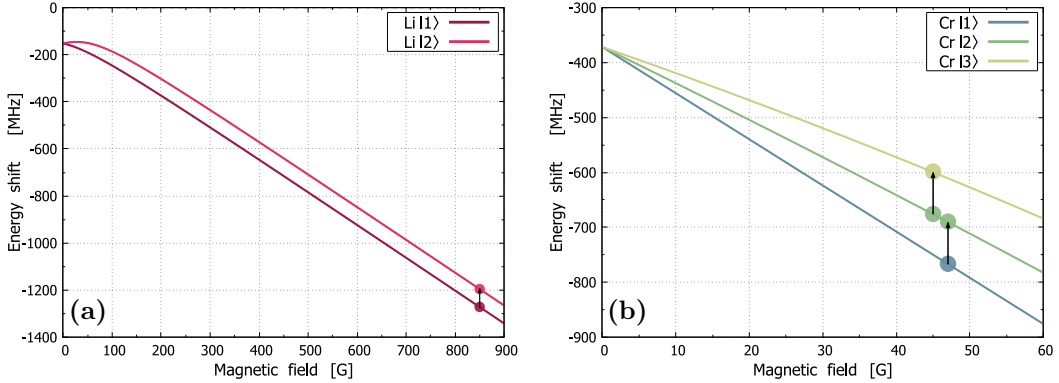
### 4.1 Sample preparation and typical experimental conditions

This section outlines the main steps to prepare the ultracold sample for Feshbach loss spectroscopy. The starting point for all the measurements presented in this chapter is an ultracold cloud of lithium and chromium, containing on average  $N_{\text{Li}} \simeq 10^6$  and  $N_{\text{Cr}} \simeq 10^5$  atoms, respectively, thermalized at  $T \simeq 5$   $\mu\text{K}$ . At this stage, following our standard BODT loading routine, Li and Cr atoms are almost entirely polarized in their lowest spin states (i.e.  $\text{Li}|1\rangle = |f = 1/2, m_f = 1/2\rangle$ , and  $\text{Cr}|1\rangle = |9/2, -9/2\rangle$ , respectively). The procedure to obtain our initial sample is described in Chapter 3. After the end of the evaporation stage, the first step is to switch off the GR laser beam, in order to ensure a better spatial overlap between the two density distributions. Indeed, at low powers, a not perfect overlap of the two BODT beams could introduce artifacts in the lithium trapping potential. The GR power is thus lowered to 0 W with a 200 ms-long linear ramp. Simultaneously, to increase the confinement, the IR power is raised to 9.4 W. This configuration provides a trap depth of roughly 200  $\mu\text{K}$  for Li, and 70  $\mu\text{K}$  for Cr. A side effect of the trap depth increase is a slight heating of the sample. We measured the temperature via time-of-flight imaging after the two 200 ms-long ramps, and we found  $T \simeq 10$   $\mu\text{K}$ . The typical sample conditions and trap parameters are reported in Tab. 4.1.

**Table 4.1** – Typical experimental conditions for our Feshbach scans.  $T$  is the temperature,  $N$  is the atom number,  $U_0$  is the trap depth,  $\nu_r$  ( $\sigma_r$ ) and  $\nu_z$  ( $\sigma_z$ ) are the radial and axial trapping frequencies ( $1/\sqrt{e}$  half-widths of the density distributions), respectively, while  $n_0$  is the peak atomic density.

	$T$ [ $\mu\text{K}$ ]	$N$	$U_0$ [ $\mu\text{K}$ ]	$\nu_r$ [Hz]	$\nu_z$ [Hz]	$\sigma_r$ [ $\mu\text{m}$ ]	$\sigma_z$ [ $\mu\text{m}$ ]	$n_0$ [ $\text{cm}^{-3}$ ]
Li	10	$10^6$	215	4260	25	4.4	750	$4.5 \times 10^{12}$
Cr	10	$10^5$	72	825	5	7.6	1250	$\sim 10^{11}$

**Figure 4.1** – Magnetic field dependence of the lowest Zeeman levels of  ${}^6\text{Li}$  (a) and  ${}^{53}\text{Cr}$  (b), schematically showing the relevant fields for RF transitions.



In order to prepare the mixture in different atomic spin states, i.e. to investigate different Li+Cr scattering channels, we employ a sequence of radiofrequency (RF) pulses, each time setting an appropriate value for the magnetic field, so that the energy splitting between the involved Zeeman sublevels matches our RF antenna at 76.3 MHz. Namely, to transfer Li atoms in the  $|2\rangle$  state, we apply a 600  $\mu\text{s}$ -long  $\pi$ -pulse at  $B = 846.5$  G. On the other hand, for Cr atoms, we lower the field down to  $B \simeq 40$  G, crossing the two atomic resonances ( $\text{Cr}|1\rangle \rightarrow \text{Cr}|2\rangle$  at  $B \simeq 47$  G, and  $\text{Cr}|2\rangle \rightarrow \text{Cr}|3\rangle$  at  $B \simeq 45$  G, respectively) in a few ms. By switching the RF field on in correspondence of these crossings, we realize one (two) Landau-Zener adiabatic passage(s), obtaining a polarized  $\text{Cr}|2\rangle$  ( $\text{Cr}|3\rangle$ ) sample. Fig. 4.1 schematically illustrates the RF population transfers. Each RF pulse is only applied when required.

Once the desired spin mixture is prepared, the magnetic field is set to the (variable) value selected for the measurement, and the sample is held in the trap for a given time  $t_{\text{hold}}$ , adjusted between 0.5 and 5 seconds according to the signal strength (a typical value is  $t_{\text{hold}} = 4$  s). After the holding time, the magnetic field is quickly ramped to a suitable value to perform spin-selective imaging of the leftover Cr cloud, the number of remaining Cr atoms being the quantity that we measure to detect (resonantly-enhanced) losses. Indeed, as better discussed in the following, given our experimental conditions (i.e.  $N_{\text{Li}} \gg N_{\text{Cr}}$ ), the Li sample is much less sensitive to atom losses involving collisions with the Cr component.

## 4.2 Relevant loss mechanisms

In the following, I provide a basic overview of the main loss mechanisms involved in our measurements. Phenomenological models to analyze the line shapes are discussed in Sec. 4.4.

In our measurements, we experimentally investigated six different scattering channels, namely all the binary combinations involving the two lowest spin states of  ${}^6\text{Li}$  (i.e.  $\text{Li}|1\rangle$  and  $\text{Li}|2\rangle$ ), and the three lowest spin states of  ${}^{53}\text{Cr}$  (i.e.  $\text{Cr}|1\rangle$ ,  $\text{Cr}|2\rangle$ , and  $\text{Cr}|3\rangle$ ). Following the discussions in Secs. 1.10.1 and 1.14, the main sources of losses are spin-exchange collisions, spin-spin (or dipolar) relaxation, and three-body recombination processes. In particular, spin-exchange collisions are caused by the exchange interaction  $\hat{H}_{\text{ex}}(r)$  (see Eqs. (1.74)), which conserves the total electronic spin,  $S$ , and the projection of the total internal angular momentum,  $M_f = m_{f_1} + m_{f_2}$ .

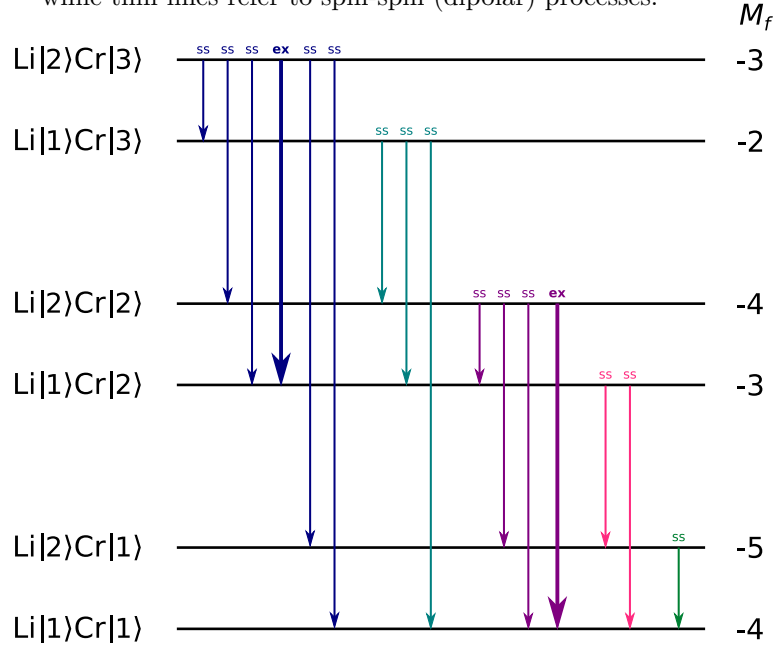
**Table 4.2** –  $M_f$  values for the six investigated scattering channels.

	Cr 1⟩	Cr 2⟩	Cr 3⟩
Li 1⟩	−4	−3	−2
Li 2⟩	−5	−4	−3

Accordingly, these collisions only affect the  $\text{Li}|2\rangle+\text{Cr}|2\rangle$  and  $\text{Li}|2\rangle+\text{Cr}|3\rangle$  scattering channels (see Tab. 4.2), via  $\text{Li}|2\rangle+\text{Cr}|n\rangle \rightarrow \text{Li}|1\rangle+\text{Cr}|n-1\rangle$  processes.<sup>1</sup> Since the exchange interaction is strong (at small interatomic distances), we expect to observe strong loss features connected with spin-exchange collisions in these two scattering channels.

By contrast, spin-spin (lossy) collisions arise from the dipolar term  $\hat{H}_{\text{dd}}(r)$  (see Eqs. 1.75), and they are expected to yield weaker and narrower loss features. Here, the conserved quantity is the total angular momentum projection,  $M_{\text{tot}} = M_f + m_\ell$ , while  $\Delta\ell = 0, \pm 2$  and  $\Delta M_f = 0, \pm 1, \pm 2$ . Accordingly, these collisions affect all the investigated scattering channels, except for the lowest in energy, i.e.  $\text{Li}|1\rangle+\text{Cr}|1\rangle$ . Fig. 4.2 summarizes the allowed two-body inelastic decays for our mixtures.

Lastly, as discussed in Sec. 1.14, three-body losses are due to collisions involving three ultracold particles, two of which form a bound state (i.e. a molecule), while the third one carries away (part of) the released binding energy as kinetic energy. Recombination processes affect every scattering channel, and, in particular, they are the only source of losses in  $\text{Li}|1\rangle+\text{Cr}|1\rangle$  collisions (neglecting  $N > 3$ -body higher-order contributions). Since we deal with binary Li-Cr mixtures, three-body recombination processes can occur both via Li-Li-Cr and Cr-Cr-Li collisions.

**Figure 4.2** – Schematic illustration of the allowed two-body inelastic decays in the six investigated scattering channels. Thick lines denote spin-exchange collisions, while thin lines refer to spin-spin (dipolar) processes.

<sup>1</sup>At ultralow temperatures of  $T \simeq 10 \mu\text{K}$ , for  $B > 0.1 \text{ G}$  the inverse processes are forbidden by energy conservation.

### 4.3 Feshbach scans

I now report the results of our Feshbach scans, organized according to the scattering channels. In particular, we began our studies by investigating  $\text{Li}|2\rangle+\text{Cr}|3\rangle$  and  $\text{Li}|2\rangle+\text{Cr}|2\rangle$  collisions, where we expected to find the strongest loss features, owing to the allowed spin-exchange mechanism. Then, we moved to the other channels featuring two-body losses, in which we expected to find fewer (and generally weaker) loss features. Lastly, we explored the lowest energy channel, namely  $\text{Li}|1\rangle+\text{Cr}|1\rangle$ , where losses are solely due to three-body collisions. In all these measurements, our main goal was to locate as many FRs as possible, in order to provide a suitable experimental input for refined theoretical models. In particular, the latter involve coupled-channel calculations (CCC) [46] carried out by our theory collaborator, Prof. A. Simoni (University of Rennes), and an asymptotic bound-state model (ABM), adapted to the Li-Cr mixture by one of our team members, Dr. A. Trenkwalder. In the early stages, both models require information about the experimentally observed positions of several FRs. Subsequently, the roles are reversed, as the models acquire predictive power over the scattering properties of the investigated atoms. Currently, both models are under refinement.

Since we expected some among the loss features to possibly be rather narrow, we initially scanned the magnetic field regions of interest with a resolution of  $\sim 150$  mG (“brute force scans”). We then adopted a different approach, which allowed us not only to considerably speed up the measurements, but also to prevent possible “misses” of narrow features due to unfortunate sampling. In practice, exploiting our two sets of magnetic coils, rather than keeping the strength of the magnetic field fixed, we applied a small linear ramp ( $\Delta B \simeq 0.6$  G), lasting for the entire hold time. This allowed us to decrease the sampling density during extensive scans, while maintaining a good sensitivity to Cr atom losses. Whenever a resonance candidate was found, we switched the magnetic ramp off, re-investigating the candidate region with the “brute-force” method. In the following, I present our experimental results.

#### $\text{Li}|1\rangle+\text{Cr}|3\rangle$ channel

In the  $\text{Li}|1\rangle+\text{Cr}|3\rangle$  channel, we selectively scanned a small region around 200 G, where preliminary results from theoretical models suggested the presence of a FR. As shown in Fig. 4.3, we indeed found a loss feature at  $B_0 \simeq 194$  G, the parameters of which are reported in Tab. 4.3.

**Figure 4.3** – Heteronuclear Feshbach resonance in the  $\text{Li}|1\rangle+\text{Cr}|3\rangle$  scattering channel. Lines are merely a guide to the eye.

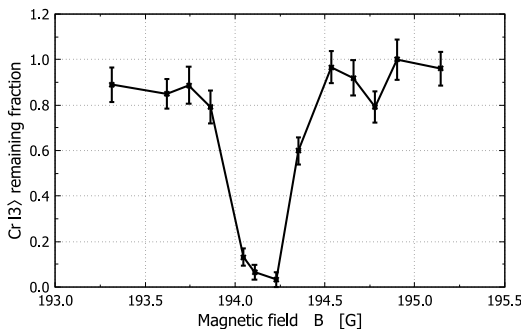


**Table 4.3** – Feshbach resonance in the  $\text{Li}|1\rangle+\text{Cr}|3\rangle$  channel. The position  $B_0$  is extracted with a model-independent analysis, by looking at the zero-crossing of the signal first derivative. The error takes into account also the magnetic field stability. The width  $\Delta B_{\text{loss}}$  is the FWHM of the loss feature, extracted directly from the data.

$B_0$ [G]	$\Delta B_{\text{loss}}$ [G]
$194.2 \pm 0.2$	0.4

**Li|2>+Cr|3> channel**

In the Li|2>+Cr|3> channel, we scanned the magnetic field region from 0 to 270 G, where we located 12 FRs. The observed loss features are shown in the panels of Fig. 4.4, whereas their positions and widths are reported in Tab. 4.4.

**Figure 4.4** – Heteronuclear Feshbach resonances in the Li|2>+Cr|3> scattering channel. The horizontal axis is the magnetic field  $B$  expressed in G, while the vertical axis is the Cr|3> remaining fraction  $f_{\text{Cr}|3>}$ . Lines are merely a guide to the eye.

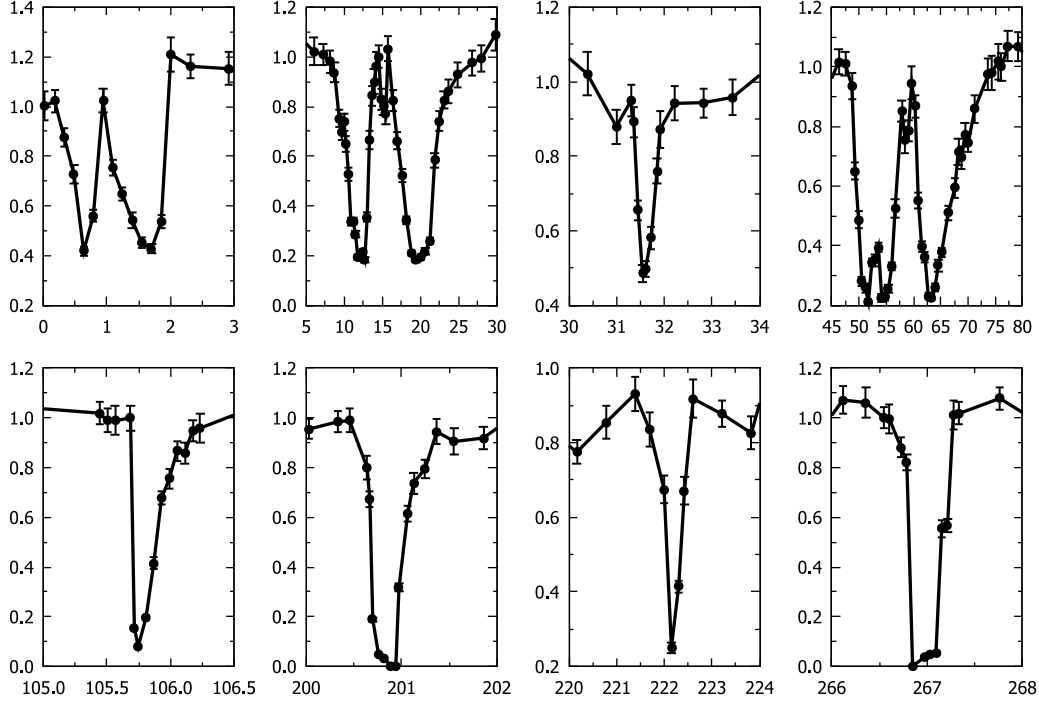


**Table 4.4** – Feshbach resonances in the Li|2>+Cr|3> channel. The positions  $B_0$  are extracted with a model-independent analysis, by looking at the zero-crossing of the signal first derivative. Errors take into account also the magnetic field stability. The widths  $\Delta B_{\text{loss}}$  are the FWHMs of the loss features, extracted directly from the data.

$B_0$ [G]	$\Delta B_{\text{loss}}$ [G]	$B_0$ [G]	$\Delta B_{\text{loss}}$ [G]
$0.62 \pm 0.12$	0.35	$54.8 \pm 0.5$	$\sim 4$
$1.56 \pm 0.14$	0.7	$63.4 \pm 0.5$	7.1
$12.2 \pm 0.2$	2.9	$105.8 \pm 0.1$	0.2
$19.8 \pm 0.5$	4.4	$200.9 \pm 0.1$	0.35
$31.6 \pm 0.1$	0.4	$222.2 \pm 0.1$	0.4
$51.5 \pm 0.4$	$\sim 4$	$267.0 \pm 0.1$	0.4

**Li|2>+Cr|2> channel**

In the Li|2>+Cr|2> channel, we thoroughly investigated the magnetic field region from 0 to 600 G, and a selected interval around 1460 G, disclosing a total of 16 FRs. The observed loss features are shown in Fig. 4.5, with their positions and widths reported in Tab. 4.5.

**Figure 4.5** – Heteronuclear Feshbach resonances in the Li|2>+Cr|2> scattering channel. The horizontal axis is the magnetic field  $B$  expressed in G, while the vertical axis is the Cr|2> remaining fraction  $f_{\text{Cr}|2>}$ . Lines are merely a guide to the eye.

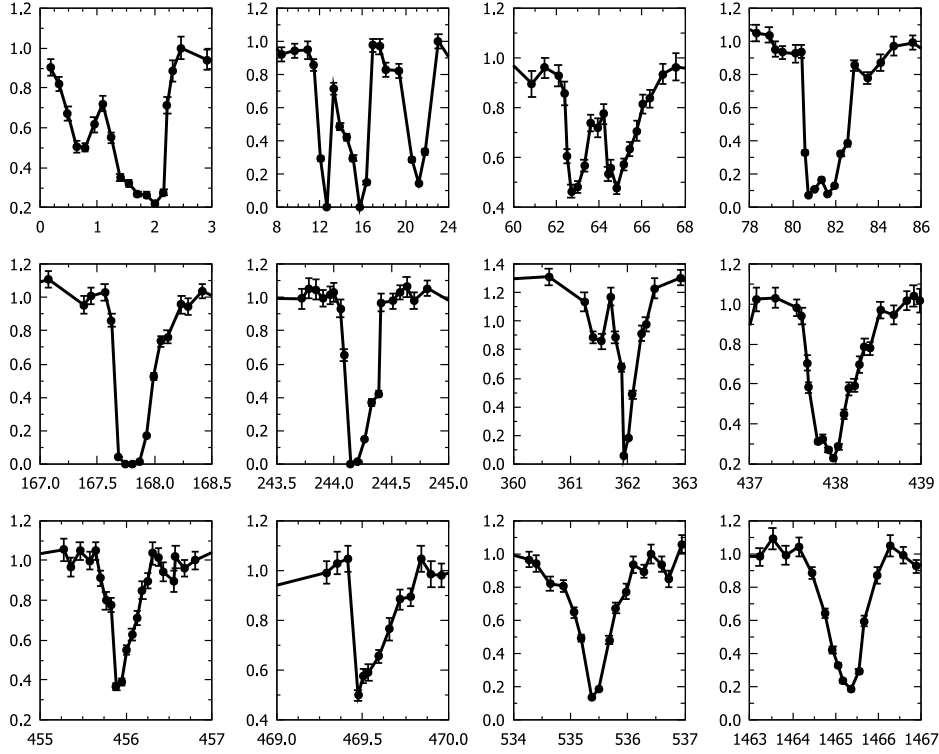


**Table 4.5** – Feshbach resonances in the Li|2>+Cr|2> channel. The positions  $B_0$  are extracted with a model-independent analysis, by looking at the zero-crossing of the signal first derivative. Errors take into account also the magnetic field stability. The widths  $\Delta B_{\text{loss}}$  are the FWHMs of the loss features, extracted directly from the data.

$B_0$ [G]	$\Delta B_{\text{loss}}$ [G]	$B_0$ [G]	$\Delta B_{\text{loss}}$ [G]
$0.73 \pm 0.11$	0.6	$167.8 \pm 0.1$	0.35
$1.95 \pm 0.14$	1.0	$244.2 \pm 0.1$	0.3
$12.9 \pm 0.2$	1.3	$361.9 \pm 0.1$	0.25
$15.5 \pm 0.2$	2.5	$438.0 \pm 0.2$	0.55
$21.1 \pm 0.2$	2.2	$455.9 \pm 0.1$	0.3
$62.8 \pm 0.3$	1.0	$469.5 \pm 0.1$	0.2
$64.9 \pm 0.3$	1.5	$535.4 \pm 0.2$	0.6
$81.1 \pm 0.4$	2.1	$1465.4 \pm 0.2$	1.0

**Li|2>+Cr|1> channel**

In the Li|2>+Cr|1> channel, we thoroughly investigated the magnetic field region from 0 to 600 G, and a selected interval around 1460 G, overall identifying 10 FRs, as shown in Fig. 4.6. The positions and the widths of the observed loss features are reported in Tab. 4.6.

**Figure 4.6** – Heteronuclear Feshbach resonances in the Li|2>+Cr|1> scattering channel. The horizontal axis is the magnetic field  $B$  expressed in G, while the vertical axis is the Cr|1> remaining fraction  $f_{\text{Cr}|1>}$ . Lines are merely a guide to the eye.

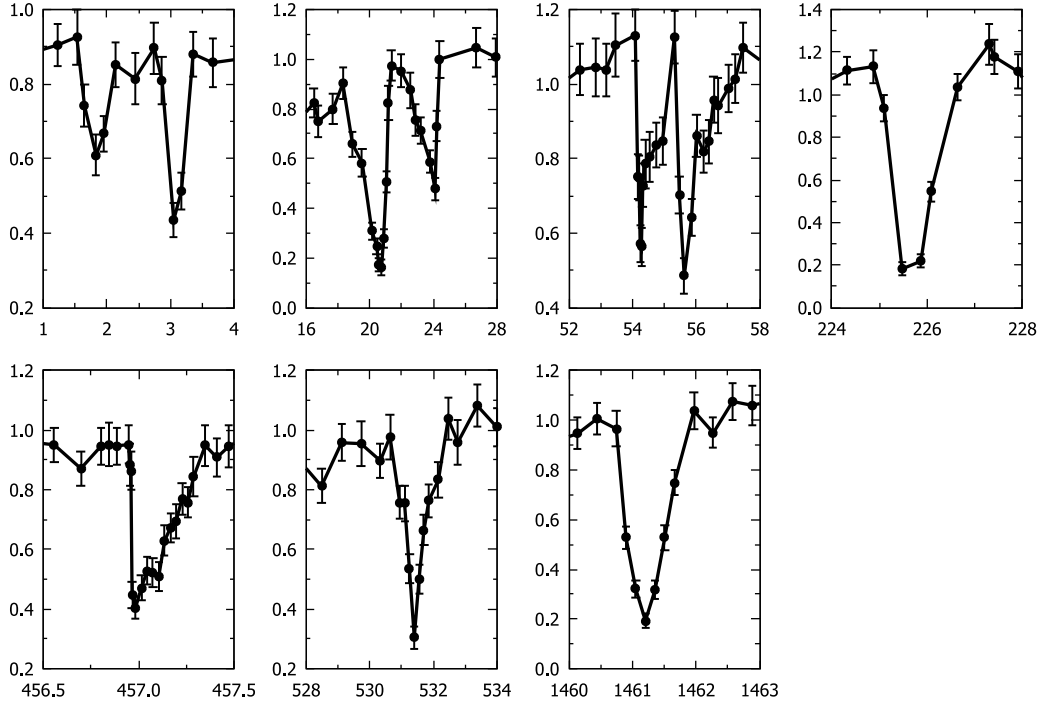


**Table 4.6** – Feshbach resonances in the Li|2>+Cr|1> channel. The positions  $B_0$  are extracted with a model-independent analysis, by looking at the zero-crossing of the signal first derivative. Errors take into account also the magnetic field stability. The widths  $\Delta B_{\text{loss}}$  are the FWHMs of the loss features, extracted directly from the data.

$B_0$ [G]	$\Delta B_{\text{loss}}$ [G]	$B_0$ [G]	$\Delta B_{\text{loss}}$ [G]
$1.8 \pm 0.2$	0.4	$55.6 \pm 0.2$	0.7
$3.1 \pm 0.2$	0.3	$225.7 \pm 0.2$	1.0
$20.8 \pm 0.2$	1.5	$457.0 \pm 0.1$	0.2
$24.1 \pm 0.2$	1.2	$531.1 \pm 0.2$	0.6
$54.3 \pm 0.2$	0.8	$1461.2 \pm 0.4$	0.7

**Li|1>+Cr|2> channel**

Also in the Li|1>+Cr|2> channel, as for the Li|2>+Cr|2> and Li|2>+Cr|1> ones, we investigated the magnetic field region from 0 to 600 G, plus a selected interval around 1420 G, unveiling the presence of 5 FRs. The observed loss features are shown in Fig. 4.7, with their positions and widths reported in Tab. 4.7.

**Figure 4.7** – Heteronuclear Feshbach resonances in the Li|1>+Cr|2> scattering channel. The horizontal axis is the magnetic field  $B$  expressed in G, while the vertical axis is the Cr|2> remaining fraction  $f_{\text{Cr}|2>}$ . Lines are merely a guide to the eye.

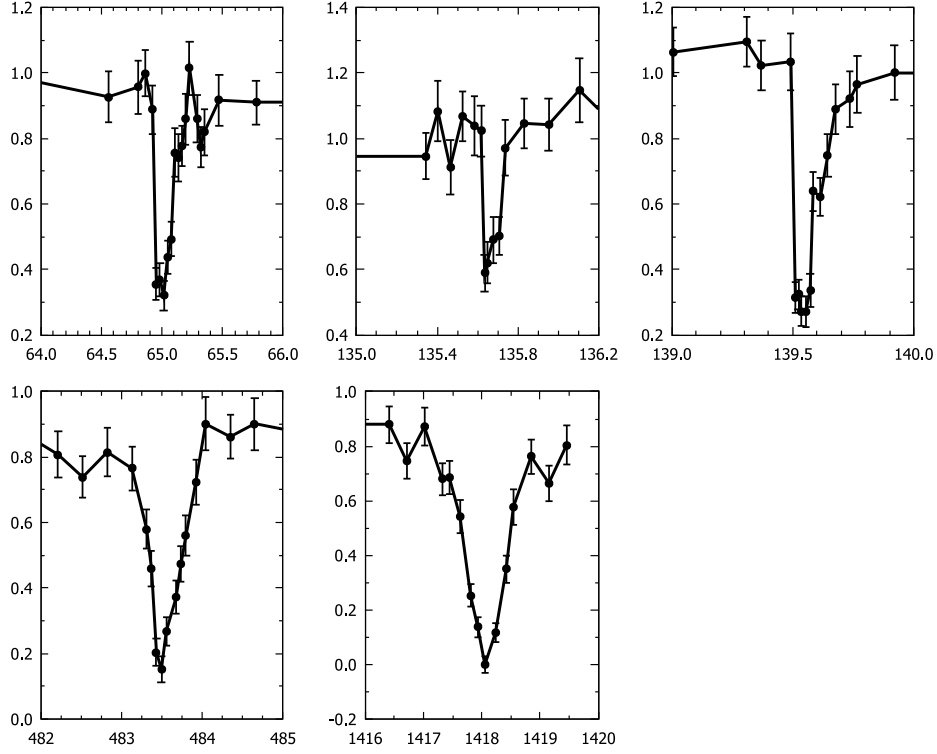


**Table 4.7** – Feshbach resonances in the Li|1>+Cr|2> channel. The positions  $B_0$  are extracted with a model-independent analysis, by looking at the zero-crossing of the signal first derivative. Errors take into account also the magnetic field stability. The widths  $\Delta B_{\text{loss}}$  are the FWHMs of the loss features, extracted directly from the data.

$B_0$ [G]	$\Delta B_{\text{loss}}$ [G]
$65.0 \pm 0.1$	0.16
$135.65 \pm 0.10$	0.10
$139.55 \pm 0.10$	0.12
$483.5 \pm 0.1$	0.45
$1418.1 \pm 0.4$	0.75

**Li|1>+Cr|1> channel**

In the Li|1>+Cr|1> channel, which represents the absolute ground state of our system, we performed Feshbach spectroscopy scans within the magnetic field region from 0 to 1000 G, plus a selected interval around 1415 G. There, we unveiled 5 FRs in total. The observed loss features are shown in Fig. 4.8, with their positions and widths reported in Tab. 4.8.

**Figure 4.8** – Heteronuclear Feshbach resonances in the Li|1>+Cr|1> scattering channel. The horizontal axis is the magnetic field  $B$  expressed in G, while the vertical axis is the Cr|1> remaining fraction  $f_{\text{Cr}|1>}$ . Lines are merely a guide to the eye.

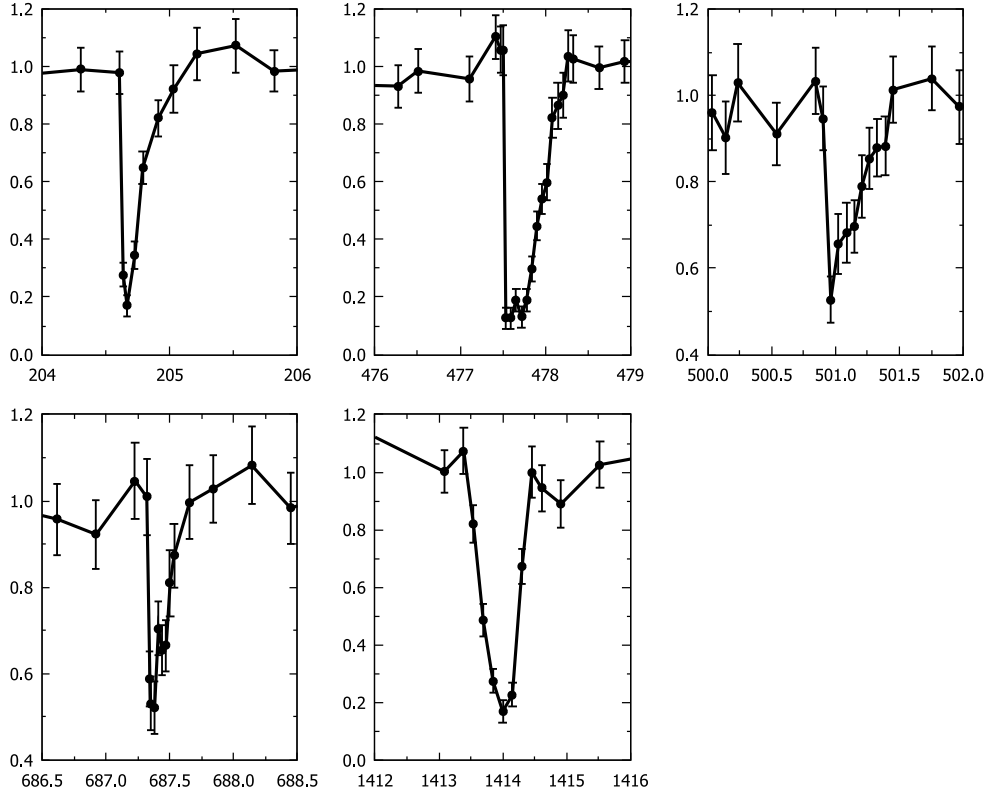


**Table 4.8** – Feshbach resonances in the Li|1>+Cr|1> channel. The positions  $B_0$  are extracted with a model-independent analysis, by looking at the zero-crossing of the signal first derivative. Errors take into account also the magnetic field stability. The widths  $\Delta B_{\text{loss}}$  are the FWHMs of the loss features, extracted directly from the data.

$B_0$ [G]	$\Delta B_{\text{loss}}$ [G]
$204.7 \pm 0.1$	0.15
$477.6 \pm 0.2$	0.5
$501.0 \pm 0.1$	0.25
$687.4 \pm 0.1$	0.17
$1414.0 \pm 0.4$	0.7

## 4.4 Analysing loss data

In this section we present a phenomenological rate-equation model to describe and interpret inelastic losses in our Li-Cr mixtures. The model, combined with lineshape analysis reported in the literature [68, 70], allows us to extract information not only about the position of the resonances, but also about the differential magnetic moments and the loss-rate coefficients, from the experimental data presented in Sec. 4.3.

In order to familiarize with the problem, let us first consider the (simpler) case of single-species experiments, retrieving a few well-known results. In the presence of only one- and two-body losses, we can write a local rate equation describing the time evolution of the atomic density

$$\dot{n}(\vec{r}, t) = -\gamma_1 n(\vec{r}, t) - 2\beta_2 n^2(\vec{r}, t) \quad (4.1)$$

where  $\gamma_1$  and  $\beta_2$  are the overall coefficients characterizing one- and two-body losses, respectively (typically measured in 1/s and cm<sup>3</sup>/s, respectively). For a thermal gas in a cigar-shaped harmonic trap

$$n(\vec{r}, t) = \frac{N(t)}{(2\pi)^{3/2} \sigma_r^2 \sigma_z} \exp\left(-\frac{x^2 + y^2}{2\sigma_r^2} - \frac{z^2}{2\sigma_z^2}\right) \quad (4.2)$$

where  $N$  is the total atom number, while  $\sigma_r$  and  $\sigma_z$  are the radial and axial ( $1/\sqrt{e}$  half-)sizes of the atomic cloud, respectively. The latter two quantities are given by

$$\sigma_r = \sqrt{\frac{k_B T}{m \omega_r^2}} \quad \text{and} \quad \sigma_z = \sqrt{\frac{k_B T}{m \omega_z^2}}, \quad (4.3)$$

with  $\omega_r$  and  $\omega_z$  being the corresponding trapping frequencies. In loss spectroscopy, one typically measures the total number of atoms remained in the trap after a given amount of time ( $t_{\text{hold}}$ ). Accordingly, by integrating Eq. (4.1) over the spatial coordinates, we obtain

$$\dot{N}(t) = -\gamma_1 N(t) - \tilde{\beta}_2 N^2(t) \quad (4.4)$$

with  $\tilde{\beta}_2 = \beta_2 / (4\pi^{3/2} \sigma_r^2 \sigma_z)$ . Given the initial condition  $N(t=0) = N_0$ , the general solution to Eq. (4.4) reads

$$N(t) = -\frac{\gamma_1}{\tilde{\beta}_2} \frac{1}{\left[1 - \left(1 + \frac{\gamma_1}{\tilde{\beta}_2 N_0}\right) e^{\gamma_1 t}\right]} \quad (4.5)$$

If one among the two loss coefficients is negligible, Eq. (4.5) reduces to

$$N(t) = N_0 e^{-\gamma_1 t} \quad (\tilde{\beta}_2 = 0) \quad (4.6a)$$

$$N(t) = \frac{N_0}{1 + \tilde{\beta}_2 N_0 t} \quad (\gamma_1 = 0) \quad (4.6b)$$

In these two simplified cases, information about the non-vanishing loss coefficient can be extracted from

$$\gamma_1 = -\frac{1}{t_{\text{hold}}} \ln(f_0) \quad (\tilde{\beta}_2 = 0) \quad (4.7a)$$

$$\tilde{\beta}_2 = \frac{1}{N_0 t_{\text{hold}}} \left( \frac{1}{f_0} - 1 \right) \quad (\gamma_1 = 0) \quad (4.7b)$$

where  $f_0 = N(t_{\text{hold}})/N_0$  is the remaining fraction of atoms. In the general case, (at least) two independent measurements are often required to determine  $\gamma_1$  and  $\beta_2$ . In particular, in single-species experiments, the one-body loss rate  $\gamma_1$  does not vary with the magnetic field, as it is essentially determined by background-gas collisions. On the other hand, the two-body loss coefficient  $\beta_2$  is sensitive to the value of the scattering amplitude, and it is thus strongly enhanced near a Feshbach resonance. For instance, in a situation in which  $\gamma_1 = \text{const} \neq 0$  and  $\beta_2 = \beta_2(B)$ , with a negligible off-resonant value  $\beta_2^{\text{off}} \simeq 0$ , information about the two loss coefficients can be obtained in two steps. First, far from any FR, one measures the lifetime of the sample, which provides knowledge of  $\gamma_1$ . Then, from Eq. (4.5), defining the rescaled remaining fraction  $\tilde{f} = N(t_{\text{hold}})/(N_0 e^{-\gamma_1 t_{\text{hold}}})$  (i.e. relatively to the background level), information about  $\tilde{\beta}_2$  is acquired from

$$\tilde{\beta}_2 = \frac{1}{N_0 t_{\text{hold}}} \left[ \frac{\gamma_1 t_{\text{hold}}}{1 - e^{-\gamma_1 t_{\text{hold}}}} \right] \left( \frac{1}{\tilde{f}} - 1 \right) \quad (4.8)$$

to be compared with Eq. (4.7b), with the factor inside square brackets taking into account the finite background lifetime of the sample.

#### 4.4.1 Two-body losses in ultracold Li-Cr mixtures

We now turn to the analysis of two-body losses in our heteronuclear Li-Cr mixtures. On the lines of the treatment in Ref. [69], we consider the two coupled equations

$$\dot{n}_{\text{Cr}}(\vec{r}, t) = -\gamma_{\text{bg}} n_{\text{Cr}}(\vec{r}, t) - K_2^{\text{LC}} n_{\text{Li}}(\vec{r}, t) n_{\text{Cr}}(\vec{r}, t) \quad (4.9a)$$

$$\dot{n}_{\text{Li}}(\vec{r}, t) = -\gamma_{\text{bg}} n_{\text{Li}}(\vec{r}, t) - K_2^{\text{LC}} n_{\text{Li}}(\vec{r}, t) n_{\text{Cr}}(\vec{r}, t) \quad (4.9b)$$

where  $\gamma_{\text{bg}}$  and  $K_2^{\text{LC}}$  are the loss rates due to (one-body) background-gas collisions, and inelastic two-body Li-Cr collisions, respectively.  $\gamma_{\text{bg}}$  is assumed to be the same for the two species, which is a fairly good approximation in our experiments. Further, since  $N_{\text{Li}} \sim 10 N_{\text{Cr}}$  (and  $n_{0,\text{Li}} \sim 50 n_{0,\text{Cr}}$ , see Tab. 4.1), we neglect the effect of Li-Cr lossy collisions on the lithium atom number, i.e. the second term on the r.h.s. of Eq. (4.9b). Under these assumptions, the solution of Eq. (4.9b) is simply  $n_{\text{Li}}(\vec{r}, t) = n_{\text{Li}}^{(0)}(\vec{r}) \cdot e^{-\gamma_{\text{bg}} t}$ , with  $n_{\text{Li}}^{(0)}(\vec{r})$  being the initial density profile of the lithium cloud. If we consider gaussian density distributions as in Eq. (4.2), integrating Eq. (4.9a) over the spatial coordinates yields

$$\dot{N}_{\text{Cr}}(t) = -\gamma_{\text{bg}} N_{\text{Cr}}(t) - (q_{\text{LC}} n_{0,\text{Li}} K_2^{\text{LC}}) e^{-\gamma_{\text{bg}} t} N_{\text{Cr}}(t) \quad (4.10a)$$

where  $n_{0,\text{Li}}$  is the initial peak density of Li, and

$$q_{\text{LC}} = \left( 1 + \frac{\sigma_{r,\text{Cr}}^2}{\sigma_{r,\text{Li}}^2} \right)^{-1} \cdot \left( 1 + \frac{\sigma_{z,\text{Cr}}^2}{\sigma_{z,\text{Li}}^2} \right)^{-1/2} \quad (4.10b)$$

is a density-density overlap factor. By defining the rescaled atom number  $N_{\text{Cr}}(t) = \tilde{N}_{\text{Cr}}(t) \cdot e^{-\gamma_{\text{bg}} t}$ , Eq. (4.10a) can be conveniently recast as

$$\dot{\tilde{N}}_{\text{Cr}}(t) = - (q_{\text{LC}} n_{0,\text{Li}} K_2^{\text{LC}}) e^{-\gamma_{\text{bg}} t} \tilde{N}_{\text{Cr}}(t) \quad (4.11a)$$

which can be readily integrated, yielding

$$\tilde{N}_{\text{Cr}}(t) = N_{0,\text{Cr}} \cdot \exp \left[ - \frac{q_{\text{LC}} n_{0,\text{Li}} K_2^{\text{LC}}}{\gamma_{\text{bg}}} (1 - e^{-\gamma_{\text{bg}} t}) \right] \quad (4.11b)$$

hence

$$N_{\text{Cr}}(t) = N_{0,\text{Cr}} \cdot \exp \left[ - \frac{q_{\text{LC}} n_{0,\text{Li}} K_2^{\text{LC}}}{\gamma_{\text{bg}}} (1 - e^{-\gamma_{\text{bg}} t}) \right] \cdot e^{-\gamma_{\text{bg}} t} \quad (4.11c)$$

In our experiments, we measure the remaining fraction of Cr atoms (with respect to the background level) after a given hold time  $t_{\text{hold}}$ , namely

$$f_{\text{Cr}} = \frac{N_{\text{Cr}}(t_{\text{hold}})}{N_{0,\text{Cr}} \cdot e^{-\gamma_{\text{bg}} t_{\text{hold}}}} \quad (4.12)$$

Hence, if  $\gamma_{\text{bg}}$  is known, information about the  $K_2^{\text{LC}}$  coefficient can be extracted from our loss measurements through

$$K_2^{\text{LC}} = - \frac{1}{n_{0,\text{Li}} t_{\text{hold}}} \left[ \frac{\gamma_{\text{bg}} t_{\text{hold}}}{q_{\text{LC}} (1 - e^{-\gamma_{\text{bg}} t_{\text{hold}}})} \right] \cdot \ln (f_{\text{Cr}}) \quad (4.13)$$

where the factor inside square brackets takes into account the finite (background) lifetime of the sample and the density-density overlap. Given our typical experimental conditions ( $t_{\text{hold}} = 2\text{--}4$  s,  $\gamma_{\text{bg}} \simeq 0.1$  s<sup>-1</sup>, and  $1/\sqrt{e}$  half-widths as reported in Tab. 4.1), this factor is roughly on the order of 10.

For a fixed hold time, the behaviour of  $K_2^{\text{LC}}$ , as a function of the magnetic field near a Feshbach resonance, can be described by analogy with photoassociation lineshapes [68]. Assuming that ( $N > 2$ )-body losses are negligible, and that one deals with narrow resonances with energy width  $\gamma_E \rightarrow 0$ , following the discussion in Ref. [68], the lineshape of the (thermally-averaged) two-body loss coefficient  $K_2(\text{B})$  reads

$$K_2(\text{B}) \simeq A_2 \cdot \left[ \frac{e}{(\ell + 1/2)} \frac{\delta\mu (\text{B} - \text{B}_0)}{k_{\text{B}} T} \right]^{\ell+1/2} \cdot \exp \left( - \frac{\delta\mu (\text{B} - \text{B}_0)}{k_{\text{B}} T} \right) \quad (4.14a)$$

where  $A_2$  is a constant (with appropriate units, e.g. cm<sup>3</sup>/s),  $\text{B}_0$  is the resonance position,  $\ell$  is the orbital angular momentum of the entrance channel, and  $\delta\mu$  is the differential magnetic moment between the two colliding atoms and the molecular state associated with the FR. This function is peaked at a field

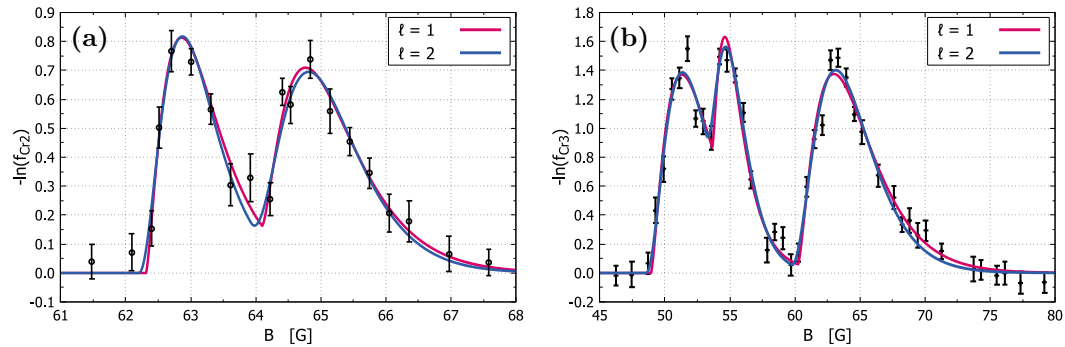
$$\text{B}_{\text{pk}} = \text{B}_0 + \frac{k_{\text{B}} T}{\delta\mu} (\ell + 1/2) \quad (4.14b)$$

where it reaches its maximum value  $K_2(\text{B}_{\text{pk}}) = A_2$ . Note that  $\delta\mu$  can be either positive or negative. Further, it is assumed that  $K_2(\text{B}) = 0$  when  $\delta\mu \cdot (\text{B} - \text{B}_0) < 0$ , i.e. on the ‘‘BEC’’ side of the resonance.

**Table 4.9** – Fit results using photoassociation lineshapes, and comparison with CCC and ABM predictions. Regarding the fit results,  $\delta\mu_{(i)}$  is the differential magnetic moment obtained for  $\ell = i$  (blank spaces denote a poor fit result), while  $B_0$  is the average over different  $\ell$  values. Numbers in parentheses are the uncertainties of the last digit(s).

Channel	Fit					CCC			ABM		
	$B_0$ [G]	$\delta\mu_{(0)}$ [ $\mu_B$ ]	$\delta\mu_{(1)}$ [ $\mu_B$ ]	$\delta\mu_{(2)}$ [ $\mu_B$ ]	$K_2^{\max}$ [ $\text{cm}^3/\text{s}$ ]	$B_0$ [G]	$\ell$	$m_\ell$	$B_0$ [G]	$\ell$	$\delta\mu$ [ $\mu_B$ ]
Li 2>+Cr 3}	0.9(1)		-1.8(4)	-2.1(4)	$1.0(5) \times 10^{-12}$						
	2.0(1)		-0.7(2)	-1.0(2)	$1.0(5) \times 10^{-12}$						
	13.6(4)		-0.20(5)	-0.25(6)	$1.7(5) \times 10^{-12}$						
	22.3(5)		-0.12(6)	-0.16(7)	$1.8(5) \times 10^{-12}$						
	31.4(1)	0.8(2)	1.3(2)	1.5(2)	$7(1) \times 10^{-13}$						
	48.7(4)		0.09(2)	0.13(3)	$1.4(4) \times 10^{-12}$						
	53.4(6)		0.18(4)	0.21(4)	$1.0(5) \times 10^{-12}$						
	59.9(7)		0.08(1)	0.10(1)	$1.3(4) \times 10^{-12}$						
	105.7(1)	2.1(2)	3.3(3)	4.3(4)	$2.5(5) \times 10^{-12}$				94		3.2
	200.7(1)	1.6(4)	1.9(3)	2.4(3)	$3(1) \times 10^{-12}$				189		3.1
	222.0(2)	1.3(5)	1.4(3)	1.8(4)	$1.4(6) \times 10^{-12}$	222.8	0	0	227	1	1.5
	267.9(3)	1.8(4)	2.7(5)	3.1(6)	$4(2) \times 10^{-12}$				288	2	3.5
Li 2)+Cr 2}	1.0(1)		-1.0(3)	-1.2(3)	$4(2) \times 10^{-13}$						
	2.4(1)		-0.5(1)	-0.7(1)	$1.0(5) \times 10^{-12}$						
	13.1(5)		-0.7(3)	-0.6(2)	$2(1) \times 10^{-12}$	12.8	1	0			
	17.0(2)		-0.2(1)	-0.3(1)	$2(1) \times 10^{-12}$	13.9	1	1			
	22.2(5)		-0.3(1)	-0.4(1)	$1.3(6) \times 10^{-12}$	22.9	1	-1			
	62.3(1)		0.4(1)	0.6(1)	$4(2) \times 10^{-13}$	62.2	1	-1			
	63.6(4)		0.3(1)	0.3(1)	$4(2) \times 10^{-13}$	64.9	1	1			
	80.3(4)		0.3(1)	0.4(1)	$1.5(5) \times 10^{-12}$	83.2	1	0			
	167.6(2)	2.1(5)	2.7(4)	2.9(4)	$> 3 \times 10^{-12}$	168.6	0	0	156	0	3.0
	244.1(2)	2.3(4)	3.0(4)	3.9(3)	$> 3 \times 10^{-12}$				252	2	3.6
	361.9(1)	2.2(4)	3.8(4)	5.1(5)	$1.7(6) \times 10^{-12}$	363.2	0	0	343	0	1.9
	437.8(3)	1.1(2)	1.5(3)	1.7(3)	$8(2) \times 10^{-13}$				419	0	1.9
	455.8(2)	1.4(3)	2.0(4)	2.3(6)	$5(3) \times 10^{-13}$						
	469.4(1)	1.5(2)	2.4(4)	3.3(6)	$4(1) \times 10^{-13}$						
535.2(3)	0.9(2)	1.1(2)	1.4(2)	$1.1(4) \times 10^{-12}$	535.7	0	0	524	2	1.7	
Li 2)+Cr 1}	2.1(2)		-0.4(2)	-0.5(2)	$6(3) \times 10^{-14}$						
	3.3(3)		-0.5(2)	-0.7(3)	$1.0(5) \times 10^{-13}$						
	21.3(2)		-0.4(1)	-0.5(1)	$1.2(4) \times 10^{-12}$	20.3	1	1			
	24.5(2)		-0.4(2)	-0.5(3)	$5(3) \times 10^{-13}$	25.1	1	-1			
	54.1(2)		1.1(3)	1.9(5)	$3(1) \times 10^{-13}$	54.1	1	-1			
	55.4(2)		0.9(3)	1.2(4)	$5(2) \times 10^{-13}$	56.0	1	1			
	225.4(3)	0.8(2)	1.1(3)	1.2(3)	$2(1) \times 10^{-12}$						
	456.9(2)	1.4(3)	2.3(4)	2.7(5)	$6(2) \times 10^{-13}$	457.3	0	0			
	531.1(3)	0.8(2)	0.7(3)	1.1(3)	$6(4) \times 10^{-12}$				520	2	1.8
Li 1)+Cr 2}	64.9(1)	1.7(3)	2.9(4)	3.6(5)	$6(1) \times 10^{-13}$	66.0	0	0	51	0	2.2
	135.6(1)	3(1)	6(2)	8(2)	$3.0(7) \times 10^{-13}$				126	0	2.7
	139.5(2)	3.1(6)	5.0(7)	7(2)	$7(1) \times 10^{-13}$						
	483.3(3)	0.8(2)	1.1(3)	1.5(3)	$1.4(9) \times 10^{-11}$				409	2	2.0

**Figure 4.9** – Examples of fits with photoassociation lineshapes, for different  $\ell$  values: (a) Li|2)+Cr|2} channel, doublet feature around 65 G, and (b) Li|2)+Cr|3} channel, triplet structure around 50 ÷ 70 G.



In the scattering channels where two-body losses are allowed, i.e. in all but  $\text{Li}|1\rangle+\text{Cr}|1\rangle$ , and, in particular, in the magnetic field regions where one expects strong spin-exchange and spin-spin induced trap losses ( $B \lesssim 1000$  G), we fit the observed loss features with the model described above. In practice, taking  $T = 10$   $\mu\text{K}$  and trying different  $\ell$  values ( $\ell = 0, 1, 2$  – kept fixed during the procedure), we fit  $-\ln(f_{\text{Cr}}(B))$  obtained from our data with Eq. (4.14a). The free parameters are  $B_0$ ,  $\delta\mu$ , and  $A_{\text{fit}}$ , a dimensionless constant that plays the role of  $A_2$ . Then, from Eq. (4.13), taking  $\max[-\ln(f_{\text{Cr}})] = A_{\text{fit}}$ , we estimate the  $K_2^{\text{LC}}$  coefficient at the loss peak. The complete results of this analysis are reported in Tab. 4.9, together with theoretical predictions based either on CCC or on the ABM, whereas two fit examples are shown in Fig. 4.9. Concerning the positions  $B_0$ , the agreement between the experimental data and the CCC results (for the FRs included in the calculations so far, i.e. those listed in the table) is quite satisfactory. At small fields, some discrepancies may arise from higher-order terms in the interaction hamiltonian, such as second order spin-orbit and spin-rotation couplings, not included in the computations yet [73]. Besides, in general, slight mismatches could also be due to experimental errors in the magnetic field calibration and/or in the determination of the temperature. Further, although at the present stage of development the experiment-theory comparison is uniquely focused on the resonances positions  $B_0$ , the best-fitted  $\delta\mu$  values, possibly extracted from (future) targeted measurements, could provide additional useful information for the theoretical models.

#### 4.4.2 Three-body losses in ultracold Li-Cr mixtures

On the basis of the rate-equation model presented in Sec. 4.4.1, we carry out a similar analysis also for three-body processes. In particular, we are mainly interested in the case of  $\text{Li}|1\rangle\text{-Cr}|1\rangle$  mixtures, where two-body losses are entirely absent. Hence, we can write the two coupled equations

$$\dot{n}_{\text{Cr}} = -\gamma_{\text{bg}} n_{\text{Cr}} - K_3^{\text{LLC}} n_{\text{Li}}^2 n_{\text{Cr}} - 2 K_3^{\text{CCL}} n_{\text{Li}} n_{\text{Cr}}^2 \quad (4.15a)$$

$$\dot{n}_{\text{Li}} = -\gamma_{\text{bg}} n_{\text{Li}} - 2 K_3^{\text{LLC}} n_{\text{Li}}^2 n_{\text{Cr}} - K_3^{\text{CCL}} n_{\text{Li}} n_{\text{Cr}}^2 \quad (4.15b)$$

where we omitted the radial and temporal dependence of the density profiles to simplify the notation. In Eqs. (4.15),  $K_3^{\text{LLC}}$  and  $K_3^{\text{CCL}}$  are the three-body inelastic loss rates for Li-Li-Cr and Cr-Cr-Li processes, respectively. Similarly to the treatment for two-body losses, under the condition  $N_{\text{Li}} \gg N_{\text{Cr}}$ , we neglect the last two terms on the r.h.s. of Eq. (4.15b), retrieving the simple exponential decay  $n_{\text{Li}}(\vec{r}, t) = n_{\text{Li}}^{(0)}(\vec{r}) e^{-\gamma_{\text{bg}} t}$ . Inserting this solution into Eq. (4.15a) and integrating over the spatial coordinates, assuming again gaussian density profiles, we find

$$\begin{aligned} \dot{N}_{\text{Cr}}(t) = & -\gamma_{\text{bg}} N_{\text{Cr}}(t) - (q_{\text{LLC}} n_{0,\text{Li}}^2 K_3^{\text{LLC}}) e^{-2\gamma_{\text{bg}} t} N_{\text{Cr}}(t) \\ & - 2 (q_{\text{CCL}} n_{0,\text{Li}} K_3^{\text{CCL}}) e^{-\gamma_{\text{bg}} t} N_{\text{Cr}}^2(t) \end{aligned} \quad (4.16)$$

where

$$q_{\text{LLC}} = \left(1 + \frac{2\sigma_{r,\text{Cr}}^2}{\sigma_{r,\text{Li}}^2}\right)^{-1} \cdot \left(1 + \frac{2\sigma_{z,\text{Cr}}^2}{\sigma_{z,\text{Li}}^2}\right)^{-1/2} \quad (4.17a)$$

$$q_{\text{CCL}} = \frac{1}{8\pi^{3/2} \sigma_{r,\text{Cr}}^2 \sigma_{z,\text{Cr}}} \left(1 + \frac{\sigma_{r,\text{Cr}}^2}{2\sigma_{r,\text{Li}}^2}\right)^{-1} \cdot \left(1 + \frac{\sigma_{z,\text{Cr}}^2}{2\sigma_{z,\text{Li}}^2}\right)^{-1/2} \quad (4.17b)$$

are the two density-(squared-)density overlap factors. Eq. (4.16) is simplified if expressed in terms of the rescaled atom number  $\tilde{N}_{\text{Cr}}(t)$ :

$$\dot{\tilde{N}}_{\text{Cr}}(t) = -e^{-2\gamma_{\text{bg}}t} \left[ (q_{\text{LLC}} n_{0,\text{Li}}^2 K_3^{\text{LLC}}) \tilde{N}_{\text{Cr}}(t) + 2 (q_{\text{CCL}} n_{0,\text{Li}} K_3^{\text{CCL}}) \tilde{N}_{\text{Cr}}^2(t) \right] \quad (4.18)$$

Further, if Li-Li-Cr processes dominate, i.e. if we can neglect the other contribution, we have, in analogy to Eq. (4.11c)

$$N_{\text{Cr}}(t) = N_{0,\text{Cr}} \cdot \exp \left[ -\frac{q_{\text{LLC}} n_{0,\text{Li}}^2 K_3^{\text{LLC}}}{2\gamma_{\text{bg}}} (1 - e^{-2\gamma_{\text{bg}}t}) \right] \cdot e^{-\gamma_{\text{bg}}t} \quad (4.19a)$$

from which

$$K_3^{\text{LLC}} = -\frac{1}{n_{0,\text{Li}}^2 t_{\text{hold}}} \left[ \frac{2\gamma_{\text{bg}} t_{\text{hold}}}{q_{\text{LLC}} (1 - e^{-2\gamma_{\text{bg}}t_{\text{hold}}})} \right] \cdot \ln(f_{\text{Cr}}) \quad (4.19b)$$

with  $f_{\text{Cr}}$  defined as in Eq. (4.12). On the other hand, in the presence of Cr-Cr-Li-type processes only, by integrating Eq. (4.18) one finds

$$N_{\text{Cr}}(t) = \frac{N_{0,\text{Cr}} e^{-\gamma_{\text{bg}}t}}{1 + N_{0,\text{Cr}} q_{\text{CCL}} n_{0,\text{Li}} \gamma_{\text{bg}}^{-1} K_3^{\text{CCL}} (1 - e^{-2\gamma_{\text{bg}}t})} \quad (4.20a)$$

with

$$K_3^{\text{CCL}} = \frac{1}{2 N_{0,\text{Cr}} n_{0,\text{Li}} t_{\text{hold}}} \left[ \frac{2\gamma_{\text{bg}} t_{\text{hold}}}{q_{\text{CCL}} (1 - e^{-2\gamma_{\text{bg}}t_{\text{hold}}})} \right] \cdot \left( \frac{1}{f_{\text{Cr}}} - 1 \right) \quad (4.20b)$$

Finally, partially resembling Eq. (4.5), the general solution of Eq. (4.18), expressed directly in terms of  $N_{\text{Cr}}(t)$ , reads

$$N_{\text{Cr}}(t) = -\tilde{\alpha}_3 \frac{N_{0,\text{Cr}} e^{-\gamma_{\text{bg}}t}}{[1 - (1 + \tilde{\alpha}_3) e^{\tilde{x}_3(t)}]} \quad (4.21a)$$

where

$$\tilde{\alpha}_3 = \frac{q_{\text{LLC}} n_{0,\text{Li}} K_3^{\text{LLC}}}{2 q_{\text{CCL}} N_{0,\text{Cr}} K_3^{\text{CCL}}} \quad \text{and} \quad \tilde{x}_3(t) = \frac{q_{\text{LLC}} n_{0,\text{Li}}^2 K_3^{\text{LLC}}}{2\gamma_{\text{bg}}} (1 - e^{-2\gamma_{\text{bg}}t}) \quad (4.21b)$$

Thus, in terms of the rescaled remaining fraction

$$\left( \frac{1}{f_{\text{Cr}}} - 1 \right) = \left( e^{\tilde{x}_3^{\text{h}}} - 1 \right) \cdot (1 + \tilde{\alpha}_3^{-1}) \quad (4.22)$$

with  $\tilde{x}_3^{\text{h}} = \tilde{x}_3(t_{\text{hold}})$ . In this form, Eq. (4.22) straightforwardly reduces to Eqs. (4.19b) and (4.20b) when  $K_3^{\text{CCL}} = 0$  and  $K_3^{\text{LLC}} = 0$ , respectively.

Our solutions for  $N_{\text{Cr}}(t)$ , namely Eqs. (4.19a), (4.20a), and (4.21a), are more easily understood in the limit of  $\gamma_{\text{bg}} \rightarrow 0$ . Indeed, in this case, they respectively simplify to

$$N_{\text{Cr}}(t) = N_{0,\text{Cr}} \cdot e^{-\gamma_{\text{eff}} \cdot t} \quad (\text{Li-Li-Cr}) \quad (4.23a)$$

$$N_{\text{Cr}}(t) = \frac{N_{0,\text{Cr}}}{1 + \beta_{\text{eff}} N_{0,\text{Cr}} \cdot t} \quad (\text{Cr-Cr-Li}) \quad (4.23b)$$

$$N_{\text{Cr}}(t) = -\frac{\gamma_{\text{eff}}}{\beta_{\text{eff}}} \frac{1}{1 - \left(1 + \frac{\gamma_{\text{eff}}}{\beta_{\text{eff}} N_{0,\text{Cr}}}\right) e^{\gamma_{\text{eff}} t}} \quad (\text{both}) \quad (4.23c)$$

with  $\gamma_{\text{eff}} = q_{\text{LLC}} n_{0,\text{Li}}^2 K_3^{\text{LLC}}$  and  $\beta_{\text{eff}} = 2 q_{\text{CCL}} n_{0,\text{Li}} K_3^{\text{CCL}}$  playing the role of effective one- and two-body loss coefficients, respectively (see again Eqs. (4.5) and (4.6)). Hence, the essential point is that, relatively to the Cr atom number, Li-Li-Cr recombination processes resemble one-particle losses, whereas Cr-Cr-Li-type losses feature a two-body-like behaviour. Given our experimental conditions (i.e.  $N_{\text{Li}} \gg N_{\text{Cr}}$ ), we expect the former processes to be more likely.

The experimental loss spectra dominated by three-body processes can be further analysed by following the theoretical model developed in Ref. [70], that describes three-body recombination in a thermal gas near a (infinitely) narrow Feshbach resonance. The latter is simply treated as a bound molecular state, at energy  $E_{\text{mol}}(\text{B}) = \delta\mu (\text{B} - \text{B}_0)$  that, for  $E_{\text{mol}}(\text{B}) > 0$  (i.e.  $\text{B} > \text{B}_0$  if  $\delta\mu > 0$ ), is weakly coupled to a continuum of scattering states, thermally-populated at positive energies. In this framework, three-body recombination events are regarded as being originated from a two-step, pairwise process [70]: Two colliding atoms at a given energy  $E > 0$  can first turn into a (virtual) closed-channel molecule, located at the same (positive) energy. Such a virtual molecule can then decay towards deeply-bound molecular levels, by further colliding with a third particle, releasing an energy greatly exceeding the trap depth of the confining potential, thereby leading to an overall atom loss. Based on such a physical picture, that follows a quantum Langevin model for reactions [71, 72] and exploits the properties of van der Waals atom-dimer interaction potential, one expects a magnetic-field dependence of the three-body recombination rate coefficient that reads<sup>2</sup>

$$K_3(\text{B}) = (2\ell + 1) K_3^{\text{pole}} \cdot \exp\left(-\frac{\delta\mu (\text{B} - \text{B}_0)}{k_{\text{B}}T}\right) \quad (4.24)$$

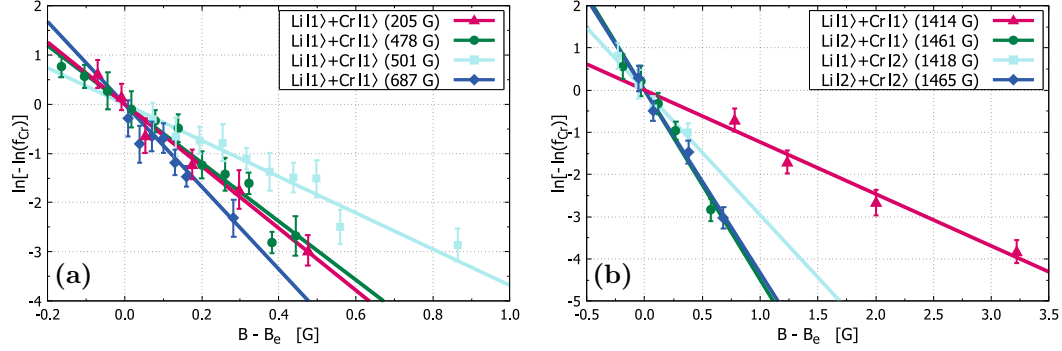
Here,  $\ell$  is the partial wave characterizing the FR,  $\delta\mu$  is the differential magnetic moment of the Feshbach dimer, and  $T$  is the temperature of the atomic gas. Further,  $K_3^{\text{pole}}(T)$  is a (temperature-dependent) maximum recombination rate, that is reached at the resonance pole ( $\text{B} = \text{B}_0$ ), and that depends upon the rate scale for atom-dimer interaction, evaluated in Ref. [70] within a van der Waals potential.

The above result is similar, though not identical, to the trend of Eq. (4.14a) for two-body inelastic processes: First, within this framework, three-body losses take place only on the ‘‘BCS’’ side of the resonance, where closed-channel molecules lay above the atomic threshold. Second, the magnetic-field dependence of  $K_3(\text{B})$  is characterized by an exponential tail that solely depends upon  $\delta\mu$  and the gas temperature. However, differently from Eq. (4.14a), the partial-wave order of the Feshbach resonance enters the above three-body rate coefficient only via a  $(2\ell + 1)$  multiplicative constant, thereby not affecting the functional form of  $K_3$ .

Therefore, as for the case of two-body losses, the analysis of three-body loss spectra may yield information about the differential magnetic moment of the molecular state that causes the resonance, which can serve as a further, relevant experimental input for theoretical models. In practice, under the assumption of dealing with FRs with narrow character, and in the experimentally relevant regime  $N_{\text{Li}} \gg N_{\text{Cr}}$ , i.e. considering Li-Li-Cr processes only, by inserting Eq. (4.24) into Eq. (4.19a) (in

<sup>2</sup>We refer the interested reader to Ref. [70] for details on the derivation of the results.

**Figure 4.10** – Examples of fits with Ref. [70] model: (a) Li|1⟩+Cr|1⟩ channel, below 1000 G, and (b) family of resonances around 1420 ÷ 1460 G. Results are plotted against  $B - B_{1/e}$  to ease the comparison.



place of  $K_3^{\text{LLC}}$ ), we obtain

$$f_{\text{Cr}}(B) = \exp \left[ - \frac{q_{\text{LLC}} n_{0,\text{Li}}^2 (1 - e^{-2\gamma_{\text{bg}} t_{\text{hold}}})}{2\gamma_{\text{bg}}} \cdot (2\ell + 1) K_3^{\text{pole}} e^{-\frac{\delta\mu(B-B_0)}{k_{\text{B}}T}} \right] \quad (4.25)$$

having defined the (rescaled) remaining fraction  $f_{\text{Cr}}$  as in Eq. (4.12). Therefore, at  $B = B_0$ , the quantity  $K_{3,\ell}^{\text{pole}} = (2\ell + 1) K_3^{\text{pole}}$  is given by Eq. (4.19b). Further, as a function of the magnetic field

$$\begin{aligned} \ln \left[ - \ln \left[ f_{\text{Cr}}(B) \right] \right] &= \ln \left[ - \ln \left[ f_{\text{Cr}}(B_0) \right] \right] - \frac{\delta\mu}{k_{\text{B}}T} (B - B_0) \\ &= - \frac{\delta\mu}{k_{\text{B}}T} (B - B_{1/e}) \end{aligned} \quad (4.26)$$

with  $f_{\text{Cr}}(B_{1/e}) = 1/e$ . Hence, to extract the differential magnetic moments of the Feshbach dimers, we fit  $\ln \left[ - \ln \left[ f_{\text{Cr}} \right] \right]$  obtained from our data with this linear model, on the BCS tail of each loss feature. The results are shown graphically in Fig. 4.10. Knowing the temperature, the fit returns the values of  $\delta\mu$  and  $B_{1/e}$ . Note that, in general, i.e. even for a linear scale fit with Eq. (4.25), it is not possible to obtain

**Table 4.10** – Fit results using Ref. [70] model, and comparison with CCC and ABM predictions. In the second column,  $B_0$  is the value extracted with the first derivative method, see Sec. 4.3, here to be intended merely as a label. Numbers in parentheses are the uncertainties of the last digit(s).

Channel	Fit			Eq. (4.19b)	CCC		ABM		
	$B_0$ [G]	$B_{1/e}$ [G]	$\delta\mu$ [ $\mu_{\text{B}}$ ]	$K_{3,\ell}^{\text{pole}}$ [ $\text{cm}^6/\text{s}$ ]	$B_0$ [G]	$\ell$	$B_0$ [G]	$\ell$	$\delta\mu$ [ $\mu_{\text{B}}$ ]
Li 1⟩+Cr 1⟩	204.7	204.7(1)	0.94(15)	$5(2) \times 10^{-25}$	204.8	$0 \rightarrow 2$	200	2	3.7
	477.6	477.9(2)	0.89(13)	$6(2) \times 10^{-25}$			473	2	1.8
	501.0	500.9(2)	0.55(16)	$2.0(6) \times 10^{-25}$			506	1	3.9
	687.4	687.4(1)	1.3(2)	$2.0(6) \times 10^{-25}$			686.9	0	667
Li 1⟩+Cr 1⟩	1414.0	1413.5(2)	0.18(6)	$6(2) \times 10^{-25}$	1413.7	0	1370	0	2.0
Li 2⟩+Cr 1⟩	1461.2	1461.4(2)	0.67(17)	$6(1) \times 10^{-25}$			1417	0	2.0
Li 1⟩+Cr 2⟩	1418.1	1418.5(3)	0.44(14)	$> 7(3) \times 10^{-25}$			1440	0	2.0
Li 2⟩+Cr 2⟩	1465.4	1465.6(2)	0.65(15)	$6(2) \times 10^{-25}$			1484	0	2.0

separate information about  $B_0$  and  $K_{3,\ell}^{\text{pole}}$  from this model,<sup>3</sup> as the fit algorithm necessarily returns only a combination of the two parameters. Accordingly, with the help of Eq. (4.19b), for each resonance we estimated a lower bound for  $K_{3,\ell}^{\text{pole}}$  using the minimum measured value for  $f_{\text{Cr}}$ . This analysis was carried out for all the FRs in the  $\text{Li}|1\rangle+\text{Cr}|1\rangle$  scattering channel, as well as for the entire family of resonances around 1400 G, where we expect a substantial contribution from three-body losses. The obtained numerical results are reported in Tab. 4.10, together with predictions from the CCC and the ABM. Contrarily to the case of two-body losses (see again Tab. 4.9), we observe here a strong mismatch between the fitted and the predicted  $\delta\mu$  values. While the reasons behind this discrepancy are currently not entirely clear, and thus they will be the subject of upcoming investigations in our lab, such a striking mismatch strongly suggests the fact that (at least) one of the assumptions of Ref. [70] model, namely to deal with ultra-narrow resonances, does not apply to our system. In turn, the fact that the observed FRs are possibly “broad” undoubtedly constitutes a promising starting point for future few- and many-body studies with degenerate Li-Cr mixtures.

## 4.5 Final remarks

In summary, in this chapter of my thesis I reported on the first observation of about 50 heteronuclear Feshbach resonances in novel ultracold Li-Cr mixtures, uniquely available in our lab worldwide. The Li-Cr Feshbach spectrum appears rather rich when compared to alkali-alkali combinations [50, 51, 52, 62], but it is apparently non-chaotic, as starkly opposed to the Feshbach spectra of lanthanide systems, such as Dy-Dy [74], Er-Er [75], Er-Dy [76], and Er-Yb [77], as well as of alkali-lanthanide mixtures [78]. This experimental effort, which constitutes one among the main achievements of my thesis work, represents a fundamental input for a quantum collisional model that is currently being developed by our theory collaborator, Prof. A. Simoni, based on coupled-channel calculations. Although such a theoretical framework still requires some fine adjustment in order to become quantitatively accurate over the whole Feshbach spectrum, based on an optimized fit of the observed *s*-wave FRs only, it currently predicts the values  $a_{5/2} \sim 14 a_0$  and  $a_{7/2} \sim 42 a_0$  for the exaplet and octuplet background scattering lengths, respectively. Based on the present assignment, most of the observed low-field loss features appear connected to *p*-wave FRs, whereas those around 1400 G are interpreted as *s*-wave resonances. Notably, very recent characterizations of the elastic scattering near one of these high-field resonances, not discussed in the present thesis work, confirm its *s*-wave nature, pointing to a magnetic field width  $\Delta B_{\text{exp}} \sim 1 \div 2$  G, thus to a sizeable – though not anomalously large – effective range parameter  $R^* \sim 1000 \div 3000 a_0$ . Further and more accurate investigations are required in the next future to fully characterize these high-field features, but our work already shapes the Li-Cr mixture as an optimally-suited system for the production of ground state bi-polar molecules, as well as for the investigation of the variety of few- and many-body quantum phenomena in mass-imbalanced fermion systems.

<sup>3</sup>Unless some further assumptions are made, e.g. that losses are exactly zeroed on the BEC side of the resonance. This can be included in the model by introducing a Heaviside step function  $\vartheta_{\text{H}}(B - B_0)$  as a multiplier of Eq. (4.24).

## Chapter 5

# Design of a bichromatic high-resolution objective

This chapter describes the design and simulation of a bichromatic high-resolution imaging system for our lithium-chromium mixture, which I carried out as a side project during my initial period in the lab. The objective relies on only six low-cost catalogue lenses, and its achromatic (i.e. blue-red) correction can be adapted to different pairs of wavelengths, making the design potentially appealing also for other ultracold mixtures. First, I briefly contextualize the problem of designing high-resolution objectives for ultracold atom experiments, explaining why the majority of state-of-the-art systems reported in the literature are not suitable for our specific case, nor for many other experiments involving ultracold mixtures of different atomic species. In this introduction, I also list the challenging target specifications that our imaging system should reach, as well as the various constraints imposed by our experimental setup.

The mathematical frameworks behind geometric and wave optics, the theory of aberrations, and image formation are extensively reported in many textbooks, see e.g. Refs. [79, 80, 81, 82, 84, 86, 87]. A detailed review of the subject is well beyond the scope of this chapter. However, to evaluate and characterize the performances of an imaging system, several specific figures of merit play a fundamental role. The most relevant ones are summarized in Sec. 5.1.

In Sec. 5.2, I briefly describe the basic concepts of longitudinal chromatic aberrations and color correction. A simplistic thin-lens model is used to derive the well-known *achromatic condition* for the realization of cemented achromats, while the case of air-spaced doublets is treated more carefully.

In Sec. 5.3, I outline the general methods and procedures that I followed during the entire design process. I also report the main settings employed for the optical simulations with the ray-tracing software OSLO.

Lastly, in Sec. 5.4, I present the most promising objective designs that were found with the simulations, reporting in detail their specifications and figures of merit.

Several future investigations with degenerate Li-Cr mixtures will benefit from an imaging system with a high spatial resolution. Unfortunately, commercially available systems often do not meet the requirements of modern ultracold atom experiments, and custom designs commissioned to specialized companies are generally quite expensive. Nonetheless, the task of designing a so-called *quantum gas microscope* is, to some extent, easier than designing usual microscopes, as the number of different

wavelengths employed to probe the atomic sample is rather low, in most cases only one. Indeed, several examples of “home-made” monochromatic high-resolution objectives for quantum gases exist in the literature [92, 93, 94, 95, 96, 97]. Many of these systems rely on a small number of catalogue lenses, making their realization considerably cheaper than commercial, custom-made solutions. Furthermore, most of them can be easily adapted to work with a wavelength different from the design one, by merely adjusting the air spacings between the single elements. However, none of them can provide an effective color-correction, i.e. simultaneous operation with more than one wavelength (unless they are relatively close in the spectrum [94]), as the various lenses are all realized with the same optical glass.

Given this framework, the question arose in the lab whether a similar “home-made” optical system could be realized for our mixture. The answer is not straightforward, as the two imaging wavelengths ( $\lambda_{\text{Li}} = 671 \text{ nm}$  and  $\lambda_{\text{Cr}} = 425.5 \text{ nm}$ , respectively) lie quite far apart in the visible spectrum. Moreover, several constraints and requirements have to be satisfied, thus making the design process rather challenging:

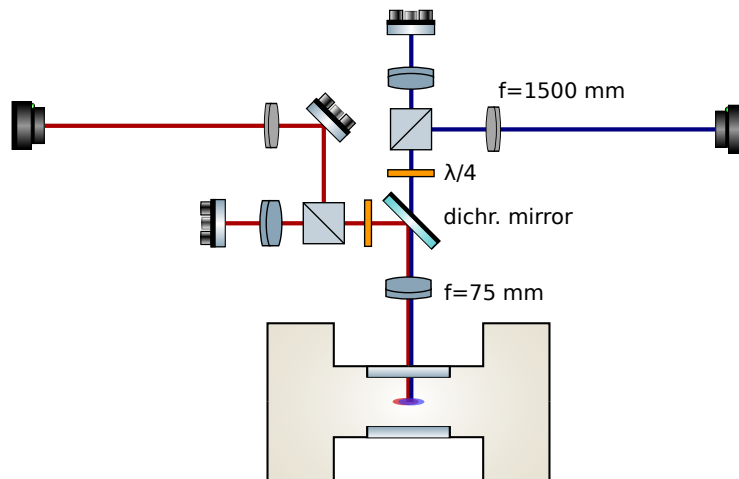
- The final spatial resolution should be on the order of, or possibly below,  $1 \mu\text{m}$ . As discussed in the following, this requires operation at a sizeable numerical aperture (NA) of  $0.3 \div 0.4$ .
- The entire size of a typical *in-situ* ultracold/degenerate atomic cloud should be at focus. Accordingly, the diffraction-limited field of view (better defined later) should be on the order of  $\pm (150 \div 200) \mu\text{m}$ .
- The system must operate at a relatively large working distance (WD) of roughly  $30 \div 35 \text{ mm}$ , due to geometrical constraints of our vacuum cell. This, combined with the requirement on NA, implies necessarily the use of large (i.e. 2”-diameter) optics.
- To achieve the desired performances, the objective must be corrected for image aberrations. The main contributions arise from the large numerical aperture, and from the 8 mm-thick silica window of the vacuum cell, through which the imaging light passes before entering the objective.
- Further, the system must also be corrected for the axial chromatic focal shift (i.e. longitudinal chromatic aberration, or longitudinal color), with respect to Li and Cr imaging wavelengths ( $\lambda_{\text{Li}} = 671 \text{ nm}$  and  $\lambda_{\text{Cr}} = 425.5 \text{ nm}$ , respectively), in order to provide a simultaneous *in-situ* imaging of the two ultracold/degenerate clouds. As discussed above, this represents a stark difference with respect to the most common “home-made” quantum gas microscopes.
- Lastly, yet importantly, the objective will be installed along the vertical direction of the experimental setup: hence, the two MOT- $z$  beams will inevitably pass through the system. Accordingly, one must find a way to split MOT and imaging lights, retro-reflecting the former towards the science chamber without affecting too much the beam quality.

On the other hand, one simplification comes from the availability of two different cameras to image Li and Cr atoms, respectively, thus requiring color-correction only in the object plane (provided the two imaging lights are split at some point in the optical path).

During the initial discussions, a first possible solution was proposed. The scheme, sketched in Fig. 5.1, relied on a simple combination of achromatic doublets, dichroic mirrors, and beam splitters. In short, light is collected by a  $f = 75$  mm achromat, and then split between red (Li) and blue (Cr) components by means of a dichroic mirror. In each path, a PBS further separates MOT and imaging lights. The former ones, after passing through a second  $f = 75$  mm achromatic doublet, are retro-reflected towards the science chamber (the two achromats essentially act as a 1:1 telescope, thereby ideally not changing the MOT beams divergence and diameter). The latter are instead focused on the two cameras with two distinct  $f = 1500$  mm achromats, providing a final magnification of 20.

It was soon realized that such a simple optical scheme would have not satisfied the resolution requirements, as the achromats are not designed to correct for the window aberrations. Furthermore, the chromatic focal shift was estimated to be on the order of  $150 \mu\text{m}$ , hence much larger than the typical *in-situ* size of a degenerate atomic cloud.<sup>1</sup> Consequently, in the first period of my thesis, I tackled the problem of trying to design a suitable high-resolution objective for our mixture. The entire design process and performance evaluation were carried out using the ray-tracing software OSLO, developed by Lambda Research Corporation, a licence of which was provided to me by Dr. Giacomo Roati (Lithium lab, LENS). This chapter describes the optimization procedures and the final results of the simulations. Unfortunately, due to time constraints and technical problems with the objective case, an actual test of the system was not carried out in this work, being however on the schedule of future pursuits in our group.

**Figure 5.1** – Sketch of the first proposal for the new imaging system (not to scale).



<sup>1</sup>These results were found performing simulations with OSLO, see below.

## 5.1 Introduction

The theories behind geometric optics, aberrations, and diffraction, which lie at the heart of microscope designing, are well-established and extensively reported in many textbooks, see e.g. Refs. [79, 80, 81, 82, 83, 84, 85, 86, 87]. However, concerning high-resolution imaging systems, several specific figures of merit play a fundamental role in the entire design process, as well as in the characterization of the final performance. In this section, I provide a basic introduction for the most relevant features that must be taken into account, and optimized, when attempting to design such a high-resolution optical setup.

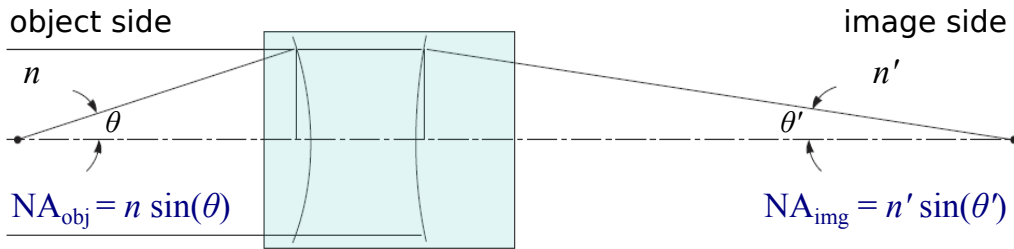
### Numerical aperture and magnification

The numerical aperture (NA) of an optical system, working at finite conjugate ratio,<sup>2</sup> is defined as the product between the sine of the maximum aperture angle and the refractive index of the medium surrounding the system, i.e.  $NA = n \cdot \sin(\theta^{\max})$ , see Fig. 5.2. Generally speaking, numerical apertures in the object and image planes can be different, and their ratio directly yields the system magnification  $M$  [81, 82]

$$M = \frac{NA_{\text{obj}}}{NA_{\text{img}}} \quad (5.1)$$

As we shall discuss in the following,  $NA_{\text{obj}}$  is a key quantity to determine the resolution limit of an optical system (see Eq. (5.2)): the larger NA, the smaller are the structures than can be resolved with an appropriate objective design. Furthermore, the numerical aperture determines the system irradiance: a large NA improves the signal-to-noise ratio (S/N), allowing the detection of objects with weak emissions [82]. However, as we shall discuss in the following, increasing the numerical aperture also has a major drawback, as it typically introduces a sizeable amount of aberrations, which, if not corrected for, can significantly lower the image quality.

**Figure 5.2** – Numerical aperture of an optical system. Figure adapted from Ref. [88].



<sup>2</sup>The definition of numerical aperture fails for infinite conjugates, i.e. when light is collimated on (at least) one side of the optical system. In that case, the relevant quantity is instead the *f-number*, defined as  $F_{\#} = f/\phi$ , where  $f$  is the effective focal length, and  $\phi$  is the aperture diameter illuminated by light. The *f-number* can also be defined for finite conjugates, being related to NA as [82]:  $F_{\#} = 0.5/NA$ .

## Resolution

In the simplest form of geometric optics, i.e. within the *paraxial approximation*, the image can be a perfect replica of the object: namely, a point source can produce a point image. Nonetheless, due to the wave-like nature of light, diffraction effects will always be present in the image plane, degrading the image quality, and thus limiting the system resolution. It is generally accepted that a reasonable estimate of the maximum achievable resolution for a monochromatic optical system is given by the Rayleigh's criterion [79, 82, 88]:

$$R = 0.61 \frac{\lambda}{\text{NA}} = (\Delta z)_{\text{Ar}} \quad (5.2)$$

where  $\lambda$  is the wavelength of the imaging light. Strictly speaking, the resolution given by Eq. (5.2) can be thought as the system's ability to distinguish between two different objects that are close together, the minimum resolvable distance being  $R$ .<sup>3</sup> Further, the value of  $R$  is also a measure of the Airy disk radius  $(\Delta z)_{\text{Ar}}$ .<sup>4</sup> According to Eq. (5.2), given an imaging wavelength  $\lambda$ , to achieve a good spatial resolution one should work with a large NA. However, Rayleigh's criterion solely accounts for diffraction effects, thus providing the effective resolution only for ideal *diffraction-limited* systems,<sup>5</sup> and representing the resolution limit for any real system. In fact, in practical applications, increasing the numerical aperture also increases the amount of aberrations, which are essentially deviations from paraxial optics. In the presence of aberrations, the image quality is degraded, and the effective resolution is lowered.

## Aberrations

The formation of perfect images is practically impossible. Aside from diffraction effects, any real optical system shows some degree of aberrations. Hence, the main goal of optical design is to reduce such aberrations to a level which is satisfactory for the desired performances.

Generally speaking, aberrations are essentially deviations from paraxial optics, which accurately describes only rays with infinitesimal heights and angles, relatively to the optical axis. In particular, monochromatic aberrations originate from the non-linearity of Snell's law, whereas chromatic aberrations are a direct consequence of dispersion, i.e. the wavelength dependence of the refractive index,  $n = n(\lambda)$ . A detailed theory of aberrations can be found in nearly every optics textbook, see e.g. Refs. [79, 80, 81, 82, 84, 87].

Without providing all the mathematical framework here, the essential point is that aberrations can be expressed as a Taylor sum over paraxial coordinates, typically aperture (i.e. ray height) and field (i.e. ray angle). The symmetry properties of the system restrict the possible combinations of polynomials in the expansion [82, 87],

<sup>3</sup>Formally, a spatial resolution should be defined as an inverse length [90], i.e. Eq. (5.2) actually expresses the *inverse* resolution. Nonetheless, it is a common practice to interchange the two terms: accordingly, a *high* resolution denotes a *low*  $R$ , and vice versa.

<sup>4</sup>The Airy disk is the area in the image plane contained within the principal ( $m = 0$ ) order of the diffraction pattern produced by a point source, when the latter is imaged through circular apertures, see e.g. Refs. [79, 81].

<sup>5</sup>An optical system is said to be *diffraction-limited* if diffraction dominates over wave aberrations, thus resulting the ultimate factor limiting the resolution.

providing also a natural way to classify aberrations. For instance, the so-called *primary* (or *Seidel*) *aberrations* can be identified as *spherical aberration*, *coma*, *astigmatism*, *field curvature*, and *distortion*, see the references indicated above for more details.

In general, image aberrations strongly increase with the numerical aperture. For instance, in the case of a thin spherical lens, it can be shown that spherical aberrations scale as the cube of NA [81, 88]. For composite systems, the total amount of aberrations can be expressed as a sum over the contributions from every single surface. Each of these contributions possesses a sign and, therefore, aberrations can be substantially reduced with a proper system design [82].

### Spot diagram

A spot diagram is a geometrical structure that provides an intuitive graphical representation of the image quality. It is formed by the intersection points between the image plane and a given set of rays, which are traced starting from a single, fixed point on the object. Spot diagrams are entirely computed by means of geometric optics, hence not considering the wave-like nature of light. Nonetheless, they are rather sensitive to all transverse aberrations, providing a fairly good estimate for the broadening of a point image when diffraction effects can be neglected [84]. In fact, as a rule of the thumb, if  $(\Delta z)_{\text{abs}}$  is the spot size generated by aberrations, the effective image spot size (including diffraction effects) can be estimated by [82]

$$(\Delta z)_{\text{tot}} \simeq \sqrt{4(\Delta z)_{\text{Ar}}^2 + (\Delta z)_{\text{abs}}^2} \quad (5.3)$$

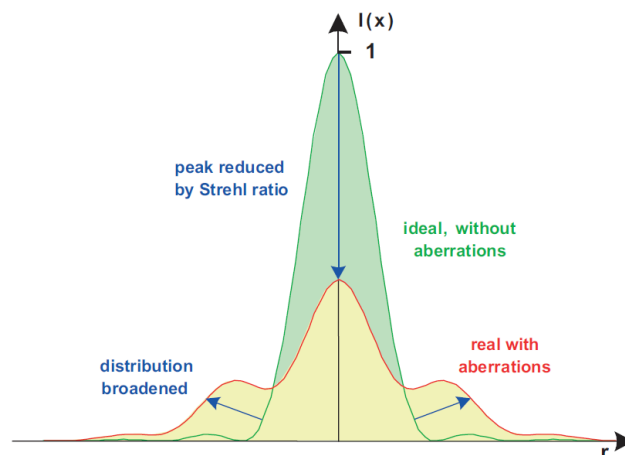
Thus, for a diffraction-limited system,  $(\Delta z)_{\text{tot}}$  is essentially given by the Airy diameter, with the geometric spot diagram entirely lying well inside the Airy disk. The opposite occurs if the system is far from being diffraction-limited, i.e. if wave aberrations dominate over diffraction. Accordingly, spot diagrams are meaningful objects only when aberrations play an important role in determining the image quality. For diffraction-limited systems, more significant figures of merit are provided by the point spread function, the modulation transfer function, and the wavefront error (see below).

It is generally accepted that, for a comprehensive description of the performance of an optical system, the spot diagram should be presented as a function of the image height (or field angle) and of the defocus, as well as of the wavelength [82].

### Point Spread Function and Strehl ratio

From a physical point of view, the point spread function (PSF) is defined as the image of an ideal point source, generated by the optical system under investigation. In the language of linear systems theory, the PSF is essentially the (spatial) impulse response function, and in mathematical language it is the Green's function of the optical system [87]. For instance, for a completely ideal system, the PSF is the Dirac delta function. Of course, since diffraction effects are always present, no such system exists in reality. For a diffraction-limited (i.e. free from aberrations) system with axial symmetry (i.e. circular apertures), the PSF is given by the well-known Airy function [87]. In general, the PSF is a rather complicated object (which can in principle be computed from diffraction integrals), that carries information about any aberration

**Figure 5.3** – Deformation of the point spread function in the presence of aberrations, and definition of the Strehl ratio. Figure taken from Ref. [84].



present in the system, taking into account also diffraction effects. In particular, it can be shown that spherical aberrations induce ring patterns, astigmatism produces diamond-shaped figures, and coma yields comet-like distributions [82]. Hence, the profile of the PSF is an essential criterion to evaluate the quality of the optical system under investigation: A complete knowledge of the PSF allows to determine the system output (i.e. image formation) for any given input (i.e. object) [87].<sup>6</sup>

Nonetheless, from a practical point of view, it is often convenient to define a single parameter that quantitatively encodes the behaviour of the PSF. This parameter is usually taken to be the *Strehl ratio*  $S_r$ , which is defined as the reduced height of the PSF central peak in the presence of aberrations, relatively to the ideal (aberration-free) case, see Fig. 5.3. As such,  $S_r$  can only take values between 0 and 1, the latter corresponding to an ideal system, and it can be regarded as a normalized aberration measure. Indeed, it can be shown that any wave aberration degrades the PSF, thus lowering the Strehl ratio [84]. However, it is clear that all the information contained in the real structure of the PSF is somehow washed out when everything is reduced to a single number: accordingly, the Strehl ratio as a figure of merit only makes sense in the regime of low aberrations, i.e. when  $S_r > 0.6$  [84]. Despite this limitation,  $S_r$  is widely regarded as a fundamental parameter in the characterization of an imaging system: By convention, an objective is said to be diffraction-limited if  $S_r \geq 0.8$  [82, 84].

### Contrast and Modulation Transfer Function

The contrast is a measure of how well the system is able to resolve details and nuances of the object. In other words, the contrast provides an indication of how effectively the intensity maxima and minima are transferred from the object to the image. When the object is a target grid made of equally-spaced dark and bright lines, characterized by a certain spatial frequency  $f$  (typically expressed in line pairs per mm, or lp/mm), the contrast is defined as the ratio [82]

$$C = \frac{I_{\max} - I_{\min}}{I_{\max} + I_{\min}} \quad (5.4)$$

<sup>6</sup>The output field distribution results from the convolution of the input one with the PSF.

where  $I_{\max}$  and  $I_{\min}$  are the image intensity maximum and minimum, respectively. Arbitrarily shaped objects can be modelled as a sum over different Fourier components, each of which accounts for structures characterized by the corresponding spatial frequency. Anyway, as a general rule, every optical system acts as a low-pass filter, so the image contrast is reduced as the spatial frequency is increased. The function that describes this trend is the modulation transfer function (MTF)  $g_{\text{MTF}}$ , which is essentially a plot of the contrast versus the spatial frequency.<sup>7</sup> For an ideal diffraction-limited system with a circular pupil, the MTF has a simple analytical representation [82]

$$g_{\text{MTF}}(\tilde{\nu}) = \frac{2}{\pi} \left[ \arccos(\tilde{\nu}) - \tilde{\nu} \sqrt{1 - \tilde{\nu}^2} \right] \quad (5.5)$$

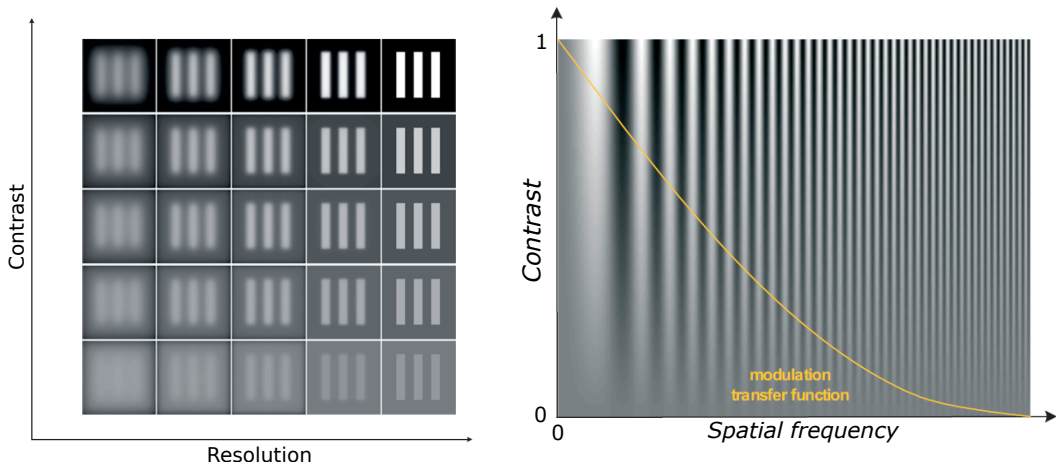
where  $\tilde{\nu} = f/f_0$  is a normalized spatial frequency, with  $f_0 = 2\text{NA}/\lambda$  being the limiting frequency, i.e.  $g_{\text{MTF}}(\tilde{\nu}) = 0$  for  $f \geq f_0$ . A plot of Eq. (5.5) is shown in Fig. 5.4 (right).

As a general rule, given NA and  $\lambda$ , the MTF of an optical system always lie below the ideal curve described by Eq. (5.5), as any aberration degrades the performances. Similarly to the case of the PSF, while accurate knowledge of the MTF provides several information about aberrations, it is generally convenient to introduce a single parameter to characterize the MTF behaviour. We take this parameter to be the *cutoff frequency*  $f_{\text{cut}}$ , defined as the value of the spatial frequency corresponding to a contrast of 0.2 (this is generally considered to be the minimum contrast that yields acceptable images [90]). Accordingly, an estimate of the effective resolution  $R^*$  of an optical system is given by

$$R^*_{[\mu\text{m}]} = \frac{1000}{f_{\text{cut}} [\text{lp}/\text{mm}]} \quad (5.6)$$

where the subscripts inside square brackets specify the units of measurement. For a diffraction-limited system,  $R^*$  is roughly 20% greater than the resolution given by

**Figure 5.4** – Effects of contrast and resolution on the image quality (left), and modulation transfer function for a diffraction-limited system (right). Figures taken from Ref. [84].



<sup>7</sup>In the framework of Fourier optics, the MTF is the modulus of the optical transfer function [82, 84].

Rayleigh's criterion (namely,  $R^* \simeq 0.73 \lambda/\text{NA}$ ). The spatial frequency corresponding to the inverse of Eq. (5.2) would instead provide a contrast of just 9%.

In any case, it should be kept in mind that resolution and contrast are two different parameters to evaluate an objective performances: A high contrast delivers a bright image, while a high resolution allows to resolve sharp edges and fine details, see Fig. 5.4 (left).

### Depth of focus and field of view

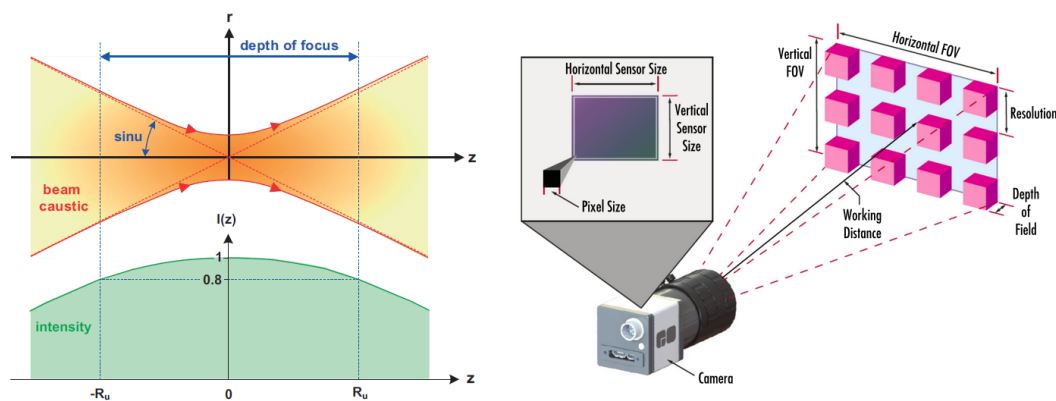
The depth of focus (DOF) is defined as the maximum defocus that still provides diffraction-limited images (i.e. with  $S_r > 0.8$ ), see Fig. 5.5 (left).<sup>8</sup> It can be shown that, for a diffraction-limited system [97]

$$\text{DOF} = \frac{\lambda \cdot \sqrt{n^2 - \text{NA}^2}}{\text{NA}^2} \simeq \frac{\lambda}{\text{NA}^2} \quad (5.7)$$

where  $n$  is the refractive index of the surrounding medium, and the final result is obtained in the limit of small NA, assuming  $n = n_{\text{air}} = 1$ . For large numerical apertures, the DOF is rather small: in other words, the more a beam is focused, the faster it will diverge when moving away from the focus position. For instance, in the visible range and for  $\text{NA} = 0.4$ , the DOF is on the order of a few microns. The final application determines whether or not a small DOF constitutes a limitation.<sup>9</sup> In any case, owing to the stronger dependence on NA, the DOF of a high-resolution objective can be increased by slightly stopping down the system, without drastically affecting the resolution.

The DOF essentially quantifies the diffraction-limited working range along the optical axis. In the transverse direction, a similar role is played by the field of view (FOV), which is defined as the maximum radial distance (in the object plane) from which

**Figure 5.5** – Illustration of the depth of focus (left), and of the fundamental parameters of an imaging system (right). Figures taken from Refs. [84, 90].



<sup>8</sup>Some authors distinguish between the *depth of field*, defined on the object side, and the *depth of focus*, defined instead on the image side. Here, we are mainly interested in the DOF in the object side.

<sup>9</sup>For instance, quantum gas microscopes for single-site-resolved imaging of atoms in optical lattices take advantage of their small DOF, as typically only one lattice plane is at focus, while the remaining ones yield a signal background that can be filtered out [97].

light produces diffraction-limited images, see Fig. 5.5 (right). In some cases (e.g. for an infinite conjugate ratio), the FOV can be expressed in angular units (angular FOV, or AFOV). The relation that links these two quantities is [90]

$$\text{FOV} = 2 \text{WD} \cdot \tan\left(\frac{\text{AFOV}}{2}\right) \quad (5.8)$$

where WD is the working distance, defined as the distance between the object and the first optical surface of the imaging system.

### Wavefront error

In the ideal case of perfect image formation, all rays traced from a given point on the object should converge to a unique point on the image, meaning that they should be perpendicular to a reference sphere centred on this latter. The wavefront error (WFE) measures the deviation of the real wavefront from this reference sphere, providing a further way to account for aberrations. It is usually measured in units of length, by converting the deviation into an optical path difference (OPD). The latter, in turn, is typically expressed in units of  $\lambda$ .

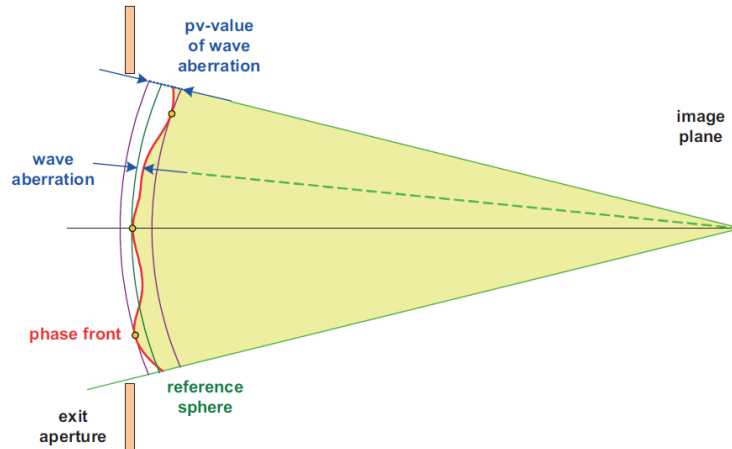
As figures of merit, the two key quantities are the peak-to-valley WFE and its root-mean-square (r.m.s.) value  $W_{\text{rms}}$  [82, 84]. By convention, an optical system is considered to be diffraction-limited if the peak-to-valley WFE is less than 0.25 waves (i.e. less than  $\lambda/4$ ), with a corresponding r.m.s. error  $W_{\text{rms}} < 0.07 \lambda$  [84]. Indeed, it can be shown that these requirements lead to a Strehl ratio greater than 0.8, e.g. with the empirical *Mahajan's formula* [91, 99]

$$S_r \simeq \frac{1}{e^{(2\pi W_{\text{rms}}/\lambda)^2}} \quad (5.9)$$

or with the *Maréchal criterion*, which yields  $W_{\text{rms}} < \lambda/14$  [83].

When evaluated off-axis, the WFE is a fundamental parameter to determine the maximum diffraction-limited field of view.

**Figure 5.6** – Graphical representation of the wavefront error. Figure taken from Ref. [84].



## 5.2 Chromatic aberrations and color correction

In this section, I discuss chromatic aberrations and the key points of achromatic (i.e. two-colour) correction in optical systems composed by two or more lenses.

First, every optical medium exhibits a dispersion-like behaviour, i.e. its refractive index is a function of the wavelength:  $n = n(\lambda)$ . The *dispersion relation* is not linear, and it is typically steeper in the blue region of the spectrum. It is often convenient to rely on a single parameter to quantify the amount of dispersion in the medium under investigation. The choice typically falls on the *Abbe number*, defined as [81, 82]

$$V_A = \frac{n_{D1} - 1}{n_F - n_C} \quad (5.10a)$$

where the subscripts denote the Fraunhofer lines that were historically taken as references ( $\lambda_{D1} = 589.6$  nm,  $\lambda_F = 486.1$  nm, and  $\lambda_C = 656.3$  nm, respectively). The Abbe number quantifies the inverse dispersion in the visible spectrum, providing a rudimentary way to classify optical media: As a rule of the thumb, glasses with a high refractive index have low Abbe numbers (*flint glasses*), hence high dispersion, and vice versa (*crown glasses*). However, it should be noted that the value of  $V_A$  is actually strongly influenced by the choice of the “red” (i.e. longer) and “blue” (i.e. shorter) wavelengths, while being less sensitive to the “central” one.<sup>10</sup> Accordingly, to better account for dispersion effects, one can introduce a generalized *V-number*

$$V = \frac{n_c - 1}{n_b - n_r} \quad (5.10b)$$

where  $n_b$ ,  $n_r$ , and  $n_c$  are the refractive indexes for  $\lambda_b$ ,  $\lambda_r$ , and  $\lambda_c$ , respectively. In the following, we will always refer to *V-numbers* calculated for  $\lambda_b = \lambda_{Cr} = 425.5$  nm,  $\lambda_r = \lambda_{Li} = 671$  nm, and  $\lambda_c = 550$  nm. Tab. 5.1 reports a comparison between Abbe numbers computed with the Fraunhofer lines and *V-numbers* relative to our imaging wavelengths, for some among the most common optical glasses.

In optical systems working with polychromatic light, dispersion effects cause a degradation of the image quality. In general, every monochromatic aberration has its own chromatic analogue [84]. However, to simplify the analysis, one typically

**Table 5.1** – Comparison between Abbe and *V-numbers* for some common optical glasses.  $V_A$  is the Abbe number calculated with the standard Fraunhofer lines.  $V_{LiCr}$  is instead the *V-number* calculated for  $\lambda_r = 671$  nm,  $\lambda_b = 425.5$  nm, and  $\lambda_c = 550$  nm.

Glass	$V_A$	$V_{LiCr}$
N-BK7	63.8	37.3
SF5	32.2	18.0
S-LAH64	47.5	27.2
N-BAF10	47.2	26.8
N-SF6HT	25.4	14.0

<sup>10</sup>Within the visible region of the spectrum,  $V_A$  (or, more generally,  $V$ ) varies only by a few percent when  $\lambda_c$  is varied in the range  $[\lambda_b; \lambda_r]$ . Here and in the following, the subscripts  $r$ ,  $b$  and  $c$  are abbreviations for “red”, “blue”, and “central”, respectively.

classifies chromatic aberrations in *lateral* (or *transverse*) and *longitudinal* (or *axial*). The transverse chromatic aberration (TCA, or *lateral color*) can be understood as a wavelength-dependent magnification. It can detrimentally affect the image quality of photographic lenses, but in practice it does not represent a serious problem for our specific system, as Li and Cr atoms are imaged with different cameras. On the other hand, the longitudinal chromatic aberration (LCA, or *longitudinal color*) is essentially the chromatic variation of the focus (or, more generally, of the image plane) position along the optical axis. Since our bichromatic objective must collect light from two overlapped degenerate atomic clouds, with typical *in-situ* sizes on the order of 10  $\mu\text{m}$ , the LCA should be highly corrected for  $\lambda_{\text{Li}}$  and  $\lambda_{\text{Cr}}$ . The following discussion is mainly centred around this topic.

Longitudinal color ultimately originates from the chromatic variation of the effective focal length. Namely, the *chromatic focal shift* of an optical system is defined as [82]

$$\Delta f_{\text{cfs}} = f_b - f_r \quad (5.11)$$

where  $f_b$  and  $f_r$  are the effective focal lengths for  $\lambda_b$  and  $\lambda_r$ , respectively. As we shall see shortly, for an ordinary singlet lens, one has  $|f_b| < |f_r|$ . Accordingly, we call the chromatic focal shift *normal* (*anomalous*) when it has the opposite (same) sign of the effective focal length.

The longitudinal chromatic aberration is closely related to  $\Delta f_{\text{cfs}}$ , but in practice their values do not necessarily coincide. For a thin singlet, this can be easily understood with the paraxial imaging equation [81, 88]

$$\frac{1}{p} + \frac{1}{q} = \frac{1}{f} \quad (5.12)$$

where  $p$  and  $q$  are the object and image distances (along the optical axis) from the center of the lens, respectively (see Ref. [88] for sign conventions). In general, the LCA is given by  $q_b - q_r$ , which coincides with  $f_b - f_r$  only for  $p_b = p_r = \infty$ .<sup>11</sup>

For compound systems, or for elements with non-negligible thickness, the relation between  $\Delta f_{\text{cfs}}$  and the amount of LCA is not straightforward. The reason is that the effective focal length is usually defined relatively to a *principal plane* (and principal planes for different wavelengths generally do not coincide), while longitudinal color is also influenced by the marginal ray height at each refractive surface [81].

In the following, we study the chromatic focal shift and the LCA for a few simple systems.

### Singlet lens

For a thin spherical singlet with refractive index  $n$ , one can easily derive an approximate relation between the  $V$ -number and  $\Delta f_{\text{cfs}}$ ; then, from the latter, the LCA can in turn be estimated. The starting point is the well-known *lens maker's equation* [81]

$$\frac{1}{f} = (n - 1) \cdot \left( \frac{1}{R_1} - \frac{1}{R_2} + \frac{(n - 1)}{n} \frac{t_c}{R_1 R_2} \right) \simeq (n - 1) \cdot k \quad (5.13)$$

<sup>11</sup>Actually, the LCA of a thin singlet accidentally coincides with  $\Delta f_{\text{cfs}}$  also for  $p_b = p_r = f/2$ , see Eq. (5.16), but this is not relevant for the present discussion.

where  $R_1$  and  $R_2$  are the two curvature radii describing the lens surfaces,<sup>12</sup>  $t_c$  is the central thickness, and  $f$  is the resulting focal length. The last result is obtained for  $t_c \ll |R_1|, |R_2|$ , i.e. in the case of a thin lens, having defined the geometric coefficient  $k = R_1^{-1} - R_2^{-1}$ . For conventional optical glasses  $n_b > n_c > n_r$ , hence  $|f_r| > |f_c| > |f_b|$ .

From Eq. (5.13),  $f_q$  (with  $q = r, b$ ) can be expressed as

$$\frac{1}{f_q} \simeq (n_q - 1) \cdot k = \frac{(n_q - 1)}{(n_c - 1)} \cdot \frac{1}{f_c} \quad \longrightarrow \quad f_q \simeq \frac{(n_c - 1)}{(n_q - 1)} \cdot f_c \quad (5.14)$$

where  $f_c$  is the focal length for  $\lambda_c$ . Thus, we can write the chromatic focal shift as

$$\Delta f_{\text{cfs}} = f_b - f_r \simeq f_c (n_c - 1) \left( \frac{1}{n_b - 1} - \frac{1}{n_r - 1} \right) \simeq -\frac{f_c}{V} \quad (5.15)$$

where the last result is obtained by approximating  $(n_b - 1) \cdot (n_r - 1) \simeq (n_c - 1)^2$  at the denominator. Eq. (5.15) directly links  $\Delta f_{\text{cfs}}$  with the (nominal) focal length via the reciprocal of the  $V$ -number, providing a fairly good approximation for singlets. The minus sign implies that the chromatic focal shift of a singlet is always normal.<sup>13</sup> In practice, since the highest  $V$ -numbers for optical glasses lie around the value of 100 (in the visible range), for a singlet lens  $\Delta f_{\text{cfs}}$  is typically on the order of a few percent of the (nominal) focal length. For many polychromatic applications, this constitutes a strong limitation to the final image quality.

As previously pointed out, chromatic focal shift and longitudinal color do not necessarily coincide, although being closely related. In particular, for a thin singlet,  $\Delta f_{\text{cfs}}$  corresponds to the total amount of LCA only if the lens is working at infinite conjugate ratio. Conversely, for a finite object distance, assuming  $p_b = p_r = p$  (i.e. no axial color on the object side), from Eq. (5.12) one finds

$$\text{LCA} \simeq \left( \frac{p}{p - f} \right)^2 \Delta f_{\text{cfs}} \quad (5.16)$$

having approximated  $(p - f_b) \cdot (p - f_r) \simeq (p - f)^2$  at the denominator. Hence, the LCA of a thin singlet has the same sign of  $\Delta f_{\text{cfs}}$ , but it is scaled by a factor  $(1 - f/p)^{-2}$ .<sup>14</sup> Accordingly, a positive (negative) singlet is always *under-corrected* (*over-corrected*) with respect to longitudinal color, i.e.  $\text{LCA} < 0$  ( $\text{LCA} > 0$ ) [82].

Lastly, yet importantly, it is worth noticing that, given an object distance  $p$ ,  $\Delta f_{\text{cfs}}$  and LCA depend only on  $f$  and  $V$ , and not on the geometrical shape of the lens. This allows for an independent optimization of the latter, with respect to minimizing spherical aberrations (e.g. via *lens bending*, see Ref. [84] for details).

### Cemented doublet

Let us now consider a doublet composed by two adjacent thin lenses, with nominal focal lengths  $f_1$  and  $f_2$ , and refractive indexes  $n_1$  and  $n_2$ , respectively. The total effective focal length  $F$  is given by [86, 88]

$$\frac{1}{F} = \frac{1}{f_1} + \frac{1}{f_2} \quad (5.17)$$

<sup>12</sup>See Refs. [81, 88] for sign conventions.

<sup>13</sup> $V$ -numbers are positive quantities for glasses with normal dispersion relations.

<sup>14</sup>For  $p = f$ , the LCA diverges, as the image forms at infinite distance, i.e. the output light is collimated. Near  $p = f$ , Eq. (5.16) might fail, in particular when  $(p - f_b) \cdot (p - f_r) < 0$ .

With respect to  $\lambda_q$  ( $q = r, b$ ), from Eqs. (5.14) and (5.17) we have

$$\frac{1}{F_q} = \frac{1}{f_{1,q}} + \frac{1}{f_{2,q}} \simeq \frac{n_{1,q} - 1}{n_1 - 1} \cdot \frac{1}{f_1} + \frac{n_{2,q} - 1}{n_2 - 1} \cdot \frac{1}{f_2} \equiv \frac{A_{1,q}}{f_1} + \frac{A_{2,q}}{f_2} \quad (5.18)$$

where we dropped the  $c$  subscript denoting the central/nominal values for  $n$  and  $f$ . In Eq. (5.18), the last passage defines the coefficients  $A_{i,q}$  (with  $i = 1, 2$  and  $q = r, b$ ), numerically close to 1. Therefore, noticing that  $A_{i,b} - A_{i,r} = 1/V_i$ , the chromatic focal shift of a cemented doublet can be estimated by

$$\begin{aligned} \Delta F_{\text{cfs}} &= F_b - F_r \simeq f_1 f_2 \cdot \left( \frac{1}{A_{2,b} f_1 + A_{1,b} f_2} - \frac{1}{A_{2,r} f_1 + A_{1,r} f_2} \right) \simeq \\ &\simeq -F^2 \cdot \left( \frac{1}{f_1 V_1} + \frac{1}{f_2 V_2} \right) \end{aligned} \quad (5.19)$$

having approximated  $(A_{2,b} f_1 + A_{1,b} f_2) \cdot (A_{2,r} f_1 + A_{1,r} f_2) \simeq (f_1 + f_2)^2$  at the denominator. Further, by two consecutive applications of Eq. (5.12), under the same conditions that yielded Eq. (5.16), after some algebraic manipulations one finds

$$\text{LCA} \simeq -\frac{F^2}{(1 - F/p)^2} \cdot \left( \frac{1}{f_1 V_1} + \frac{1}{f_2 V_2} \right) = \frac{\Delta F_{\text{cfs}}}{(1 - F/p)^2} \quad (5.20)$$

i.e. a relation between longitudinal color and chromatic focal shift essentially analogous to the one of a thin singlet. Nevertheless, the main point of doublets is that, with a proper lens combination,  $\Delta F_{\text{cfs}}$  (and, hence, the LCA) can be eliminated for two selected wavelengths. In particular, if the two lenses are made with the same optical glass ( $n_1 = n_2 = n$ ) or, more generally, if they have the same  $V$ -number ( $V_1 = V_2 = V$ ), Eq. (5.19) reduces to

$$\Delta F_{\text{cfs}} \simeq -\frac{F}{V} \quad (5.21)$$

in complete analogy to Eq. (5.15). In this case,  $\Delta F_{\text{cfs}} = 0$  has only the trivial solution  $F = 0$ . On the other hand, for  $V_1 \neq V_2$ , Eq. (5.19) shows that the chromatic focal shift can be eliminated even for a non-vanishing  $F$ . This yields the celebrated *achromatic condition* for the realization of (cemented) achromatic doublets

$$f_1 \cdot V_1 = -f_2 \cdot V_2 \quad (5.22)$$

Since for common glasses  $V$ -numbers are positive quantities, Eq. (5.22) requires  $f_1 = -f_2$  to be satisfied. For instance, in the case of a positive achromat (i.e.  $F > 0$ ), the only possible combination consists in a positive lens ( $f_1 > 0$ ) realized in a crown glass, and a negative element ( $f_2 < 0$ ) realized in a flint glass, with  $f_1 < |f_2|$  and  $V_1 > V_2$ . Indeed, by combining Eqs. (5.17) and (5.22), one finds

$$f_1 = F \left( \frac{V_1 - V_2}{V_1} \right); \quad f_2 = -F \left( \frac{V_1 - V_2}{V_2} \right) \quad (5.23)$$

Importantly, Eqs. (5.22) and (5.23) do not explicitly depend on the three curvature radii of the cemented doublet, which can thus be optimized to minimize spherical aberrations. It can be shown that, given  $f_1$  and  $f_2$  from Eq. (5.23), four different geometries exist to simultaneously correct for axial color and spherical aberration [84]. However, we remark that the achromatic condition only allows for color-correction with respect to *two* specified wavelengths. Any other colour exhibits some degree of LCA, an effect known as *secondary spectrum* [79].

**Air-spaced doublet**

Let us now consider a system of two thin lenses separated by a certain distance  $d$ . In this case, the effective focal length is given by [86, 88]

$$\frac{1}{F} = \frac{1}{f_1} + \frac{1}{f_2} - \frac{d}{f_1 f_2} \quad (5.24)$$

Following a procedure analogous to the one that yielded Eq. (5.19), we now obtain

$$\Delta F_{\text{cfs}} \simeq -F^2 \cdot \left[ \frac{1}{f_1 V_1} + \frac{1}{f_2 V_2} - \frac{d}{f_1 f_2} \left( \frac{1}{V_1} + \frac{1}{V_2} \right) \right] \quad (5.25a)$$

having approximated  $A_{1,b}A_{2,b} - A_{1,r}A_{2,r} \simeq V_1^{-1} + V_2^{-1}$ . We explicitly note here that, for  $V_1 = V_2 = V$ , Eq. (5.25a) reduces to

$$\Delta F_{\text{cfs}} \simeq -\frac{F}{V} \frac{f_1 + f_2 - 2d}{f_1 + f_2 - d} \quad (5.25b)$$

Further, following the steps that led to Eq. (5.20), one finds

$$\text{LCA} \simeq -\frac{F^2}{\left[1 - \frac{F}{p}\left(1 - \frac{d}{f_2}\right)\right]^2} \cdot \left[ \frac{1}{f_1 V_1} + \frac{1}{f_2 V_2} \cdot \left(1 - \frac{d}{f_1} \left(2 - \frac{f_1}{p}\right) + \frac{d^2}{f_1^2} \left(1 - \frac{f_1}{p}\right)^2\right) \right] \quad (5.26a)$$

which, for an object at infinite distance, becomes

$$\text{LCA}(p \rightarrow \infty) \simeq -F^2 \cdot \left[ \frac{1}{f_1 V_1} + \frac{1}{f_2 V_2} \left(1 - \frac{d}{f_1}\right)^2 \right] \quad (5.26b)$$

The case of air-spaced doublets is richer than those encountered before, as the air layer introduces one additional degree of freedom.<sup>15</sup> First, we note that, for any finite  $d$ , longitudinal color is not simply proportional to the chromatic focal shift. Therefore, a vanishing  $\Delta F_{\text{cfs}}$  does not guarantee correction for the LCA. In fact, according to Eq. (5.26b), the generalized achromatic condition (i.e. LCA = 0) for an air-spaced doublet (working at infinite conjugate ratio) reads

$$(1 - \mu_{12})^2 \cdot f_1 V_1 = -f_2 V_2 \quad (5.27)$$

with  $\mu_{12} = d/f_1$ . In general, for positive  $V$ -numbers, Eq. (5.27) still requires  $\text{sign}(f_1) \neq \text{sign}(f_2)$  to be satisfied. However, differently from cemented achromats, some particular solutions exist also for  $V_1 = V_2$ . Namely, under this condition, Eq. (5.27) is satisfied for

$$d_{\pm} = f_1 \cdot \left(1 \pm \sqrt{\left|\frac{f_2}{f_1}\right|}\right) \quad (5.28)$$

With the physical constraint of a positive distance, Eq. (5.28) has always at least one acceptable solution for  $F < 0$ , whereas for  $F > 0$  a solution only exists if the positive element is the first lens. In any case, however, the image is always virtual,

<sup>15</sup>With respect to monochromatic aberrations, the additional degrees of freedom are two, as the two facing curvature radii need not to be the same.

i.e. it forms before the second lens. Requiring a real image yields no solutions for  $V_1 = V_2$ , i.e. two different glasses are needed to correct for axial color in real images. As a final remark, let us comment on the elimination of the chromatic shift. From Eqs. (5.25), one can easily find the specific distance  $d$  that yields  $\Delta F_{\text{cfs}} = 0$ . Namely,  $d = (f_1 V_1 + f_2 V_2)/(V_1 + V_2)$ , which becomes simply  $d = (f_1 + f_2)/2$  for  $V_1 = V_2$ . Although not being corrected for axial color, such a scheme provides a fairly good correction for lateral color (i.e. TCA) [81, 86]. In particular, the single-glass doublet with  $d = (f_1 + f_2)/2$ , firstly proposed by Huygens in 1661 (and since then known as the *Huygens eyepiece*), was historically the first system to show some degree of color correction.<sup>16</sup>

### Multi-lens systems

For a system composed by  $N$  adjacent thin lenses, the total focal length reads

$$\frac{1}{F} = \sum_{i=1}^N \frac{1}{f_i} \quad (5.29)$$

and Eq. (5.19) simply generalizes to

$$\Delta F_{\text{cfs}} = -F^2 \cdot \sum_{i=1}^N \frac{1}{f_i V_i} \quad (5.30)$$

with a relation between  $\Delta F_{\text{cfs}}$  and axial color analogous to Eq. (5.20).

On the other hand, if finite air gaps between the (thin) lenses are included, the analysis becomes more complicated. In Ref. [98], the author derives an exact formula for the effective focal length of such a system, with arbitrary singlet focal lengths and air spacings. As in the case of air-spaced doublets, the relation between chromatic focal shift and axial color is not straightforward. Nonetheless, for an object free from LCA, it can be shown that on the final image [81]

$$\text{LCA} = -\frac{1}{u_N^2} \sum_{i=1}^N \frac{y_i^2}{f_i V_i} \quad (5.31)$$

where  $y_i$  are the marginal ray heights at the position of each lens, while  $u_N = y_N/q_N$  is the paraxial angle on the image side. For instance, in the case of an air-spaced doublet with no internal focal points, one has  $y_2 = y_1 (1 - d/q_1)$ . Further, for an infinitely distant object, one has  $q_2 = F (1 - d/f_1) = F (1 - \mu_{12})$ . Therefore, from Eq. (5.31) one retrieves Eq. (5.26b). Hence, the factor  $(1 - \mu_{12})^2$  essentially takes into account the different marginal ray heights at the positions of the two elements, which in turn affect longitudinal color.

Lastly, we stress that Eq. (5.31) only applies to a system composed by thin lenses. If the glass thicknesses cannot be neglected, the sum must be performed over every single refracting surface, and the final expression becomes more complicated, see e.g. Ref. [81].

<sup>16</sup>At that time, the dispersive properties of glasses were not known. About two years later, Newton began the study of this topic. Then, in 1729, C. Hall accidentally invented achromatic doublets, laying the ground for the realization of optical systems free from axial color [81].

## 5.3 Simulations with OSLO

OSLO is a ray-tracing software developed by Lambda Research Corporation. A free educational version is available on the company website, but for most practical applications it results rather unsuitable, as many functionalities are strongly limited. A licence for the professional version was provided to me by Dr. Giacomo Roati, head of the Lithium lab at LENS. Dr. Lorenzo Marconi and Dr. Francesco Scazza (from the K-Rb and the Lithium lab, respectively) explained to me the fundamentals of this software, delivering also some useful advice for the design process.

In this section, I briefly report on the general methods, program settings, and optimization routines that I found more suitable to carry out the simulations. This will not be a comprehensive guide to use OSLO, nor to design a microscope objective, but rather a minimal description that allows for an independent user to check and reproduce the obtained results.

### General methods

1. First, when designing a microscope objective, it is a common practice to start from the optimization of the *reversed system*, i.e. to study the (equivalent) problem of properly focusing a light beam into a tiny spot [96]. Although it might initially appear counterintuitive, this technique actually offers several advantages. For instance, optimization via software turns out to be more straightforward for a reversed objective, as most of the optimization routines rely on the production of a clean spot in the “image” plane. Focusing and defocusing, as well as the impact of aberrations, are also quite easier to visualize and understand. On top of that, optimization of the reversed system is particularly suitable for *infinity-corrected objectives*, i.e. optical systems where light is first collected and collimated by the front lens (or lens group, referred to as the *objective lens*), and then focused onto the camera by the so-called *tube lens*. Infinity-corrected objectives are quite common in modern scientific experiments, as the space between the objective lens and the tube lens (*infinity space*) can be exploited to introduce polarization optics or dichroic mirrors, without affecting the image quality. Furthermore, they effectively decouple the problems of collecting light from the object and focusing it onto the image plane, thereby allowing extreme flexibility to change the magnification. Indeed, the following relation holds [96]

$$M = \frac{f_{\text{tube}}}{f_{\text{obj}}} \quad (5.32)$$

where  $f_{\text{tube}}$  and  $f_{\text{obj}}$  are the focal lengths of the tube and the objective lens, respectively.

2. To increase the probability of success in finding a suitable design, one should start with a reasonable and realistic guess for the system, which of course may be difficult to find. While direct experience in the field is arguably the most helpful tool in choosing the initial design, useful inspiration can be taken by analysing existing models described in the literature. In the worst case, i.e. in the absence of any initial hints, one can start by optimizing a positive singlet lens. Then, a second element is included, and the system is re-optimized.

The process is iterated until the desired performances are achieved. This last method is often the least effective, as the optimization routine is likely to get stuck on a local minimum of the error function.

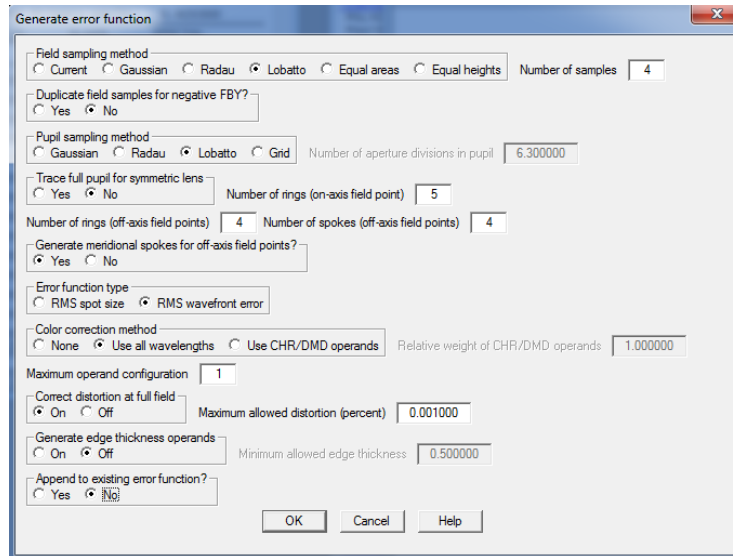
3. Generally speaking, the basic idea underlying the optimization routine is that the thickness and radii of curvature of each element, as well as the air spacings between consecutive optics, are initially fitting variables. During the various iterations, once the desired performances are achieved, the element that is found to be more similar to a catalogue lens gets replaced by the latter, with its parameters kept fixed in the subsequent optimization stages. This replacement procedure is repeated until a complete convergence to a set of catalogue lenses is found. In the very last step, only the air spacings are optimized.
4. In principle, following the above point, for the first optimization runs one wishes to have as many free parameters as possible. However, sometimes the algorithm fails to find a good solution if it has to deal with a large number of fitting variables. Accordingly, in the first stages, it may be more convenient to optimize iteratively single elements, or better couples of elements (e.g. a positive and a negative lens) at a time. When a stable, working configuration is found, the system can be optimized as a whole.
5. Since the most common optical glass in catalogues is N-BK7 (for the visible range), we initially choose this material for every singlet lens. However, as pointed out in Sec. 5.2, one should keep in mind that longitudinal color in real images cannot be corrected with a system made of a single type of glass. To this end, unfortunately, 2"-diameter negative lenses realized in flint glasses lack in commercial catalogues, preventing an intuitive correction of LCA based on the idea underlying achromatic doublets (see again Eq. (5.22)), and thus posing additional constraints in the design process.

### Program settings

We report here the main global settings of the program:

- In the *Setup* menu, one should fix the *Image NA* and the *Maximum field angle* (which ultimately determine the resolution limit and the field of view, respectively). We found this more convenient than working with a fixed *Entrance beam radius* (which is the default option), as in this way the target resolution and FOV are kept fixed during optimization.
- In the *Wavelength* menu, OSLO needs three different wavelengths (namely  $\lambda_1$ ,  $\lambda_2$ , and  $\lambda_3$ , which correspond to "green", "blue", and "red", respectively) in order to properly evaluate chromatic aberrations. In our specific case, one should set  $\lambda_2 = 425.5$  nm,  $\lambda_3 = 671$  nm, and an arbitrary  $\lambda_1$  that satisfies  $\lambda_2 < \lambda_1 < \lambda_3$  ( $\lambda_1$  is not important for the blue-red color correction).
- In the *Variables* menu, one should set reasonable bounds for the optimization variables, especially for the lens thicknesses (the default values are too large).
- In *Optimize*  $\rightarrow$  *Optimization conditions*, one should set a large value (e.g.  $10^7$ ) for the *Weight of boundary conditions violation* (the default value is too small).

Figure 5.7 – OSLO settings to generate the error function.



Another group of fundamental settings are those used for the generation of the error function, which is arguably the most critical object of the entire optimization algorithm: an improper choice of the error function may lead to an undesired outcome, meaning that the system will not be optimized according to its original purposes. For sake of clarity, the complete OSLO error function settings (*Optimize* → *Generate Error Function* → *OSLO Spot Size/Wavefront*) are reported in Fig. 5.7 as they appear in the user interface.

## 5.4 Simulations results

In this section we report on the results obtained from the ray-tracing simulations with OSLO. To better explain the process that led to the final designs, we start by briefly discussing the first steps taken in the study of this problem, which ultimately provided fundamental hints towards the solution.

Initially, we tried to re-optimize some among the objective lenses for quantum gases presented in the literature [92, 93, 94, 95, 96, 97], trying to adapt them to the lithium-chromium mixture and to our experimental setup. Most of these systems are essentially different implementations of the original Alt's scheme [92]. This objective exploits solely four singlets: the first three are positive lenses, while the last one (the so-called *field lens*) is negative. In particular, in most implementations, the first two elements are positive meniscus or plano-convex lenses, the third one is double-convex, whereas the field lens is plano-concave. It was argued that this represents the minimal system of spherical lenses that is able to correct for the spherical aberrations introduced by the vacuum window [92, 94]. However, since in every implementation the various lenses are all realized with the same optical glass, these systems cannot correct for longitudinal chromatic aberrations, as pointed out in Sec. 5.2 (and by the authors themselves).

These initial attempts of re-optimization consisted firstly in varying the air spacings between the singlets, as suggested by the authors, subsequently allowing for more degrees of freedom if an acceptable solution was not found. In short, in some

cases we were able to obtain relatively good corrections for spherical aberrations, reaching diffraction-limited operation for at least one of the two imaging wavelengths ( $\lambda_{Li} = 671$  nm and  $\lambda_{Cr} = 425.5$  nm, respectively). However, as expected, every solution we found suffered from a sizeable amount of longitudinal color, on the order of  $1.5 \div 2$  mm. Such a large LCA could not be corrected – in the very last step of optimization – by adjusting the position of the tube lens. For compactness, these re-optimized designs are not reported here, their overall performances (especially those concerning color correction) being rather far from the desired ones.

After a careful examination of the similarities in the schemes discussed above, and following the discussion in Sec. 5.2, the first idea to try to achieve axial color correction was simply to introduce a negative lens made with a dispersive glass. In particular, the natural choice would be to replace the field lens in Alt’s design with an analogous plano-concave flint lens, to implement a color-correction scheme conceptually analogous to the one used for achromatic doublets (see again Eq. (5.22)). Unfortunately, the scarcity of 2” plano-concave flint lenses in commercial catalogues forced us to abandon this solution.<sup>17</sup>

The second attempt relied instead on a totally different variation of Alt’s scheme: namely, replacing the double-convex lens with an achromatic doublet. Ultimately, this turned out to be a successful intuition,<sup>18</sup> leading to the first scheme (*Design #1*) able to provide a relatively good, simultaneous correction for spherical aberrations and longitudinal color, with respect to  $\lambda_{Li}$  and  $\lambda_{Cr}$ . In particular, at least on a qualitative level, correction for spherical aberrations in this design can be understood on the basis of the similarities with Alt’s scheme, namely the geometrical shape of the lenses, and the correspondences between curvature radii of different surfaces. On the other hand, the blue-red longitudinal color correction originates from the combined action of the achromatic doublet and the field lens, which (to a very rough approximation) act as a low-power (i.e. long focal length) positive element, with a large and anomalous chromatic focal shift (i.e. a significantly over-corrected LCA). On the lines of Eqs. (5.15) and (5.21), an optical system with an anomalous CFS can be thought as an “effective” lens with a negative  $V$ -number. Such a peculiar system, when in turn combined with the remaining two positive lenses of *Design #1* (which act as a normal positive element), can fulfil an (approximate) achromatic condition similar to Eqs. (5.22) and (5.27), thereby enabling correction for longitudinal color.<sup>19</sup> With regard to the optimization routines, the introduction of an achromatic doublet poses some additional constraints on the fitting variables. In fact, commercial achromats are realized with several different combinations of crown and flint glasses,

<sup>17</sup>As previously noted, a diameter of 2” is required to achieve good numerical apertures, given the large working distance of roughly 30 mm (constrained by the geometry of our vacuum chamber).

<sup>18</sup>We later found that a conceptually similar achromatized scheme was already implemented in Ref. [99]. However, despite employing merely three elements (the details of which are not reported by the author), this design relies on two aspheric surfaces, which significantly increase manufacturing difficulties and costs.

<sup>19</sup>Strictly speaking, Eqs. (5.22) and (5.27) are not particularly accurate in this case, as the glass thicknesses are not always negligible, and the generalization of these formulae to a system composed by more than two lenses turns out to be less obvious than expected, see e.g. the results for the effective focal lengths in Ref. [98]. On the other hand, as discussed in the following, Eq. (5.31) provides better results. Anyway, the main point here is that an effective negative  $V$ -number allows for more sign combinations of focal lengths in the fulfilment of an achromatic condition.

but typically for each combination only a few different lenses are available. For this reason, it results rather inconvenient to optimize the system with the achromat parameters as fitting variables, meaning that – while very good solutions can indeed be obtained – in the end it will be nearly impossible to find a matching doublet in commercial catalogues. Accordingly, aiming to converge to a set of catalogue lenses for the final design, to carry out the simulations we kept the achromat “fixed”, picking one among those available in commercial catalogues, and we optimized the remaining lenses and air spaces. This procedure was carried out for different initial choices of the achromatic doublet.

The first design of this kind that converged to a set of catalogue lenses (namely, *Design #1*) relied on a  $f = 80$  mm achromatic doublet (Thorlabs, AC508-080) as a starting point. Although not completely reaching the desired performances (having a quite narrow field of view), nor totally fulfilling the initial requirements (its main drawback being the rather inconvenient position of the MOT beams focus), *Design #1* is nonetheless briefly illustrated in the following, as it represents the fundamental building block for subsequent schemes.

#### 5.4.1 Design #1

As anticipated above, the first design that featured an acceptable degree of color correction, together with diffraction-limited operation, was based on Alt’s scheme [92]. The core idea has been the replacement of the double-convex lens with an achromatic doublet. As shown in the following, such a combination of lenses can provide a relatively good, simultaneous correction for (monochromatic) wave aberrations and longitudinal color, relatively to two design wavelengths.

The final design for this objective lens is sketched in Fig. 5.8, with the surface data reported in detail in Tab. 5.2, following the conventions adopted by OSLO. Note that the vacuum window thickness is slightly over-estimated (10 mm instead of 7.94 mm, see the following designs), as the precise value was not known when this scheme was firstly being optimized (it was measured later).

The overall performances and the relevant figures of merit (for the objective lens system, i.e. not including a tube lens) are summarized in Tab. 5.3. On axis, the objective reaches diffraction-limited operation (with  $S_r > 0.95$ ,  $WFE < 0.25$ ,  $W_{\text{rms}} < 0.07$ ) up to a numerical aperture  $NA = 0.35$ , providing a theoretical resolution close to  $1 \mu\text{m}$  for both wavelengths. Further, the longitudinal chromatic aberration between  $\lambda_{\text{Cr}}$  and  $\lambda_{\text{Li}}$  is on the order of a few tens of microns, considerably lower than in the aforementioned re-optimized systems (even though still not perfectly zeroed). The main limitation regarding the imaging performances lies in the rather

**Figure 5.8** – *Design #1*: plan and solid drawings with ray caustics.

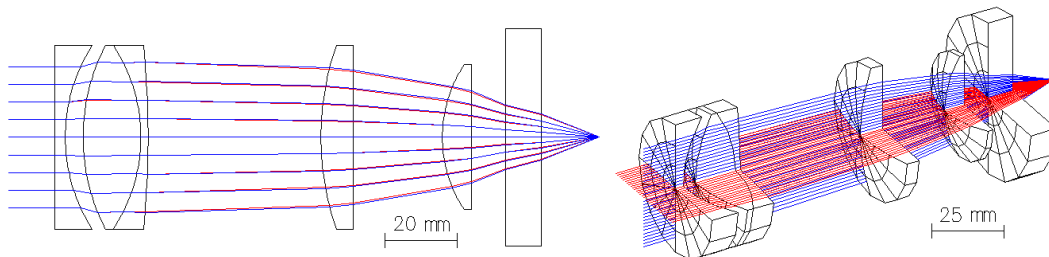


**Table 5.2** – Surface data for *Design #1*. For each element,  $F$  is the nominal focal length. Then, for each refracting surface,  $R$  is the curvature radius, while  $t_c$  is the central thickness of the subsequent layer, whose medium is specified in the last column. Following the convention adopted by OSLO, a null curvature radius denotes a plan surface.

Element	$F$ [mm]	$R$ [mm]	$t_c$ [mm]	Medium
[O $\Sigma$ ] SLB-50.8-90NM	- 90	0.00	3.00	N-BK7
		46.71	4.94	Air
[TL] AC508-080-A	80	54.90	16.00	N-BAF10
		- 46.40	2.00	N-SF6HT
		- 247.20	47.93	Air
[EO] 32-975	150	77.52	9.00	N-BK7
		0.00	24.67	Air
[O $\Sigma$ ] SLB-40-70NM	70	36.33	8.00	N-BK7
		0.00	9.50	Air
Window	-	0.00	10.00	Silica
		0.00	16.00	Vacuum

TL stands for Thorlabs, O $\Sigma$  for OptoSigma, and EO for Edmund Optics.

narrow AFOV, which in practice restricts the off-axis diffraction-limited operation to a region of merely some tens of microns. It was later realized that this originated from a wrong setting in the OSLO *Setup* menu, which was corrected in subsequent designs.

Nevertheless, it is interesting to try to understand, at least at a qualitative level, how this scheme implements longitudinal color correction. Although the glass thicknesses are not entirely negligible, we apply Eq. (5.31) to the system, considering the achromatic doublet as two distinct singlets. Lenses are labelled by  $i = 1, \dots, 5$  from left to right in Fig. 5.8. First, with OSLO, the nominal focal lengths of the two elements forming the achromat ( $f_2 = 39.9$  mm and  $f_3 = -70.7$  mm, respectively) can be readily obtained. The  $V$ -numbers for the three glasses of this design can be found in Tab. 5.1, while the air spacings  $d_{i,i'}$  between the singlets are specified in Tab. 5.2. Hence, our main goal is to determine the (relative) heights  $y_i$  at the position of each element. As we shall see, we can express any  $y_i$  in units of  $y_1$ , and in the end the latter will simplify from the calculation. In the reversed system (see Fig. 5.8), the entrance beam is parallel to the optical axis. Therefore, with simple geometric considerations,  $y_2 = y_1 \cdot (1 + d_{1,2}/|f_1|)$ . Inside the achromatic doublet,

**Table 5.3** – *Design #1*: Figures of merit. The nominal focal length is  $F = 55.3$  mm, and the working distance is  $WD = 35.5$  mm. At  $NA = 0.35$ , the longitudinal chromatic aberration is  $LCA = +28$   $\mu\text{m}$ .

$\lambda$ [nm]	NA	AFOV	$S_r$	$f_{\text{cut}}$ [ $\text{mm}^{-1}$ ]	$f_{\text{cut}}^{-1}$ [ $\mu\text{m}$ ]	$R$ [ $\mu\text{m}$ ]	DOF [ $\mu\text{m}$ ]	WFE <sub>0</sub>	$W_{\text{rms},0}$	WFE <sub>ff</sub>	$W_{\text{rms},\text{ff}}$
671.0	0.35	$\pm 0.025^\circ$	0.95	725	1.4	1.2	$\pm 2.2$	0.186	0.038	0.241	0.051
425.5	0.35	$\pm 0.015^\circ$	0.96	1175	0.85	0.74	$\pm 1.4$	0.133	0.034	0.236	0.050

NA is the maximum numerical aperture, at which the other quantities are evaluated. AFOV is the diffraction-limited angular field of view.  $S_r$  is the monochromatic Strehl ratio at best focus.  $f_{\text{cut}}$  is the frequency cutoff of the monochromatic MTF.  $R$  is the Rayleigh resolution limit. DOF is the diffraction-limited depth of focus (on-axis). WFE and  $W_{\text{rms}}$  are the peak-to-valley wavefront error and its r.m.s. value (in units of  $\lambda$ ), respectively, with the subscripts ‘0’ and ‘ff’ specifying whether they are evaluated on-axis or at full-field, respectively.

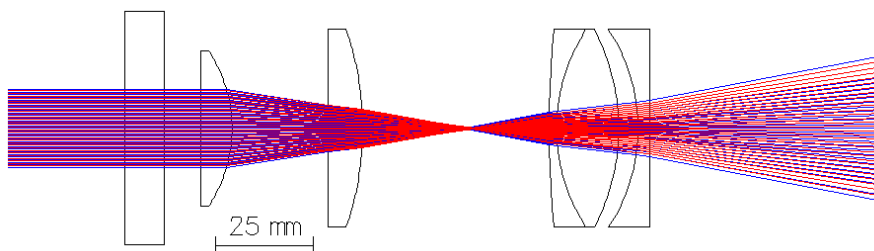
light travels again almost parallel to the optical axis, so we can take  $y_3 \simeq y_2$ . Rays emerge from the doublet rightmost surface forming an image at a distance  $q_{123}$ . With OSLO, we can readily obtain  $q_{123} \simeq 543$  mm for the central wavelength  $\lambda_c = 550$  nm. Hence,  $y_4 \simeq y_3 \cdot (1 - d_{3,4}/q_{123})$ . Repeating this procedure for the following singlet, we obtain  $q_{1234} = 108.2$  mm and  $y_5 \simeq y_4 \cdot (1 - d_{4,5}/q_{1234})$ . Lastly, if we remove the vacuum window, the final image forms at a distance  $q_{12345} = q_5 = 32.1$  mm from the rightmost surface of the last lens, thus  $u_5 \simeq y_5/q_5$ . Adding up all the contributions as in Eq. (5.31), we eventually get  $LCA \simeq 8$   $\mu\text{m}$ , i.e. a value essentially close to 0. Although the precise value extracted with OSLO (when the vacuum window is removed) is  $LCA_{\text{OSLO}} = -34$   $\mu\text{m}$ , the thin-lens model is able to provide a relatively good understanding for the axial color correction in this design. The small discrepancy likely arise from the finite thickness of the lenses, as well as from the effective air spacings being affected by the curvature radii. For instance, light does not travel parallel to the optical axis inside the last two singlets, so  $y_4$  and  $y_5$  are slightly over-estimated by the simple geometrical method outlined above, and the distances  $d_{i,i'}$  are not simply those measured along the optical axis, as for  $y \neq 0$  they are affected by the surfaces curvature. Nonetheless, the main point is that the achromat and the field lens behave as a positive element with a large over-corrected LCA, whereas the last two singlets act as a normal positive lens, hence with an under-corrected LCA. With a proper combination of these two contributions, longitudinal color can be corrected in the final image.

### MOT beams focus

As anticipated, the major drawback of *Design #1* consists in the rather inconvenient position of the MOT beams focus, which lies in the middle of the objective, as shown in Fig. 5.9. To carry out this analysis, we reversed the entire system, including the vacuum window, and we considered (for each wavelength) a collimated entrance beam with a diameter of 10 mm.

There are basically two different ways to retro-reflect such a beam: The first one consists in placing a (flippable) mirror at the focus position, similarly to a *cat-eye* configuration. The second one relies on collimating the divergent output beam with a positive lens, and then retro-reflecting such a collimated beam. Both these solutions were tested in OSLO, and were found, at least in principle, to work properly. In particular, the LCA at the MOT focus position, on the order of 1 mm, does not prevent an appropriate retro-reflection, meaning that the two reflected beams are nearly-collimated over the length scale of the science chamber. However, from a practical point of view, these two methods may suffer from technical problems. For instance, retro-reflecting the MOT beams at the focus position requires a flippable mirror, which in turn is not directly employable with a standard design of the objective tube. At the same time, using two different tubes would presumably affect

**Figure 5.9** – *Design #1*: plan drawing with ray caustics showing the MOT beams focus.



the mechanical stability of the system, making also the alignment more challenging. On the other hand, collimating the output beam requires a minimum of work space: In a fixed setup, MOT lights must first be divided from the imaging ones, and the most conceivable way to accomplish this is by means of a 2" PBS (MOT beams optics should not clip imaging lights).<sup>20</sup> An alternative is to install the collimating lens and the retro-reflecting mirror on a flippable mount (typically, the time interval between the MOT switching off and the imaging pulse is on the order of  $5 \div 10$  s). In any case, the divergent MOT beams will exceed a diameter of 2" only 9 cm away from the field lens (in free-space), thus requiring a rather compact optical setup to achieve a proper retro-reflection. Unfortunately, the geometry of our experimental setup does not allow for such a close-packed arrangement of optics along the vertical direction. Accordingly, having in mind the basic working principles of *Design #1*, we started a second "stage" of the design process, aiming to find a more suitable configuration. In particular, the underlying idea was to try to shift the MOT beams focus outside the objective, at a position where a flippable mirror could be more easily installed. The first attempts relied on trying different achromatic doublets as starting points for analogue Alt-like schemes. In short, we were able to obtain new working configurations, with simulated performances and figures of merit comparable to those of *Design #1*. In particular, it was found that reducing the focal length of the achromat yields more compact schemes, i.e. with smaller air spacings, and vice versa. However, the shortest focal length for 2"-diameter commercial achromats is  $f = 75$  mm, hence not much different from the  $f = 80$  mm achromat of *Design #1*. The design obtained starting with this shorter  $f$  (essentially analogous to *Design #1* regarding the imaging performances, and thus not reported here for the sake of compactness) features a MOT beams focus that lies inside the achromatic doublet. Clearly, such a focus position is even more inconvenient than the one of *Design #1*. A totally different approach, which ultimately turned out to be successful, relied instead on increasing the number of optics. In particular, it was realized that the MOT beams focus could have been shifted towards the outside by introducing an additional negative lens between the achromatic doublet and the nearest plano-convex lens. To keep the total focal length unchanged, the focal length of the field lens has to be increased (in magnitude) accordingly. As a starting point, we split the field lens into two  $f = -150$  mm elements, placing one of these two after the achromat, as described above. However, the resulting curvature radius of this "new" field lens is, in turn, increased, and starkly differs from the one of the first surface of the achromatic doublet. Such a mismatch introduces a substantial amount of spherical aberrations, and makes the whole design extremely sensitive to small variations of the parameters, e.g. the air spacings. To overcome this problem, we simply split the achromatic doublet into two adjacent doublets, keeping the total focal length the same.<sup>21</sup> This approach has laid the ground for the "second generation" of designs, which are reported in the following.

<sup>20</sup>A more compact solution could be obtained by employing a wire-grid polarizer. However, these devices can significantly lower the image quality, and they cannot be simulated with OSLO.

<sup>21</sup>*Power splitting* consists in replacing a singlet with focal length  $f_s$  with a doublet formed by two adjacent lenses with  $f_1 = f_2 = 2f_s$  [84]. The net effect is that the effective focal length is unchanged (see Eq. (5.17)), while the amount of spherical aberrations is reduced. Intuitively, this owes to the smaller angles of incidence at each surface, see Ref. [84] for more details.

### 5.4.2 Design #2a

Following the idea outlined at the end of Sec. 5.4.1, aiming to move the MOT beams focus outside the objective, we included two more lenses in our scheme, essentially power splitting the field lens and the achromatic doublet. As a starting point, we chose two identical  $f = 150$  mm achromats (Thorlabs, AC508-150) to replace the doublet of *Design #1*. We then split the field lens into two negative elements, inserting one of these two in the space between the last achromat and the first plano-convex lens. We then optimized the whole system, keeping only the achromats parameters as fixed values. By progressively replacing each optimized singlet with the most similar catalogue lens, we eventually converged to a set of commercial elements, referred to as *Design #2a*. The final optical scheme is sketched in Fig. 5.10, and, as shown in Fig. 5.11, the (reverse) system features a MOT beams focus that lies roughly 16 mm after the field lens. The complete surface data of this design are reported in Tab. 5.4, and its simulated performances are summarized in Tab. 5.5, omitting a more detailed discussion. In fact, when we contacted the company manufacturing the  $f = -300$  mm meniscus, they informed us that the item was out of stock, and not on their schedule of future productions. As such, the manufacturing cost for the element would have been basically the same as those for a custom lens, hence nearly ten times higher. Anyway, since the objective performances were rather good, we decided not to discard this design, but, given the unavoidably increased price,

**Figure 5.10** – *Design #2a*: plan and solid drawings with ray caustics.

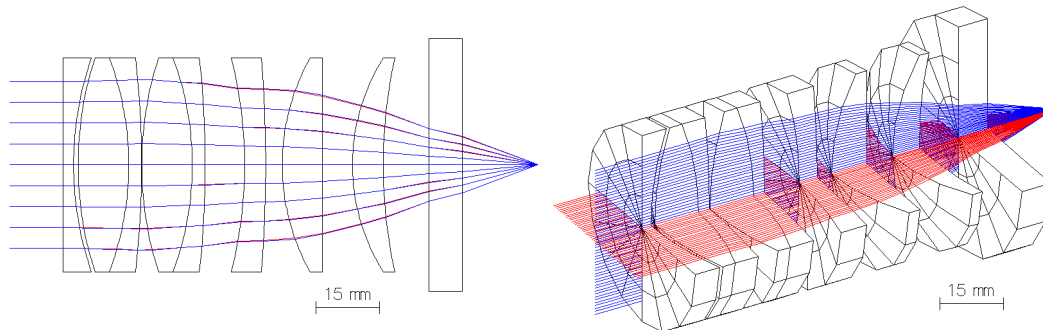


**Figure 5.11** – *Design #2a*: reverse plan drawing showing the MOT beams focus, successfully moved outside the objective.

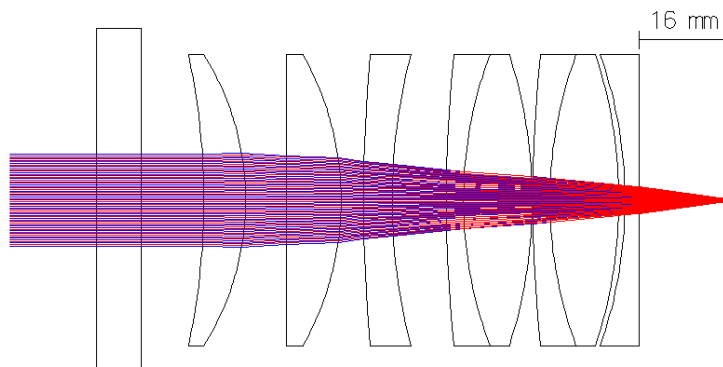


**Table 5.4** – Surface data for *Design #2a*. For each element,  $F$  is the nominal focal length. Then, for each refracting surface,  $R$  is the curvature radius, while  $t_c$  is the central thickness of the subsequent layer, whose medium is specified in the last column. Following the convention adopted by OSLO, a null curvature radius denotes a plan surface.

Element	$F$ [mm]	$R$ [mm]	$t_c$ [mm]	Medium
[NP] KPC073AR.14	- 150	0.00	2.50	N-BK7
		77.52	1.10	Air
[TL] AC508-150-A	150	83.18	12.00	N-BK7
		-72.12	3.00	SF5
		-247.70	0.10	Air
[TL] AC508-150-A	150	83.18	12.00	N-BK7
		-72.12	3.00	SF5
		-247.70	9.45	Air
[UN] UF1129K-A	- 300	-101.41	5.00	N-BK7
		-300.00	3.92	Air
[O $\Sigma$ ] SLB-50.8-100PM	100	51.90	9.60	N-BK7
		0.00	7.09	Air
[TL] LE1418-A	150	47.87	7.29	N-BK7
		119.32	10.88	Air
Window	-	0.00	7.94	Spectrosil-2000
		0.00	18.00	Air

NP stands for Newport, TL for Thorlabs, UN for Unice, and O $\Sigma$  for OptoSigma.

**Table 5.5** – *Design #2a*: Figures of merit. The nominal focal length is  $F = 57$  mm, and the working distance is  $WD = 36.8$  mm. At  $NA = 0.4$ , the longitudinal chromatic aberration is  $LCA = +0.6$   $\mu\text{m}$ .

$\lambda$ [nm]	NA	AFOV	$S_r$	$f_{\text{cut}}$ [ $\text{mm}^{-1}$ ]	$f_{\text{cut}}^{-1}$ [ $\mu\text{m}$ ]	$R$ [ $\mu\text{m}$ ]	DOF [ $\mu\text{m}$ ]	WFE <sub>0</sub>	$W_{\text{rms},0}$	WFE <sub>ff</sub>	$W_{\text{rms},\text{ff}}$
671.0	0.35	$\pm 0.12^\circ$	0.967	720	1.4	1.2	$\pm 2.5$	0.118	0.026	0.145	0.032
425.5	0.35	$\pm 0.20^\circ$	0.997	1150	0.87	0.74	$\pm 1.7$	0.037	0.009	0.127	0.025

NA is the maximum numerical aperture, at which the other quantities are evaluated. AFOV is the diffraction-limited angular field of view.  $S_r$  is the monochromatic Strehl ratio at best focus.  $f_{\text{cut}}$  is the frequency cutoff of the monochromatic MTF.  $R$  is the Rayleigh resolution limit. DOF is the diffraction-limited depth of focus (on-axis). WFE and  $W_{\text{rms}}$  are the peak-to-valley wavefront error and its r.m.s. value (in units of  $\lambda$ ), respectively, with the subscripts ‘0’ and ‘ff’ specifying whether they are evaluated on-axis or at full-field, respectively.

we took the opportunity to further improve the system, by re-optimizing it with the meniscus parameters as fitting variables. This procedure yielded *Design #2b*, an improved version of *Design #2a*, which is presented in more detail in the next section.

### 5.4.3 Design #2b

*Design #2b*, sketched in Fig. 5.12, is an improved version of *Design #2a*. As anticipated, since the  $f = -300$  mm meniscus was not available from the company (Unice), we decided to re-optimize the system, allowing the parameters of this element (i.e. curvature radii and central thickness) to be optimization variables. Air spacings were optimization variables as well, except the thinner one (between the field lens and the first achromat), which – to simplify future assembly – was kept fixed at the value corresponding to an edge air thickness of 0.5 mm (that is, the smaller thickness of commercial lens spacers, namely Newport’s *Delrin* spacers). The remaining elements were kept fixed.

The final list of lenses employed for this design is reported in Tab. 5.6. In the following, we present in detail the simulated results for the objective performances.

**Figure 5.12** – *Design #2b*: plan and solid drawings with ray caustics.

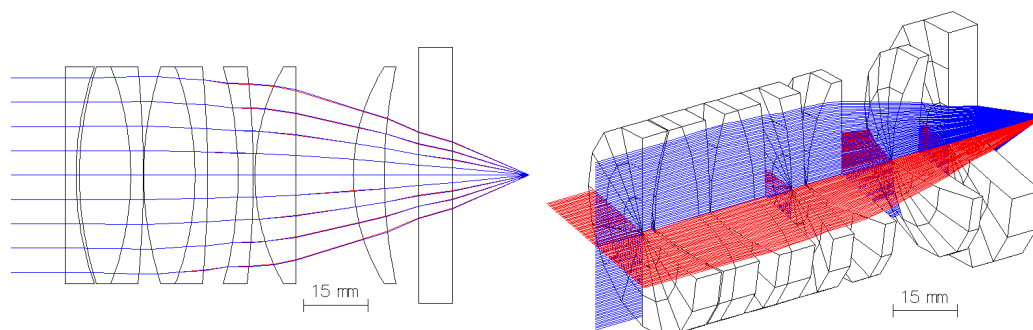


**Table 5.6** – Surface data for *Design #2b*. For each element,  $F$  is the nominal focal length. Then, for each refracting surface,  $R$  is the curvature radius, while  $t_c$  is the central thickness of the subsequent layer, whose medium is specified in the last column. Following the convention adopted by OSLO, a null curvature radius denotes a plan surface.

Element	$F$ [mm]	$R$ [mm]	$t_c$ [mm]	Medium
[NP] KPC073AR.14	- 150	0.00	2.50	N-BK7
		77.52	0.81	Air
[TL] AC508-150-A	150	83.18	12.00	N-BK7
		-72.12	3.00	SF5
		-247.70	0.10	Air
[TL] AC508-150-A	150	83.18	12.00	N-BK7
		-72.12	3.00	SF5
		-247.70	7.09	Air
[SP] Custom	- 300	-95.00	3.50	H-K9L
		-244.60	0.50	Air
[O $\Sigma$ ] SLB-50.8-100PM	100	51.90	9.60	N-BK7
		0.00	13.46	Air
[TL] LE1418-A	150	47.87	7.29	N-BK7
		119.32	8.00	Air
Window	-	0.00	7.94	Spectrosil-2000
		0.00	18.00	Air

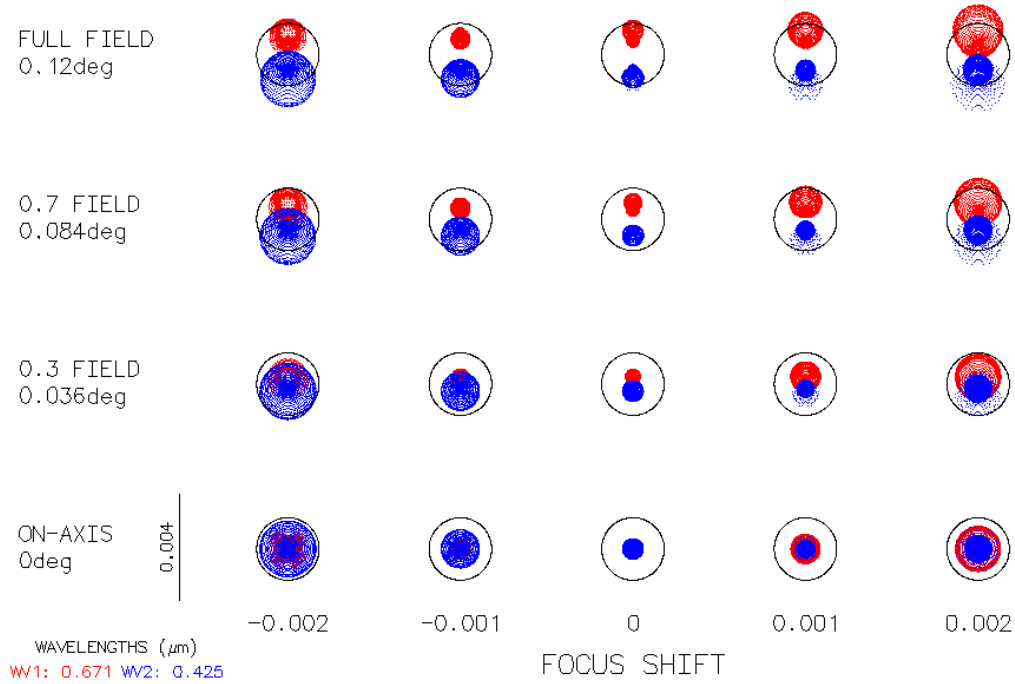
NP stands for Newport, TL for Thorlabs, SP for Solid Photon, and O $\Sigma$  for OptoSigma.

### Spot diagram

In Fig. 5.13, we plot the geometrical spot diagram for the two imaging wavelengths ( $\lambda_{Li}$  in red, and  $\lambda_{Cr}$  in blue, respectively) versus the field angle and the defocus. Black circles represent the Airy disk for  $\lambda_{Li}$ . On axis and at best focus, for numerical apertures up to 0.4, the spot diagram entirely lies well inside the Airy disk, a first sign pointing to a generally good correction for aberrations. This holds true also at full field ( $\pm 0.12^\circ$ ), and up to a  $\pm 2 \mu\text{m}$  defocus, even though some aberrations start to appear. In particular, for high field values in the image plane, one can notice the presence of a small degree of coma, while defocusing introduces mainly spherical aberrations (i.e. a circularly symmetric increase of the spot size). For  $\lambda_{Cr}$ , the trend is not symmetric around the best common focus, with negative defocus values having a larger impact on the spot size.

Besides, with increasing field angles, one also notices a small lateral color, on the order of  $1 \mu\text{m}$  at full field. As pointed out in Sec. 5.2, transverse chromatic aberrations do not affect the performances our imaging system, as the two wavelengths are eventually recorded on different cameras.

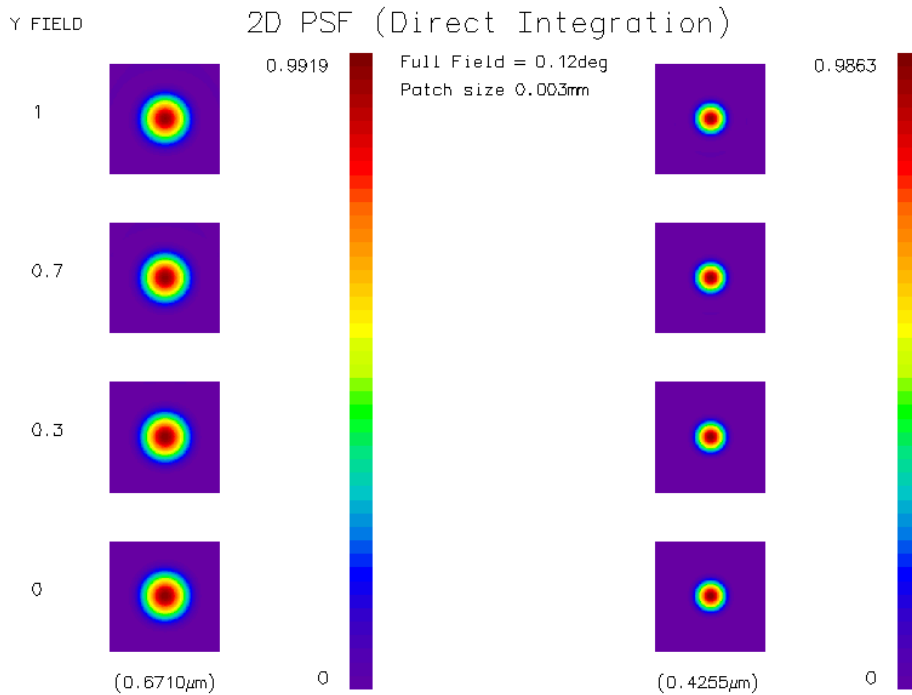
**Figure 5.13** – *Design #2b*: spot diagrams as a function of the field angle and of the defocus.



### Point spread function and Strehl ratio

The two monochromatic PSFs at best focus are shown in Fig. 5.14, for  $NA = 0.35$  and different field values, up to  $\pm 0.12^\circ$ . For both wavelengths, the Strehl ratio is always close to 1, i.e. the objective can be considered diffraction-limited.

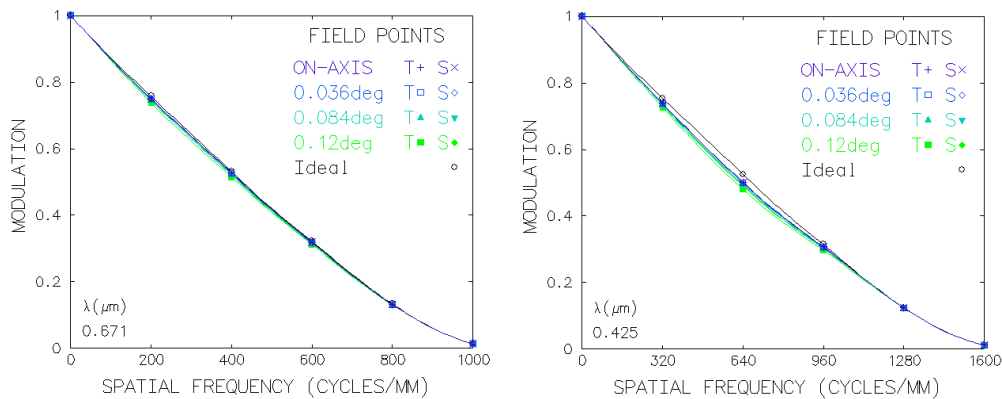
**Figure 5.14** – *Design #2b*: monochromatic PSFs versus the field angle, at best common focus. The maximum value of each color scale corresponds to the (on-axis) Strehl ratio.



### Modulation transfer function

For  $NA \leq 0.4$ , the two monochromatic MTFs at best focus, plotted in Fig. 5.15 for different field values, are essentially coincident with the respective diffraction-limited curves. The best compromise between resolution and contrast is obtained for  $NA = 0.35$ , with two cutoff frequencies being 725 lp/mm (Li) and 1150 lp/mm (Cr), respectively.

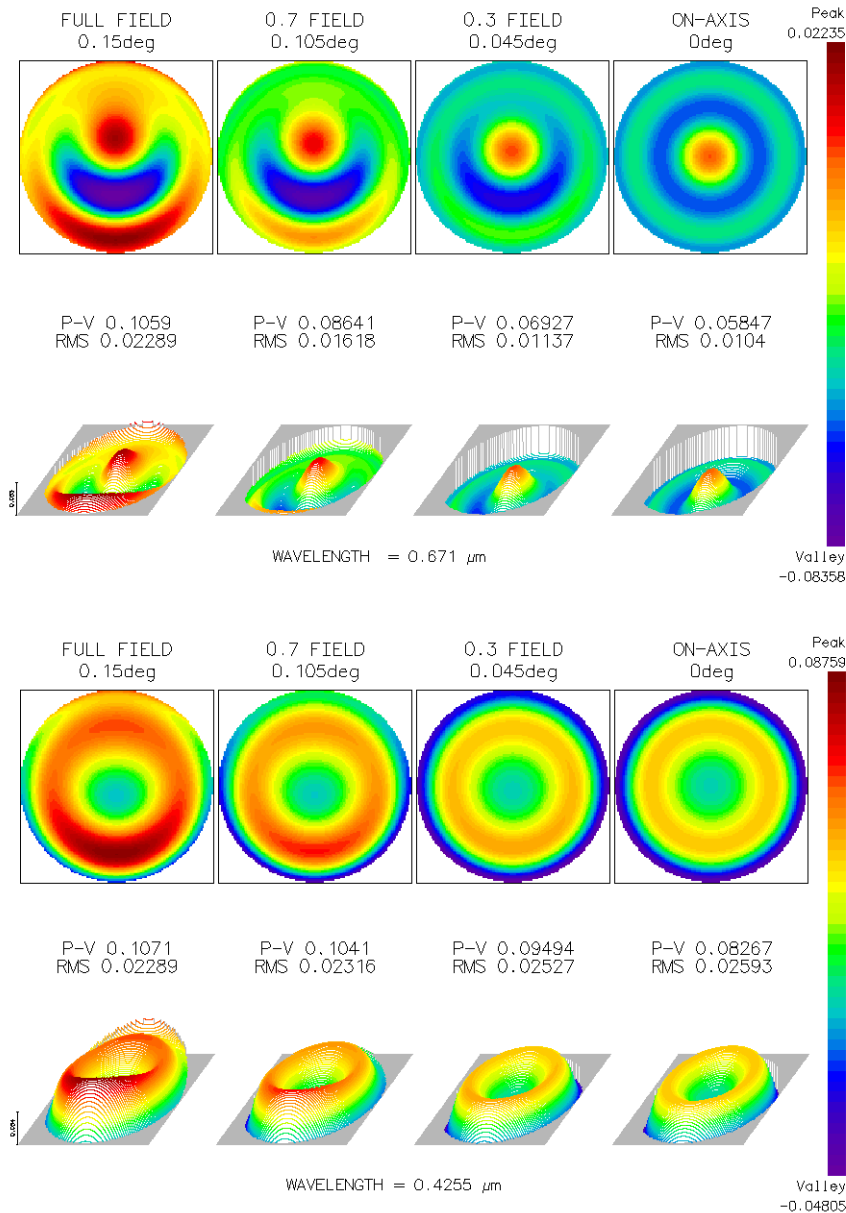
**Figure 5.15** – *Design #2b*: monochromatic MTFs at best focus, for  $NA = 0.35$  and different field values. Black lines represent the diffraction-limited curves.



### Wavefront error

In Fig. 5.16 we present the results of the wavefront error analysis, which in turn confirms a diffraction-limited operation for both wavelengths. The analysis is carried out at each respective monochromatic best focus (i.e. *monochromatic MIN OPD, field averaged* in OSLO). These two points are separated by  $-0.4 \mu\text{m}$  along the optical axis, a value that we can consider as the effective LCA (and, essentially, coincident with 0). In both cases, performances are evaluated for the maximum NA ( $\text{NA}_{\text{max}}^{\text{Li}} = 0.4$  and  $\text{NA}_{\text{max}}^{\text{Cr}} = 0.35$ , respectively) and field angle ( $\pm 0.15^\circ$ ) that yield a peak-to-valley WFE and a r.m.s. error – at full field – that are lower than the diffraction-limited thresholds by a factor of 2. This safety margin has been included to account for possible imperfections and system tolerances in the practical realization and assembly of the objective.

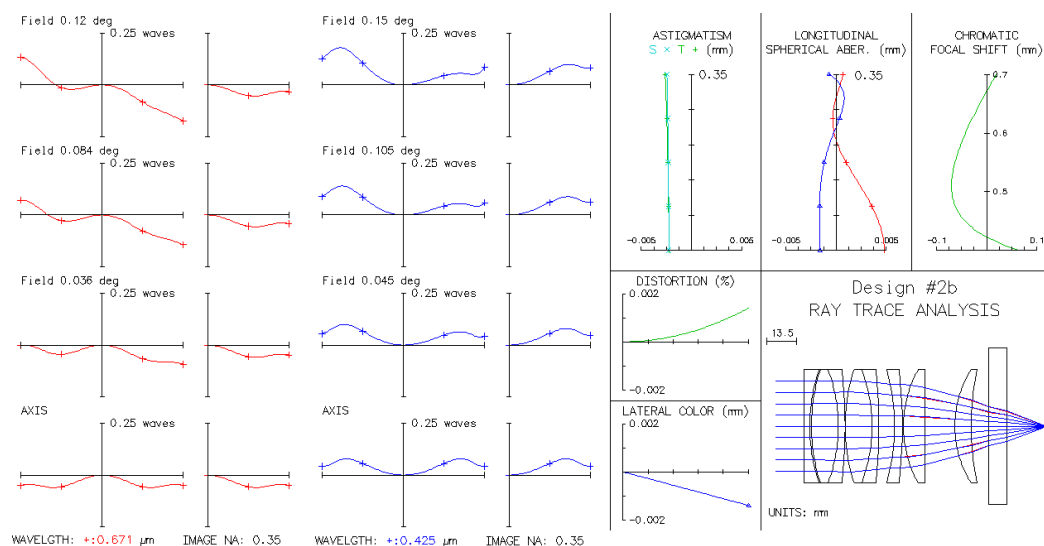
**Figure 5.16** – *Design #2b*: WFEs for the two imaging wavelengths, as a function of the field angle. Simulations are carried out at each monochromatic best focus.



### Ray analysis

In Fig. 5.17, we present a detailed ray analysis that provides an overall overview of the objective performances. In the left half of the picture, we show the OPD curves for  $\lambda_{Li}$  (red) and  $\lambda_{Cr}$  (blue), evaluated at each monochromatic best focus for different field angles. For both wavelengths, the peak-to-valley OPD is always below 0.25 waves, corroborating the diffraction-limited performance. In the right half, we report the behaviour of other aberrations. In particular, the system exhibits negligible astigmatism and distortion, and a small amount of lateral color (below  $2 \mu\text{m}$ ), as already noticed from the spot diagrams. Further, the chromatic focal shift is rather corrected over the entire visible range, with a maximum secondary spectrum on the order of  $100 \mu\text{m}$ . We stress that the CFS of a multi-lens system does not coincide with the actual amount of LCA. The latter is instead shown in the *Longitudinal Spherical Aberration* plot, which represents the variation of the image position for the two wavelengths, as a function of the pupil height (i.e. of the numerical aperture). For  $0.2 \leq \text{NA} \leq 0.35$ , longitudinal color is always below  $1 \mu\text{m}$  (in absolute value), allowing simultaneous operation of the system with the two imaging lights.

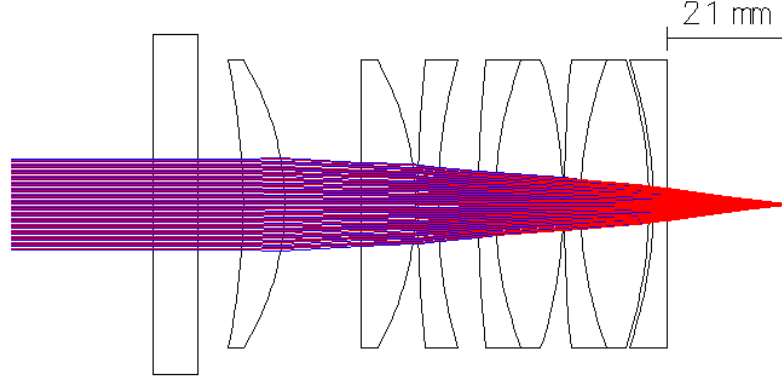
**Figure 5.17** – Design #2b: ray trace analysis, showing OPD curves and aberrations plot.



### MOT beams focus

Fig. 5.18 shows the position of the MOT beams focus, which lies approximatively 2 cm outside the objective, providing enough space to install a small flippable mirror.

**Figure 5.18** – *Design #2b*: reversed sketch and ray caustics showing the MOT beams focus, lying roughly 2 cm outside the objective.



### Figures of merit

Gathering all the previous results together, Tab. 5.7 reports the figures of merit for the objective lens system. In the case of  $\lambda_{Cr}$ , the maximum numerical aperture and field angle have been reduced to 0.35 and  $0.12^\circ$ , respectively, in order to guarantee a safety margin of a factor of 2 on the WFE at full field.

The complete system includes also the two tube lenses that focus the imaging lights onto the two cameras. These are two  $f = 1500$  mm plano-convex lenses, which provide a final magnification  $M \simeq 26$ . The pixel size of the two detectors is nominally  $13 \mu\text{m}$ , thus an area of  $1 \mu\text{m}^2$  in the object plane is mapped on a  $2 \times 2$  array of pixels. When the two tube lenses are included, the performances of the objective (as a whole) slightly increase for each wavelength. Besides, for finite conjugates, OSLO provides the FOV in length units (as opposed to afocal systems, where only the AFOV is a meaningful quantity). We obtain  $\text{FOV}_{\text{max}} = \pm 150 \mu\text{m}$  for both wavelengths (for  $\text{NA}_{Li} = 0.4$  and  $\text{NA}_{Cr} = 0.35$ , respectively), always considering the safety margin on the WFE at full field.

**Table 5.7** – *Design #2b*: Figures of merit for the objective lens system. The nominal focal length is  $F = 57$  mm, and the working distance is  $\text{WD} = 34$  mm. At  $\text{NA} = 0.35$ , the longitudinal chromatic aberration is  $\text{LCA} = +0.4 \mu\text{m}$ .

$\lambda$ [nm]	NA	AFOV	$S_r$	$f_{\text{cut}}$ [ $\text{mm}^{-1}$ ]	$f_{\text{cut}}^{-1}$ [ $\mu\text{m}$ ]	$R$ [ $\mu\text{m}$ ]	DOF [ $\mu\text{m}$ ]	WFE <sub>0</sub>	$W_{\text{rms},0}$	WFE <sub>ff</sub>	$W_{\text{rms},\text{ff}}$
671.0	0.40	$\pm 0.15^\circ$	0.996	825	1.2	1.0	$\pm 2.0$	0.056	0.010	0.112	0.024
425.5	0.35	$\pm 0.12^\circ$	0.985	1125	0.89	0.74	$\pm 1.6$	0.067	0.019	0.105	0.024

$\text{NA}_{\text{max}}$  is the maximum numerical aperture. AFOV is the diffraction-limited angular field of view (for  $\text{NA} = \text{NA}_{\text{max}}$ ).  $S_r$  is the monochromatic Strehl ratio at best focus.  $f_c$  is the frequency cutoff of the monochromatic MTF.  $R$  is the Rayleigh resolution limit (given  $\text{NA}_{\text{max}}$ ). DOF is the diffraction-limited depth of focus. WFE and  $W_{\text{rms}}$  are the peak-to-valley wavefront error and its r.m.s. value, respectively, with the subscripts ‘0’ and ‘ff’ specifying whether they are evaluated on-axis or at full-field, respectively.

### 5.4.4 Design #3

We also searched for solutions to replace the  $f = -300$  mm meniscus in *Design #2a* that did not require custom optics. In particular, owing to the scarcity of 2"-diameter meniscus lenses in commercial catalogues, we opted for a (negative) double-concave element. Concerning the optimization, this removes one degree of freedom, as the two curvature radii of the new singlet coincide in modulus. Hence, while re-optimizing the system, we also allowed the field lens parameters to change. Air spacings were set as fitting variables as well, while the remaining elements were kept fixed. Eventually, we managed to converge to a new set of catalogue lenses, referred to as *Design #3*. The prototype is sketched in Fig. 5.19, with lens and surface data reported in Tab. 5.8. In the following, we present the results for the simulated performances.

**Figure 5.19** – *Design #3*: plan and solid drawings with ray caustics.

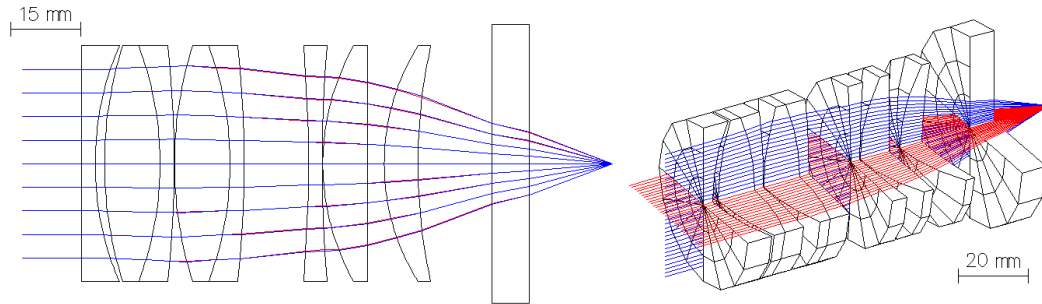


**Table 5.8** – Surface data for *Design #3*. For each element,  $F$  is the nominal focal length. Then, for each refracting surface,  $R$  is the curvature radius, while  $t_c$  is the central thickness of the subsequent layer, whose medium is specified in the last column. Following the convention adopted by OSLO, a null curvature radius denotes a plan surface.

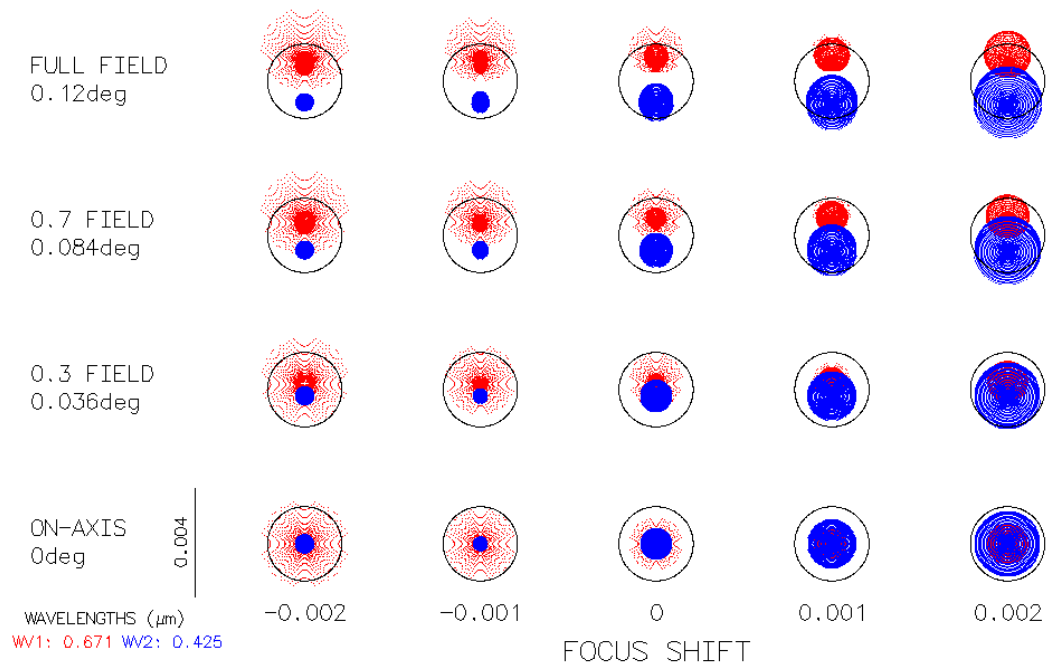
Element	$F$ [mm]	$R$ [mm]	$t_c$ [mm]	Medium
[CVI] LPK-50.0-64.8-C	-125	0.00	3.00	N-BK7
		64.8	2.00	Air
[TL] AC508-150-A	150	83.18	12.00	N-BK7
		-72.12	3.00	SF5
		-247.70	0.10	Air
[TL] AC508-150-A	150	83.18	12.00	N-BK7
		-72.12	3.00	SF5
		-247.70	13.93	Air
[O $\Sigma$ ] SLB-50.8B-300NM	-300	-311.40	3.00	N-BK7
		311.40	0.10	Air
[O $\Sigma$ ] SLB-50.8-100PM	100	51.90	9.60	N-BK7
		0.00	3.666	Air
[TL] LE1418-A	150	47.87	7.29	N-BK7
		119.32	16.00	Air
Window	-	0.00	7.94	Spectrosil-2000
		0.00	18.00	Air

CVI stands for CVI Laser Optics, TL for Thorlabs, and O $\Sigma$  for OptoSigma.

### Spot diagram

In Fig. 5.20, we plot the geometrical spot diagram for the two imaging wavelengths ( $\lambda_{Li}$  in red, and  $\lambda_{Cr}$  in blue, respectively) versus the field angle and the defocus. Black circles represent the Airy disk for  $\lambda_{Li}$ . On axis and at best focus, for numerical apertures up to 0.35, the performances are comparable to those of *Design #2a*, with the spot diagrams lying almost entirely well inside the Airy disk (for  $\lambda_{Li}$ , a fraction of marginal rays actually fall outside, but the spot size r.m.s. radius is nonetheless on the order of the Airy radius). As for *Design #2a*, increasing the field angle introduces a bit of coma (aside from  $1 \div 2 \mu\text{m}$  of lateral color), while defocusing introduces spherical aberrations. However, the overall performances in this case are slightly worse.

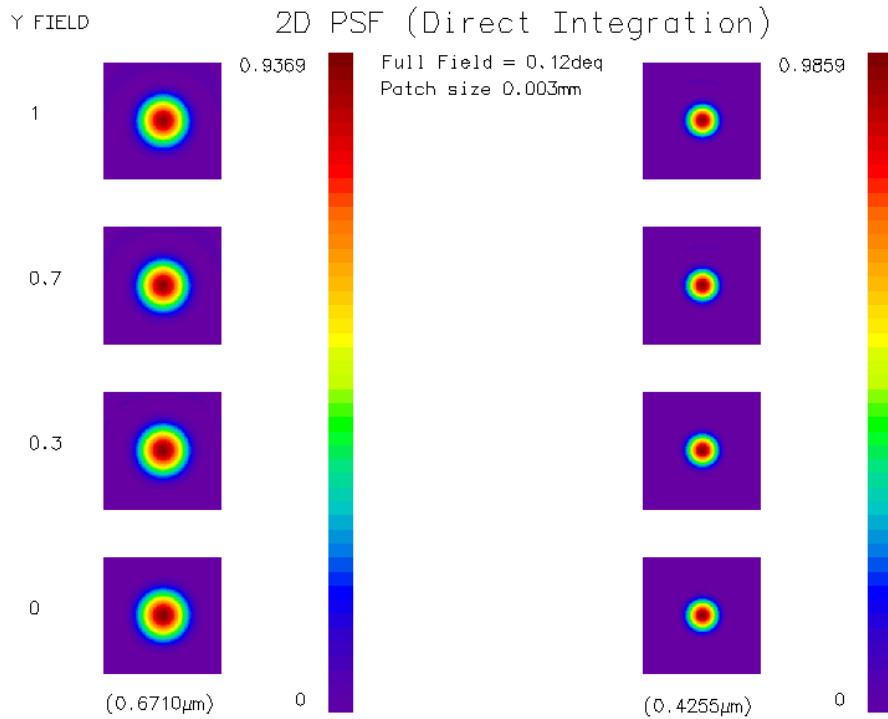
**Figure 5.20** – *Design #3*: spot diagrams as a function of the field angle and of the defocus.



### Point spread function and Strehl ratio

In Fig. 5.21, we plot the monochromatic PSFs for the two wavelengths, for  $NA = 0.35$  and different field values, up to  $\pm 0.12^\circ$ . Although  $S_r$  is always well above 0.8, the performances for  $\lambda_{Li}$  are a bit worse compared either to  $\lambda_{Cr}$  or to *Design #2a*.

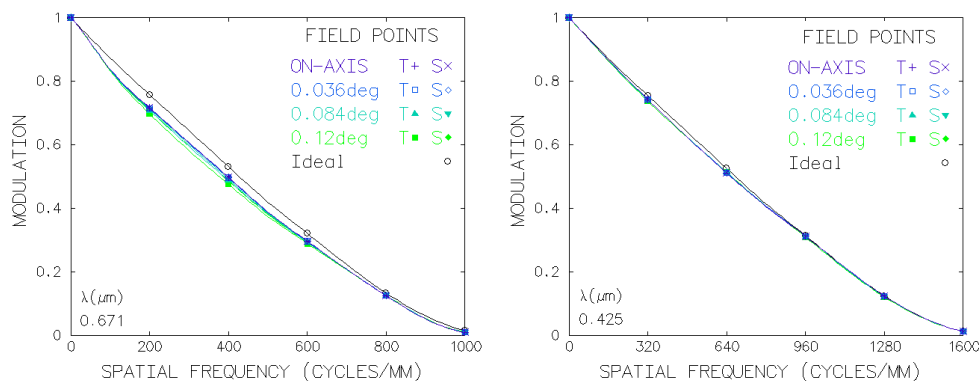
**Figure 5.21** – *Design #3*: monochromatic PSFs versus the field angle, at best common focus. The maximum value of each color scale corresponds to the (on-axis) Strehl ratio.



### Modulation transfer function

In Fig. 5.22, we plot the MTFs for  $\lambda_{Li}$  and  $\lambda_{Cr}$  (left and right panels, respectively), for  $NA = 0.35$  and different field values (up to  $\pm 0.12^\circ$ ). In general, the performances are rather good, with the simulated curves lying quite close to the ideal, diffraction-limited ones. However, also here one can notice that the system behaves slightly worse for the lithium wavelength.

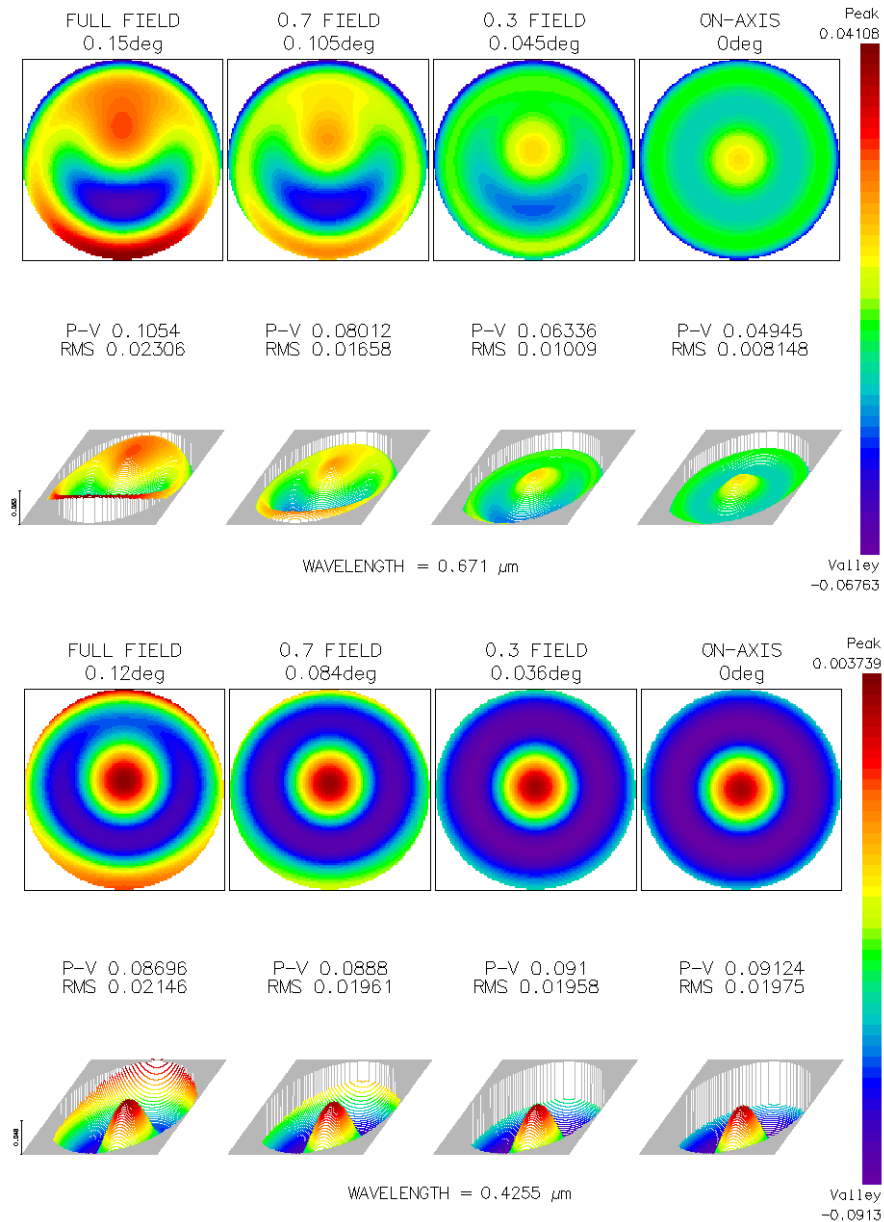
**Figure 5.22** – *Design #3*: monochromatic MTFs at best focus, for  $NA = 0.35$  and different field values. Black lines represent the diffraction-limited curves.



### Wavefront error

The wavefront error analysis, carried out as for *Design #2b*, is presented in Fig. 5.23. The two monochromatic best focuses are in this case separated by roughly  $-1 \mu\text{m}$ . To keep the safety margin on the WFE at full field, we had to decrease the numerical aperture for  $\lambda_{Li}$  down to 0.3 (being however able then to increase the AFOV up to  $\pm 0.15^\circ$ ). In this configuration, the system is diffraction-limited, and it can operate simultaneously with the two imaging wavelengths.

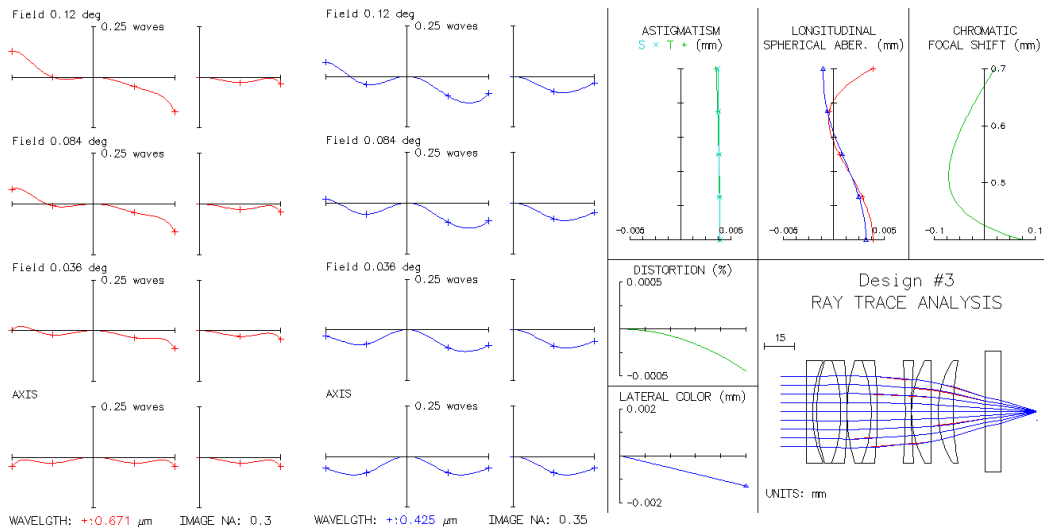
**Figure 5.23** – *Design #3*: WFEs for the two imaging wavelengths, as a function of the field angle. Simulations are carried out at each monochromatic best focus.



### Ray analysis

Fig. 5.24 shows the results of OSLO's ray analysis. Under the same conditions of the WFE analysis, the OPD curves always feature a peak-to-valley difference smaller than  $\lambda/4$ . Further, *Design #3* is also essentially free from astigmatism and distortion. Lastly, differently from *Design #2a*, longitudinal color is highly corrected for  $NA \leq 0.27$ , while it increases for larger apertures.

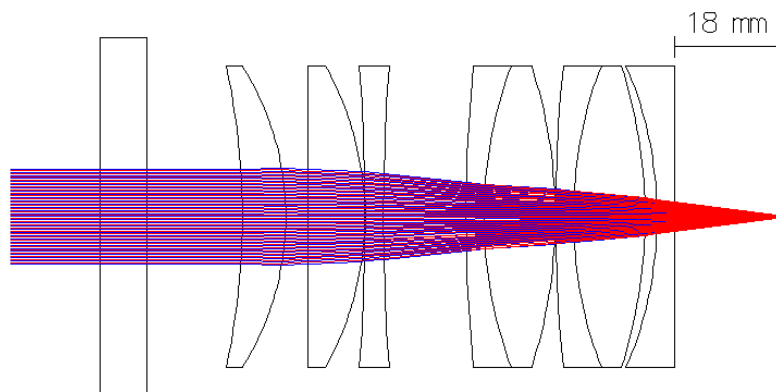
**Figure 5.24** – *Design #3*: ray trace analysis, showing OPD curves and aberrations plot.



### MOT beams focus

Fig. 5.25 shows the position of the MOT beams focus, which also in this case lies approximately 2 cm outside the objective, thus providing enough space for installing and operating a flippable mirror.

**Figure 5.25** – *Design #3*: reversed sketch and ray caustics showing the MOT beams focus.



### Figures of merit

Gathering all the previous results together, Tab. 5.9 reports the figures of merit for the objective lens system. The objective satisfies the initial requirements, although its performances are slightly worse than *Design #2a*

**Table 5.9** – *Design #3*: Figures of merit for the objective lens system. The nominal focal length is  $F = 57$  mm, and the working distance is  $WD = 42$  mm. At  $NA = 0.35$ , the longitudinal chromatic aberration is  $LCA = +2.5$   $\mu\text{m}$ .

$\lambda$ [ $\mu\text{m}$ ]	$NA_{\text{max}}$	AFOV	$S_r$	$f_c$ [lp/mm]	$10^3/f_c$ [ $\mu\text{m}$ ]	$R$ [ $\mu\text{m}$ ]	DOF [ $\mu\text{m}$ ]	WFE <sub>0</sub>	$W_{\text{rms},0}$	WFE <sub>ff</sub>	$W_{\text{rms},\text{ff}}$
0.671	0.30	$\pm 0.15^\circ$	0.997	625	1.6	1.4	$\pm 3.6$	0.034	0.008	0.111	0.025
0.425	0.35	$\pm 0.12^\circ$	0.985	1150	0.87	0.74	$\pm 1.6$	0.083	0.019	0.124	0.029

$NA_{\text{max}}$  is the maximum numerical aperture. AFOV is the diffraction-limited angular field of view (for  $NA=NA_{\text{max}}$ ).  $S_r$  is the monochromatic Strehl ratio at best focus.  $f_c$  is the frequency cutoff of the monochromatic MTF.  $R$  is the Rayleigh resolution limit (given  $NA_{\text{max}}$ ). DOF is the diffraction-limited depth of focus. WFE and  $W_{\text{rms}}$  are the peak-to-valley wavefront error and its r.m.s. value, respectively, with the subscripts '0' and 'ff' specifying whether they are evaluated on-axis or at full-field, respectively.

## 5.5 Final remarks

In this chapter, I described the design and simulation of a bichromatic high-resolution imaging system for our Li-Cr mixture. Two different prototypes are proposed: The former (*Design #2b*), involving a custom meniscus, exhibits in general remarkably good performances, with all the relevant figures of merit pointing towards diffraction-limited operation. The latter (*Design #3*), relying on commercial lenses only, still satisfies our initial requirements, although with slightly worse performances for the lithium wavelength, which can anyway be considerably improved by moderately decreasing the numerical aperture.

In Tab. 5.10 we compare our two designs with other Alt-like schemes reported in the literature. Albeit still lacking a practical realization, which is on the schedule of near-future pursuits in our group, results from our ray-tracing simulations are certainly promising.

**Table 5.10** – Comparison between different objectives.

$\lambda$ [ $\mu\text{m}$ ]	NA	$R$ [ $\mu\text{m}$ ]	FOV [ $\mu\text{m}$ ]	$F$ [mm]	WD [mm]	$t_w$ [mm]	Ref.
0.852	0.29	1.8	$\pm 500$	36	37	5.00	[92]
0.780	0.36	1.3	$\pm 180$	47	35	5.00	[93]
0.852	0.29	1.8	$\pm 440$	67	65	6.40	[94]
0.780	0.44	1.1	$\pm 105$	53	36	5.00	[95]
0.589	0.52	0.71	$\pm 170$	41	23	9.53	[96]
0.461	0.44	0.63	$\pm 100$	25	18	3.13	[97]
0.671	0.40	1.0	$\pm 150$	57	34	7.94	[#2b]
0.425	0.35	0.74	$\pm 120$				
0.671	0.30	1.4	$\pm 150$	57	42	7.94	[#3]
0.425	0.35	0.74	$\pm 120$				

$\lambda$  specifies the design wavelength(s), NA is the numerical aperture,  $R$  is the resolution, FOV is the diffraction-limited field of view,  $F$  is the effective focal length, WD is the working distance, and  $t_w$  is the vacuum window thickness.

# Conclusions

My thesis work has encompassed three main activities: the first realization of ultracold  ${}^6\text{Li}$ - ${}^{53}\text{Cr}$  Fermi mixtures, the investigation of their interspecies scattering properties via Feshbach loss spectroscopy, and the design of a bichromatic high-resolution objective.

To attain ultralow temperatures in our novel system, we have devised and optimized an all-optical strategy, loading atoms into a bichromatic optical dipole trap directly from the steady-state double-species MOT. Our procedure starkly differs from the ones previously employed to cool chromium samples [65] – one of the key points being the IR light-shift compensation via 532 nm light – and it allowed us to attain more than a 100-fold increase in the number of cold Cr atoms, relative to previous studies. In the BODT we perform a sympathetic cooling stage, relying on highly-efficient evaporative cooling of the two lowest Zeeman states of  ${}^6\text{Li}$  near the 832 G homonuclear Feshbach resonance. In turn, the remarkable efficiency with which the sympathetic cooling stage works constitutes a first indication for favorable Cr-Li interspecies collisional properties, and it represents an optimum starting point for future studies in the degenerate regime.

With our ultracold samples we have performed extensive Feshbach loss spectroscopy, exploring up to six different Li+Cr scattering channels. Our experimental effort was primarily targeted at the detection of heteronuclear Feshbach resonances, the (magnetic) positions of which constitute the fundamental input for quantum collisional models. The main outcome of our investigation is a set of about 50 Li-Cr FRs, pinpointed within a magnetic field region that spans from 0 to 1500 G.

On the theoretical side, the coupled-channel model developed by our collaborator, Prof. A. Simoni, still requires some fine adjustment in order to become quantitatively accurate over the whole  ${}^6\text{Li}$ - ${}^{53}\text{Cr}$  Feshbach spectrum, and possibly over those of other isotopic combinations as well. According to the current assignment, however, it already reliably predicts the values  $a_{5/2} \sim 14 a_0$  and  $a_{7/2} \sim 42 a_0$  for the exaplet and octuplet background scattering lengths, respectively. Further, most of the observed low-field loss features appear connected to  $p$ -wave FRs, whereas those around 1400 G are interpreted as  $s$ -wave resonances.

Notably, on the experimental side, a very recent characterization of the elastic scattering near one of these high-field resonances, not discussed in this work, confirms its  $s$ -wave nature, pointing to a magnetic field width  $\Delta B$  on the order of  $\sim 1 \div 2$  G. Our work lays the ground for a wealth of next-future experimental studies in the quantum-degenerate regime: From the investigation of exotic few- and many-body phenomena in resonantly interacting, mass-imbalanced Fermi mixtures, to the realization of quantum gases of CrLi ground-state bi-polar molecules.

Lastly, the design and simulation of the high-resolution imaging system was a totally independent side project, that I carried out during my initial period in the lab, when the Cr oven was temporarily unavailable. The final optical scheme

is the result of subsequent implementations of the original Alt's design [92], a starting point for many "home-made" high-resolution objectives for ultracold atom experiments. The introduction of achromatic doublets has enabled the achievement of an almost perfect correction for longitudinal chromatic aberrations, relatively to our two imaging wavelengths ( $\lambda_{\text{Li}} = 671 \text{ nm}$  and  $\lambda_{\text{Cr}} = 425.5 \text{ nm}$ ), an essential requirement to take simultaneous images of our two atomic samples. According to ray-tracing simulations, the system that I designed is diffraction-limited up to numerical apertures on the order of  $0.35 \div 0.40$ , and over a field of view of about  $250 \div 300 \text{ }\mu\text{m}$  in size, with overall performances completely comparable to similar, but monochromatic, Alt-like schemes reported in the literature.

On the practical side, the next challenges are the design of a suitable objective case to firmly hold the lenses in place, accommodating the tight tolerances of this kind of systems, and the subsequent assembly and test of the prototypes. If the simulated performances will be confirmed and attained with the real objective, the latter will be installed on our experimental setup, allowing us to increase our current optical resolution by a factor of 10.

# Bibliography

- [1] A. D. Ludlow, M. M. Boyd, J. Ye, E. Peik, P. O. Schmidt, *Optical atomic clocks*, Rev. Mod. Phys. **87**, 637 (2015)
- [2] I. Bloch, J. Dalibard, W. Zwerger, *Many-Body Physics with Ultracold Gases*, Rev. Mod. Phys. **80**, 885 (2008)
- [3] M. H. Anderson, J. R. Ensher, M. R. Matthews, C. E. Wieman, E. A. Cornell, *Observation of Bose-Einstein Condensation in a Dilute Atomic Vapor*, Science, **269** (5221), 198–201 (1995)
- [4] K. B. Davis, M.-O. Mewes, M. R. Andrews, N. J. van Druten, D. S. Durfee, D. M. Kurn, W. Ketterle, *Bose-Einstein Condensation in a Gas of Sodium Atoms*, Phys. Rev. Lett. **75**, 3969 (1995)
- [5] M. R. Andrews, C. G. Townsend, H.-J. Miesner, D. S. Durfee, D. M. Kurn, W. Ketterle, *Observation of Interference Between Two Bose Condensates*, Science, **275** (5300), 637–641 (1997)
- [6] C. Raman, M. Köhl, R. Onofrio, D. S. Durfee, C. E. Kuklewicz, Z. Hadzibabic, W. Ketterle, *Evidence for a Critical Velocity in a Bose-Einstein Condensed Gas*, Phys. Rev. Lett. **83**, 2502 (1999)
- [7] K. W. Madison, F. Chevy, W. Wohlleben, J. Dalibard, *Vortex formation in a stirred Bose-Einstein condensate*, Phys. Rev. Lett. **84**, 806 (2000)
- [8] W. Ketterle, D. S. Durfee, D. M. Stamper-Kurn, *Making, probing, and understanding Bose-Einstein condensates*, Proceedings of the International School of Physics Enrico Fermi, (Varenna, 1998)
- [9] E. A. Cornell, J. R. Ensher, C. E. Wieman, *Experiments in dilute atomic Bose-Einstein condensation*, Proceedings of the International School of Physics Enrico Fermi, Varenna (1998)
- [10] D. A. Butts, D. S. Rokhsar, *Trapped Fermi gases*, Phys. Rev. A **55**, 4346 (1997)
- [11] B. DeMarco, D. S. Jin *Onset of Fermi Degeneracy in a Trapped Atomic Gas*, Science, **285** (5434), 1703-1706 (1999)
- [12] A. G. Truscott, K. E. Strecker, W. I. McAlexander, G. B. Partridge, R. G. Hulet, *Observation of Fermi Pressure in a Gas of Trapped Atoms*, Science **291**, 5513 (2001)
- [13] F. Schreck, L. Khaykovich, K. L. Corwin, G. Ferrari, T. Bourdel, J. Cubizolles, C. Salomon, *Quasipure Bose-Einstein Condensate Immersed in a Fermi Sea*, Phys. Rev. Lett. **87**, 080403 (2001)
- [14] L. Tarruell, L. Sanchez-Palencia, *Quantum simulation of the Hubbard model with ultracold fermions in optical lattices*, C. R. Physique **19**, 365-393 (2018)

- [15] K. M. O'Hara, S. L. Hemmer, M. E. Gehm, S. R. Granade, J. E. Thomas, *Observation of a Strongly Interacting Degenerate Fermi Gas of Atoms*, *Science* **298** (5601), 2179-2182 (2002)
- [16] J. Cubizolles, T. Bourdel, S. J. J. M. F. Kokkelmans, G. V. Shlyapnikov, C. Salomon *Production of Long-Lived Ultracold Li<sub>2</sub> Molecules from a Fermi Gas*, *Phys. Rev. Lett.* **91**, 240401 (2003)
- [17] S. Jochim, M. Bartenstein, A. Altmeyer, G. Hendl, C. Chin, J. Hecker Denschlag, R. Grimm, *Pure Gas of Optically Trapped Molecules Created from Fermionic Atoms*, *Phys. Rev. Lett.* **91**, 240402 (2003)
- [18] M. Greiner, C. A. Regal, D. S. Jin, *Emergence of a molecular Bose-Einstein condensate from a Fermi gas*, *Nature* vol. **426**, 537-540 (2003)
- [19] S. Jochim, M. Bartenstein, A. Altmeyer, G. Hendl, S. Riedl, C. Chin, J. Hecker Denschlag, R. Grimm, *Bose-Einstein Condensation of Molecules*, *Science* **302** (5653), 2101-2103 (2003)
- [20] M. W. Zwierlein, C. A. Stan, C. H. Schunck, S. M. F. Raupach, S. Gupta, Z. Hadzibabic, W. Ketterle, *Observation of Bose-Einstein Condensation of Molecules*, *Phys. Rev. Lett.* **91**, 250401 (2003)
- [21] W. Ketterle, M. W. Zwierlein, *Making, probing, and understanding ultracold Fermi gases*, *Proceedings of the International School of Physics Enrico Fermi, Varenna* (2006)
- [22] K.-K. Ni, S. Ospelkaus, M. H. G. de Miranda, A. Pe'er, B. Neyenhuis, J. J. Zirbel, S. Kotochigova, P. S. Julienne, D. S. Jin, J. Ye, *A High Phase-Space-Density Gas of Polar Molecules*, *Science*, **322** (5899), 231-235 (2008)
- [23] V. N. Efimov, *Energy levels of three resonantly interacting particles*, *Nucl. Phys. A* **210**, 157 (1973)
- [24] B. Bazak, D. S. Petrov, *Five-Body Efimov Effect and Universal Pentamer in Fermionic Mixtures*, *Phys. Rev. Lett.* **118**, 083002 (2017)
- [25] O. I. Kartavtsev, A. V. Malykh, *Low-energy three-body dynamics in binary quantum gases*, *J. Phys. B: At. Mol. Opt. Phys.* **40**, 1429 (2007)
- [26] S. Endo, P. Naidon, M. Ueda, *Universal physics of 2+1 particles with non-zero angular momentum*, *Few-Body Syst.* **51**, 207 (2011)
- [27] J. E. Baarsma, K. B. Gubbels, H. T. C. Stoof, *Population and mass imbalance in atomic Fermi gases*, *Phys. Rev. A* **82**, 013624 (2010)
- [28] P. Fulde, R. A. Ferrell, *Superconductivity in a Strong Spin-Exchange Field*, *Phys. Rev.* **135**, A550 (1964)
- [29] A. I. Larkin, Y. N. Ovchinnikov, *Nonuniform state of superconductors*, *Zh. Eksp. Teor. Fiz.* **47** (1964)

- [30] G. Sarma, *On the influence of a uniform exchange field acting on the spins of the conduction electrons in a superconductor*, J. Phys. Chem. Solids **24** (1963)
- [31] W. V. Liu, F. Wilczek, *Interior Gap Superfluidity*, Phys. Rev. Lett. **90**, 047002 (2003)
- [32] D. Blume, *Universal Four-Body States in Heavy-Light Mixtures with a Positive Scattering Length*, Phys. Rev. Lett. **109**, 230404 (2012)
- [33] C. J. Joachain, *Quantum Collision Theory*, North-Holland Publishing Company (1975)
- [34] E. Merzbacher, *Quantum Mechanics*, 3<sup>rd</sup> edition, John Wiley & Sons Inc. (1998)
- [35] M. Abramowitz, I. A. Stegun, *Handbook of Mathematical Functions with Formulas, Graphs, and Mathematical Tables*, 10<sup>th</sup> printing, U.S. Government Printing Office (1972)
- [36] B. H. Bransden, C. J. Joachain, *Physics of Atoms and Molecules*, 2<sup>nd</sup> edition, Pearson (2000)
- [37] C. A. Bertulani, P. Danielewicz, *Introduction to Nuclear Reactions*, 1<sup>st</sup> edition, Taylor & Francis Ltd (2004)
- [38] C. Cohen-Tannoudji, B. Diu, F. Laloe, *Quantum Mechanics*, Vol. 2, Wiley (2005)
- [39] A. Messiah, *Quantum Mechanics*, Vol. 1, North-Holland Publishing Company (1967)
- [40] E. P. Wigner, *On the Behavior of Cross Sections Near Thresholds*, Phys. Rev. **73**, 1002-1009 (1948)
- [41] N. Levinson, *On the uniqueness of the potential in a Schrödinger equation for a given asymptotic phase*, Kgl. Danske Videnskab Selskab. Mat. Fys., **25**, 9 (1949)
- [42] D. S. Petrov, *The few-atom problem*, Oxford University Press (2012)
- [43] J. S. Townsend, V. A. Bailey, *XCVII. The motion of electrons in gases*, The London, Edinburgh, and Dublin Philosophical Magazine and Journal of Science, Series 6, **42** (252), 873–891 (1921)
- [44] C. Ramsauer, *Über den Wirkungsquerschnitt der Gasmoleküle gegenüber langsamen Elektronen*, Wiley, Annalen der Physik, **369** (6), 513–540 (1921)
- [45] G. Breit, E. Wigner, *Capture of slow neutrons*, Phys. Rev. **49**, 519-531 (1936)
- [46] C. Chin, R. Grimm, P. Julienne, E. Tiesinga, *Feshbach resonances in ultracold gases*, Rev. Mod. Phys. **82**, 1225 (2010)
- [47] L. D. Landau, E. M. Lifshitz, J. B. Sykes, J. S. Bell, *Quantum Mechanics, Non-Relativistic Theory: Vol. 3 of Course of Theoretical Physics*

- [48] J. T. M. Walraven, *Quantum Gases, lectures*, University of Amsterdam (2018)
- [49] J. M. Hutson, *Feshbach resonances in ultracold atomic and molecular collisions: threshold behaviour and suppression of poles in scattering lengths*, *New J. Phys.* **9**, 152 (2007)
- [50] K. Pilch, *Optical trapping and Feshbach spectroscopy of an ultracold Rb-Cs mixture*, PhD Thesis, Universität Innsbruck (2009)
- [51] M. Zaccanti, *Tuning of the interactions in ultracold K-Rb quantum gases*, PhD Thesis, LENS and Università di Firenze (2007)
- [52] T. G. Tiecke, *Feshbach resonances in ultracold mixtures of the fermionic quantum gases  $^6\text{Li}$  and  $^{40}\text{K}$* , PhD Thesis, University of Amsterdam (2009)
- [53] P. Naidon, L. Pricoupenko, *Width and shift of Fano-Feshbach resonances for van der Waals interactions*, *Phys. Rev. A* **100**, 042710 (2019)
- [54] M. Jag, M. Cetina, R. S. Lous, R. Grimm, J. Levinsen, D. S. Petrov, *Lifetime of Feshbach dimers in a Fermi-Fermi mixture of  $^6\text{Li}$  and  $^{40}\text{K}$* , *Phys. Rev. A* **94**, 062706 (2016)
- [55] E. Neri, *Mass imbalanced Fermi mixtures with 2- and 3-body resonant interactions*, PhD Thesis, Università di Firenze (2019)
- [56] E. Neri, A. Ciamei, C. Simonelli, I. Goti, M. Inguscio, A. Trenkwalder, M. Zaccanti, *Realization of a Cold Mixture of Fermionic Chromium and Lithium Atoms*, *Phys. Rev. A* **101**, 063602 (2020)
- [57] I. Goti, *Towards the production of ultracold mixtures of Lithium and Chromium atoms*, Master Thesis, Università di Firenze (2019)
- [58] C. Simonelli, E. Neri, A. Ciamei, I. Goti, M. Inguscio, A. Trenkwalder, M. Zaccanti, *Realization of a high power optical trapping setup free from thermal lensing effects*, *Optics Express* **27**, 19 (2019)
- [59] M. E. Gehm, *Properties of  $^6\text{Li}$* , (2003)  
<https://www.physics.ncsu.edu/jet/techdocs/pdf/PropertiesOfLi.pdf>
- [60] P. O. Schmidt, *Scattering properties of ultra-cold chromium atoms*, PhD Thesis, Universität Stuttgart (2003)
- [61] G. Breit, I. I. Rabi, *Measurement of nuclear spin*, *Phys. Rev.* **38**, 2082-2083 (1931)
- [62] A. Trautmann, *Spin Dynamics and Feshbach Resonances in Ultracold Sodium-Lithium Mixtures*, PhD Thesis, University of Heidelberg (2016)
- [63] A. Burchianti, G. Valtolina, J. A. Seman, E. Pace, M. De Pas, M. Inguscio, M. Zaccanti, G. Roati, *Efficient all-optical production of large  $^6\text{Li}$  quantum gases using D1 gray-molasses cooling*, *Phys. Rev. A* **90**, 043408 (2014)

- [64] I. Fritsche, *Sub-Doppler Cooling of Fermionic Lithium*, Master Thesis, University of Innsbruck (2015)
- [65] B. Naylor, A. Reigue, E. Maréchal, O. Gorceix, B. Laburthe-Tolra, L. Vernac, *Chromium dipolar Fermi sea*, Phys. Rev. A **91**, 011603(R) (2015)
- [66] F. M. Spiegelhalter, A. Trenkwalder, D. Naik, G. Kerner, E. Wille, G. Hendl, F. Schreck, R. Grimm, *All-optical production of a degenerate mixture of  $^6\text{Li}$  and  $^{40}\text{K}$  and creation of heteronuclear molecules*, Phys. Rev. A **81**, 043637 (2010)
- [67] S. Krinner, T. Esslinger, J.-P. Brantut, *Two-terminal transport measurements with cold atoms*, J. Phys.: Condens. Matter **29**, 343003 (2017)
- [68] K. M. Jones, P. D. Lett, E. Tiesinga, P. S. Julienne, *Fitting line shapes in photoassociation spectroscopy of ultracold atoms: A useful approximation*, Phys. Rev. A **61**, 012501 (1999)
- [69] A. Green, H. Li, J. H. S. Toh, X. Tang, K. C. McCormick, M. Li, E. Tiesinga, S. Kotochigova, S. Gupta, *Feshbach Resonances in  $p$ -Wave Three-Body Recombination within Fermi-Fermi Mixtures of Open-Shell  $^6\text{Li}$  and Closed-Shell  $^{173}\text{Yb}$  Atoms*, Phys. Rev. X **10**, 031037 (2020)
- [70] J. Li, J. Liu, L. Luo, B. Gao, *Three-Body Recombination near a Narrow Feshbach Resonance in  $^6\text{Li}$* , Phys. Rev. Lett. **120**, 193402 (2018)
- [71] B. Gao, *Universal Model for Exoergic Bimolecular Reactions and Inelastic Processes*, Phys. Rev. Lett. **105**, 263203 (2010)
- [72] B. Gao, *Quantum Langevin model for exoergic ion-molecule reactions and inelastic processes*, Phys. Rev. A **83**, 062712 (2011)
- [73] A. Simoni, Private communication.
- [74] K. Baumann, N. Q. Burdick, M. Lu, B. L. Lev, *Observation of low-field Fano-Feshbach resonances in ultracold gases of dysprosium*, Phys. Rev. A **89**, 020701(R) (2014)
- [75] A. Frisch, M. Mark, K. Aikawa, F. Ferlaino, J. L. Bohn, C. Makrides, A. Petrov, S. Kotochigova, *Quantum chaos in ultracold collisions of gas-phase erbium atoms*, Nature **507**, 475-479 (2014)
- [76] T. Maier, H. Kadau, M. Schmitt, M. Wenzel, I. Ferrier-Barbut, T. Pfau, A. Frisch, S. Baier, K. Aikawa, L. Chomaz, M. J. Mark, F. Ferlaino, C. Makrides, E. Tiesinga, A. Petrov, S. Kotochigova, *Emergence of Chaotic Scattering in Ultracold Er and Dy*, Phys. Rev. X **5**, 041029 (2015)
- [77] M. B. Kosicki, M. Borkowski, P. S. Żuchowski, *Quantum chaos in Feshbach resonances of the ErYb system*, New J. Phys. **22**, 023024 (2020)
- [78] C. Ravensbergen, E. Soave, V. Corre, M. Kreyer, B. Huang, E. Kirilov, R. Grimm, *Resonantly Interacting Fermi-Fermi Mixture of  $^{161}\text{Dy}$  and  $^{40}\text{K}$* , Phys. Rev. Lett. **124**, 203402 (2020)

- [79] M. Born, E. Wolf, *Principles of Optics*, 7<sup>th</sup> ed., Cambridge University Press (1999)
- [80] S. Rolt, *Optical Engineering Science*, John Wiley & Sons Ltd (2020)
- [81] R. Kingslake, R. B. Johnson, *Lens Design Fundamentals*, 2<sup>nd</sup> ed., Academic Press (2010)
- [82] H. Gross, *Handbook of optical systems, Vol. 1: Fundamentals of Technical Optics*, Wiley-VCH (2005)
- [83] W. Singer, M. Totzek, H. Gross, *Handbook of optical systems, Vol. 2: Physical Image Formation*, Wiley-VCH (2005)
- [84] H. Gross, H. Zügge, M. Peschka, F. Blechinger, *Handbook of optical systems, Vol. 3: Aberration Theory and Correction of Optical Systems*, Wiley-VCH (2007)
- [85] H. Gross, F. Blechinger, B. Achtner, *Handbook of optical systems, Vol. 4: Survey of Optical Systems*, Wiley-VCH (2008)
- [86] F. A. Jenkins, H. E. White, *Fundamentals of Optics*, 4<sup>th</sup> ed., McGraw-Hill (2001)
- [87] A. Ghatak, K. Thyagarajan, *Contemporary Optics*, Springer (1978)
- [88] *Fundamental Optics*, CVI Melles-Griot technical guide (2009)
- [89] *Gaussian Beam Optics*, CVI Melles-Griot technical guide (2009)
- [90] *Imaging Resource Guide*, Edmund Optics
- [91] V. N. Mahajan, *Strehl ratio for primary aberrations in terms of their aberration variance*, J. Opt. Soc. Am. **73**, 6 (1983)
- [92] W. Alt, *An objective lens for efficient fluorescence detection of single atoms*, Optik **113**, 3 (2002)
- [93] L. M. Bennie, P. T. Starkey, M. Jasperse, C. J. Billington, R. P. Anderson, L. D. Turner, *A versatile high resolution objective for imaging quantum gases*, Optics Express **21**, 7 (2013)
- [94] J. D. Pritchard, J. A. Isaacs, M. Saffman, *Long working distance objective lenses for single atom trapping and imaging*, Rev. Sci. Instrum. **87**, 073107 (2016)
- [95] X. Li, F. Zhou, M. Ke, P. Xu, X.-D. He, J. Wang, M.-S. Zhan, *High-resolution ex vacuo objective for cold atom experiments*, Applied Optics **57**, 26 (2018)
- [96] M. W. Gempel, T. Hartmann, T. A. Schulze, K. K. Voges, A. Zenesini, S. Ospelkaus, *An adaptable two-lens high-resolution objective for single-site resolved imaging of atoms in optical lattices*, Rev. Sci. Instrum. **90**, 053201 (2019)

- 
- [97] I. H. A. Knottnerus, S. Pyatchenkov, O. Onishchenko, A. Urech, F. Schreck, G. A. Siviloglou, *Microscope objective for imaging atomic strontium with 0.63 micrometer resolution*, arXiv:1906.07167 [physics.optics] (2020)
- [98] G. J. C. L. Bruls, *Exact formulas for a thin-lens system with an arbitrary number of lenses*, *Optik* **126**, 6 (2015)
- [99] F. Serwane, *Deterministic preparation of a tunable few-fermion system*, PhD Thesis, University of Heidelberg (2011)